Measurement of Cross Section and Single Spin Asymmetries of $W^\pm$-Boson Production in Polarized pp Collisions at $\sqrt{s} = 500$ GeV

Kenichi Karatsu

Department of Physics
Kyoto University

A Dissertation Submitted in Partial Fulfillment of
the Requirements for the Degree of Doctor of Science

March, 2011

Abstract

The cross section and non-zero parity-violating asymmetry of W and Z production in polarized pp collisions at $\sqrt{s} = 500$ GeV have been measured for the first time with the PHENIX detector in the RHIC (Relativistic Heavy Ion Collider) Year-2009 run (Run 9).

The data are from polarized $pp \rightarrow e^{\pm} + X$ over a pseudo-rapidity range of $|\eta| < 0.35$, where the $e^{\pm}$ with transverse momentum of $p_T > 30$ GeV/c mainly come from W and Z decays. The results were obtained using the integrated luminosity of 8.56 pb^{-1} accumulated during the Run 9. Averaged beam polarization was about 39 % for the selected runs. Large parity violating longitudinal single-spin asymmetries of $A_L^{e^+} = -0.88^{+0.27}_{-0.12}$ and $A_L^{e^-} = 0.91^{+0.09}_{-0.71}$ are observed for inclusive high transverse momentum $e^{\pm}$'s. The obtained $W^{\pm}$ boson production cross sections for the $e^{\pm}$ channels are $\sigma(pp \rightarrow W^+ X) \times BR(W^+ \rightarrow e^+ \nu_e) = 146.3 \pm 21.0(\text{stat.})^{+3.5}_{-10.5}(\text{sys.}) \pm 23.3(\text{norm.})$ pb, and $\sigma(pp \rightarrow W^- X) \times BR(W^- \rightarrow e^- \nu_e) = 34.2 \pm 13.1(\text{stat.})^{+7.4}_{-8.8}(\text{sys.}) \pm 5.6(\text{norm.})$ pb.

This is the first measurement of the cross section of W production in pp collisions and the results are consistent with NLO (Next-to-Leading Order) and NNLO (Next Next-to-Leading Order) perturbative QCD (pQCD) calculations. The measurement of A_L performed in this thesis establishes a new and direct way to probe flavor-separated polarized quark and anti-quark distribution functions (polarized PDFs) using parity-violating weak interactions. The results are also consistent with NLO pQCD based predictions from polarized PDFs which are extracted from previous polarized (Semi-Inclusive) Deep Inelastic Scattering (DIS) experiments. Although the uncertainties of the obtained results are quite large due to limited statistics, the results indicate that RHIC luminosity and PHENIX detector upgrades in progress will make it possible in the future to significantly reduce the uncertainties of A_L and improve our knowledge of flavor-separated quark and anti-quark spin contribution to the proton spin.

Contents

Chapter 1

Introduction

The proton is one of fundamental particles which comprise the universe, and a variety of researches have been carried out to understand its properties. Our recognition is that every matter can be constructed from a single atomic nucleus with a distinct number of protons and neutrons, surrounded by a cloud of electrons. We never imagined the proton had substructure before 1950s.

The situation has changed in the late 1950s to 1960s with the construction of large particle accelerators. A number of "elementary" particles, called hadrons, were produced by experiments, and their properties are very similar to the nucleons (protons and neutrons). It suggests that the proton is only a part of hadrons, and we began to suspect the proton also consists of more elementary components.

In 1964, Gell-Mann and Zweig independently proposed a scheme to categorize many observed hadrons [1], in which hadrons are composed of smaller particles; quarks. All hadrons are described as combination of quarks, and its quantum numbers are calculated from those of quarks which form the hadron. Baryons including the proton and the neutron consist of three quarks, and mesons, such as pions and kaons, consist of a pair of quark and anti-quark. This simple model (constituent quark model) has been developed based on flavor-SU(3) symmetry of the light quarks; u, d and s quarks. For instance, the proton is described by uud quarks. Although the flavor-SU(3) is not an exact symmetry, it is approximately satisfied due to small difference in mass of these three quarks. Because of this feature, the model successfully categorizes hadrons, and also explains various physics observables of hadrons, such as mass and magnetic moment. The constituent quark model seemed to achieve successful outcomes.

Since late 1960s to 1970s, the existence of structure within the proton was established by experiments of electron-proton Deep Inelastic Scattering (DIS) through γ^* exchange. However, the proton structure revealed by the DIS experiments is more complicate than the static constituent quarks. The results show that about a half the momentum of the proton can be described by the charged components, quarks, but neutral particles have to be introduced to explain another half of the momentum. The neutral particles are gluons. In the proton, gluons are created by dynamic processes; quarks radiate or absorb gluons, a gluon converts into a quark anti-quark pair, and a quark anti-quark pair annihilates into gluons. Such dynamical quarks and gluons in the proton (or hadrons) are called "partons" (parton model). The theoretical framework to explain the interactions between quarks and gluons was developed

3

based on color-SU(3) symmetry and Quantum Chromo Dynamics (QCD), a theory of strong interaction, was established as a part of the Standard Model of the modern physics. In the parton model, partons are categorized into three groups; "valence quarks" which carry the quantum numbers of hadrons, "sea quarks" which are quark and anti-quark pairs generated by pair creation in the hadron vacuum, and "gluons" which are the mediators of the strong force. It was considered that quantum numbers (such as charge, spin, magnetic moment and mass) of the proton could be explained in terms of valence quark in the model.

Although some properties of the proton are explained by valence quarks, it was revealed by polarized DIS experiments that quarks and anti-quarks in the proton carry only ~ 25 % of the proton spin [2, 3, 4, 5]. Combining with the data from β-decay of baryon octet [6], these results indicate that sea quarks are negatively polarized to cancel out the polarization of valence quarks. This picture contradicts to our expectation that quantum numbers can be explained by valence quarks, and various efforts to understand the proton spin structure are stimulated. Because the DIS measurements only involve γ^* exchange, they only provide sensitivity to the combined contributions of quarks and anti-quarks summed over all flavors, and cannot provide information on the flavor-separated polarized quark and anti-quark contributions. In particular, the anti-quark polarizations cannot be determined by the DIS. As the polarized DIS results indicate sea quarks (anti-quarks) also contribute the proton spin, direct measurement of individual polarized anti-quark distributions is an important task to clarify the overall picture of the proton spin structure. More generally, it leads to our deeper understanding of the vacuum of QCD because the anti-quarks are dynamically created from the vacuum inside the proton.

Semi-Inclusive DIS (SIDIS) measurements [7, 8, 9] are one approach to probe a separated quark and anti-quark contribution to the proton spin. The method of SIDIS is almost same as DIS except that part of the final state hadrons are also identified in SIDIS. This method combines information from the proton and the neutron (or deuteron) targets, and uses correlations in the fragmentation process between the type of observed hadron and the flavor of its originating parton. The fragmentation process is quantified in terms of fragmentation functions. However, the dependence on the details of the fragmentation process limits the accuracy of this method, and we still have a vague picture of the individual polarizations especially on the light anti-quarks ($\bar{u}$, $\bar{d}$).

An alternative and more direct way is to utilize the weak interaction. The features of the weak interaction are that it violates the parity conservation and couples to the weak charge which is highly correlated with the flavor. The latter characteristic is useful to select quark flavor in a reaction. Relativistic Heavy Ion Collider (RHIC) is a polarized proton-proton (pp) collider located at Brookhaven National Laboratory. At RHIC, direct sensitivity to the polarization of $u, \bar{u}, d,$ and $\bar{d}$ quarks in the proton becomes available using the production of W bosons [10, 11]. W bosons only couple to the left-handed quarks (q_L) and right-handed anti-quarks ($\bar{q}_R$), i.e. $u_L \bar{d}_R \rightarrow W^+$ and $d_L \bar{u}_R \rightarrow W^-$, so the asymmetry of the W yield from flipping the helicity of a polarized proton is sensitive to the flavor separated quark and

anti-quark contribution. The asymmetry is called single spin asymmetry and defined as:

$$A_L^W = \frac{d\sigma_+ - d\sigma_-}{d\sigma_+ + d\sigma_-},\tag{1.1}$$

where subscripts of $+$ and $-$ on $d\sigma$ indicate the helicity states of proton beam. As W production in polarized pp collisions can observe the pure weak interaction, parity is maximally violated and large A_L^W is expected. This parity-violating single spin asymmetry of W production provides us direct accesses to individual $\Delta u/u, \Delta \bar{u}/\bar{u}, \Delta d/d$ and $\Delta \bar{d}/\bar{d}$ [1]. The merits of this measurement are that the production of W bosons occur at a scale of W boson mass ($M_W \sim 80$ GeV/c^2) where reliable perturbative-QCD calculations are possible and it is free from uncertainties in fragmentation functions when detecting leptons from W decays [12, 13].

In addition to the polarized sector of quark distribution functions, the W production at RHIC also has potential to constrain unpolarized quark distribution functions. In pp collision, the charge ratio of unpolarized W^+ and W^- cross sections ($R = d\sigma(W^+ \to l^+)/d\sigma(W^- \to l^-)$) will directly probe the $\bar{d}/\bar{u}$ ratio [14, 15, 16], while W production in $p\bar{p}$ collision involves much larger valence components and has sensitivity to d/u ratio [17, 18, 19]. Isospin dependence in Drell-Yan (DY) production of muon pairs in pp, pd scattering [20, 21, 22, 23, 24], violation of the Gottfried Sum Rule (GSR) [25, 26], and SIDIS measurements [27] have shown a strong breaking of SU(2) symmetry in the anti-quark sea, with the ratio $\bar{d}/\bar{u}$ rising to 1.6 or higher. A distinct advantage of extracting the $\bar{d}/\bar{u}$ ratio from W boson production in pp collision is that no correction for the nuclear effect in the deuteron and no assumption on the validity of charge symmetry (i.e. $u_p = d_n$, $u_n = d_p$, $\bar{u}_p = \bar{d}_n$ etc.) is required. This is in contrast to the DY experiments and the Gottfried-sum measurement, which require nuclear binding corrections on the effect in the deuteron and the assumption of charge symmetry to relate the neutron with the proton parton distributions.

As described above, the production of W bosons at RHIC have rich aspects to probe both polarized and unpolarized anti-quark distributions, therefore provide us deeper understanding of the proton structure. This probe is quite unique on the point that rich and complicated structure of the QCD can be directly accessed by means of the well-understood weak interaction. Moreover, combining results from other accelerators such as Tevatron and LHC, W measurement at RHIC extends our knowledge of the W production in wide kinematic range, therefore it will benefit new particle searches, e.g. Higgs boson or SUSY (super symmetry) particle search utilizing W-boson production, which are now ongoing at LHC.

In this thesis, the first observations of W-boson production in polarized pp collisions was performed with the PHENIX detector for $\sqrt{s} = 500$ GeV at RHIC. The parity-violating single spin asymmetry of W production is also measured for the first time. The data are from polarized $pp \to e^\pm + X$ over a pseudo-rapidity range of $|\eta| < 0.35$, where the $e^\pm$ with transverse momentum of $p_T > 30$ GeV/c mainly come from W and Z decays. The results, obtained from the data accumulated during RHIC Year-2009 run, are reported.

---

[1] Here, q and Δq represent the unpolarized and polarized quark distribution in the proton, respectively

In this chapter, the parton model and parton distribution function (PDF) is introduced in Sec. 1.1. The current experimental knowledges about the PDF is shown in Sec. 1.2. In Sec. 1.3, the details of W boson production is described with expected charge ratio and single spin asymmetries at RHIC. The organization of this thesis follows in Sec. 1.4.

1.1 Parton Distribution Function (PDF)

1.1.1 Unpolarized PDF

The structure of the proton has been studied with DIS experiments. The detailed discussion on the formalism of DIS can be found in [28]. DIS is a high-energy inelastic scattering between leptons and nucleons. Here we take ep DIS as an example:

$$e(E, \vec{k}) + P(M, 0) \rightarrow e(E', \vec{k'}) + X, \tag{1.2}$$

where $k_\mu = (E, \vec{k})$ is the four-vector of the incident electron, and $k'_\mu = (E', \vec{k'})$ represents that of the scattered electron. In a similar way, $P_\mu = (M, 0)$ shows the four-vector of the target proton, where M denotes the proton mass, and the final state hadron(s) is written as X. Figure 1.1 displays the diagram of ep inelastic scattering.
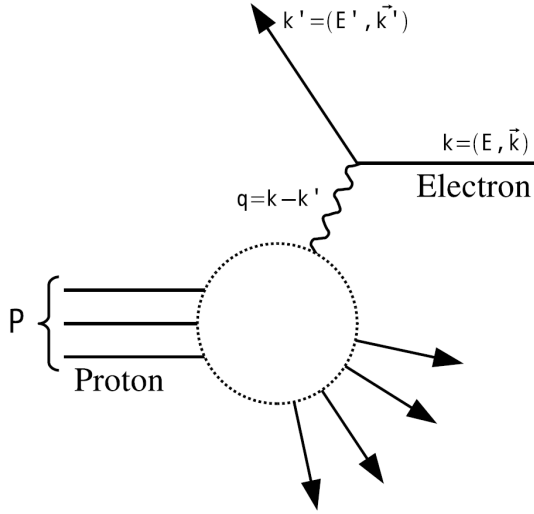
Figure 1.1: Diagram of ep inelastic scattering. The target proton is destructed by the scattering.
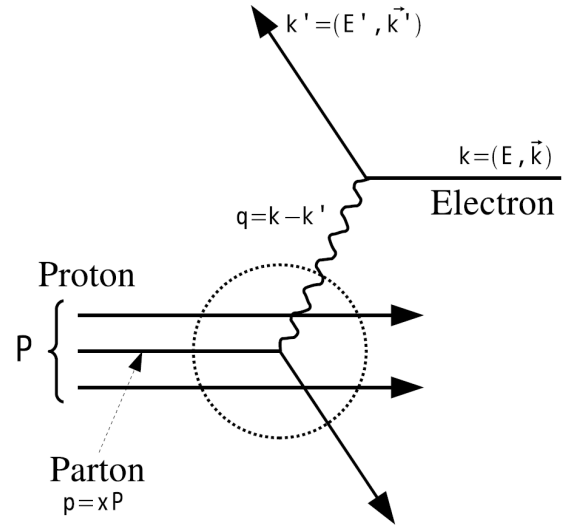
Figure 1.2: Diagram of ep inelastic scattering. It is assumed that the electron beam is scattered by a single parton in the proton. Interaction between partons is ignored in this approximation.

Bjorken scaling variable x (also called "Bjorken x") is defined as:

$$x \equiv \frac{-q^2}{2P \cdot q} = \frac{Q^2}{2P \cdot q}, \tag{1.3}$$

where Q^2 is defined as $Q^2 = -q^2$ so that $Q^2 > 0$. It can be interpreted as the fractional momentum of parton as described later. A Lorentz invariant variable ν is introduced as $\nu = P \cdot q / M$ which is equal to

$E - E'$ in the laboratory frame. Another Lorentz invariant variable y is defined as $y = P \cdot q / P \cdot k$ and is equal to ν / E in the laboratory frame.

The exact calculation of cross section is not possible due to the lack of the knowledge on the structure of the proton, but the structure can be parametrized with structure functions since the form is restricted by QCD. The unpolarized cross section is written as:

$$\frac{d^2\sigma}{dxdQ^2} = \frac{4\pi\alpha^2}{xQ^4}[(1-y)F_2(x,Q^2) + xy^2 F_1(x,Q^2)], \tag{1.4}$$

where F_1 and F_2 are the structure functions.

The formalism introduced so far does not depend on the parton model. Here, the process is interpreted in the parton model. In the parton model, the structure of the proton is specified by a set of "parton distribution functions" (PDFs).

It can be shown that the Bjorken x (Eq. 1.3) is interpreted as the fractional longitudinal momentum of the participating parton when the Q^2 is high enough to neglect the proton and the parton masses [2]. Let ξP be the momentum of the parton, so that ξ is the fractional momentum of the parton. Since the parton and the proton masses are neglected:

$$
\begin{aligned}
(\xi P + q)^2 &= 0 \\
2\xi P \cdot q + q^2 &= 0 \\
\xi &= \frac{-q^2}{2P \cdot q}.
\end{aligned}
\tag{1.5}
$$

Therefore, $\xi = x$ and the Bjorken x can be interpreted as the fractional momentum of parton.

In the parton model, the (unpolarized) PDF is represented with $q(x)$, and $q(x)dx$ is defined as the probability that quark with flavor q and momentum fraction x to $x + dx$ is observed in the scattering. Similarly, PDF for the gluon in the proton is defined as $g(x)$ and PDF for anti-quark is $\bar{q}(x)$. By definition, sum of the parton momentum results in the proton momentum:

$$\int_0^1 x \left[\sum_q (q(x) + \bar{q}(x)) + g(x) \right] dx = 1. \tag{1.6}$$

In addition, as the quantum number of the proton is carried by uud constituent quarks, following equations are satisfied:

$$\int_0^1 [u(x) - \bar{u}(x)]dx = 2, \qquad \int_0^1 \left[d(x) - \bar{d}(x)\right]dx = 1, \qquad \int_0^1 [s(x) - \bar{s}(x)] \, dx = 0. \tag{1.7}$$

Figure 1.2 shows the parton model interpretation of DIS, where a parton with momentum fraction of x interact with the virtual photon. The cross section can be calculated as an incoherent sum of parton-photon scatterings, and the structure functions F_1 and F_2 are identified as:

$$F_1(x,Q^2) = \frac{1}{2x}F_2(x,Q^2) = \frac{1}{2}\sum_{q,\bar{q}} e_q^2 q(x), \tag{1.8}$$

---

[2] Initial transverse momentum of the parton, which is called the intrinsic k_T, is also neglected in the parton model.

where e_q is electric charge of the parton in unit of the electron charge. The relationship between F_1 and F_2 is called "Callan-Gross relationship", and is a consequence of scattering from spin 1/2 partons [29]. The relation is confirmed by experiments at SLAC [30]. The equation also indicates that $F_1(x, Q^2)$ and $F_2(x, Q^2)$ are independent of Q^2. The scaling behavior was derived for $Q^2 \to \infty$ at fixed x (DIS limit), and is called "Bjorken scaling". In fact, the scaling is proved by measurements except for small Q^2 dependence. The violation of the Bjorken scaling does not indicate substructure of the parton, but it is caused by higher order effect such as interaction between partons.

1.1.2 Polarized PDF

To describe spin-dependent reaction, unpolarized PDF needs to be extended to spin-dependent PDF. Spin-dependent PDF is defined as $q_H^h(x)$, where H and h denote helicity of the proton and that of the parton in the proton. In similar way to unpolarized PDF, $q_+^+(x)dx$ means the probability that in the scattering one observes the quark with flavor q, momentum fraction x to $x + dx$ and positive helicity in the proton with positive helicity. It is same for the gluon. It is easy to derive equations:

$$q_+^+(x) = q_-^-(x), \qquad q_+^-(x) = q_-^+(x), \tag{1.9}$$

by Parity invariance. Obviously, unpolarized PDF is obtained by combining spin-dependent PDFs as $q(x) = q_+^+(x) + q_+^-(x)$. Instead of directly discussing spin-dependent PDF, we often use the difference of spin-dependent PDFs:

$$\Delta q(x) \equiv q_+^+(x) - q_+^-(x). \tag{1.10}$$

$\Delta q(x)$ is referred to as polarized PDF in this thesis. Based on the fact that the proton spin is 1/2, sum of contributions from spin and orbital angular momentum of the parton in the proton should reconstruct the proton spin:

$$\frac{1}{2} = \int_0^1 \left[\frac{1}{2} \sum_q (\Delta q(x) + \Delta\bar{q}(x)) + \Delta g(x) \right] dx + L, \tag{1.11}$$

where L indicates contribution of the orbital angular momentum carried by quarks and gluons.

At polarized sector, it is also possible to relate structure functions to PDFs. The cross sections for polarized DIS are parametrized as:

$$
\begin{aligned}
\frac{d^2\Delta\sigma_\parallel}{dxdQ^2} &\equiv \frac{d^2\sigma_{\Leftarrow}^{\to}}{dxdQ^2} - \frac{d^2\sigma_{\Rightarrow}^{\to}}{dxdQ^2} \\
&= \frac{16\pi\alpha^2 y}{Q^4}[(1 + \frac{y}{2} - \gamma^2\frac{y^2}{4})g_1(x, Q^2) - \gamma^2\frac{y}{2}g_2(x, Q^2)],
\end{aligned}
\tag{1.12}
$$

where $\Rightarrow$ and $\Leftarrow$ denote the nucleon helicity state, $\to$ and $\leftarrow$ denote helicity state of the incident lepton, $\gamma = 4M^2x^2/Q^2$, and g_1 and g_2 are the polarized structure functions. The polarized structure functions are found to be:

$$g_1(x, Q^2) = \frac{1}{2} \sum_{q,\bar{q}} e_q^2 \Delta q(x), \qquad g_2(x, Q^2) = 0, \tag{1.13}$$

in the zeroth order parton model. $g_2(x)$ was measured by several groups [31, 32] and $g_2 = 0$ holds approximately.

1.2 Current Experimental Knowledge on PDF

It is difficult to theoretically calculate x dependence of PDFs from the first principle. PDFs have been extracted from several types of experiments so far, including DIS, $p\bar{p}$ collision, and Drell-Yan production in hadron-hadron collisions. Since any particular experiment covers a limited range of x and Q^2, fixed by the center of mass energy, measurements from a variety of experiments are combined into "global analyses" that attempt to extract the distributions for all partons in the proton or the neutron simultaneously. To extract PDFs from these huge amount of data points [3], it is necessary to adopt a certain theoretical model to fit the data. As described above, the Bjorken scaling is violated and PDFs depend on Q^2 because of higher order effect such as interaction between partons. The Q^2 evolution of PDF follows the DGLAP equation obtained by QCD [33, 34, 35]. Therefore, in global analysis, model of PDF for the analysis is parameterized as a function of Bjorken x at fiducial Q^2, which is usually around a few GeV^2, and the Q^2 dependence of the model is calculated based on the DGLAP equation. Though the parameterization is different in analysis groups, the number of the parameters is roughly 10 to 20.

It is important to note about the charge (isospin) symmetry between the proton and the neutron. The symmetry relates PDFs of the neutron to those of the proton:

$$u_p(x) = d_n(x), \qquad d_p(x) = u_n(x), \qquad s_p(x) = s_n(x), \tag{1.14}$$

where p and n at subscript of PDF denote the proton and the neutron, respectively. The similar relation is obtained for anti-quark PDFs and polarized PDFs. To extract structure function of the neutron, DIS experiment with deuteron target is utilized, assuming the deuteron as the proton and the neutron which are bound very weakly and almost independent.

1.2.1 Unpolarized PDF

Since DIS experiments can measure only structure function of F_2 which is sum of PDFs (Eq. 1.8), it is hard to divide F_2 into PDFs of each flavor. To disentangle F_2, several kinds of experiments are utilized in addition to DIS with the proton or the deuteron target. DIS with neutrino beam [36] is useful because charged weak current (W boson coupling) selects quark flavor. The reaction with negatively charged lepton detected in the final state selects s, d or $\bar{u}$ quarks. Similarly, W boson production in collision of proton and anti-proton ($p\bar{p}$) [17, 18, 19] is used for the flavor separation of u and d quarks. PDF of c quark is tagged by Semi-Inclusive DIS (SIDIS) with D meson detected in the final state [37, 38, 39, 40, 41]. Lepton pair production (Drell-Yan process) in pp or pd (proton-deuteron) collision [20, 21, 22, 23, 24] is available to distinguish PDFs of $\bar{u}$ and $\bar{d}$ since lepton pair is produced by annihilation of the quark and the anti-quark. Measurement of inclusive jet production in $p\bar{p}$ collision [42, 43, 44, 45] contributes to determination of gluon PDF, especially at higher x region ($x > \sim 0.01$). DIS measurements with wide Q^2 range also contribute to constrain on gluon PDF through the Q^2 evolution at small x region ($x < \sim 0.1$). Table 1.1 summarizes a rough indication of particular PDFs that the various data constrain [46].

---

[3]Number of data points for unpolarized PDF analysis is ~ 2600 while it for polarized PDF analysis is ~ 500.

Process	Subprocess	Partons	x range
$l^{\pm}\{p,n\} \to l^{\pm}X$	$\gamma^* q \to q$	$q, \bar{q}, g$	$x >\sim 0.01$
$l^{\pm}n/p \to l^{\pm}X$	$\gamma^* d/u \to d/u$	d/u	$x >\sim 0.01$
$pp \to \mu^+\mu^- X$	$u\bar{u}, d\bar{d} \to \gamma^*$	$\bar{q}$	$0.015 <\sim x <\sim 0.35$
$pn/pp \to \mu^+\mu^- X$	$(u\bar{d})/(u\bar{u}) \to \gamma^*$	$\bar{d}/\bar{u}$	$0.015 <\sim x <\sim 0.35$
$\nu(\bar{\nu})N \to \mu^-(\mu^+)X$	$W^* q \to q'$	$q, \bar{q}$	$0.01 <\sim x <\sim 0.5$
$\nu N \to \mu^-\mu^+ X$	$W^* s \to c$	s	$0.01 <\sim x <\sim 0.2$
$\bar{\nu}N \to \mu^+\mu^- X$	$W^* \bar{s} \to \bar{c}$	$\bar{s}$	$0.01 <\sim x <\sim 0.2$
$e^{\pm}p \to e^{\pm}X$	$\gamma^* q \to q$	$g, q, \bar{q}$	$0.0001 <\sim x <\sim 0.1$
$e^+p \to \bar{\nu}X$	$W^+\{d,s\} \to \{u,c\}$	d, s	$x >\sim 0.01$
$e^{\pm}p \to e^{\pm}c\bar{c}X$	$\gamma^* c \to c, \gamma^* g \to c\bar{c}$	c, g	$0.0001 <\sim x <\sim 0.01$
$e^{\pm}p \to jet + X$	$\gamma^* g \to q\bar{q}$	g	$0.01 <\sim x <\sim 0.1$
$p\bar{p} \to jet + X$	$gg, qg, qq \to 2jets$	g, q	$0.01 <\sim x <\sim 0.5$
$p\bar{p} \to (W^{\pm} \to l^{\pm}\nu)X$	$ud \to W, \bar{u}\bar{d} \to W$	$u, d, \bar{u}, \bar{d}$	$x >\sim 0.05$
$p\bar{p} \to (Z \to l^+l^-)X$	$uu, dd \to Z$	d	$x >\sim 0.05$

Table 1.1: The main processes included in the current global PDF analysis ordered in three groups: fixed-target experiments, HERA and the Tevatron. An indication of their dominant partonic subprocesses, the primary partons which are probed and the approximate range of x constrained by the data are shown [46].

There are several groups extracting PDF from the experimental data [47, 48, 49, 50, 46, 51]. Their results show reasonable agreement each other. Figure 1.3 shows the MSTW2008 results of PDFs at NLO at $Q^2 = 10$ and 10^4 GeV^2 [46]. The PDFs of u and d have a peak around $x \sim 0.1$ to 0.2, since they are the valence quark flavors [4]. The rises in low x of $u, d, \bar{u}$ and $\bar{d}$ distributions, which is originated from the coupling to gluon evolution, cancel for valence distribution. The PDFs of $s(= \bar{s})$ and $c(= \bar{c})$ are suppressed compared to other flavors (u, d) because of their larger mass.

1.2.2 Polarized PDF

There are some predictions about integral of PDF over x, which is called "sum rule". For example, some trivial sum rules are Eq. 1.6 and 1.7, in addition to Eq. 1.11. The most fundamental sum rule for polarized PDF is derived by Bjorken [52, 53] based on the charge (isospin) symmetry of the nucleon:

$$\int_0^1 (g_1^p(x) - g_1^n(x))dx = \frac{1}{6}\left|\frac{g_A}{g_V}\right|\left[1 - \frac{\alpha_s(Q^2)}{\pi} + ...\right], \qquad \left|\frac{g_A}{g_V}\right| = 1.2695 \pm 0.0029, \qquad (1.15)$$

where g_1^p and g_1^n are polarized structure functions for the proton and the neutron, respectively (see Eq. 1.13 for g_1). g_V and g_A are the vector and the axial-vector weak coupling constants of the neutron β-decay and determined precisely by experiments [6]. The term of $1 - \alpha_s/\pi + ...$ in the right hand side is from higher order correction of QCD. This Bjorken sum rule is well verified by measurements [4, 54].

By assuming flavor SU(3) symmetry for the spin 1/2 baryon octet, the β-decay of hyperons can be described by two parameters, F and D [55, 56]. At the same time, certain combinations of integral of the polarized PDF is related to F and D as follows:

$$\int_0^1 \left[(\Delta u(x) + \Delta\bar{u}(x)) - (\Delta d(x) + \Delta\bar{d}(x))\right]dx = F + D = \left|\frac{g_A}{g_V}\right|, \qquad (1.16)$$

---

[4] The valence quarks are $u - \bar{u}$ and $d - \bar{d}$ to be exact.
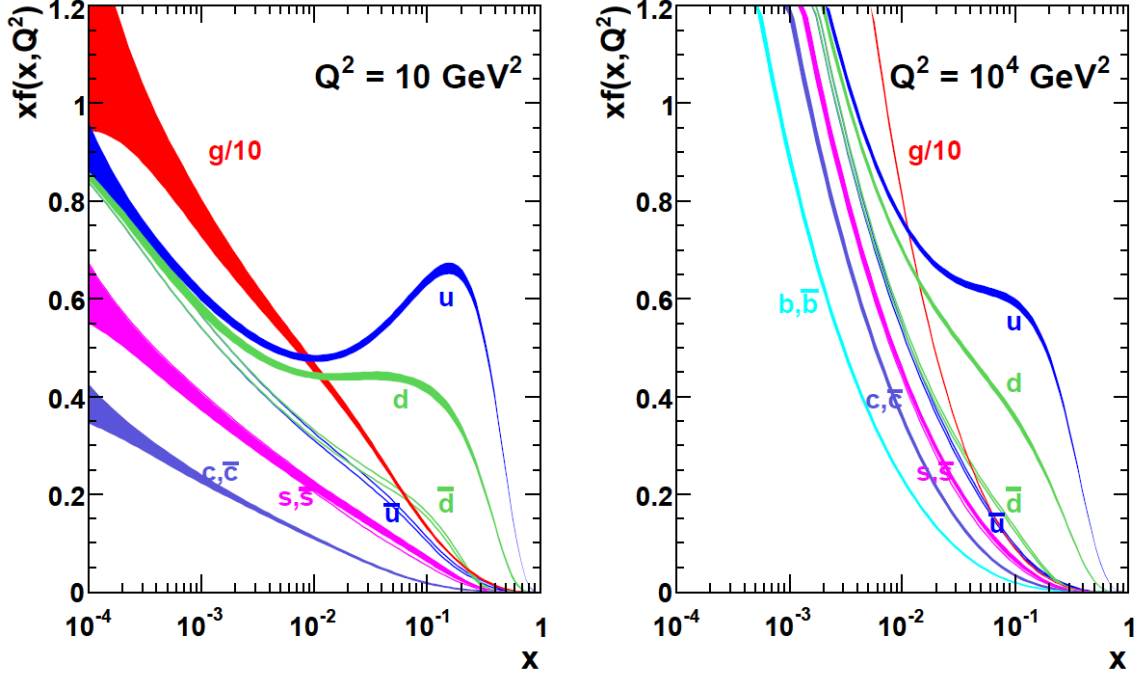
MSTW 2008 NLO PDFs (68% C.L.)

Figure 1.3: The MSTW 2008 NLO PDFs at $Q^2 = 10$ and 10^4 GeV^2 [46].

$$\int_0^1 \left[(\Delta u(x) + \Delta \bar{u}(x)) + (\Delta d(x) + \Delta \bar{d}(x)) - 2(\Delta s(x) + \Delta \bar{s}(x))\right] dx = 3F - D = 0.586 \pm 0.031. \quad (1.17)$$

Note that these linear combinations of PDF is independent of Q^2 in up to NLO. Equation 1.16 is identical to the Bjorken sum rule of Eq. 1.15. Because the charge symmetry is included in the flavor SU(3) symmetry, the Bjorken sum rule also appears in this model. The right-hand side of Eq. 1.17 is evaluated using measured g_A/g_V for hyperon decays ($\Lambda \to p$, $\Xi \to \Lambda$ and $\Sigma \to n$) [6], where F and D is fixed by Eq. 1.16.

In global analysis of polarized PDFs, some constraints, which is generally tighter than the unpolarized case due to limited experimental precision, are often imposed depending on analysis groups. What is frequently utilized are sum rules of Eq. 1.15, 1.16 and 1.17. Symmetric sea quark distributions, $\Delta \bar{u}(x) = \Delta \bar{d}(x) = \Delta \bar{s}(x) = \Delta s(x)$, are also often assumed.

Following pioneering polarized DIS experiments at SLAC [57, 58, 59, 60] to measure g_1, EMC (European Muon Collaboration) at CERN measured g_1 in x range of 0.01 to 0.7 with polarized muon beam and extracted integral of g_1 [2, 3]. When only three light-flavor quarks, u, d and s, are taken into account, integral of each polarized PDF of the quarks are extracted by assuming Eq. 1.16 and 1.17 based on the flavor SU(3) symmetry. The EMC results were interpreted as quarks and anti-quarks carry only $\sim$10 % of the proton spin, even though the uncertainty is large. This conclusion is a contrast to that

valence quarks carry quantum numbers of hadrons. Many polarized DIS and SIDIS experiments have been performed to confirm the EMC results (see references in [61, 62, 63, 64, 65, 66, 67, 68]), and the contribution of the quarks and the anti-quarks to the proton spin obtained by the recent analyses [61, 62, 63, 64, 65, 66, 67, 68] is $20 - 35$ %. However, compared with unpolarized experiments, precision of the polarized experimental data is still limited and the measured range of Q^2 and x is much smaller. This means the uncertainties of polarized PDFs remain much larger than unpolarized PDFs.

Figure 1.4 shows the result of a global analysis including both inclusive DIS and SIDIS measurements [64]. While the sum of quark and anti-quark distributions, separately shown for u and d quarks, is well known, anti-quark distributions ($\bar{u}$, $\bar{d}$) are unconstrained. The uncertainties of anti-quark distributions are caused by two different sets of fragmentation functions, which is used in SIDIS measurements, referred to as KRE [69] and KKP [70]. It is known that KRE and KKP sets of fragmentation functions have significant differences for the gluon fragmentation function and also non-negligible differences for flavor separation [64] (see Appendix A for the detail of fragmentation function). While the KRE fit favors SU(3) symmetric sea, KKP fit finds the polarization of $\bar{u}$ is opposite to $\bar{d}$ and $\bar{s}$ in this global analysis.

Figure 1.5 displays other result from a global analysis [67, 68]. The difference from the Fig 1.4 is that this global analysis includes A_{LL} (double-spin asymmetry) of π^0 and jet production in pp collision at RHIC [71, 72] as well as more data points from SIDIS experiments. Since gluon polarization is constrained by those A_{LL} measurements, Δg in the figure is rather smaller than Fig. 1.4 in the range of $0.05 < x < 0.2$. Thanks to more data from SIDIS, anti-quark distributions are also much constrained than Fig. 1.4. However, the uncertainty is still large because of the uncertainty of fragmentation function, and the result of this global analysis still provides an argument that further experimental work is needed to improve the accuracy of anti-quark polarized PDFs ($\Delta\bar{u}$, $\Delta\bar{d}$).

Measurement of single spin asymmetry of W production in polarized pp collision is one of unique ways which can put more constraints on anti-quark polarized PDFs. Determining flavor separated polarized PDFs is very important task to reveal overall picture of the proton spin structure, and it leads to our deeper understanding of QCD. The detail of W measurement with pp collider is described in the next section.

Figure 1.4: Parton PDFs from global analysis, named DNS, at $Q^2 = 10$ GeV^2 along with uncertainty bands corresponding to $\Delta\chi^2 = 1$ and $\Delta\chi^2/\chi^2 = 2$ % [64].
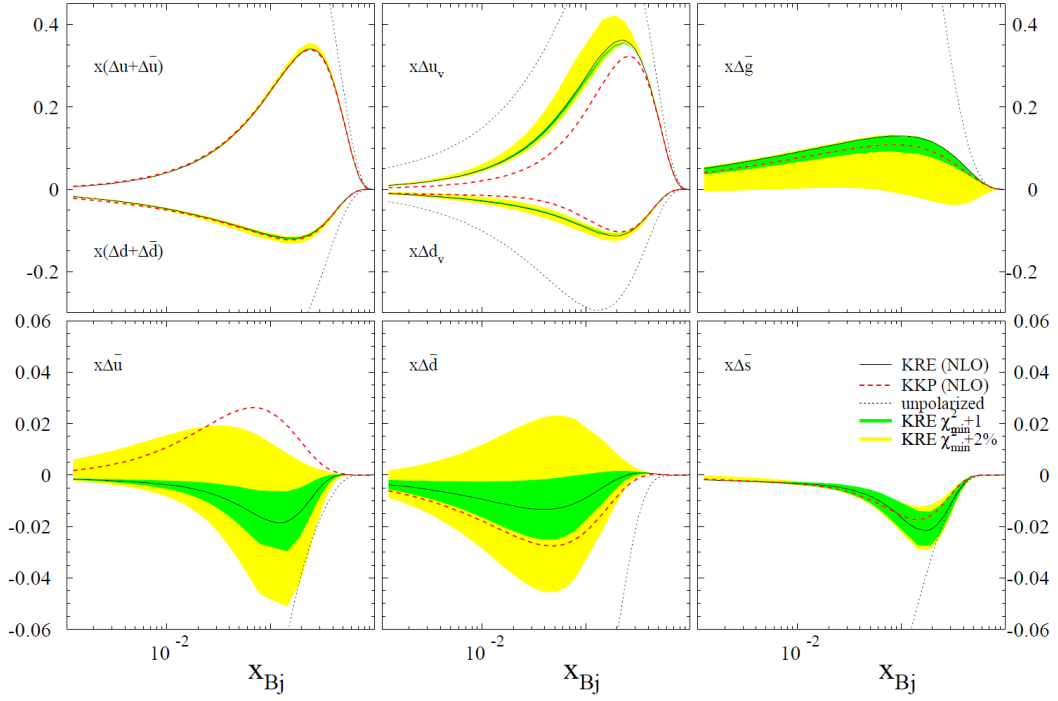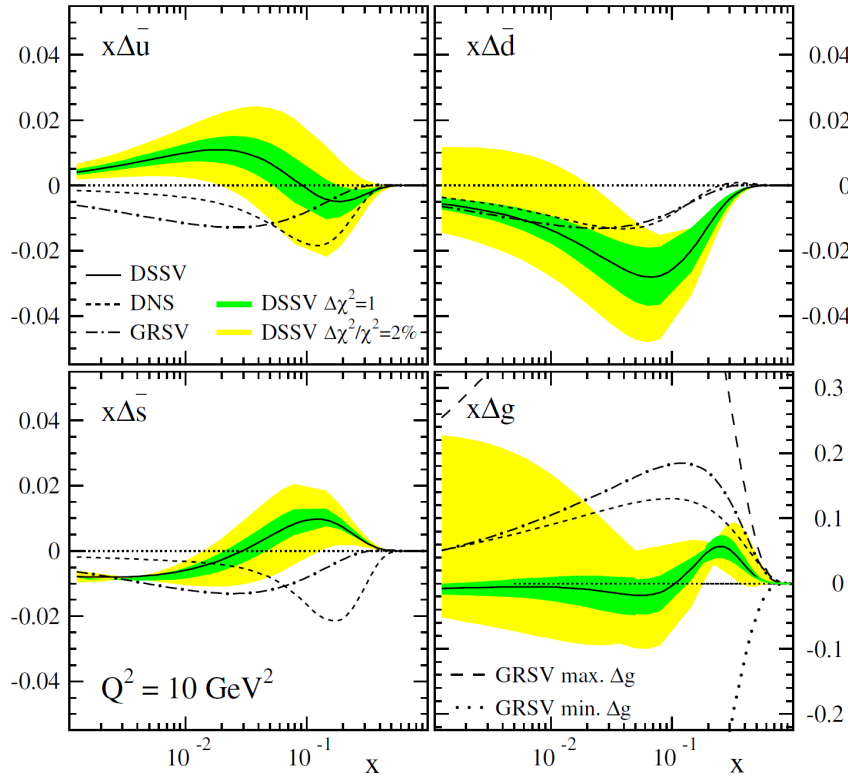

Figure 1.5: Parton PDFs from global analysis, named DSSV, at $Q^2 = 10$ GeV^2 along with uncertainty bands corresponding to $\Delta\chi^2 = 1$ and $\Delta\chi^2/\chi^2 = 2$ % [67]. The result from DNS, GRSV global analysis [64, 62] are also indicated in the figure.

1.3 Hadronic Production of W-boson

Our goal is to explore the details behind the small total quark and anti-quark spin contribution to the proton spin, which is currently determined by (SI)DIS, using W boson production. Highlights of the W measurement at RHIC are the sensitivity to $\Delta \bar{u}$ from W^- asymmetries in the backward rapidity region and the similarly large sensitivity to the $\Delta \bar{d}$ from W^+ asymmetry in the central and forward rapidity region. In addition, it has been recognized that charge ratio of $W^\pm$ boson production at RHIC provides unique and clean test of an SU(2) symmetry breaking in the anti-quark sea by measuring the unpolarized $\bar{d}/\bar{u}$ ratio in the protons.

The basic aspects of W production at hadron collider, charge ratio and parity-violating single spin asymmetries are explained in the following subsections.

1.3.1 Cross Section and Kinematics

W bosons in pp colliders are produced by hard scatters between the quarks which are inside the protons. Protons consist of partons, which are quarks and gluons as discussed in previous section. Figure 1.6 shows a schematic diagram of the leading-order (LO) W production process with a hard scatter between a quark and a anti-quark. These two quarks couple to a W, and the W subsequently decays into a lepton and a neutrino. The other partons in the protons are spectators to the event, and they form the "underlying event".
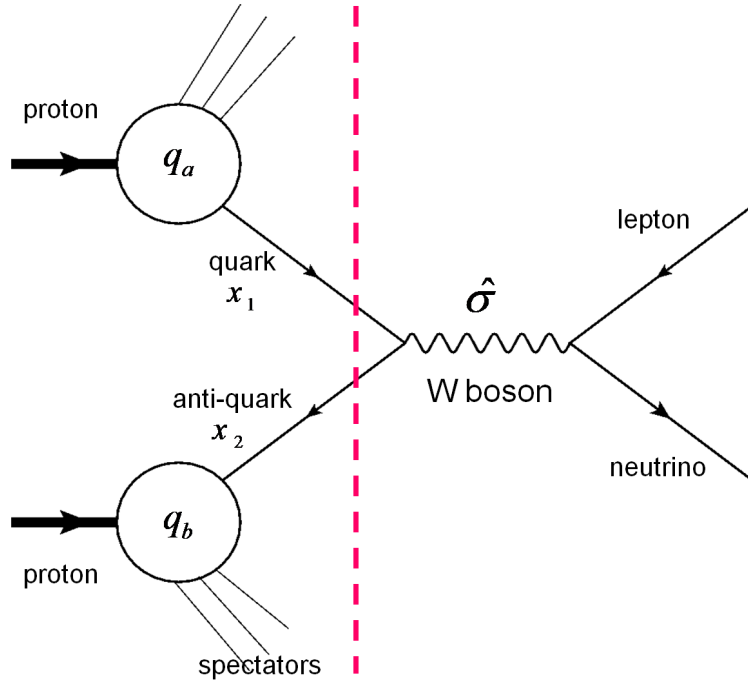

Figure 1.6: Schematic diagram of W production at pp collisions. The process is divided into two parts: PDFs (q_a, q_b) and partonic cross section $(\hat{\sigma})$.

In order to calculate the cross section for any process at a hadron collider, it is necessary to convolute the partonic cross section with the PDFs within the proton. The differential cross section of W production in pp collisions is written as:

$$d\sigma(pp \to WX) = \int dx_1 dx_2 \sum_{a,b} q_a(x_1, Q^2) q_b(x_2, Q^2) d\hat{\sigma}(ab \to W), \qquad (1.18)$$

where the sum is over all possible partons; $d\hat{\sigma}(ab \to W)$ is the cross section for parton a and parton b to create W boson. $q(x, Q^2)$ represents PDF, and x_1, x_2 are the fractional momenta carried by the partons in the colliding hadron pair. Q^2 is chosen renormalization and factorization scale, and it is M_W^2 (M_W: mass of W boson) in W production.

In this framework, W production is divided into two parts: PDFs and partonic (or subprocess) cross sections. The treatment is called the "factorization theorem" [73]. Factorization theorem plays an important role as it ensures that the partonic cross section, $d\hat{\sigma}(ab \to W)$, only depends on the parton species a, b, and does not depend on the choice of the initial state hadron (proton), nor the choice of the final state. The partonic cross sections can be calculated with perturbative QCD. All the non-perturbative phenomena are carried by PDFs and the theorem ensures that PDFs are universal. The same PDFs can be used for both pp collisions and ep DIS.

At LO, the differential cross section for W^+ production can be written as:

$$\frac{d\sigma}{dx_F}(W^+) = K \frac{\sqrt{2}\pi}{3} G_F (\frac{x_1 x_2}{x_1 + x_2}) [\cos^2 \theta_c \{u(x_1)\bar{d}(x_2) + \bar{d}(x_1)u(x_2)\}$$
$$+ \sin^2 \theta_c \{u(x_1)\bar{s}(x_2) + \bar{s}(x_1)u(x_2)\}], \qquad (1.19)$$

where $u(x)$, $d(x)$, and $s(x)$ represent the up, down, and strange quark distribution functions in the hadrons, and $x_F = x_1 - x_2$. G_F is Fermi coupling constant and θ_c is the Cabbibo angle. The factor K takes into account the contributions from first-order QCD corrections:

$$K \sim 1 + \frac{8\pi}{9}\alpha_s(Q^2). \qquad (1.20)$$

In Eq. 1.19, the $u(x)$, $d(x)$ and $s(x)$ are all evaluated at $Q^2 = M_W^2$, and $\alpha_s \sim 0.1158$ and $K \sim 1.323$ at the scale. It indicates that QCD processes are relatively unimportant for W production. An analogous expression for W^- production cross section is given as:

$$\frac{d\sigma}{dx_F}(W^-) = K \frac{\sqrt{2}\pi}{3} G_F (\frac{x_1 x_2}{x_1 + x_2}) [\cos^2 \theta_c \{\bar{u}(x_1)d(x_2) + d(x_1)\bar{u}(x_2)\}$$
$$+ \sin^2 \theta_c \{\bar{u}(x_1)s(x_2) + s(x_1)\bar{u}(x_2)\}]. \qquad (1.21)$$

From momentum and energy conservation, we can derive relations between x values and the rapidity of the W boson (y_W) as:

$$x_1 = \frac{M_W}{\sqrt{s}} e^{y_W}, \qquad x_2 = \frac{M_W}{\sqrt{s}} e^{-y_W}, \qquad (1.22)$$

where $\sqrt{s}$ denotes the center mass of energy of the colliding protons.

In a hadron (pp) collider, W bosons are identified primarily from $W \to \mu\nu$ or $e\nu$ leptonic decays. This is because $W \to q\bar{q}'$ hadronic decay is usually buried inside a large QCD background ($pp \to jets$), as are

the τs from the $W \to \tau\nu$ process. Approximately 10 % of the W bosons decay into an electron and a neutrino.

The LO W boson production mechanism results in the W boson being polarized by means of the $V - A$ structure of the weak interaction as shown in Fig. 1.7. The top panel shows the helicity configuration of the incoming quark and anti-quark. The lower panel displays the preferred direction of $e^{\pm}$ quoting the scattering angle θ^* in the W center-of-mass system measured with respect to the positive z axis. The $V - A$ structure means that the weak current couples only to left-handed u and d quarks (or to right-handed $\bar{u}$ and $\bar{d}$ quarks). For ultra-relativistic quarks, helicity [5] and chirality (handedness) are approximately equivalent, and this results in full polarization of the produced W bosons. The W leptonic decay process also couples only to left-handed e^- and right-handed $\bar{\nu}$ (or right-handed e^+ and left-handed ν). The conservation of angular momentum favors a decay with the final state lepton at a small angle with respect to the initial state quark direction (and a similar small angle between the initial state anti-quark and final anti-lepton). As a result, the $W \to l\nu$ decay distribution has angle dependence of:

$$\frac{d\sigma_{W \to l_+^- \nu}}{d(\cos \theta^*)} \propto (1 \pm \cos \theta^*)^2. \tag{1.23}$$
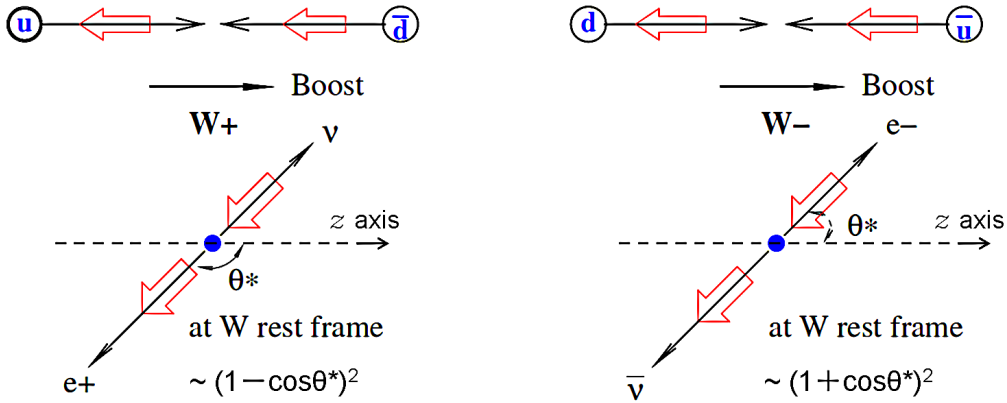
Figure 1.7: Helicity configuration of W^+ (Left) and W^- (Right) production showing on top the helicity configuration of the incoming quark and anti-quark. The lower panel displays the preferred direction of $e^{\pm}$ quoting the scattering angle θ^* in the W center-of-mass system measured with respect to the positive z axis.

It is necessary to relate the lepton kinematics to y_W, so that one can assign the momentum fraction (x_1, x_2) of the quark or anti-quark through Eq. 1.22. Only then would it be possible to translate the measured single spin asymmetry or charge ratio into a determination of the quark or anti-quark PDFs. The rapidity of the W (y_W) is related to the lepton rapidity in the W rest frame (y_l^*) and in the lab frame (y_l) by:

$$y_l = y_W + y_l^*, \quad \text{where } y_l^* = \frac{1}{2} \ln \left[\frac{1 + \cos \theta^*}{1 - \cos \theta^*} \right]. \tag{1.24}$$

---

[5]Helicity is the projection of the spin onto the direction of momentum.

The term of $\cos\theta^*$ can be determined from the transverse momentum (p_T) of the lepton at LO [6] by:

$$p_T = p_T^* = \frac{M_W}{2}\sin\theta^*. \tag{1.25}$$

In this reconstruction, however, the transverse momentum of the W boson (Q_T) is ignored. In reality, it has a Q_T, resulting from higher-order contributions such as $q\bar{q}' \to W^\pm g$ and $qg \to W^\pm q'$, or from transverse momentum of initial-state partons. Even though the W mass sets a large Q^2 scale so that the coupling constant (α_s) is not large, the corrections certainly need to be known for a reliable theoretical extraction of PDFs from data. Therefore, the Monte-Carlo like code "CHE" (standing for "Collisions at High Energies") [12], which implements the Next-to-Leading-Order (NLO) calculation, is used for reliable predictions of single spin asymmetry of W production. The CHE provides access to the full kinematics of the final state particles, allowing the computation of any infrared-safe observable in hadronic collisions and the implementation of realistic experimental cuts such as lepton p_T cut. It is worth noticing that the same code can compute the unpolarized, the single polarized and the double polarized cross sections.

Figure 1.8 shows the correlation between the averages of the momentum fractions, $\langle x_{1,2}\rangle$, and y_l computed by CHE for W production (Left: W^-, Right: W^+) [12]. A remarkably strong correlation is found between $\langle x_{1,2}\rangle$ and y_l in both cases. Large negative lepton rapidity corresponds to small (large) momentum fractions x_1 (x_2). The opposite occurs for large positive rapidities. As a rough approximation, one can parameterize these correlations by the simple formulas:

$$\langle x_1\rangle \sim \frac{M_W}{\sqrt{s}}e^{y_l/2}, \qquad \langle x_2\rangle \sim \frac{M_W}{\sqrt{s}}e^{-y_l/2}. \tag{1.26}$$

Since RHIC experiments (PHENIX and STAR) cover the rapidity range of $|y_l| \sim< 2$, one can expect sensitivity to the polarized quark and anti-quark distributions in the region $0.05 < x < 0.4$.

1.3.2 Identification of W Event - Jacobian Peak

$W \to e\nu$ is the decay mode which we use to measure the W production in this thesis. The neutrino passes through the detector without interacting. The electron, on the other hand, leaves a track in the tracking chamber, and also deposits its energy in the calorimeters that surround the interaction region at PHENIX. Usually W production is identified by isolated charged leptons with large p_T and large missing transverse energy, due to the undetected neutrino. However, we only measure p_T of decay leptons in this thesis because our detector (PHENIX) is not hermetic and measurement of missing p_T is not available.

Since the angle dependence of $W \to e$ cross section is given by Eq. 1.23, the differential cross section is written as:

$$\frac{d\sigma_{W\to e_+^-\nu}}{d(\cos\theta^*)} = \sigma_{W\to e_+^-}\frac{3}{8}(1 \pm \cos\theta^*)^2. \tag{1.27}$$

The transverse momentum (p_T) of the $e^\pm$ at LO is shown in Eq. 1.25 and its squared value is:

$$p_T^2 = \frac{M_W^2}{4}\sin^2\theta^* = \frac{M_W^2}{4}(1 - \cos^2\theta^*). \tag{1.28}$$

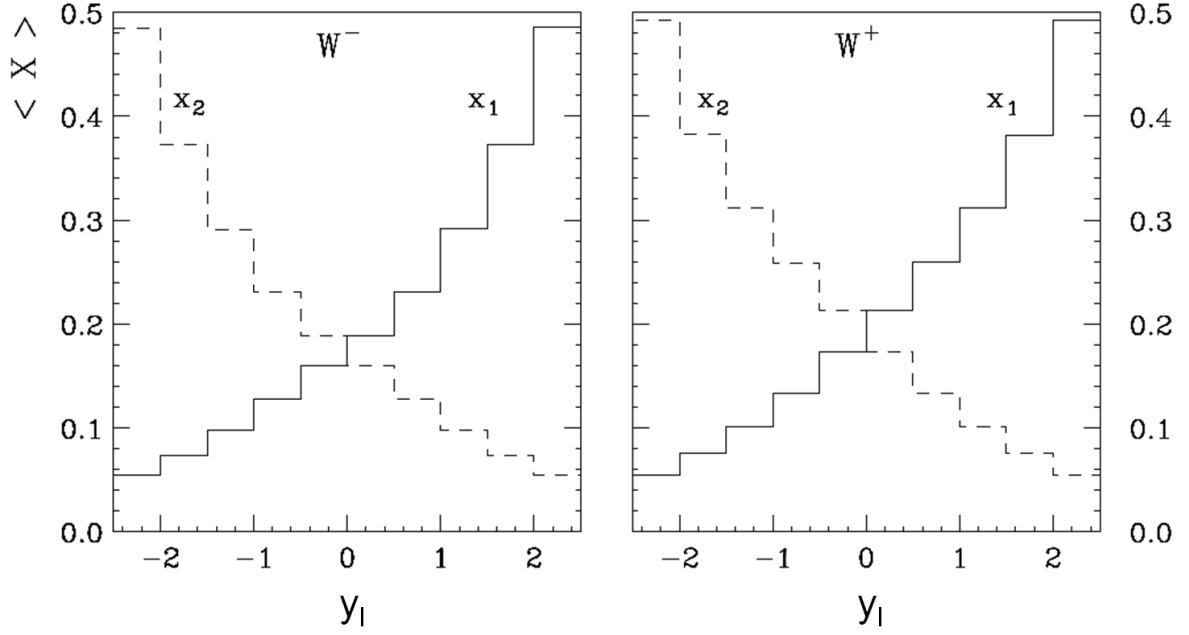[6]Note that there is an irreducible uncertainty of the sign

Figure 1.8: Averages of the momentum fractions x_1, x_2 as functions of the lepton rapidity for W^- (Left) and W^+ production (Right) at RHIC [12].

Therefore, the p_T dependence of the cross section can be calculated as:

$$
\begin{aligned}
\frac{d\sigma}{dp_T^2} &= \frac{2}{M_W^2 \cos\theta^*} \frac{d\sigma}{d(\cos\theta^*)} \\
&= \frac{3}{4}\sigma_{W\to e} \frac{1+\cos^2\theta^*}{M_W^2 \cos\theta^*} \\
&= \frac{3}{2}\frac{\sigma_{W\to e}}{M_W^2} \frac{(1-2p_T^2/M_W^2)}{\sqrt{1-4p_T^2/M_W^2}}.
\end{aligned}
\tag{1.29}
$$

Here, the term of $\cos\theta^*$ in numerator of the second line is ignored because p_T is symmetric against $\theta^* \leftrightarrow \pi - \theta^*$. As we can notice from the last line, the p_T distribution has a singularity at $p_T = M_W/2$ and this is called "Jacobian peak" which is the feature of two body decay. If W boson does not have a Q_T (transverse momentum) and $\Gamma_W = 0$ (Γ_W: mass width of W boson), the p_T distribution would have the singularity. In practice, however, the observed distribution is with integration over the momentum distributions of interacting partons and that results in smeared p_T distribution with finite peak.

Figure 1.9 displays the Jacobian peak of $W \to e\nu$ decay (Left) and its real distribution from UA2 experiment (Right) [74]. The event of $W \to e\nu$ decay can be identified by measuring high p_T $e^\pm$s, and the requirement adopted in this thesis is $p_T > 30$ GeV/c. Note that the PHENIX cannot distinguish between $e^\pm$s from W decays and them from Z decays due to its limited acceptance. Therefore, the contamination by $e^\pm$s from Z decays are unavoidable in this thesis.
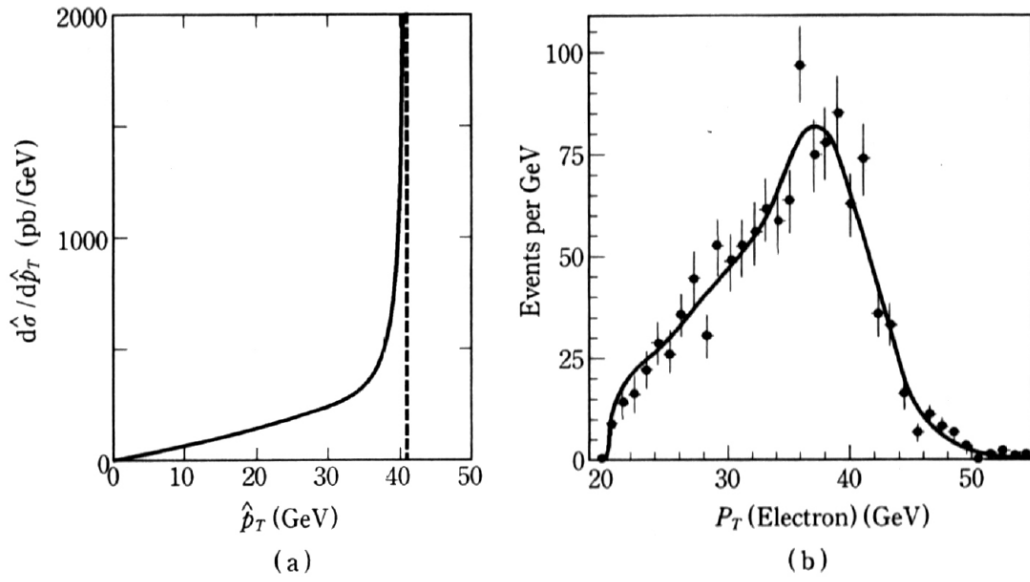
Figure 1.9: (a): Ideal Jacobian peak of $u\bar{d} \to W^+ \to e^+\nu$ reaction. (b): Smeared Jacobian peak measured at UA2 experiment [74].

1.3.3 Charge Ratio

A variety of models have been proposed to describe the sea quarks in the nucleon. The earliest models have assumed SU(3) flavor symmetry of sea quarks in the nucleon. However, it has already been shown by neutrino-induced charm (c) production experiments that the s quark contribution to the nucleon is not as large as u and d sea quarks [75]. This asymmetry can be attributed to the large mass difference between s quark and u and d quarks. For the light u and d quarks, it was still possible that their distributions in the nucleon sea are symmetric. To test the flavor symmetry of the u and d quarks in the nucleon sea, one can measure the Gottfried sum [76]:

$$S_G = \int_0^1 [F_2^p(x) - F_2^n(x)]/x dx = \frac{1}{3} + \frac{2}{3}\int_0^1 [\bar{u}_p(x) - \bar{d}_p(x)]dx, \qquad (1.30)$$

where F_2^p and F_2^n are the proton and neutron structure functions measured in DIS experiments. The second step in Eq. 1.30 follows from the assumption of the charge symmetry (Eq. 1.14: $u_p(x) = d_n(x)$, $d_p(x) = u_n(x)$, and $\bar{u}_p(x) = \bar{d}_n(x)$). With the assumption of a symmetric sea, $\bar{u}_p = \bar{d}_p$, S_G equals 1/3 (Gottfried Sum Rule: GSR). The most accurate test of the GSR is the result from the New Muon Collaboration (NMC), which measured F_2^p and F_2^n over the region of $0.004 \leq x \leq 0.8$ with muon DIS [25, 26]. They determined the S_G to be 0.235 ± 0.026, significantly below 1/3. This result provided the first strong evidence that $\bar{u}(x) \neq \bar{d}(x)$.

Following the NMC measurement, the $\bar{d}/\bar{u}$ ratios as a function of x were measured using other experimental techniques. These new measurements include the NA51 and E866 experiments with the Drell-Yan (DY) process [21, 22, 23, 24] and the HERMES experiment with SIDIS [27]. The $\bar{d}/\bar{u}$ asymmetry is clearly established from these experiments.

Various theoretical models, such as meson-cloud model etc., have been proposed to explain the $\bar{d}/\bar{u}$ asymmetry, which are reviewed in [77, 78]. While these models can describe the general trend of the $\bar{d}/\bar{u}$ asymmetry, they all have difficulties explaining the $\bar{d}/\bar{u}$ data at large x ($x > 0.2$), where the E866 data suggest a rapid fall-off of this ratio. Therefore, it is very important to have new measurements sensitive to the $\bar{d}/\bar{u}$ ratios at $x > 0.2$ in order to better determine mechanisms which generate the flavor asymmetric nucleon sea. The upcoming Fermilab E906 Drell-Yan experiment plans to extend the measurement to larger x region [79].

With the pp colliders at RHIC, an independent technique to study the $\bar{d}/\bar{u}$ asymmetry is available. By measuring the ratio of W^+ versus W^- production in unpolarized pp collision, the $\bar{d}/\bar{u}$ asymmetry can be determined with some distinct advantages over the existing methods [14, 15, 16]. The advantages are:

- **Not necessary to assume the charge symmetry**: All existing experimental results of $\bar{d}/\bar{u}$ asymmetry depend on the comparison of the scattering cross sections of hydrogen and deuterium targets. It is pointed out that the violation of the GSR and the results of DY experiments can be caused by charge symmetry violation as well as by flavor asymmetry of the nucleon sea [80, 81]. A comparison between W production in pp collision with the DY experiments would disentangle the flavor asymmetry from the charge symmetry violation effects.

- **Free from any nuclear effect**: The nuclear modification of parton distributions should be taken into account for DIS and DY process involving deuterium targets [82, 83, 84, 85]. The nuclear shadowing effect for deuteron at small x could lead to a 4 % to 10 % decrease in the evaluation of the S_G by the NMC [82, 85]. Moreover, the nucleon Fermi motion at large x also affects the extraction of neutron structure function and would cause additional uncertainty in the evaluation of the S_G [83]. The nuclear effects and the associated uncertainty are absent in W production in pp production.

- **Large Q^2 scale**: The W production is sensitive to $\bar{d}/\bar{u}$ flavor asymmetry at a Q^2 scale of $\sim$ 6400 GeV$^2/c^2$, significantly larger than all existing measurements. This offers the opportunity to examine the QCD evolution of the sea-quark flavor asymmetry.

An observable directly related to the $\bar{d}/\bar{u}$ ratio is the ratio of the x_F distributions for W^+ and W^- production. When ignoring the smaller contribution from the strange quarks, the ratio can be derived from Eq. 1.19 and 1.21:

$$R(x_F) = \frac{d\sigma/dx_F(W^+)}{d\sigma/dx_F(W^-)} = \frac{u(x_1)\bar{d}(x_2) + \bar{d}(x_1)u(x_2)}{\bar{u}(x_1)d(x_2) + d(x_1)\bar{u}(x_2)}. \tag{1.31}$$

For pp collision, it is evident that $R(x_F)$ is symmetric with respect to $x_F = 0$ ($R(x_F) = R(-x_F)$). At large x_F (i.e. $x_1 \gg x_2$), the terms of $\bar{d}(x_1)u(x_2)$ and $\bar{u}(x_1)d(x_2)$ are negligible, thus we have:

$$R(x_F \gg 0) \sim \frac{u(x_1)}{d(x_1)}\frac{\bar{d}(x_2)}{\bar{u}(x_2)}. \tag{1.32}$$

At $x_F = 0$, where $x_1 = x_2 = x$, one obtains:

$$R(x_F = 0) = \frac{u(x)}{d(x)}\frac{\bar{d}(x)}{\bar{u}(x)}. \tag{1.33}$$

As the $u(x)/d(x)$ ratios are already well known by experiments at Tevatron [17, 18, 19], a measurement of $R(x_F)$ in pp collision gives an accurate determination of the ratio $\bar{d}(x)/\bar{u}(x)$ at x of ~ 0.05 to 0.16 (see Fig. 1.8).

It is not the x_F distributions of the W which are measured in practice but the charged leptons from the decay of the W bosons. The measured lepton ratio is defined as:

$$R(y_l) = \frac{d\sigma/dy_l(W^+ \to l^+)}{d\sigma/dy_l(W^- \to l^-)}. \tag{1.34}$$

The differential cross section $d\sigma/dy_l$ is obtained by convoluting the $q\bar{q}' \to W$ cross section for each x_F with the relevant $W \to l\nu$ decay distribution (Eq. 1.23).

Figure 1.10 shows the predicted lepton ratios $R(y_l)$ calculated for four different PDFs [86]. The first PDF used here is MRS S0' [87]. It assumes symmetric $\bar{u}$ and $\bar{d}$ distributions. The other three PDFs allow flavor asymmetry in nucleon sea. New experimental data from DY measurement by E866 Collaboration is included in the global analysis performed by CTEQ6 [49], GJR08 [50] and MSTW2008 [46]. Therefore $R(y_l)$ for those three PDF are similar at $y_l = 0$ ($x_F \sim 0$, $x_1 \sim x_2 \sim 0.16$) and are significantly higher

than the MRS S0' case. Considering the acceptance of PHENIX experiment, which covers $|\eta| < 0.35$ in central rapidity, Fig. 1.10 shows that a measurement of $R(y_l)$ at PHENIX central rapidity region is able to distinguish flavor symmetric and flavor asymmetric nucleon sea.
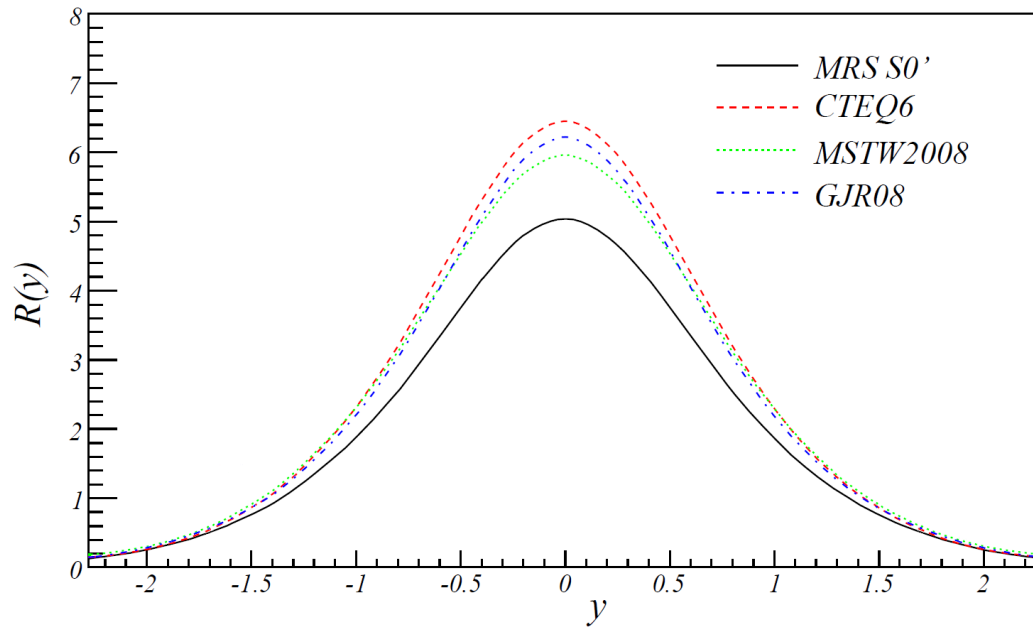

Figure 1.10: Prediction of the charge ratio $R(y_l)$ as a function of lepton rapidity for pp collision at $\sqrt{s} = 500$ GeV using various PDFs [86].

1.3.4 Single Spin Asymmetry

W production in polarized pp collisions at RHIC can observe the pure weak interaction and generate large parity-violating single spin asymmetries (A_L). A_L of W production will provide the first direct (flavor separated) measurement of the polarized PDF of quark and anti-quark especially for u and d quarks in the proton ($\Delta u, \Delta \bar{u}, \Delta d$, and $\Delta \bar{d}$). Past measurements in (SI)DIS were carried out with significant experimental precision only for the u quark polarized PDF (Δu). The W measurements can complete the knowledge of quark and anti-quark polarizations.

The standard model production of W bosons proceeds through a pure $V - A$ interaction. Thus, the helicity of the incoming quark and anti-quark is fixed. In addition, the W boson couples to a weak charge that correlates directly to flavors. The production of W bosons in pp collisions is dominated by $u, d, \bar{u}$ and $\bar{d}$, with some contamination from $s, c, \bar{s}$, and $\bar{c}$, mostly through quark mixing. Therefore, W boson production is an ideal tool to study the spin-flavor structure of the nucleon. The LO production of a W^+ boson, $u\bar{d} \to W^+$, with polarized pp collision is illustrated in Fig. 1.11.

The parity-violating single spin asymmetry is defined by:

$$A_L = \frac{d\sigma_+ - d\sigma_-}{d\sigma_+ + d\sigma_-}, \tag{1.35}$$

where subscripts of $+$ and $-$ on $d\sigma$ indicate the helicity states of proton beam. At RHIC, one can determine this asymmetry from either polarized beam by summing over the helicity states of the other beam.

For example, if the production of the W^+ proceeded only through the diagram in Fig. 1.11 (a), the single spin asymmetry would directly equal the longitudinal polarization asymmetry of the u quark in the proton. When ignoring the smaller contribution from the strange quarks, the A_L can be derived using Eq. 1.19 as:

$$A_L^{W^+}(x_F) = \frac{u_+^-(x_1)\bar{d}(x_2) - u_-^-(x_1)\bar{d}(x_2)}{u_+^-(x_1)\bar{d}(x_2) + u_-^-(x_1)\bar{d}(x_2)} = -\frac{\Delta u(x_1)}{u(x_1)}. \tag{1.36}$$

The second step in this equation follows from Eq. 1.9. Similarly, for Fig. 1.11 (b) alone,

$$A_L^{W^+}(x_F) = \frac{\bar{d}_+^+(x_1)u(x_2) - \bar{d}_-^+(x_1)u(x_2)}{\bar{d}_+^+(x_1)u(x_2) + \bar{d}_-^+(x_1)u(x_2)} = \frac{\Delta \bar{d}(x_1)}{\bar{d}(x_1)}. \tag{1.37}$$

In general, the asymmetry is a superposition of the two cases:

$$A_L^{W^+}(x_F) = \frac{-\Delta u(x_1)\bar{d}(x_2) + \Delta \bar{d}(x_1)u(x_2)}{u(x_1)\bar{d}(x_2) + \bar{d}(x_1)u(x_2)}. \tag{1.38}$$

The asymmetry for W^- can be obtained by interchanging u and d.

By identifying the rapidity of the W (y_W) [7] relative to the polarized proton, we can obtain direct measures at LO of the quark and anti-quark polarizations, which is separated by quark flavor: as the quark (anti-quark) distribution is large (small) in large x_F limit (i.e. $x_1 \gg x_2$), the asymmetry will be dominated by the quark distribution and give direct access to $-\Delta u(x_1)/u(x_1)$. Likewise, for small x_F

---

[7] (x_1, x_2) can be derived by y_W through Eq. 1.22.

(a)

Proton helicity ="+"   Proton helicity ="−"

(b)

Proton helicity ="+"   Proton helicity ="−"
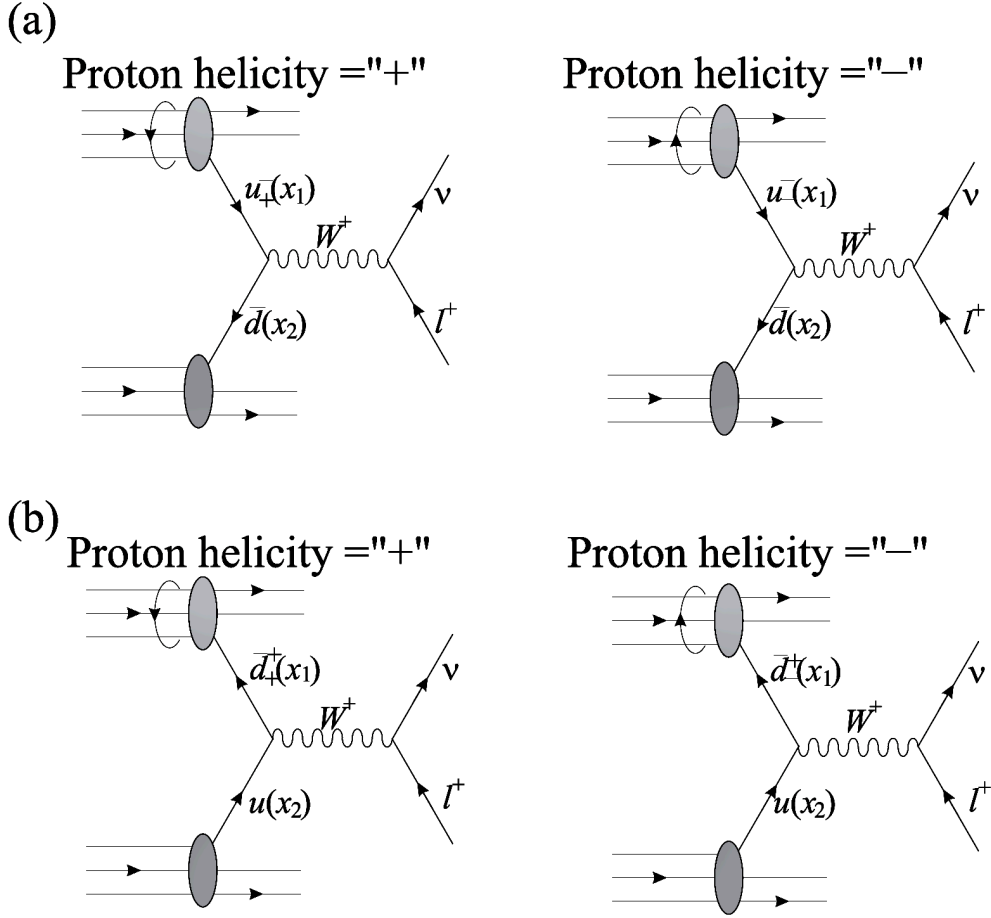
Figure 1.11: Production of W^+ bosons in $\bar{p}p$ collisions [10]. (a) Δu is probed. (b) Δd d is probed. The proton on the top in each panel is taken to be the polarized proton, with either positive (left) or negative (right) helicity.

limit $(x_1 \ll x_2)$, the term of $u(x_1)\bar{d}(x_2)$ is negligible and the asymmetry is given by $\Delta\bar{d}(x_1)/\bar{d}(x_1)$. The asymmetry of W^- production is the direct probe for $\Delta d/d$ and $\Delta\bar{u}/\bar{u}$ with similar calculation.

This picture is valid for the predominant production of W bosons at $Q_T \sim 0$. The experimental difficulty is that the W boson is observed through its leptonic decay $W \to l\nu$, and only the charged lepton is observed. The four momenta of the W boson cannot be determined from the momenta of its decay products. Therefore, the rapidity of the W boson cannot be measured directly. While it is certainly valuable to determine the asymmetry, $A_L(x_F)$, it has been shown that the directly measurable asymmetries in terms of the observed lepton, $A_L(y_l)$, is a viable alternative to the asymmetry of $A_L(x_F)$ [13].

Experimentally, $A_L(y_l)$ is measured by the difference of leptons from W boson decays between positive and negative helicity of protons in a particular rapidity region $(N^+(l), N^-(l))$, divided by the sum, and

normalized by the beam polarization (P):

$$A_L(y_l) = \frac{1}{P} \cdot \frac{N^+(l) - N^-(l)}{N^+(l) + N^-(l)}. \tag{1.39}$$

One can expect that, at least to some extent, the relation between momentum fractions (x_1, x_2) and rapidity of the W boson (y_W) will be inherited by the lepton. The correlation is already shown in Fig. 1.8, and it indicates the combinations of PDFs predominantly probed by $A_L(y_l)$ will vary with y_l. However, the underlying structure of the weak interactions also enters here. For W^- production, neglecting all partonic processes but the dominant $\bar{u}d \to W^- \to e^-\nu$ one, the asymmetry at LO is given by:

$$A_L^{e^-}(y_l) = \frac{\int_{\otimes(x_1,x_2)}[\Delta\bar{u}(x_1)d(x_2)(1-\cos\theta^*)^2 - \Delta d(x_1)\bar{u}(x_2)(1+\cos\theta^*)^2]}{\int_{\otimes(x_1,x_2)}[\bar{u}(x_1)d(x_2)(1-\cos\theta^*)^2 + d(x_1)\bar{u}(x_2)(1+\cos\theta^*)^2]}, \tag{1.40}$$

where $\int_{\otimes(x_1,x_2)}$ denotes an appropriate convolution over momentum fractions, and θ^* is the polar angle of the lepton in the W rest frame, with $\theta^* > 0$ in the forward direction of the polarized proton. Note that θ^* itself depends on the momentum fractions and the rapidity of lepton (see Eq. 1.24). At large negative y_l, one has $x_2 \gg x_1$ and $\theta^* \sim \pi$. In this case, the first terms in the numerator and denominator of Eq. 1.40 strongly dominate, because the combination of parton distributions, $\Delta\bar{u}(x_1)d(x_2)$, and the angular factor, $(1-\cos\theta^*)^2$, dominate over the second term. Therefore, the asymmetry provides a clean probe of $\Delta\bar{u}(x_1)/\bar{u}(x_1)$ at medium x_1 values ($x_1 \sim 0.05$). With similar reason, the second terms in the numerator and denominator of Eq. 1.40 dominate at forward rapidity of $y_l \gg 0$, and one can access to $\Delta d(x_1)/d(x_1)$ at relatively high x_1 ($x_1 \sim 0.4$).

For the W^+ production channel, the single spin asymmetry is written as:

$$A_L^{e^+}(y_l) = \frac{\int_{\otimes(x_1,x_2)}[\Delta\bar{d}(x_1)u(x_2)(1+\cos\theta^*)^2 - \Delta u(x_1)\bar{d}(x_2)(1-\cos\theta^*)^2]}{\int_{\otimes(x_1,x_2)}[\bar{d}(x_1)u(x_2)(1+\cos\theta^*)^2 + u(x_1)\bar{d}(x_2)(1-\cos\theta^*)^2]}. \tag{1.41}$$

Here, the distinction of the two contributions by considering large negative or positive lepton rapidities (y_l) is less clear than the case of W^-. For example, the partonic combination $\Delta\bar{d}(x_1)u(x_2)$ will dominate at negative y_l $(y_l \ll 0)$, but $\theta^* \sim \pi$ at the same time so that the angular factor $(1+\cos\theta^*)^2$ become small. Likewise, the dominant combination of $\Delta u(x_1)\bar{d}(x_2)$ is suppressed by the angular factor at positive y_l because $\theta^* \sim 0$. Therefore, both terms in Eq. 1.41 will compete for all y_l of interest.

Figure 1.12 shows $A_L(y_l)$ at RHIC calculated using the CHE MC program [12]. This framework allows the prediction of the A_L for various polarized PDFs of quark and anti-quark, and different curves in the figures correspond to the different sets of polarized PDFs of DSSV [67, 68], GRSV [62] and DNS [64]: the "standard" and "valence" sets from GRSV ("GRSV std" and "GRSV val") have SU(2) symmetric and broken sea distributions, respectively. The "DNS kre" and "DNS kkp" sets correspond to fits to the same data of DIS and SIDIS, but obtained using different sets of fragmentation functions [69, 70] to analyze the SIDIS data. In the figure, a clear discrimination to the underlying PDF is observed in the backward region ($y_l < 0$) of W^- production, which is caused by the uncertainty of $\Delta\bar{u}$. Moreover, this kinematic region allows to connect the detected lepton back to the W production kinematics (x_1, x_2), and

the sea quark polarization. The asymmetry becomes large and positive at large y_l, which reflects the fact that $\Delta d(x)$ remains negative at high x for all sets of polarized PDFs considered here (see Fig. 1.4). For W^+ production, the sensitivity is similar in the forward and central region ($y_l \geq 0$), which is originated from the uncertainty of $\Delta \bar{d}$. Overall, the asymmetry is negative because of the contribution from Δu in Eq. 1.41, which is known to be positive from (SI)DIS measurements.

In addition to the contribution from W exchange, the CHE code can also compute the background arising from Z-boson and/or photon exchange at the same accuracy in perturbative QCD. The contribution from photon exchange, $q\bar{q} \to \gamma^* g$ followed by $\gamma^* \to l^+ l^-$, may generate large contributions at NLO when the high-transverse momentum photon splits almost collinearly into the lepton pair, producing high-p_T leptons with a very low invariant mass. A proper treatment of this background would require the addition of a fragmentation contribution which is based on parton-to-dilepton fragmentation functions [88].

Figure 1.13 displays the asymmetries calculated with including leptons produced by Z/γ exchange [12]. As expected, the inclusion of "background" leptons results in a reduction of the asymmetry due to the increase of the unpolarized cross section. Because the PHENIX detector cannot distinguish electrons from W/Z decay, this figure shows the prediction of A_L for the PHENIX. Even though the asymmetry is smaller than the asymmetry of pure W sample, it still has a large band in backward region of negative charge and in central and forward region of positive charge. The distinct A_L corresponds to the different polarized PDFs, which all describe the (SI)DIS data, due to the differences in the sea quark polarizations. As the acceptance of the PHENIX covers $|\eta| < 0.35$ in central rapidity, $-2.2 < \eta < -1.1$ and $1.1 < \eta < 2.4$ in forward rapidities, the measurement of A_L of high p_T leptons, which mainly come from W/Z decays, at PHENIX will significantly improve the knowledge of the quark polarizations, and enable the first direct determination of the anti-quark polarizations when it is used as an input to a global analysis together with the (SI)DIS data. It will be possible to determine, first at a lower luminosity, whether the anti-quarks are polarized, and at an increased luminosity, whether there is a symmetry between the polarizations of $\bar{u}$ and $\bar{d}$ in the proton or not.

Figure 1.12: Rapidity dependence of the NLO single spin asymmetries $A_L^{e^-}$ for electrons and $A_+^{e^+}$ for positrons at RHIC, for the various sets of polarized parton distribution functions. Only leptons produced by $W^\pm$ boson exchange are considered [12].
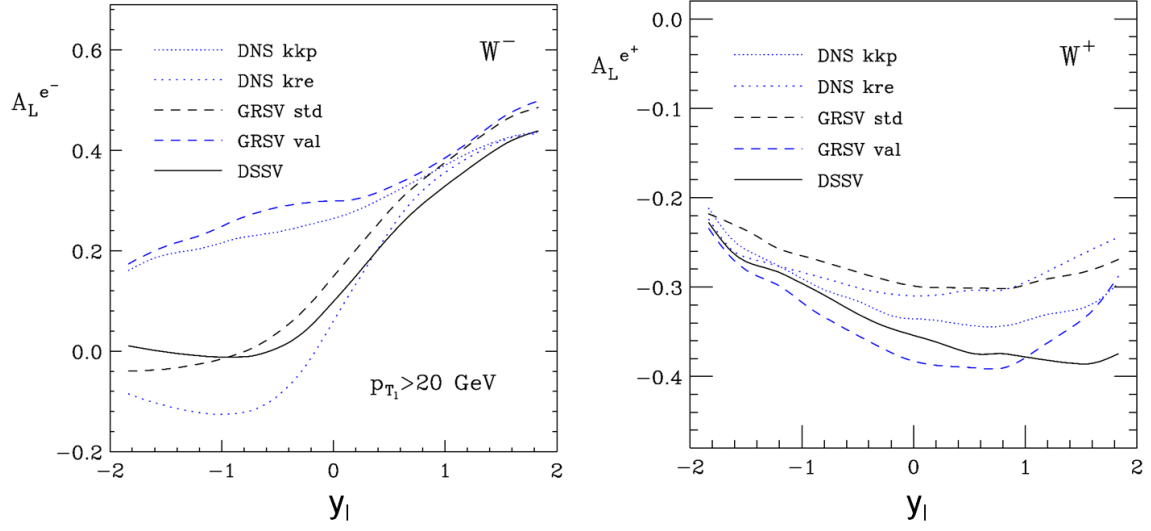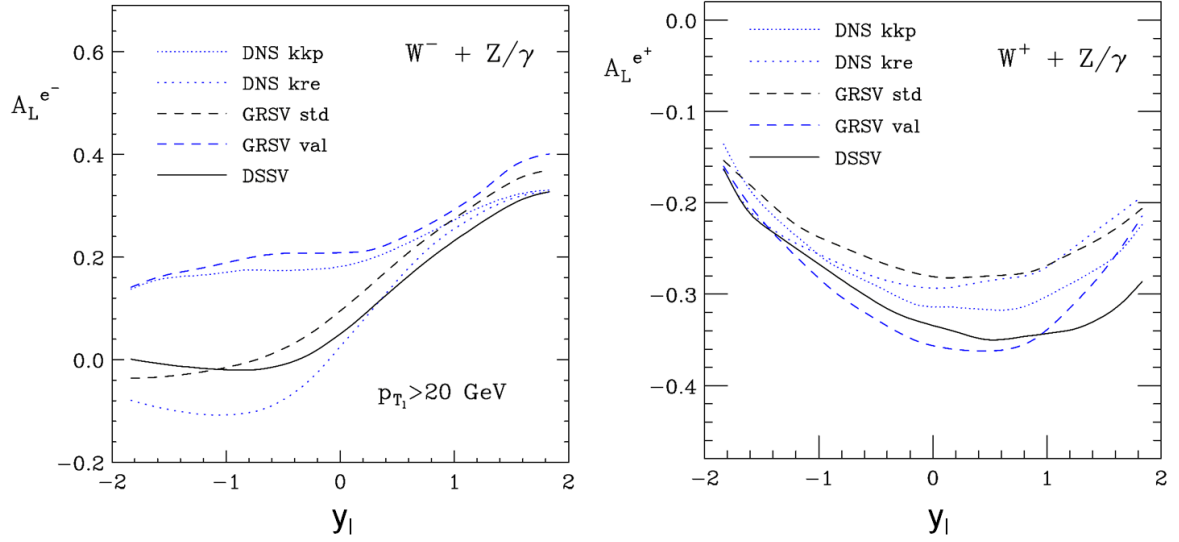

Figure 1.13: Rapidity dependence of the NLO single spin asymmetries $A_L^{e^-}$ for electrons and $A_+^{e^+}$ for positrons at RHIC, for the various sets of polarized parton distribution functions. Leptons produced by $W^\pm$ and Z boson exchange are considered [12].

1.4　Organization of Thesis

As discussed in the previous section, measurement of parity-violating single spin asymmetry of W boson production in polarized pp collision at RHIC is crucial for further understanding of proton spin structure. The measurement of cross section and charge ratio of W production in spin-averaged collisions also provides a sensitive test of current unpolarized PDFs, as well as it is an important confirmation of the theoretical understanding of the W production. For these purposes, production of W boson in pp collisions at $\sqrt{s} = 500$ GeV at RHIC Year-2009 run has been studied via electrons from their leptonic decays in the central rapidity region of the PHENIX detector ($|\eta| < 0.35$) at RHIC. The Year-2009 run was the first time to have pp collisions with $\sqrt{s}$ of 500 GeV at RHIC, and also the first opportunity to measure W bosons.

In analysis procedure, firstly, the p_T distribution of inclusive electron-candidate particles is measured. Then the background from photons and charged hadrons are estimated using both real data and MC simulation. The remnant includes electrons from both W and Z decay, because the PHENIX cannot distinguish them due to its limited acceptance. The cross section and charge ratio of $W \rightarrow e\nu$ is extrapolated from the measured distribution based on NLO (Next-to-Leading Order) and NNLO (Next Next-to-Leading Order) perturbative QCD calculations. Finally, single spin asymmetry of $W + Z$ production is evaluated and compared to theory predictions. The results obtained in this thesis is the first measurement of parity-violating single spin asymmetry of $W + Z$ production as well as it is the first observation of $W + Z$ boson production in pp collision.

The organization of this thesis is as follows: Chapter 2 introduce the RHIC accelerator complex and the PHENIX detectors. In Chapter 3, the conditions of RHIC Year-2009 run are summarized. Then, in Chapter 4, the analysis of measurement of the electrons from W and Z decays is explained. The analysis to evaluate the single spin asymmetry of $W + Z$ production is also described here. In Chapter 5, results of the measurement and the comparison to theoretical calculations are shown. The future prospects of measurements of charge ratio and single spin asymmetry of W production with expected constraint on PDFs are also presented in this chapter. Chapter 6 is the conclusion of this thesis.

Chapter 2

RHIC PHENIX

This thesis is based on the data which were taken at the RHIC (Relativistic Heavy Ion Collider) with the PHENIX detector at BNL (Brookhaven National Laboratory) in the United States during the Year-2009 run (called Run 9). RHIC Run 9 was the first time of the polarized pp collision at CMS (Center of Mass System) energy of $\sqrt{s} = 500$ GeV. The detail of Run 9 is described in Chapter 3.

The data analyzed in this thesis are collected with the PHENIX detector using its two central arm spectrometers. Each spectrometer covers $|\eta| < 0.35$ in pseudo-rapidity and $\Delta\phi = \pi/2$ in azimuth in a nearly back-to-back configuration. The capability of charged particle tracking and electron identification is necessary to measure single electrons from W or Z decay. The arms include drift chambers (DC), pad chambers (PC) for electron tracking, an electromagnetic calorimeter (EMCal) for energy measurement, and trigger electronics (ERTLL1). Beam-beam counters (BBCs), positioned at pseudo-rapidity $3.1 < |\eta| < 3.9$, measure the position of the collision vertex along the beam (z_{vertex}) and provide the interaction trigger (BBCLL1). In this chapter, the RHIC and the details of PHENIX detectors are presented.

2.1 RHIC

RHIC can accelerate and collide polarized proton beams for the first time in the world, which provides us unique opportunity to study the spin property of proton through strong and weak interactions. The spin structure of proton has been studied with DIS (Deep Inelastic Scattering) experiment where the interactions are mediated by virtual photons. Gluons interact at leading order in pp collisions while gluons only participate at higher order in DIS. Therefore, pp collisions are a good probe for the gluon spin contribution to the proton. The W-boson production in polarized pp collisions provide information on the flavor separation of the quark spin contribution. RHIC can accelerate polarized protons up to an energy of 250 GeV which results in collisions at $\sqrt{s} = 500$ GeV with design luminosity of 2×10^{32} cm^{-2}s^{-1}.

Figure 2.1 displays a schematic of RHIC accelerator complex. The polarized proton beam is produced at optically-pumped polarized ion source (called OPPIS, see Sec. 2.1.1) with the polarization of about 85 %. Its intensity reaches 500 μA in a single pulse of $300 - 400$ μs, which corresponds to $9 - 12 \times 10^{11}$ polarized protons. The protons are accelerated by a LINAC (Linear Accelerator) to a kinetic energy of

200 MeV. It is injected into a Booster, and is accelerated up to 1.5 GeV. Then it is transferred to AGS (Alternating Gradient Synchrotron) and accelerated up to 24.3 GeV. It is injected into two independent rings at RHIC, via the AGS-to-RHIC transfer line and is accelerated up to 250 GeV. Each beam travels in opposite direction and collides at the IPs (Interaction Points). Two independent beams are called the Blue (clockwise) and the Yellow (counter-clockwise) beams. RHIC has six IPs and they are referred to as IP12, IP2, IP4, IP6, IP8, and IP10 as shown in Fig. 2.1. Once RHIC is filled with beams, the beams are kept circulating in the rings to provide collisions at the IPs. When the luminosity becomes too low, the beams are dumped and refilled. The sequence from injection to dump of the beam is called a fill. One fill typically lasts ∼8 hours.

The beam in RHIC has bunch structure and each ring contains 120 bunches of polarized proton beam, with a time interval of 106 nsec. One of the remarkable features of RHIC is that the spin pattern of the bunches is arbitrary by freely flipping the spin of the protons at OPPIS. Figure 2.2 shows an example of a spin pattern assignment. The Blue beam has a spin pattern " $++--$ " while the Yellow beam has a spin pattern " $+-+-$ ". In this way, all possible spin combinations ($++$, $+-$, $-+$, $--$) can be obtained. This feature greatly reduced systematic uncertainty which comes from time dependence of the detector responses. The structure of the sequence of filled and unfilled bunches help to confirm the bunch IDs which are sent from the accelerator control system to the experiments. The exact bunch identification is crucial for precise calculation of the spin asymmetries.
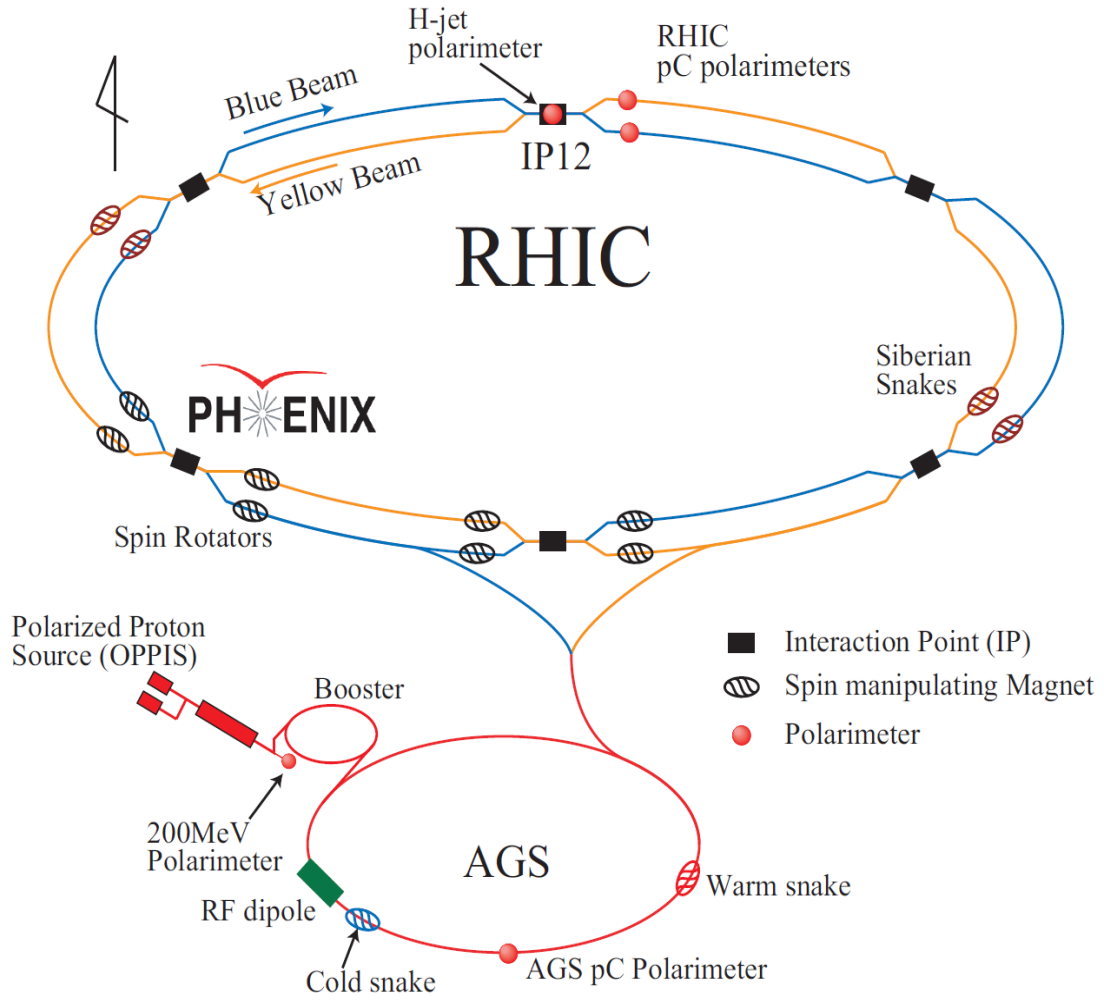
Figure 2.1: The accelerator complex of RHIC for the polarized proton collision.
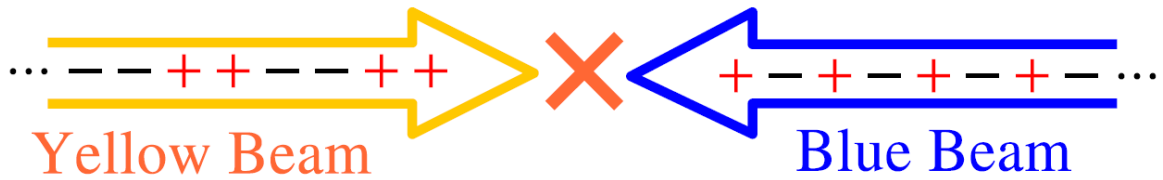
Figure 2.2: Example of the spin pattern of the beams. This spin pattern allows us to detect particles from the collision with any helicity combinations at the same time.

2.1.1 Polarized Proton Source

The polarized proton beam is produced at optically-pumped polarized ion source (OPPIS) [89]. The OPPIS technique for polarized H ion beam production was developed in the early 80's at KEK, INR Moscow, LAMPF and TRIUMF. Figure 2.3 displays a schematic drawing of the OPPIS, and its polarizing scheme is illustrated in Fig. 2.4. The source of angular momentum is high-power lasers. Rb atoms are optically pumped by titanium-sapphire lasers and electron-spin-polarized Rb atoms are produced. H^+ atoms are created with 29 GHz Electric Cyclotron Resonance (ECR) proton source. While they pass through the Rb vapor cell, the polarized electrons are transferred from Rb to H atoms, and H^+ atoms becomes electron-polarized H^0 atoms. To prevent depolarization in the charge-exchange collisions, the optically pumped cell is situated inside the strong (2.5 Tesla) superconducting solenoid. Then the polarization is transfered from electron to the H nucleus by the Sona transition [90]. Finally, electrons are attached by the Na-jet ionizer cell and H^- ions are produced.

Figure 2.3: A schematic drawing of the OPPIS.

Figure 2.4: The polarizing scheme of the OPPIS.

2.1.2 Polarized Proton Accelerator

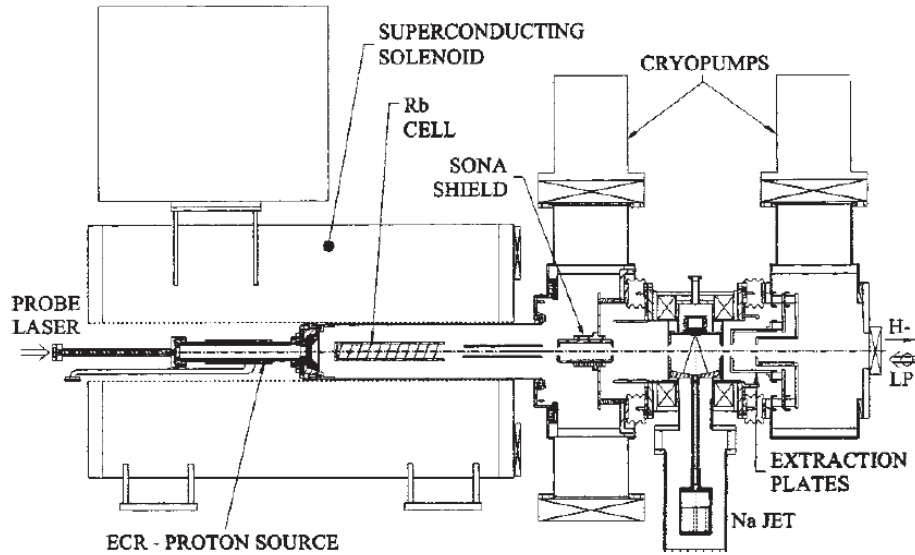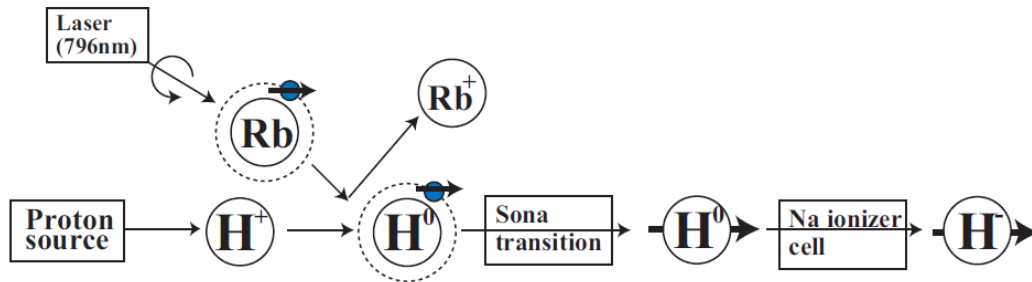The spin of the beam is oriented to the vertical direction, which is the stable direction during the acceleration in the normal synchrotron accelerator because the magnetic field to bend the beam is vertical. However, there are many depolarizing resonances at certain beam energies, depending on parameters of the accelerator. The "Siberian Snake" magnets play important role to overcome the depolarization and maintain the beam polarization [91]. Two Snakes are placed in each ring of RHIC and the location of one Snake is opposite side of the other (3 o'clock and 9 o'clock) to avoid additional depolarizing resonance caused by installing the single Snake. Each Snake in RHIC consists of four superconducting helical dipole magnets of identical structure. The strength and the direction of the field are different between four magnets (−4 to +4 Tesla), while they are independent of beam energy. By reversing the spin direction of the beam without an orbit distortion at the entrance and the exit of the Snake, the resonance conditions are shifted and the depolarization is avoided. Similarly, one other type of the Snake magnet is placed in AGS. Unlike the Snake in RHIC, the AGS Snake is just one normal-conducting helical dipole magnet and rotates the direction of the beam spin by only 9 degrees, which is enough to maintain the polarization in the lower-energy synchrotron, such as AGS, with weaker depolarizing resonances. This partial rotation forces to induce full spin flip at the beam energy on the depolarizing resonances, while it keeps spin direction unperturbed except for such a depolarizing conditions.

It is necessary to collide beams with polarized longitudinally to measure single spin asymmetry of W production process. To realize this, spin rotators are located before and after the interaction region of PHENIX in each ring. The former rotates the beam spin from the vertical to the longitudinal direction, the latter restores it to the vertical direction. Figure 2.5 shows a schematic drawing of the RHIC beams around the PHENIX interaction point. It is also possible to collide beams with radial transverse polarization. One spin rotator consists of four helical dipole magnets, whose structure is same as that for the Snake magnet except two of them have alternate handedness of helical magnet. They are powered independently to generate appropriate field needed for the spin rotation, which depends on the beam energy (−3 to +3 Tesla at around 100 GeV).
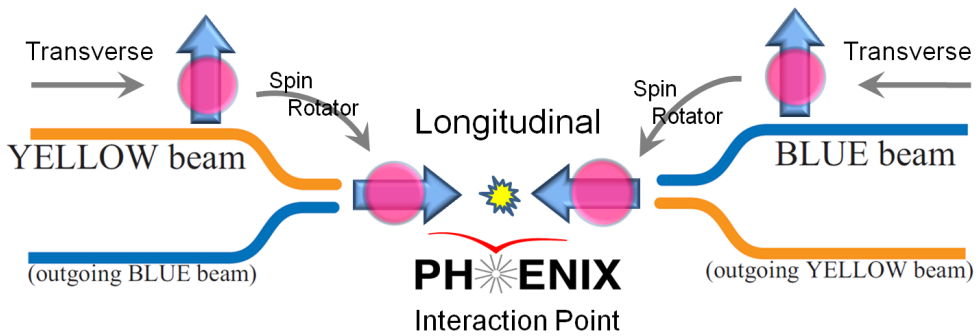

Figure 2.5: A schematic drawing of the RHIC beam near the PHENIX interaction point, when the longitudinally polarized collisions are required.

2.1.3 Polarimeters

Three polarimeters are used to measure and monitor the beam polarization. Two in RHIC and one at PHENIX experimental hall. Two types of polarimeters utilized in RHIC are proton-carbon polarimeter (pC polarimeter) [92], and polarized hydrogen gas jet target polarimeter (H-jet polarimeter) [93]. At PHENIX experiment, the orientation of the beam polarization is monitored by PHENIX local polarimeter [94]. These three types of polarimeters utilize a sizable single transverse spin asymmetry A_N. A_N is defined for a reaction between transversely-polarized beam and unpolarized beam (or target). It is defined as:

$$A_N = \frac{\sigma_{left} - \sigma_{right}}{\sigma_{left} + \sigma_{right}}, \tag{2.1}$$

where $\sigma_{left\ (right)}$ is the cross section that the outgoing particle goes left (right) side when the polarization is upward in view of the polarized beam. The measured raw asymmetry ε_N is $\varepsilon_N = PA_N$, where P denotes the beam polarization. Thus once the physics asymmetry A_N is known, the beam polarization can be calculated as $P = \varepsilon_N/A_N$. The three types of polarimeters are described in this subsection.

Proton-Carbon Polarimeter (pC Polarimeter)

The proton-carbon polarimeter (pC polarimeter) utilizes A_N in the elastic scattering between polarized proton beams and carbon target (A_N^{pC}) at very forward region, with four-momentum transfer of $-t = (0.01 - 0.02)\ (\mathrm{GeV}/c)^2$. The size of A_N^{pC} in the measured kinematic region is about 1.4 %. Due to the small scattering angle of protons, recoil carbons are detected instead of the scattered protons. The target should be thin for recoil carbon with small energy of 0.1 to 1 MeV to escape the target, and not to influence on the beam. However, it is required to achieve high statistics at the same time. The requirements are satisfied by using ultra-thin carbon ribbon target of 3 to 5 μg/cm^2 with a width of 10 μm.

Figure 2.6 displays the experimental setup of the pC polarimeter. The target ribbon is inserted into the beam and taken out after the measurement. Slow recoil carbons are detected by the silicon detectors placed on both sides of the target. The pC polarimeter collects $\sim 4 \times 10^6$ events per one measurements which is typically one minute. It corresponds to a statistical uncertainty of 4 % which is smaller compared to the systematic uncertainty (see Sec. 3.2). The pC polarimeter confirms that the bunch by bunch polarization variation is within the uncertainty of the measurements. The A_N^{pC} was not known at the RHIC energy and cannot be measured with the pC polarimeter system. Therefore, the pC polarimeter only provides relative variation of polarization for each fill. The H-jet target polarimeter was utilized to obtain the absolute normalization of the polarization. The polarization from the H-jet polarimeter were used to normalize the pC polarimeter results.

Polarized Hydrogen Gas Jet Target Polarimeter (H-jet Polarimeter)

The polarized hydrogen gas jet polarimeter (H-jet polarimeter) utilizes A_N in pp elastic scattering (A_N^{pp}). Since both beam and target are polarized, A_N^{pp} can be calculated for either beam or target polarization,
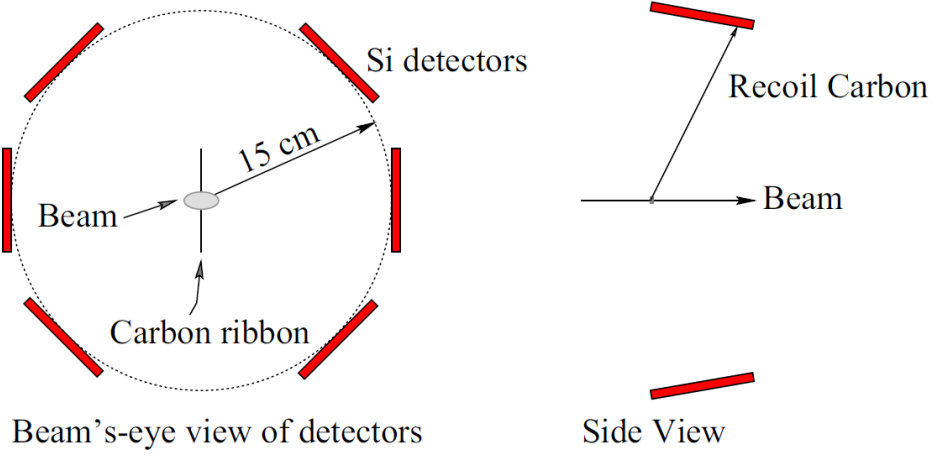
Figure 2.6: The experimental setup of the pC polarimeter. Left: beam view of the detectors. The beam runs into the paper and hit the carbon ribbon target in the center of the beam pipe. Right: side view of the detectors. The beam runs from left to right. The recoil carbon is detected with the Si detectors.

by averaging target or beam polarization. The relation between measured asymmetries $(\varepsilon_{beam}, \varepsilon_{target})$ and physics asymmetry (A_N^{pp}) is:

$$A_N^{pp} = \varepsilon_{beam}/P_{beam} = \varepsilon_{target}/P_{target}. \tag{2.2}$$

Here, P_{beam} (P_{target}) denotes the polarization of beam (target). P_{target} is measured by the Breit-Rabi polarimeter. Therefore, A_N^{pp} and P_{beam} can be obtained from measured asymmetries. One of the beautiful aspects in this measurement is that the physics asymmetry and the beam polarization are obtained with the same experimental setup, which reduces systematic uncertainty. Figure 2.7 illustrates the pp elastic scattering process (Left) and the experimental setup of the H-jet polarimeter (Right). The measured kinematic range is $-t \sim (0.001 - 0.02)$ $(\text{GeV}/c)^2$ where the asymmetry is large. The hydrogen gas jet target crosses the RHIC beam from top to bottom at a speed of 1.6×10^3 m/sec. The density of the gas jet target is $\sim 10^2$ H atoms/sec. The target spin direction is vertical, and is reversed in every 10 minutes. The recoil particle is detected with the silicon detectors which are placed on both sides of the targets.

Figure 2.8 displays the measured A_N^{pp} as a function of $-t$ in the range of $0.001 < |t| < 0.032$ GeV/c^2 at $\sqrt{s} = 13.7$ GeV [93]. The A_N^{pp} is about 4 % in the measured kinematic range, and the statistical uncertainty is about 2.5 % for a single beam for the whole run. This is not enough for measurement of polarization variation for each fill. The pC polarimeter is used for this purpose instead, which provides polarization with statistical uncertainty of the same level within one minute of measurement. The absolute beam polarization obtained with H-jet target is used to calibrate the pC measurement.
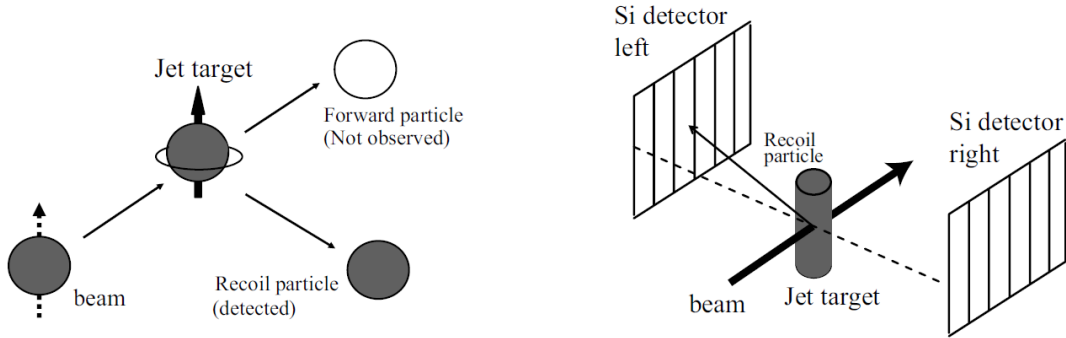
Figure 2.7: Left: The schematics of the pp elastic scattering process. The recoil proton is observed while the forward proton is not. Right: The experimental setup of the H-jet polarimeter. The beam runs through the jet target. The recoil particle is detected with the Si detectors.
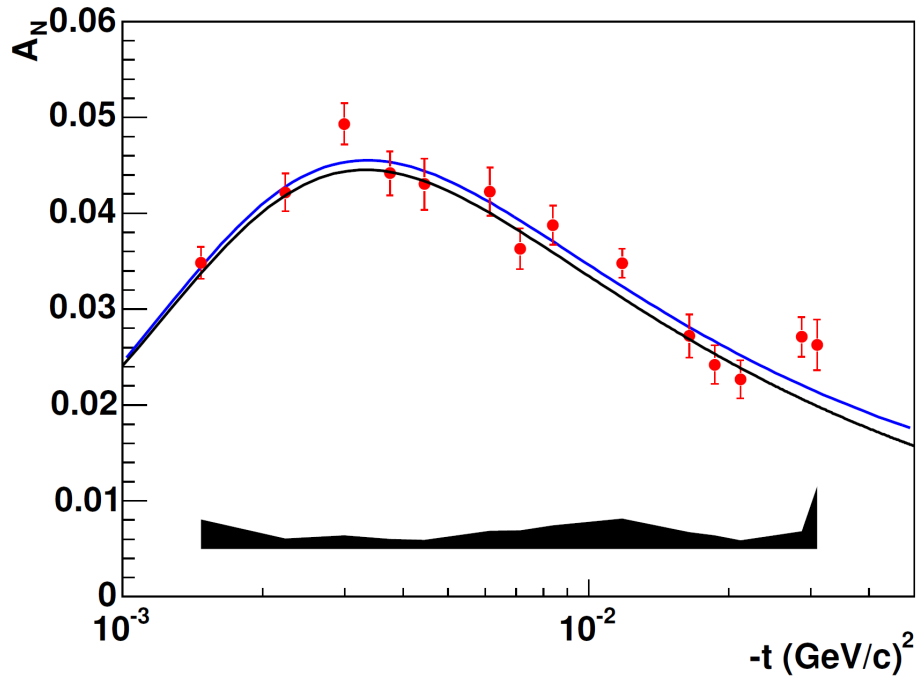
Figure 2.8: A_N as a function of $-t$ at $\sqrt{s} = 13.7$ GeV. The error bars on the data points represent statistical uncertainties. The lower band represents the total systematic uncertainties. The black line shows the prediction for A_N with the electromagnetic spin-flip, and the blue line is a fit to the data allowing for a hadronic spin-flip contribution to A_N [93].

PHENIX Local Polarimeter

For the study of the sea quark polarization, longitudinally polarized proton collisions are necessary while the stable polarization direction of the beam in RHIC ring is transverse as explained in Sec. 2.1.2. To obtain longitudinally polarized proton collisions, the polarization direction is rotated from transverse direction to longitudinal direction just before the interaction point (IP). Therefore, the polarization orientation should be monitored at the PHENIX IP. It is done by utilizing single spin asymmetry A_N of forward neutron production in polarized pp collisions. A_N vanishes when the beam polarization is in longitudinal direction, and A_N is non-zero for transversely polarized collisions (the size of A_N is ~ 10 %). In the longitudinally polarized proton collisions, the residual transverse component of the beam polarization (P_T) can be determined by comparing the size of A_N measured with spin rotator on and off. Neutrons are detected with PHENIX Zero-Degree Calorimeters (ZDCs) and Shower Max Detectors (SMDs), which details are described in Sec. 2.2.2. Since the extraction of P_T and P_L are performed at the PHENIX IP locally [1], it is called "Local Polarimeter".

At the commissioning period for the spin rotator tuning, the data for the local polarimeter analysis is collected with full PHENIX DAQ bandwidth [2] to know P_T and P_L. The spin direction is checked within one hour and the result is provided to the Collider Accelerator Department as a feedback in order to minimize the transverse component (P_T) [3]. The local polarimeter is also used to monitor the polarization direction during the longitudinal run period. The data for the local polarimeter analysis is collected with $100 - 200$ Hz through the physics run period, and the transverse and longitudinal components through the run is estimated by offline analysis.

---

[1] P_T and P_L show transverse and longitudinal components of polarization as $P^2 = P_T^2 + P_L^2$.

[2] Full DAQ bandwidth is ~ 5 kHz (see Sec. 2.2.6).

[3] A new method of local polarimeter utilizing scaler information from SMDs has been developed during Run 9 at PHENIX. It enables us to obtain enough data for the feedback within five minutes [95].

2.2 PHENIX

PHENIX [96] is one of the largest experiments at RHIC, located at the 8 o'clock intersection point (IP8). PHENIX was designed to measure photons, leptons, and hadrons with excellent particle identification capability and to deal with both high-multiplicity heavy-ion collisions and high event-rate pp collisions.

Figure 2.9 shows the definition of global coordinate system used in the PHENIX experiment, which defines the geometrical center of the interaction point as the origin $(0, 0, 0)$. Taking the beam-line as a z-axis (North is positive z direction), the direction to West arm is defined as x-axis, and upward is defined as y-axis. The azimuthal angle ϕ is measured counter-clockwise relative to the positive x direction, and the negative x direction is $\phi = \pi$ rad. The polar angle θ is defined as the angle relative to z-axis. Using the polar angle θ, the pseudo-rapidity variable is expressed as:

$$\eta = -\ln\left[\tan\frac{\theta}{2}\right]. \tag{2.3}$$
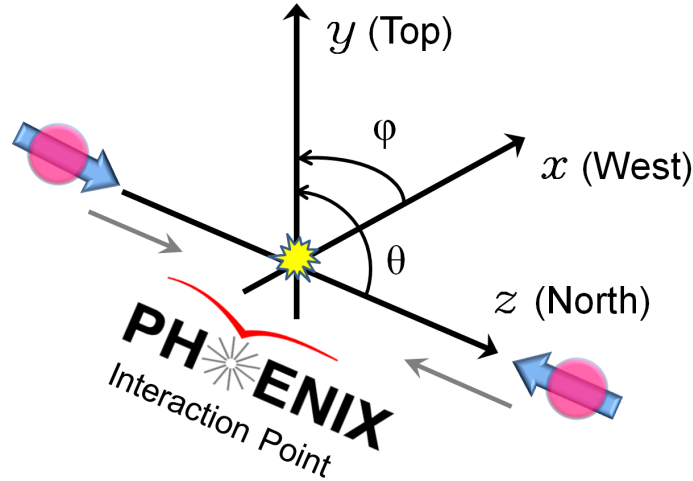
Figure 2.9: The PHENIX coordinate system.

The PHENIX experiment is composed of many sets of detectors. A collection of detectors with the same type is called a subsystem. The subsystems can be categorized into three groups: global detectors, two central arms and two muon arms. The global detectors consist of several subsystems and measure the collision information. Two central arms, East and West arms, cover the pseudo-rapidity range of $|\eta| < 0.35$ and half in azimuthal angle ($\Delta\phi = \pi/2 \times 2$). They are designed to detect photons, electrons and hadrons. Two muon arms, north and south arms, cover $1.2 < \eta < 2.4$ and $-2.2 < \eta < -1.2$ respectively with a full azimuthal coverage. They are designed to detect muons. PHENIX has three magnets: central magnet and two muon magnets. These magnets provide magnetic fields for momentum measurement of charged particles.

Figure 2.10 displays a schematic view of the PHENIX detector setup. The global detectors are Beam Beam Counters (BBCs), Zero Degree Calorimeters (ZDCs) which can be found in the lower panel. Shower

Max Detector (SMDs) are also placed inside ZDCs and are not displayed in the figure. These are used in this thesis and is described in Sec. 2.2.1 and 2.2.2. The upper panel is a beam view of the central arm detectors. The proton beams run perpendicular to the paper, at the center of the detectors. The beam pipe is surrounded by the central arm detectors: Hadron Blind Detectors (HBD), Drift Chambers (DC), Pad Chambers (PC1, 2, and 3), Ring Imaging Cerenkov detectors (RICH), Aerogel Cherenkov detectors, Time Expansion Chamber (TEC), and Electromagnetic Calorimeters (EMCal). The central arm detectors used in this thesis are DC, PC1 and EMCal. The DC and PC1 are utilized to measure the momentum of electrons from W decays. The details of the PHENIX tracking system at central arms which include DC and PC are introduced in Sec. 2.2.3. The EMCal is used for the energy measurement and the most important detector in this thesis. The details of the EMCal are described in Sec. 2.2.4. The lower panel of the figure is a side view of the setup. The proton beams collide at the interaction point (IP), which is the center of the panel. The collision vertex distributes along with the z-axis approximately in a Gaussian shape, with its center at $z \sim 0$ and with a width of $\sigma \sim 60$ cm. The pole piece of the central magnet, which is called nose cone, surrounds the beam pipe for $|z| > 41$ cm and it limits the acceptance of the central arms. The muon arm detectors are also shown in this panel: Muon Tracker (MuTr) and Muon Identifier (MuID), which are utilized to detect muons. The acceptance and purpose of PHENIX subsystems which are used in this thesis are summarized in Table 2.1.

As the event rate at RHIC is too high to take and record every collision events at PHENIX, the trigger which efficiently selects events of interest is necessary. Such trigger system is implemented to the PHENIX, and explained in Sec. 2.2.5. At the end of this section, the PHENIX data acquisition (DAQ) system is summarized (Sec. 2.2.6).

subsystem	η	ϕ	purpose
BBC	$\pm$(3.1 - 3.9)	2π	primary vertex detection, luminosity, time-zero, level-1 trigger
ZDC	±2 mrad	2π	primary vertex detection, luminosity, level-1 trigger
DC	±0.35	$\pi/2 \times 2$	charged particle detection, tracking
PC	±0.35	$\pi/2 \times 2$	pattern recognition, tracking
EMCal (PbSc, PbGl)	±0.35	$\pi/2 \times 2$	photon and electron detection, level-1 trigger

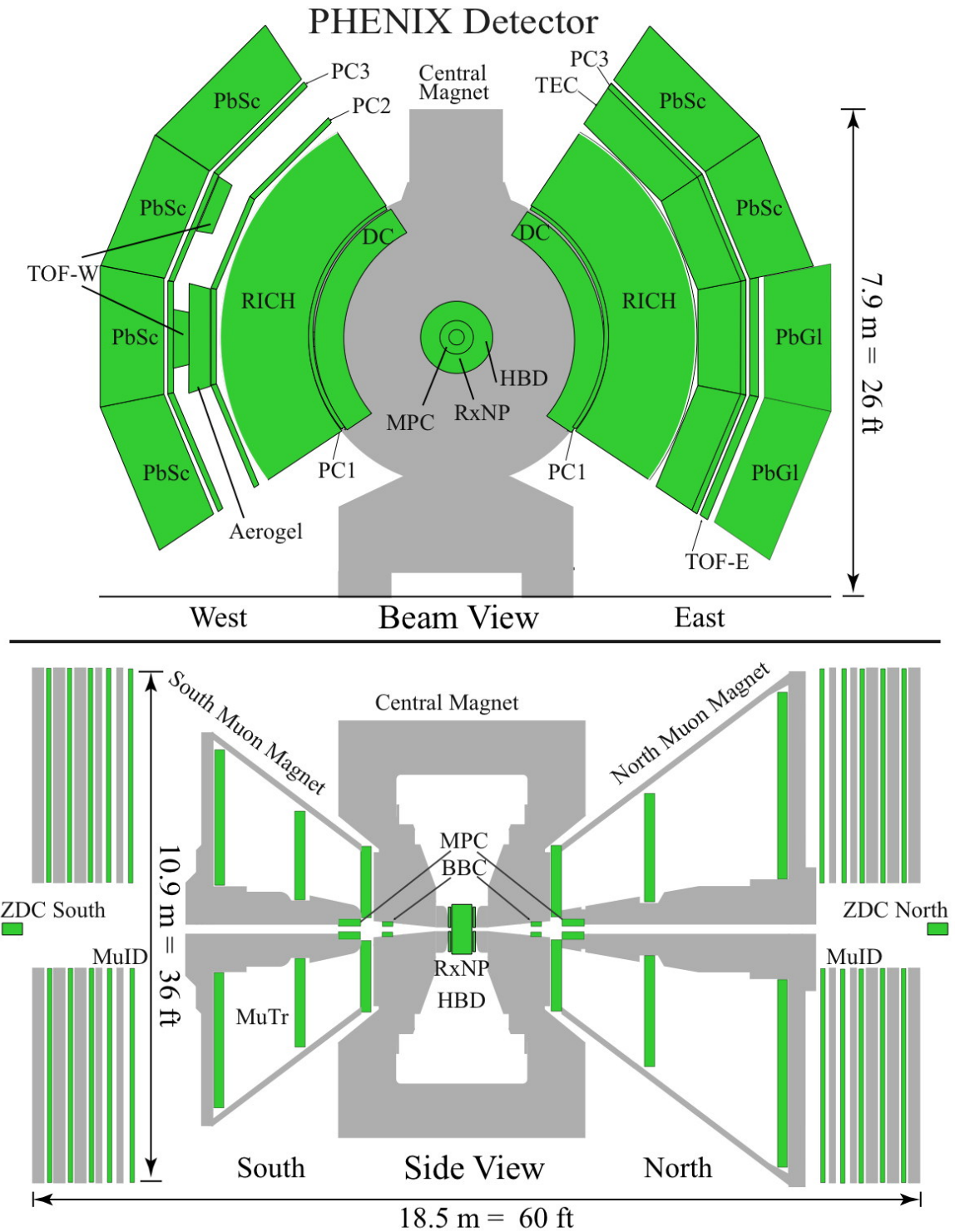Table 2.1: PHENIX subsystems and their acceptance and purpose.

Figure 2.10: The PHENIX detector. The upper panel shows a beam view of the PHENIX central arm detectors. The lower panel shows a side view of the PHENIX global and muon arm detectors.

2.2.1 Beam-Beam Counters (BBC)

The Beam-Beam Counters (BBC) provide the information of collision point and start signal for time of flight measurement [97]. There are two arrays of quartz Cherenkov detectors in PHENIX along the beam line. They locate at 144 cm from the interaction point and surround the beam axis with the 10 cm of inner diameter and 30 cm of outer diameter. The pseudo-rapidity coverage is $3.0 < |\eta| < 3.9$. Each counter consists of 64 one-inch diameter mesh-dynode (15 step) Photo Multiplier Tubes (PMT: Hamamatsu R6178) equipped with 3 cm quartz on the head of PMT as a Cherenkov radiator. They are sensitive to charged particles with β greater than 0.7, and BBC detects the particles such as $\pi^{\pm}$ from collisions. The pictures of BBC are displayed in Fig. 2.11.

The start signal for timing measurement (T_0) and the beam-beam collision point along beam axis (z_{vertex}) are provided by using the average arriving time of particles between North (T_N) and South BBC (T_S) and their difference. They are calculated from:

$$T_0 = \frac{T_N + T_S}{2} - \frac{L}{c}, \tag{2.4}$$

$$z_{vertex} = \frac{c(T_S - T_N)}{2}, \tag{2.5}$$

where L is the half of the distance between the two BBCs (144 cm), and c is the speed of light. When the collision vertex position is outside of the BBCs ($|z| > 144$ cm), the vertex position is reconstructed as $z = \pm144$ cm, where $\pm$ correspond to on either side ($z > 144$ or $z < -144$ cm) of the collision vertex.

With slewing correction, ~ 2 cm of the position resolution is achieved in offline analysis for pp collisions.
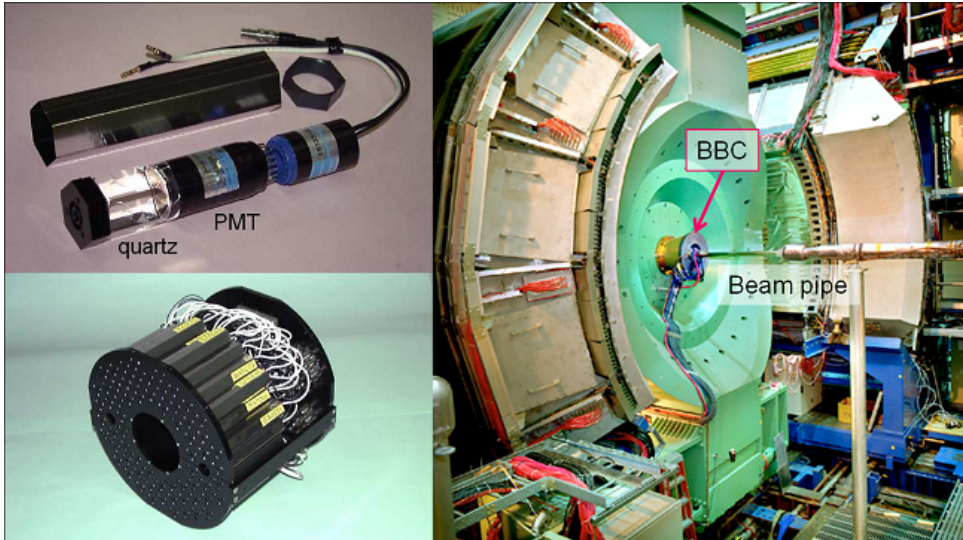
Figure 2.11: Pictures of BBC. Left top: The element of BBC. Left bottom: A BBC array comprising 64 BBC elements. Right: BBC after installation. The collision point is the left side of the picture, and BBC is attached behind the central magnet.

2.2.2 Zero-Degree Calorimeters (ZDC)

The Zero-Degree Calorimeters (ZDCs) [98], together with Shower Max Detectors (SMDs) were equipped to detect neutrons at very forward angle of less than 2.8 mrad. They are placed at 18 m away from the IP, and sit behind the DX dipole magnet as shown in Fig. 2.12. The DX magnets serve to sweep away most of the charged particles, and neutral particles with long life, which are mainly neutrons and photons, hit the ZDCs. Since protons which experience elastic or diffractive scatterings at the IP may hit the beam pipes and induce showers, the resulting charged particles may hit the ZDCs. A scintillation counter are placed in front of each ZDC for charged particle veto.
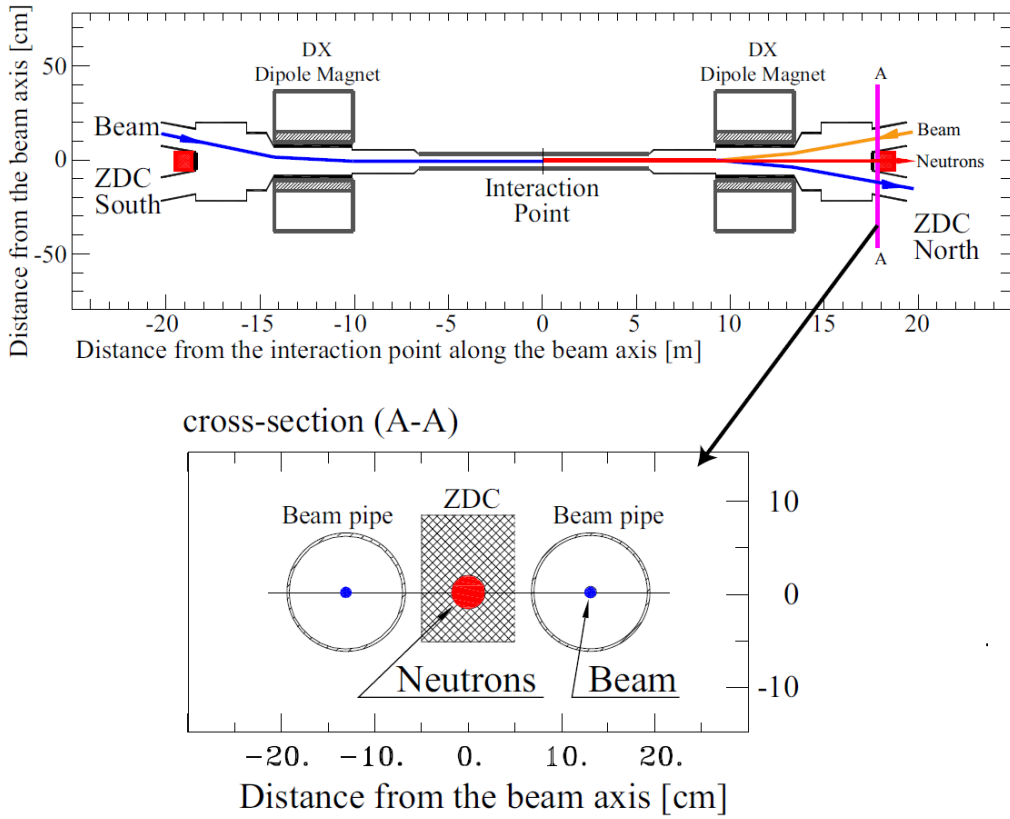
Figure 2.12: The ZDC location.Top: top view of the ZDC location.Bottom: beam view of the ZDC location.Charged fragments are bended by the Dipole magnets towards the outside of the acceptance of ZDC.

The ZDC consists of three ZDC modules each of which has 1.7 interaction length or 51 radiation length of absorber. The three ZDC modules are placed in series to comprise a ZDC. Figure 2.13 shows the mechanical design of a module of the ZDC. A module consists of 27 layers of tungsten absorber plates and PMMA (polymethylmethacrylate) optical fibers. A neutron generates a hadronic shower in the tungsten plates, and charged particles in the shower emit Cerenkov radiation. The radiation is detected through the optical fibers with a PMT (Hamamatsu R329-02). The size of a tungsten plate is 10 cm wide, 18.7 cm high and 0.5 cm thick. The energy resolution of ZDC was obtained to be $\delta E/E \simeq 218/\sqrt{E \text{ (GeV)}}$ %

from the test beam results. Neutrons can be separated from photons with the energy deposit in the 2nd module of the ZDC, since the electromagnetic showers from photons cannot penetrate the 1st module with 51 radiation length and do not reach the 2nd module. Taking the correlation between North and South ZDC also provides the background rejection due to single-beam interaction with the residual gas in the beam pipe.

The SMD consists of scintillator hodoscopes: 7 scintillator strips with a width of 15 mm in the vertical direction (to provide x-coordinate), and 8 strips with a width of 20 mm in the horizontal direction (to provide y-coordinate). The SMD is placed between the 1st and the 2nd ZDC modules where the neutron-induced shower reaches its maximum. The hits of the showers at the SMD were weight-averaged to provide the shower position. The position resolution of ~ 1 mm is achieved for neutrons with an energy of 100 GeV.

The vertex position is reconstructed from the hit timing in the two ZDCs as in the case of BBCs, and the position resolution is obtained to be ~ 30 cm in online and ~ 10 cm in offline.

The coincidence of hits in the two ZDCs defines ZDC trigger. The ZDC trigger serve as an independent luminosity measure as well as the BBC trigger (BBCLL1), which is explained in Sec. 2.2.5. There are two types of ZDC trigger with different vertex position cuts. One is ZDC narrow trigger which is defined with the vertex position cut of $|z| < 30$ cm, and the other is ZDC wide trigger which is defined with the vertex position cut of $|z| < 150$ cm. Since the width of the vertex position variation is ~ 60 cm, most of the collisions are covered by the ZDC wide trigger. The ZDC trigger information is used in vernier scan for estimating z dependence of the BBC efficiency (Sec. 3.3).
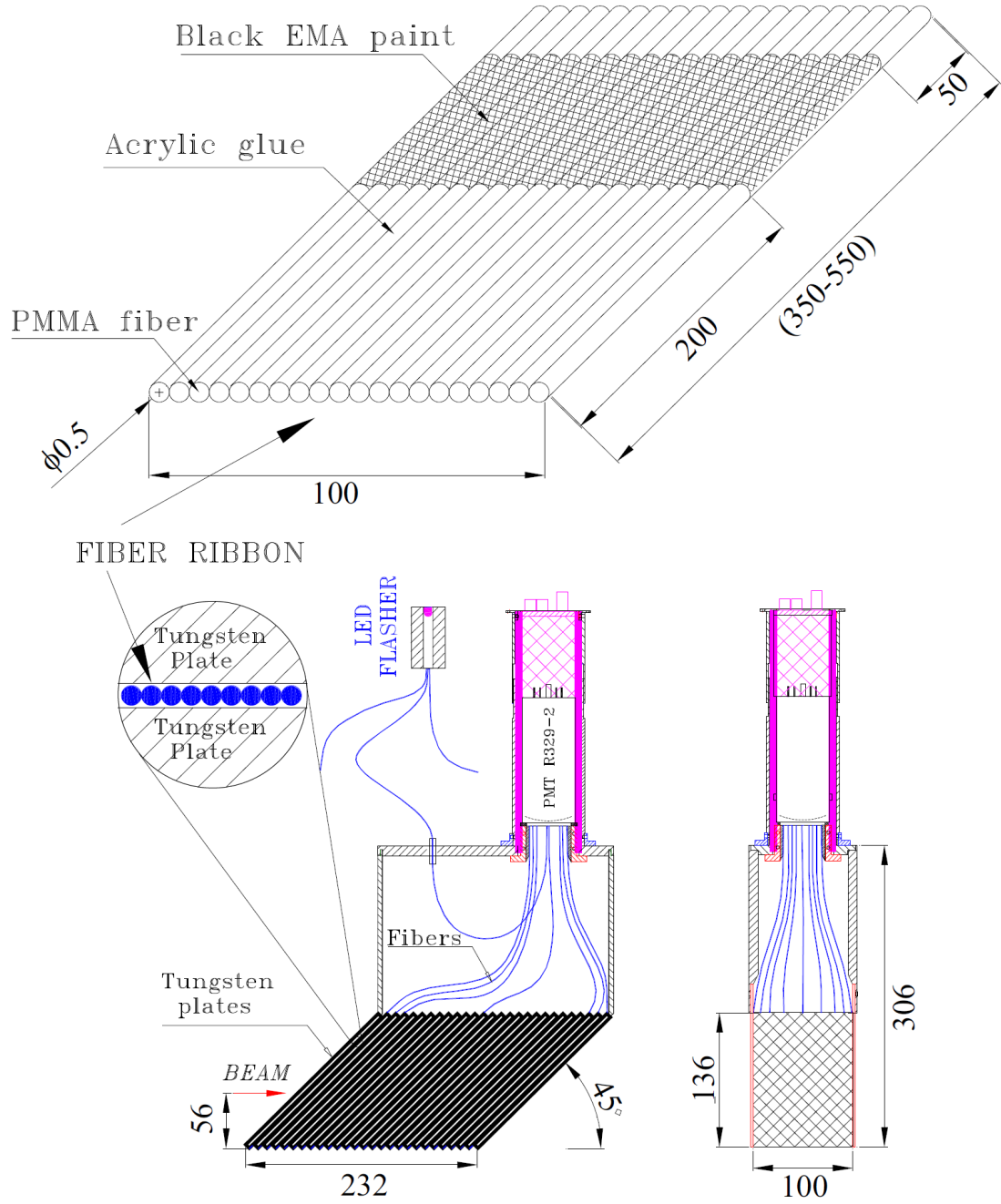
Figure 2.13: ZDC Mechanical Design. The mechanical design of ZDC. Dimensions shown are in millimeter. Top: one layer of the PMMA fibers. Bottom left: The side view of one module. Bottom right: The beam view of one module.

2.2.3 PHENIX Tracking System

The tracking devices of PHENIX central arms reconstruct momenta of charged particles from their bending angle in the magnetic field. The tracking system consists of the central magnet, DC (Drift Chamber) and PC (Pad Chamber). In this subsection, the details about the tracking system of the PHENIX central arm are described.

Central Magnet

PHENIX Central Magnet provides the axial field of $\int B \cdot dl = 0.78$ T·m at $\theta = \pi/2$ rad. It is used to determine the momentum of charged particles using magnetic bending. The Central Magnet is energized by two, inner and outer, pairs of concentric coils, which can be operated separately, with the same polarities or opposite polarities. In Run 9 period, the same polarity operation was chosen to maximally bend high p_T electrons from W decay, so that the charge sign of $e^{\pm}$ can be separated. The operation is called as "++ mode" according to the polarity of the magnetic field. The magnetic field produced by the magnets is shown in Fig. 2.14. The pole faces of the magnet, which is called nose cone, are positioned at ± 45 cm in z direction covering the rapidity range of ± 0.35. The nose cone also serves as the hadron absorbers for the muon spectrometers.

Drift Chambers (DC)

The Drift Chambers (DC) are used to measure the charged particle trajectories in r-ϕ plane and to provide the high resolution momentum determination.

The DC is located in the East and West arm at a radial distance of $2.02 < R < 2.46$ m, respectively. One of them is the mirror copy of each other, and each DC covers 90 degrees in azimuth and 1.8 m along the z-direction which corresponds to $|\eta| < 0.35$ (see Fig. 2.10). They are filled with the gas mixture of 50 % Argon and 50 % Ethane.

The schematic drawing of the DC frame is shown in Fig. 2.15. Each DC consists of 20 sectors, each of which covers 4.5 degrees in azimuth. In each sector, there are six types of wire modules stacked radially. They are called X1, U1, V1, X2, U2, V2 plane. The sketch of a sector and the layout of wire position are shown in Fig. 2.16.

The wires in X1 and X2 plane run in parallel to the beam axis in order to perform the track measurements in r-ϕ plane. They are followed by two sets of small angle U, V wire planes. U1, V1, U2, and V2 wires have stereo angle of about 6 degrees relative to the X wires in order to measure the z-coordinate of the track. The X wire modules contain 12 sense (anode) planes and 4 cathode planes. Both U and V wire modules contain 4 sense (anode) planes and 4 cathode planes. They form the cells with a $2 \sim 2.5$ cm drift space in ϕ direction. In this scheme, 40 drift cells are located at different radii in the DC frame.

The DC system contains roughly 6,500 anode wires ($\sim (12 \times 2 + 4 \times 4) \times 4 \times 40$). Each wires are separated into two halves by the Kapton support at $z = 0$, and the signals are independently extracted. Thus, the number of total readout channel is 13,000. The anode wires are separated by Potential (P) wires
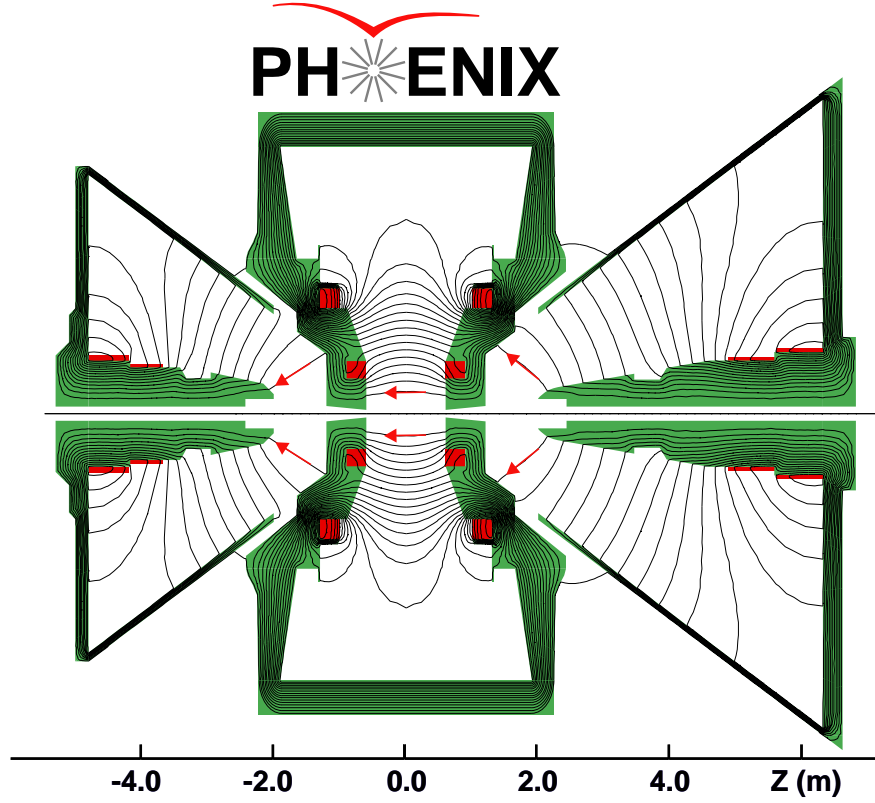
Magnetic field lines for the two Central Magnet coils in combined (++) mode

Figure 2.14: The magnetic field lines of the Central Magnet and Muon Magnets shown on a vertical cutaway drawing of the PHENIX magnets. The beams travel along the $r = 0$-axis in this figure and collide at $r = z = 0$. Arrows indicate the field direction.

and surrounded by Gate (G) and Back (B) wires. The P wires form a strong electric field and separate sensitive regions of individual anode wires. The G wires limit the track sample length to roughly 3 mm and terminate the unwanted drift line. The B wire has a rather low potential and terminates most of the drift lines from side. With a 50-50 mixture of argon-ethane gas, the stable drift velocity plateau at 5.3 cm/μsec is achieved for the field gradation from 800 V cm up to 1.4 kV cm. Therefore, the maximum drift time in a cell is approximately 470 nsec ($= 2.5/5.3$ μsec). The position resolution was measured to be 1.1 mrad along the ϕ-direction.
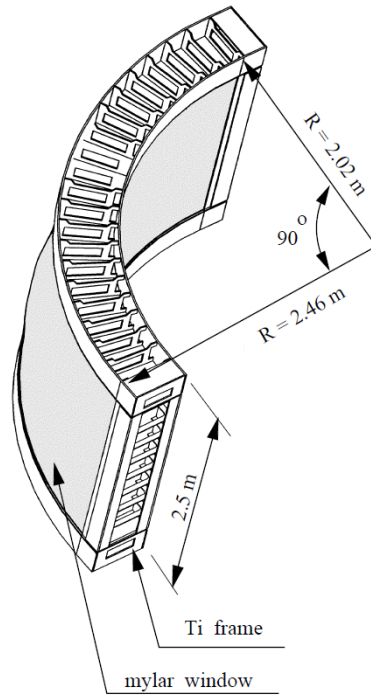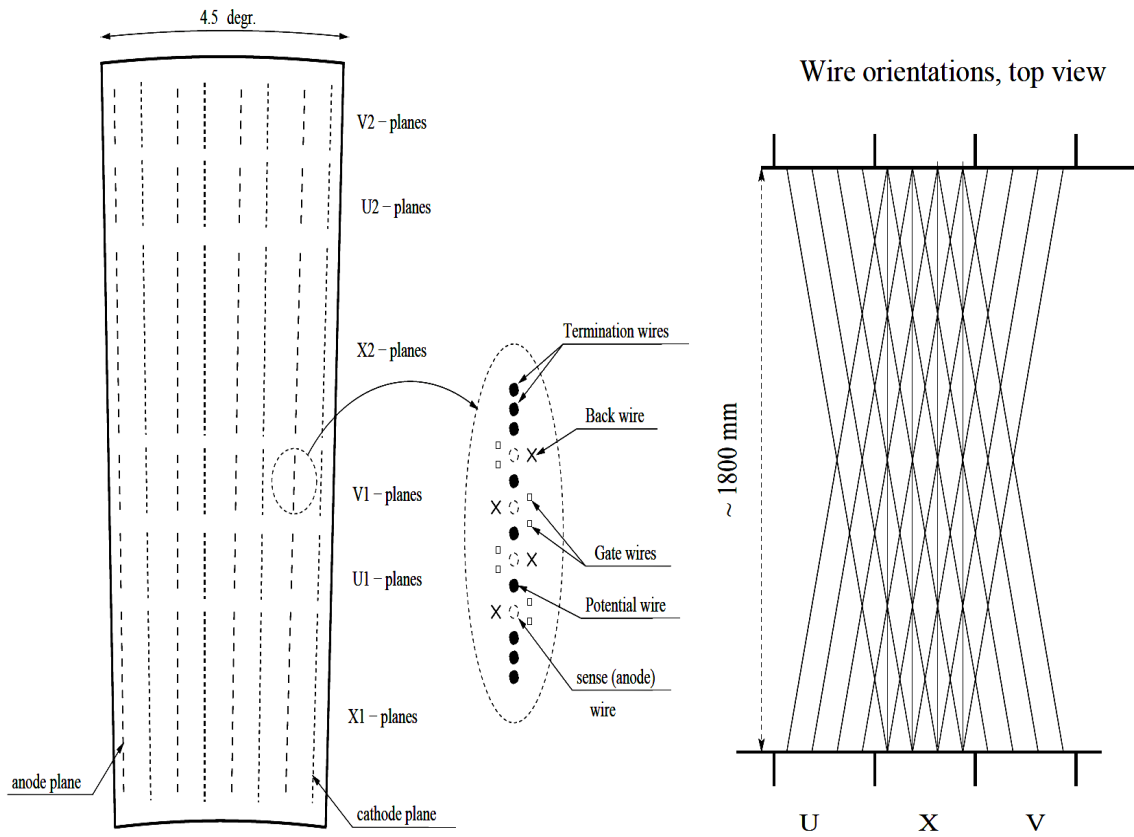
Figure 2.15: The construction of a DC frame.

Figure 2.16: Left: The layout of wire position within one sector of the DC and inside the anode plane. Right: A schematic diagram of the stereo wire orientation.

Pad Chambers (PC)

The Pad Chambers (PC) is used to determine the space points which are used for momentum determination in the z-direction (p_z). The PCs are the multi-wire proportional chambers with cathode readout that form three separate layers (PC1, PC2 and PC3) in the central arms. The PC1 layer is innermost chamber located between DC and RICH, occupying 2.47 m through 2.52 m in radial distance from the interaction point, the PC2 layer is placed behind RICH occupying 4.15 m through 4.21 m, and the PC3 is located in front of EMCal occupying 4.91 m through 4.98 m. The PC1 is essential for determination of the three dimensional momentum by providing the z-coordinate at the exit of the DC. The combination of the DC and the PC1 information provides the direction vector through RICH. The PC2 and the PC3 are needed to resolve ambiguities in outer detectors where about 30 % of the particle striking the EMCal are produced by either secondary interactions or the particle decays outside the aperture of the DC and the PC1.

Each detector contains a single plane of wires inside a gas volume bounded by two cathode planes as shown in Fig. 2.17. The gas was chosen to be the mixture of 50 % Argon and 50 % Ethane at atmospheric pressure. One cathode is finely segmented into an array of pixels, and a cell area of 8.4×8.4 mm^2 was adopted from the requirement of good position resolution in z-direction and a low occupancy even in the high track multiplicities. The position resolution was measured to be 1.7 mm for the PC1 along the wire (z-direction).

When a charged particle starts an avalanche on an anode wire, the charge induced on a number of pixels is read out through specially designed readout electronics. Figure 2.18 shows the schematic diagram of the PC. In order to reduce the amount of electric and other noise, each cell of the PC contains three pixels and an avalanche must be sensed by all three pixels to form a valid hit in the cell (Fig. 2.18 (a)). Because of huge electronic channels with this arrangement, the interleaved pixels are gathered together as shown in Fig. 2.18 (b). Nine pixels are connected to a group and to a common readout channel, such that the three pixels in a cell are always connected to different but neighbor channels and each cell is defined by its unique channel triplet (Fig. 2.18 (c), (d)). This solution saves a factor of nine in readout channels compared to readout of every pixel.
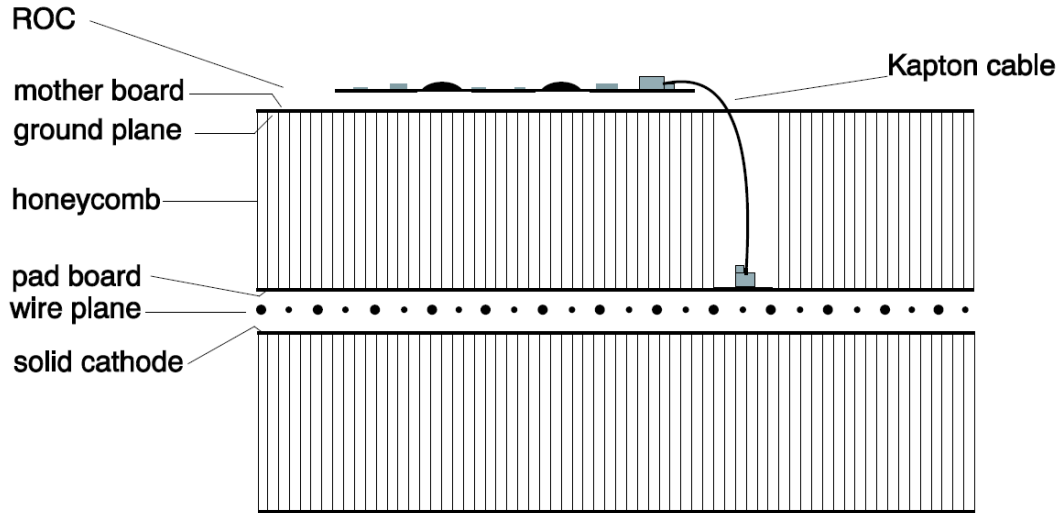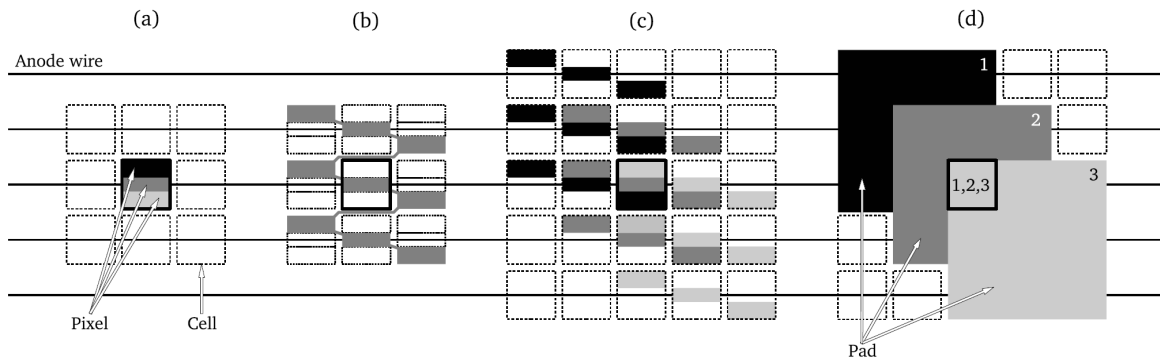
Figure 2.17: The vertical cut through a PC.

Figure 2.18: The schematic diagram of the PC. (a) Each cell is divided into three pixels. (b) Nine pixels are electrically connected to form one pad. (c) Pixels are connected to provide pads shifted each other. (d) The layers of the pads are virtually produced. The signals from three overlapped pads identify the hit in the corresponding cell.

2.2.4   Electro-Magnetic Calorimeters (EMCal)

The primary role of the Electro-Magnetic Calorimeters (EMCal) is to provide a measurements of energy and hit position of both photons and electrons [99, 100]. The EMCal covers central rapidity ($|\eta| < 0.35$) and half in azimuthal angle ($\Delta\phi = \pi/2 \times 2$). Two kinds of EMCal are installed in PHENIX as shown in Fig. 2.10. One is Lead-Scintillator calorimeter (PbSc) and the other is Lead-Glass calorimeter (PbGl). PHENIX has 8 sectors of EMCal, 6 of them are PbSc type, and other two are PbGl type. The PbGl occupies the lower two sectors of East Arm (named E1, E2 sector in this thesis) and the PbSc occupies other six sectors (named W0 - W3, E2, E3 sector). The EMCal surface is placed at 510 cm (PbSc) and 550 cm (PbGl) in radial distance from the interaction point. The total numbers of towers are 15552 for PbSc and 9216 for PbGl, and the other basic parameters of EMCal are summarized in Table 2.2. A detailed description of each type of the EMcal is explained in this subsection.

parameters	PbSc	PbGl
Radiation length (X_0)	2.1 cm	2.8 cm
Moliere radius	~ 3.0 cm	3.7 cm
Nuclear interaction length (λ_I)	44 cm	38 cm
Total η coverage	0.7	0.7
Total ϕ coverage	$\pi/2 + \pi/4$	$\pi/4$
Size of sector surface	4(wide)$\times$2(high) m^2	4(wide)$\times$2(high) m^2
Number of towers in one sector	72(wide)$\times$36(high)	96(wide)$\times$48(high)
Tower cross section	5.2×5.2 cm^2	4.0×4.0 cm^2
Tower $\eta \times \phi$ coverage	0.011×0.011	0.008×0.008
Tower depth	37.5 cm (18 X_0, 0.85 λ_I)	40.0 cm (14 X_0, 1.05 λ_I)

Table 2.2: Basic parameters of two types of PHENIX EMCal.

Lead-Scintillator Calorimeter (PbSc)

The PbSc is a sampling calorimeter which is composed of 65 lead tiles and 66 scintillator tiles, stacked in alternate way. The thickness of lead tile (scintillator tile) is 1.5 mm (4.0 mm). The scintillator is made of polystyrene (the bulk material), 1.5 % of p-Terphenyl (the primary fluorescent material) and 0.01 % of POPOP (wavelength shifting material).

A PbSc module consists of four towers (2×2), which are optically isolated and read out individually. Figure 2.19 shows the internal view of the module. A module has 64 holes for the read-out fibers to pass through, with 1.2 mm diameter and 9.27 mm spacing. The read-out fibers are made of wave length shifter (0.5 % POPOP) which pass through the entire module from the back side to the front side then return to the back side after following smooth curves. The both edges of the fibers are gathered and attached to 1 inch diameter PMT (FEU115M, MELS, Russia). The attenuation length of the fiber is approximately 1 m, which affects the linearity of the energy measurement.

The four edges of the scintillator tiles are coated by aluminum to reflect the scintillation light except one corner at the center. For calibration, a fiber is inserted in the center of the module and provides laser

light into four towers from the corners. Figure 2.20 shows a schematic drawing of the laser calibration system [99]. The laser light is split in three steps and delivered into 3888 modules (= 15552/4); its amplitude is monitored with a PMT and photo diodes in all the light splitters. This calibration system is to normalize the gain change of the PMT due to the operation conditions. The gain of the amplifier for the photo diodes is also monitored by test pulses.

The energy resolutions were evaluated as follows from the test experiments using electron beams:

$$\frac{\Delta E}{E} = \frac{8.1 \text{ \%}}{\sqrt{E(\text{GeV})}} \oplus 2.1 \text{ \%}, \tag{2.6}$$

where E is energy and $\oplus$ means quadratic sum. The 8.1 % in the first term of Eq. 2.6 is close to the expected resolution from sampling as predicted by GEANT simulation. The main contributors to the constant term are intrinsic non-uniformity, in particular tower boundaries, hot spots at fiber positions and shower depth fluctuations. There is also a loss in the calorimeter response when a particle hits the corner of the towers (shower leakage). Shower depth fluctuations are responsible for the variations in the amount of the light seen, and in the energy leakage via the front and the back surface of the calorimeter.

The position resolution depends on both energy and the incident angle of the beam (θ: a polar angle orthogonal to the front surface of the module) due to the fluctuation of the shower depth. It is expressed as:

$$\Delta x = \Delta x_0 \oplus L \sin \theta, \ \Delta x_0 = 1.55 \text{ mm} \oplus \frac{5.7 \text{ mm}}{\sqrt{E(\text{GeV})}}, \tag{2.7}$$

where L is $\sim X_0 (= 2.1 \text{ cm})$. These results are reproduced by GEANT simulation.

At the same test experiments, the response to the proton and charged pions with momentum of a few GeV/c was studied. Only a part of the total energy is deposited in PbSc because of the small nuclear interaction length. MIP (minimum ionizing particle) energy for the charged pions penetrating the tower was measured to be 270 MeV.

Front side

Layers of lead and
scintillator tiles

Wavelength
shifting fibers

Towers

Back side
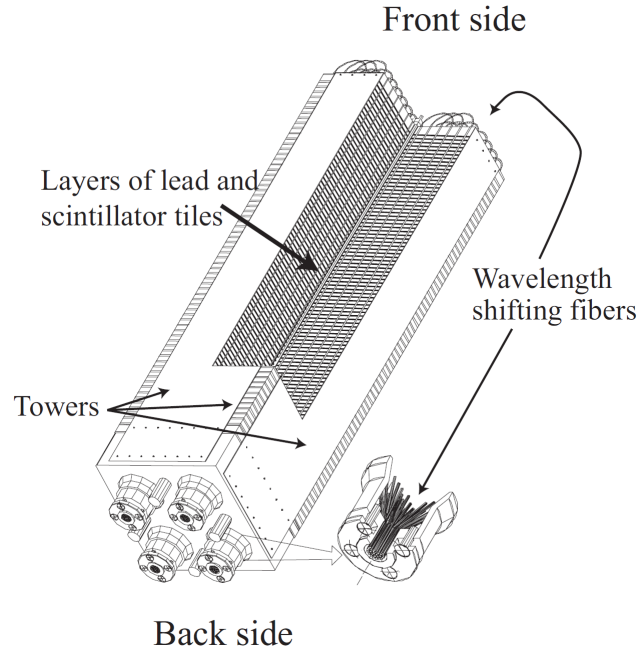
Figure 2.19: The module of PbSc. One module consists of 4 towers. The fiber for the laser system is inserted at the center of the module and along the tower axis.
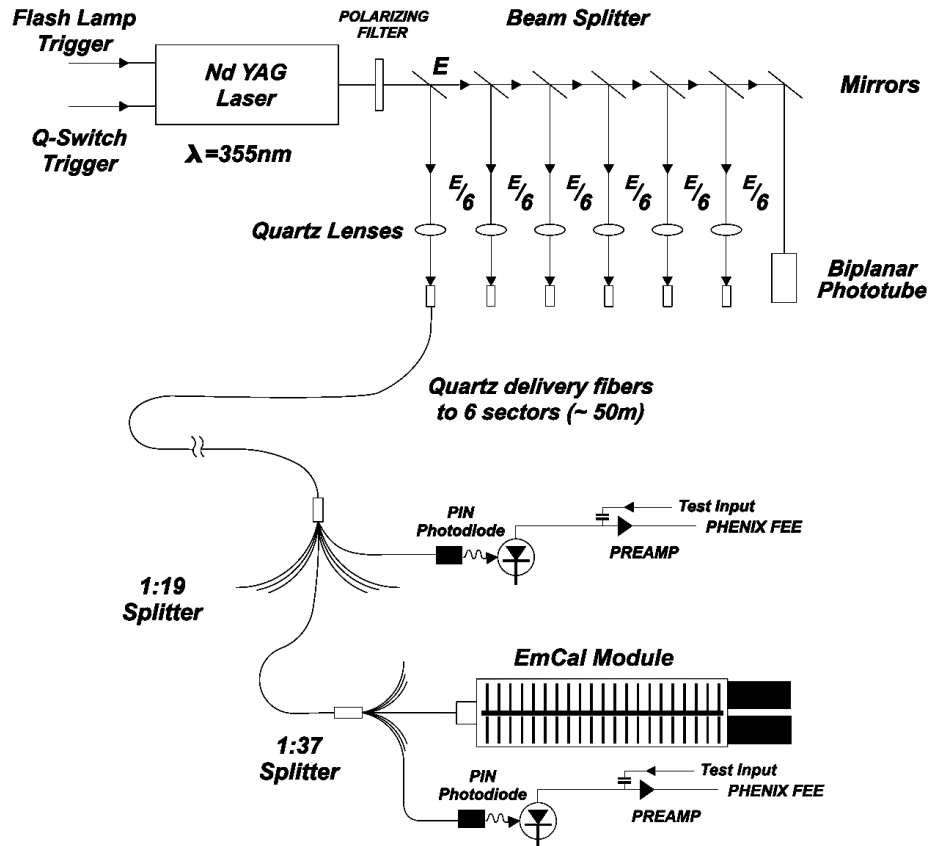
Figure 2.20: Schematic drawing of laser calibration system for PbSc.

Lead-glass Calorimeters (PbGl)

The PbGl is a Cherenkov calorimeter with 1.648 of index of refraction. The modules, which were previously used in WA98 [101] experiment at CERN, was re-used at PHENIX.

Each PbGl sector comprises 192 super-modules (SM) in an array of 16 (wide) by 12 (high). Figure 2.21 shows a PbGl SM which consists of 24 Lead-Glass towers (6×4). The towers within the SM are optically isolated with aluminized Mylar foils and each tower is attached to an PMT (FEU84). Steel sheets of 0.5 mm thickness are used to house the entire towers and PMTs.

The PbGl LED calibration system are installed to monitor the gain drift. Three LEDs with different wave length are placed on the front of every SMs. The mirror foil on the top surface have a hole for each PbGl tower for LED light to enter. A polystyrene reflective dome covers the LED system.

The intrinsic performance of PbGl was also evaluated with the test experiments using electron beams. The measured energy resolutions is well described as:

$$\frac{\Delta E}{E} = \frac{5.9 \text{ \%}}{\sqrt{E(\text{GeV})}} \oplus 0.8 \text{ \%},$$ (2.8)

and the measured position resolution of PbGl is:

$$\Delta x = 0.2 \text{ mm} \oplus \frac{8.4 \text{ mm}}{\sqrt{E(\text{GeV})}}.$$ (2.9)

The response of PbGl to hadrons is different from that of PbSc since PbGl is based on Cerenkov detection. The deposit energy is suppressed for hadrons due to its Cerenkov threshold (106 MeV/c for charged pions). The energy deposit of charged pions was evaluated at the test experiments, and it was ~ 460 MeV for 1 GeV/c, and ~ 540 MeV for 4 GeV/c.
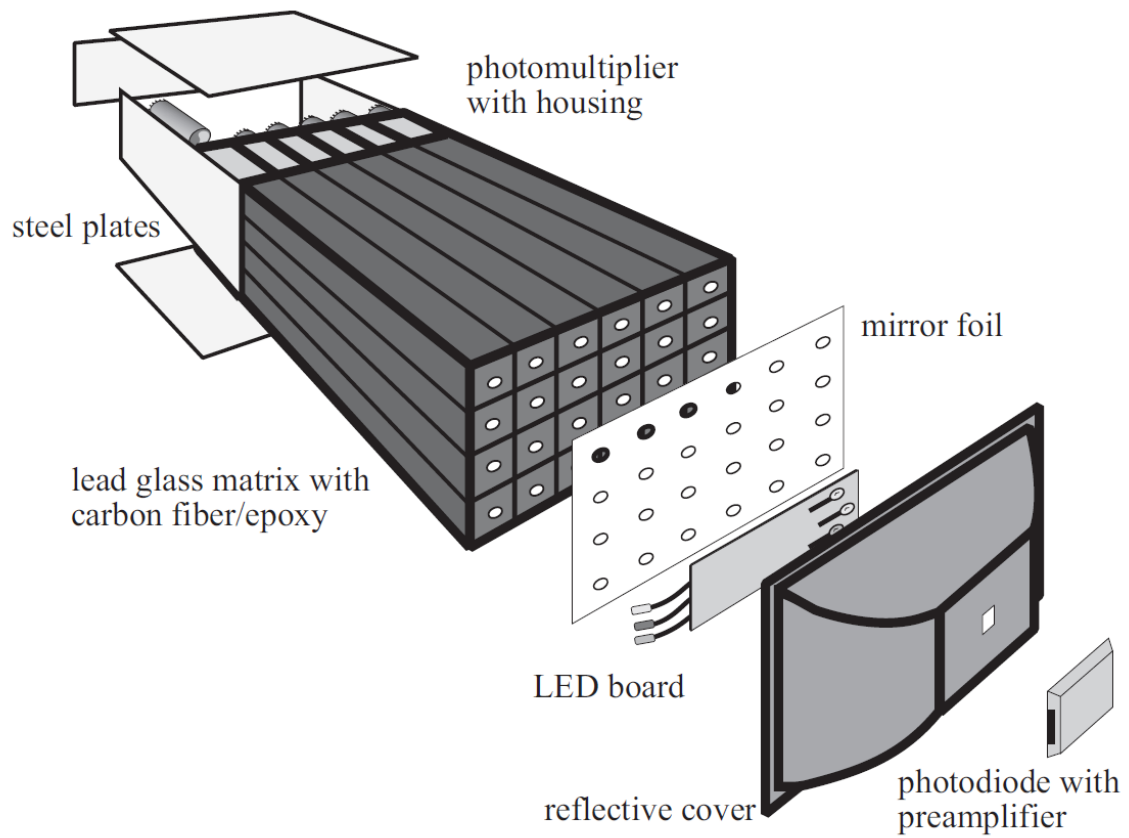
Figure 2.21: The schematic view of the super-module (SM) of PbGl including the LED system for the calibration. The SM consists of 24 towers.

2.2.5 Trigger

The Level-1 trigger (LVL1) have been designed to record a significant fraction of the physics events of interest. The LVL1 trigger system is a pipelined and dead-time less. The triggers consist of two types: one is the Local Level-1 (LL1) system, and the other is the Global Level-1 (GL1) system. The LL1 system communicates directly with the detectors such as BBC and EMCal. The input data from these detectors are processed by the LL1 algorithms at each RHIC beam crossing, and the trigger information is transferred to GL1. The GL1 receives and combines the LL1 data to make a trigger decision. A particular LL1 is often combined with other LL1 at GL1 [4].

The BBC LL1 trigger (BBCLL1) and EMCal LL1 trigger (ERTLL1) are described in this section. These triggers were utilized to select the physics events of interest in this thesis.

BBC LL1 Trigger (BBCLL1)

The main trigger for events in PHENIX relies on a coincidence between the two BBC modules. The timing information of BBC is used to determine the position of the collision point. The vertex position cut of $|z| < 30$ cm can be applied in the BBCLL1 trigger using position information obtained online, and its position resolution is ~ 5 cm. The vertex cut roughly matches to the acceptance of the PHENIX central arms. Two types of BBCLL1 triggers with and without the vertex position cut are implemented. In this thesis, the BBCLL1 trigger with the 30 cm vertex cut is simply referred to as the "BBCLL1(Vtxcut)", while we explicitly write the BBCLL1 trigger without vertex cut as the "BBCLL1(noVtx)".

The BBCLL1 is defined as minimum-bias (MB) trigger-condition for the data in pp collisions, and it also serves as a luminosity monitor: the number of BBCLL1 is used in the integrated luminosity and vernier scan measurement.

EMCal LL1 Trigger (ERTLL1)

The EMCal provides signals of the high energy electron and photon events. Basic idea of ERTLL1 is to select events with a deposit energy on the EMCal over a certain threshold. As the shower generated by a particle hit on EMCal usually spreads over several towers, it is necessary for the efficient trigger to sum the energy deposits on the neighboring towers. When a particle hits the corner of the tower, the typical energy deposit in one tower is ~ 20 % of total energy, while it is ~ 80 % with a hit at the center.

The conceptual diagram of the actual procedure to select the events is displayed in Fig. 2.22. The energies of 2×2 towers are summed at first by on an ASIC chip. The information of the 6×6 ASIC chip (12×12 towers) are read out by one FEM (Front-end Electronics Module). At this stage, towers do not overlap, and hence 36 energy sums of 2×2 towers are produced per one FEM. To eliminate the inefficiency in the case of a particle hit at the border of the 2×2 block, the energy sum of 4×4 towers is formed from four 2×2 energy-sum, allowing the overlap of 2×2 regions. The communication among ASIC chips is relayed over FEMs and the trigger organization is seamless over the EMCal sector. In

---

[4]For example, ERTLL1 is combined with BBCLL1 to require the vertex cut of $|z| < 30$ cm.

total, 36 signals of 4×4 energy sum is obtained for one FEM. This enables us to collect more than 90 % of the energy of a particle hit in at least one of the 4×4 energy sum. Each 4×4 energy sum, as well as the 2×2 energy sum, is compared to a certain threshold for a trigger decision. To avoid the effect of noisy towers, which always provide a large signal due to the electrical noise, the trigger can be masked with a unit of the FEM.

In the experiment, three thresholds are applied for the 4×4 energy sum. The values of the thresholds are summarized in Table 2.3 with that for the 2×2 energy sum. The triggers are named "ERT4x4a", "ERT4x4b", "ERT4x4c" and "ERT2x2", respectively. Because the gain setting of EMCal is different between $\sqrt{s} = 200$ GeV and 500 GeV pp collision, the energy thresholds are different. The gain is reduced by roughly factor of 2 at 500 GeV run, so that the dynamic range of EMCal covers high p_T electrons from W decay (~ 40 GeV/c).
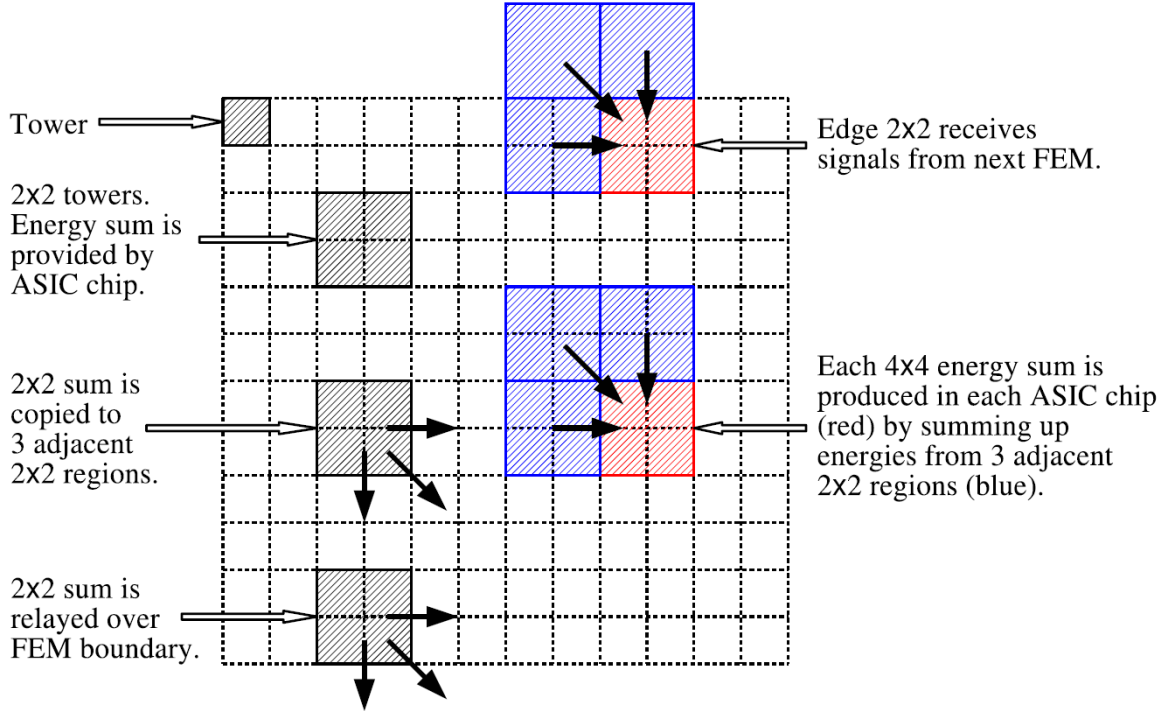
Figure 2.22: The method to produce the signal for the EMCal trigger. The region of 12×12 towers displayed in the figure are processed by one FEM. Signals of 2×2 energy sum are relayed across the boundary of 12×12 region.

$\sqrt{s}$	ERT4x4a	ERT4x4b	ERT4x4c	ERT2x2
200 GeV	2.1 GeV	2.8 GeV	1.4 GeV	0.8 GeV
500 GeV	4.2 GeV	5.6 GeV	2.8 GeV	1.6 GeV

Table 2.3: The energy thresholds for the ERTLL1. The threshold is compared to the energy sum of the 4×4 or 2×2 towers in ERTLL1.

2.2.6 The Data Acquisition System

The PHENIX data acquisition (DAQ) system processes the signals from each detector, produces the trigger decision, and stores the triggered data. The typical data logging rate of PHENIX was ~ 1 kHz for AuAu collisions and ~ 5 kHz for pp collisions. The zero-suppressed event sizes are 160 kbytes for AuAu and 40 kbytes for pp, respectively.

The block diagram of the data acquisition flow is shown in Fig. 2.23. The DAQ system employs the concept of granule and partition. A granule is smallest unit, which consists of individual timing control and data collection for each detector. A partition is the combination of granules, that share busy signals and accept signals. This configuration makes it possible to run the DAQ in desired combination of detectors.

Since the RHIC beams have the bunch structures, the PHENIX data stream has to be synchronized with the RHIC beams. The RHIC beam clock of 9.4 MHz is provided by the accelerator control system, and is transfered to the Master Timing Module (MTM). The MTM distributes the clock into the Granule Timing Modules (GTM) which are equipped into all detectors and the Global Level-1 (GL1). The GTM delivers the clock, the control commands (Mode Bits) and event accept signal to FEMs of each detector, and is capable of a fine delay tuning of the clock phase in ~ 50 ps step in order to compensate the timing difference among FEMs. The GL1 produces the first Level-1 (LVL1) trigger decision, combining LL1 (Local Level-1) signals from detector components. The event trigger issued by GL1 is sent to the FEMs of all detectors.

FEMs manipulate FEE (Front-End Electronics) to process the raw signals of the PHENIX detectors. At the same time, LL1 trigger signals are generated. FEE has buffering scheme and store the processed signals for up to 40 bunch crossings for read-out by request from the event trigger.

When a event trigger is issued by the GL1, FEMs send processed signals into Data Collecting Modules (DCMs). The DCM has capability to receive 100 Gbytes of uncompressed event data per second at the highest trigger rate. It provides data buffering, zero suppression, error checking, and data formatting. The information from the DCMs are collected by the Partitioner and then sent to the Sub-Event Buffers (SEBs). The SEB is the front-end of Event Builder (EvB) and communicate with each granule. The SEBs then transfer the data on request to a set of the Assembly and Trigger Processors (ATPs) under the control of the Event-Builder Controller (EBC). Here, granule-by-granule information is rearranged, and assembled as an event.

The event data are sent to the online monitoring system for online-level quality insurance, and sent to the DAQ Linux machines to record it in hard drives. The stored data is used for generation of trigger decision by the second level (LVL2) software trigger. The data storage is finally provided by HPSS-based tape storage system with maximum transfer rate of 20 Mbytes/s. Combining the buffering to local disk, the maximum data logging rate become ~ 60 Mbytes/s.
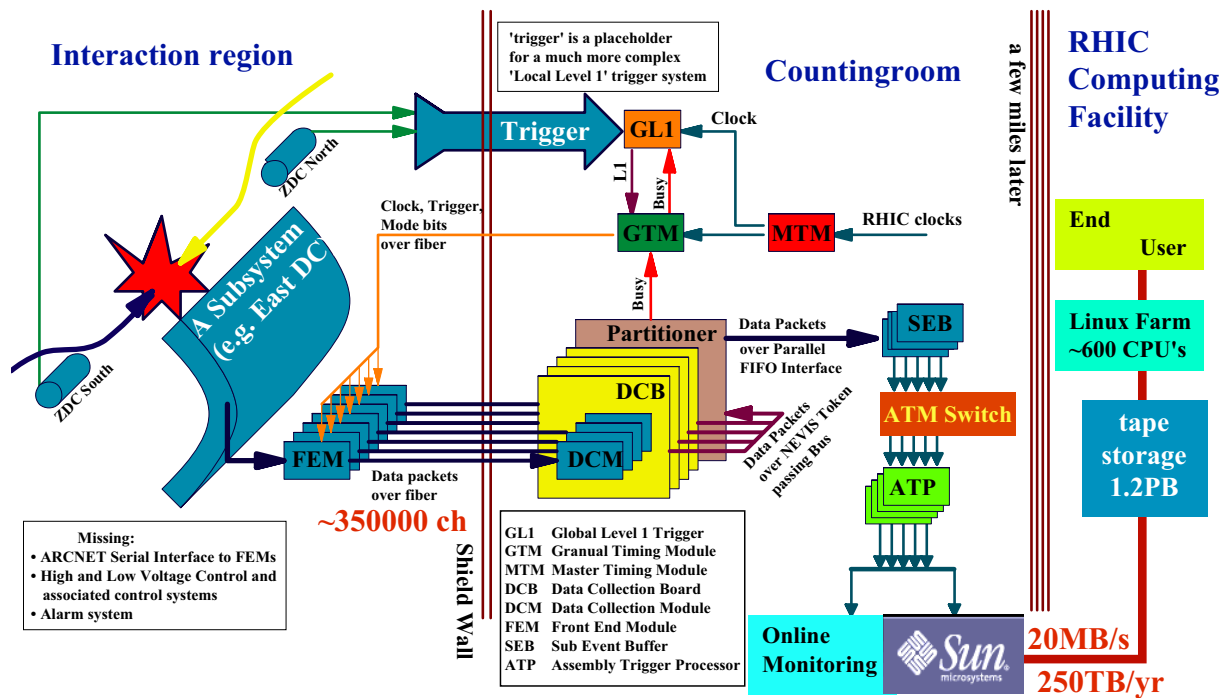
Figure 2.23: PHENIX DAQ system.

Chapter 3

RHIC Run 9

3.1 Luminosity and Delivered Integrated Luminosity

The data for this thesis were taken by means of the PHENIX detector with polarized proton beam of RHIC at BNL during the Year-2009 run (Run 9). The duration of the Run 9 polarized pp run was about 6 weeks (first 2 weeks were for commissioning: March 5th to March 17th, and following 4 weeks were for physics running: March 17th to April 13th) with the beam energy of 250 GeV, which corresponds to a center-of-mass energy ($\sqrt{s}$) of 500 GeV, and with the beam spin polarized longitudinally at the collision point of PHENIX. The data taken in the period of physics running was used in the analysis. RHIC achieved the maximum luminosity of 8.5×10^{31} cm^{-2}sec^{-1} and the average luminosity of 5.5×10^{31} cm^{-2}sec^{-1}. Delivered integrated luminosity at PHENIX through 6 weeks was about 60 pb^{-1}. Figure 3.1 displays the delivered integrated luminosity as a function of time [102].

PHENIX accumulated the integrated luminosity of about 17.2 pb^{-1}. After various quality assurance selections for polarized beam, total amount of data used in this thesis is 8.56 pb^{-1} (see Sec. 4.3.1).

3.2 Beam Polarization

The beam polarization was measured at pC polarimeter normalized by the physics asymmetry (A_N) which is calibrated by H-jet polarimeter (see Sec. 2.1.3). The luminosity weighted polarization is 0.38 ± 0.03 for Blue beam, 0.40 ± 0.05 for Yellow beam, and the averaged polarization (($P_B + P_Y$)/2) is 0.39 ± 0.04.

The uncertainties related to the beam polarization are summarized in Table 3.1 [103]. The systematic uncertainty of the H-jet measurements includes an uncertainty on molecular-hydrogen contamination in the polarized atomic hydrogen jet, which is represented as "H-jet (molecular)" in the table. Other backgrounds to the H-jet measurement (shown as "H-jet (other sys.)" in the table) was estimated from the asymmetry in "non-signal" strips, and variation in the results due to applying different cuts. In Run 9, the pC measurement suffered from systematic problems related to high event rates due to smaller transverse beam size at $\sqrt{s} = 500$ GeV and on thicker targets, compared to previous $\sqrt{s} = 200$ GeV runs. This uncertainty is shown as "pC (time/rate dependence)" in the table. There is also an uncertainty from non-flat profile of the beam polarization. Due to the non-flat polarization profile, the beam polarization
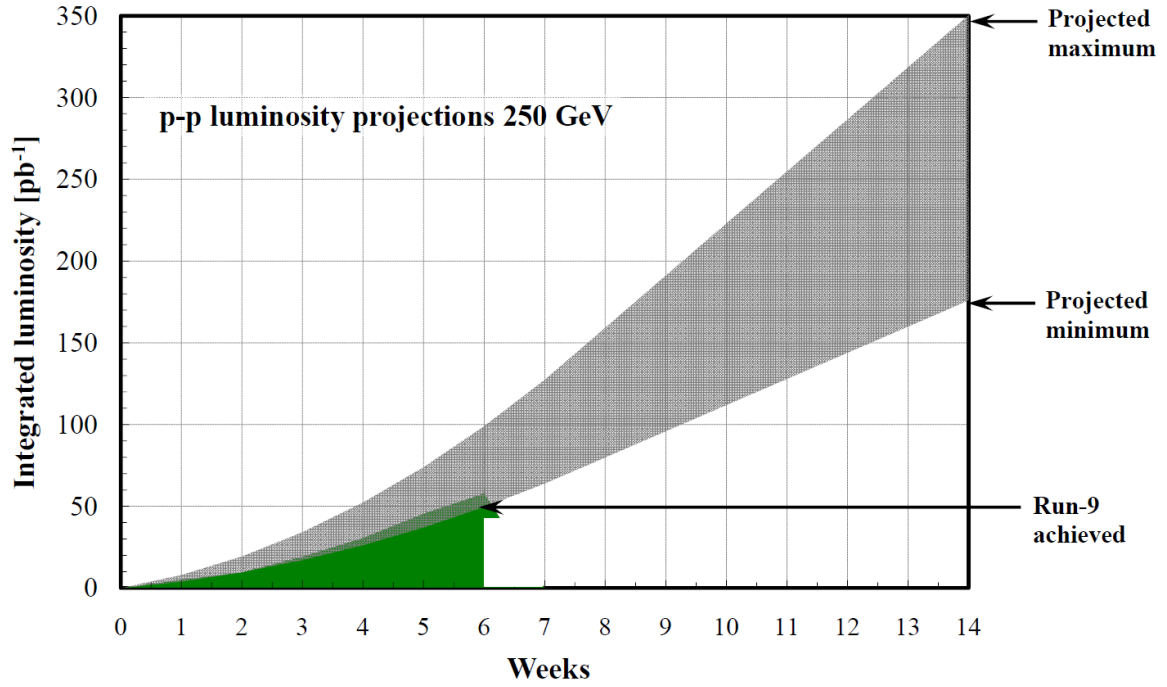
Figure 3.1: Projected minimum and maximum integrated luminosities for polarized proton collisions at 250 GeV beam energy, with achieved luminosity at Run 9.

was seen differently by the H-jet polarimeter, the pC polarimeter (in fixed target measurement case), and when colliding beams at the interaction points (IPs) of RHIC experiments. The jet target at the H-jet polarimeter was much wider than the beam width, such the polarization profile was weighted with the beam intensity profile in the average beam polarization. The polarization measurement in pC polarimeter depended on the positioning of the carbon target, and whether a horizontal or vertical target is used for the measurements (beam profiles are different for the horizontal and the vertical targets). For colliding beams, the polarization profile is weighted by a product of two beam intensity profiles in the transverse plane for evaluation of average beam polarization. These difference between average beam polarizations are taken into account when normalizing the pC measurements to the H-jet absolute polarization measurement, and when providing the polarization values for RHIC experiments [1]. The uncertainty due to this reason is represented as "pC (pol. profile)" in Table 3.1 which reflects the uncertainty in the average over all fills polarization profile. As a result, relative uncertainties of $\Delta P/P$ is 8.3 % (12.1 %) for the Blue (Yellow) beam.

For a product of two beam polarizations $P_B \cdot P_Y$ (used in double spin asymmetry measurements), the relative uncertainty $\Delta(P_B \cdot P_Y)/(P_B \cdot P_Y)$ is 18.5 %. The uncertainty is 9.2 % for the average between two beam polarization $(P_B + P_Y)/2$ (used in single spin asymmetry measurements, when data from two polarized beams are combined). These uncertainty was calculated assuming that the H-Jet systematic un-

---

[1] Scanning a carbon ribbon target across the beam allows to measure intensity and polarization profiles in both vertical and horizontal directions in transverse plane.

certainties as well as time/rate dependence uncertainty of the pC measurement are maximally correlated between Blue and Yellow beams.

uncertainty	Blue beam	Yellow beam
H-jet (stat.)	2.5 %	2.7 %
H-jet (molecular)	2.0 %	2.0 %
H-jet (other sys.)	3.0 %	3.0 %
pC (time/rate dependence)	5.0 %	10.0 %
pC (pol. profile)	5.0 %	5.0 %
total	8.3 %	12.1 %

Table 3.1: Uncertainties in the beam polarization measurement.

3.3 Absolute BBC Cross Section

The absolute integrated luminosity is required for the cross section measurement. BBC was utilized as a luminosity counter at PHENIX and therefore, the calibration of the collision cross section seen by the BBC is necessary. The calibration of BBC is defined as BBC cross section (σ_{BBC}):

$$L_{BBC} = \frac{R_{BBC}}{\sigma_{BBC}}, \tag{3.1}$$

where R_{BBC} is the event rate measured by BBC and L_{BBC} is the effective luminosity delivered to the PHENIX.

The BBCLL1(Vtxcut) trigger requires at least one hit on both North and South components of the detector and it requires an online vertex cut of $|z| < 30$ cm. To calculate the absolute calibration of BBC, number of events for each bunch crossing from BBCLL1(Vtxcut) triggered data is counted and the luminosity of each bunch crossing is calculated by:

$$L_{machine}^{bunch} = \frac{f_{beam} N_B N_Y}{2\pi \sigma_x \sigma_y}, \tag{3.2}$$

where f_{beam} is the frequency of each bunch crossing ($\sim$ 78 kHz), N_B and N_Y are number of protons ($\sim 10^{11}$) in Blue and Yellow beams respectively. σ_x and σ_y are the horizontal and vertical widths of the overlap profiles of Gaussian beams.

To measure the σ_x and σ_y, the technique of Vernier Scan (or Van der Meer scan) [104] is used. The method (suggested by Simon Van der Meer) scans one beam across the other in small steps to measure transverse profile (horizontal and vertical). The triggered event rate for each step was measured. The rate as a function of the beam-step position ("beam-step position vs. rate" plot) was plotted. Global level-1 (GL1) scaler (scaler for each crossing) kept the track of the event counts for BBCLL1(Vtxcut) trigger. This scaler information was utilized to calculate the event rate for each step. A Gaussian fit to the plot gives the resultant width (σ_x, σ_y). The beam intensity information of N_B, N_Y is obtained from the Wall Current Monitor (WCM), and $L_{machine}$ can be calculated for each bunch crossing by Eq. 3.2.

It needs to evaluate the acceptance (ε_{vertex}) of the BBCLL1(Vtxcut) trigger (out of the total machine luminosity) in order to calculate L_{BBC} from $L_{machine}$. It was obtained by comparing BBCLL1(Vtxcut) with a wide unrestricted trigger BBCLL1(noVtx) (see Sec. 2.2.5). Using the machine luminosity, the trigger acceptance and event rate at the maximal overlap point (R_{max}), which was obtained from the "beam-step position vs. rate" plot, the BBC calibration for each bunch crossing was calculated from:

$$\sigma_{BBC}^{bunch} = \frac{R_{max}^{bunch}}{L_{machine}^{bunch} \cdot \varepsilon_{vertex}}.$$

(3.3)

By averaging this value over all good non-empty bunches, σ_{BBC} was evaluated.

Experimental Procedures

The data of vernier scans were taken near the end of a fill, before dumping a given fill and most often before the polarization measurement. The main feature of the procedure was that one of the beams was moved in steps in transverse directions while keeping the other steady. The step sizes were chosen to be of the order of or smaller than expected width of the Gaussian profile of the beam in transverse directions, typically a few hundred microns. Beams were moved in steps and stayed for typically 30 to 40 seconds at each step to enable PHENIX to acquire enough events. The beam positions were recorded by several different Beam Position Monitors (BPMs) at different positions along the beam ring. Intensity of circulating beams were monitored by two different monitors: the Wall Current Monitor (WCM) and the Direct Current Current Transformer (DCCT). The DCCT measures the average current induced in a solenoidal coil around the beam pipe in a rather long time period (1 sec), and this large sample time allows the DCCT to measure the total number of ions in RHIC to ~ 0.2 % accuracy [105]. One drawback of the DCCT was that, because of its large integration time, it also included debunched beam in its measurement. To remedy this, the DCCT was used with the WCM. The WCM measured induced voltage in an RLC circuit in a particular section of the beam pipe. The WCM samples at a very fast rate (~ 0.25 nsec) so as to give the bunch profile in beam (z) direction and was insensitive to debunched beam/beam-gas. For the number of protons in beam, the WCM data, which is calibrated at the beginning of the fill when there is none or very little debunched beam, was utilized.

Result

In the evaluation of σ_{BBC}, corrections due to following effects were applied [106]:

- The loss of intensity (N_B, N_Y) due to collisions and scraping during the scan.

- The hour glass effect due to beam focusing (beam transverse profile (σ_x, σ_y) depends on z-position along beam axis) and beam crossing angle (beam may collide not head-on).

- The scale factor for the beam-step size (or σ_x, σ_y) to match to the data from BPMs.

- The loss of counts due to multiple collision effect.

- The correction for ε_{vertex}, because the BBC has a z-depending efficiency of detecting events.

The first, second and third items affect to $L_{machine}$ calculation, the third item affects to R_{max} measurement and the forth item affects to ε_{vertex}.

The first effect was corrected by seeing the $N_B \cdot N_Y$ value as a function of time. This is a small correction (~ 1 % at most).

To correct for the second effect, the z-vertex profile of events at the different beam-step position was utilized. As the beam centers moved further away, overlap area becomes less and less in the near the focal point ($z = 0$) and relatively higher on away-sides along the beam direction. This produces a double hump structure of the z-vertex profile. The crossing angle between the beams makes this double-hump structure askew. The vertex distribution was compared to the simulation which took into account the beam focusing parameter (β^*) and crossing angle to extract these parameters [2]. The simulation determined β^* and crossing angles to ~ 10 % precision.

The fourth effect was corrected by the method described in Appendix C.

The final effect is corrected using the ZDC information. The ZDC is another luminosity counter located far from the nominal collision center and is free of any z-dependence. The z-depending efficiency was evaluated by comparing events that fired both the BBC and ZDC triggers with only ZDC triggered events as a function of z-vertex measured by the ZDC. This z-dependence is taken into account in the calculation of ε_{vertex}.

Applying those corrections, the final BBC cross section σ_{BBC} value was obtained as $\sigma_{BBC} = 32.51 \pm 3.01$(sys.) ± 1.19(stat.) mb., with averaging over all vernier scan runs, The uncertainties related the σ_{BBC} measurement are summarized in Table 3.2 [106]. The uncertainty is varied among different vernier scan runs as indicated in the table.

uncertainty	value	comment
ε_{BBC}	2.0 %	from the fit
$N_B \cdot N_Y$	0.4 to 1.1 %	from DCCT and WCM measurement
σ_x, σ_y	1.5 to 3.3 %	from the fit
σ_x, σ_y	7.6 %	correction of hour glass effect and crossing angle
R_{max}	3.1 to 4.5 %	from the fit and correction of multiple collision effect
total	9.3 %	total systematic uncertainties
total	10 %	stat. $\oplus$ sys.

Table 3.2: Uncertainties in the σ_{BBC} measurement.

---

[2]The beam profiles in the simulation is Gaussian for both transverse and longitudinal direction.

Chapter 4

Analysis

4.1 Overview

The PHENIX is not hermetic, unlike most of the hadron collider detectors. It means that missing-momentum technique for the final states of charged-lepton and neutrino cannot be used to identify the W and reconstruct its momentum. Instead, the strategy adopted is to detect the charged decay lepton to determine its transverse momentum p_{Tl} and rapidity η_l. The relevant process therefore becomes the single-inclusive reaction $pp \rightarrow lX$. This chapter describes the data analysis to extract differential cross section ($d\sigma/dy$) and single spin asymmetry (A_L) of high p_T ($30 < p_T < 50$ GeV/c) single $e^\pm$ over a pseudo-rapidity range of $|\eta| < 0.35$, in pp collisions at $\sqrt{s} = 500$ GeV. At this energy, such high p_T electrons/positrons are mainly produced from W or Z decays. Since the PHENIX cannot distinguish between $e^\pm$s from W decays and them from Z decays, $d\sigma/dy$ and A_L measured must include both contributions [1].

The data taken with the ERT4x4b trigger [2] is used in this analysis. The brief analysis procedure is as follows:

1. Calibrations of EMCal and DC/PC1 are carried out. (Sec. 4.2)

2. p_T spectrum of inclusive electron-candidate is obtained with several analysis cuts. (Event Selection, Sec. 4.3.2)

3. p_T spectrum of single electrons from W and Z decays is obtained by statistically subtracting background. The contribution of background is estimated using both real data and MC simulation. (Sec. 4.3.3)

4. The differential cross section ($d\sigma/dy$) is evaluated. (Sec. 4.3.7)

5. The single spin asymmetry (A_L) of $W + Z$ production is calculated. (Sec. 4.4)

Figure 4.1 displays the flow chart of the procedure of this analysis.

---

[1] The treatment of the Z fraction in the cross section calculation is described in Sec. 5.1.
[2] The 4×4 tiled EMCal trigger with energy threshold of ~ 6 GeV (see Sec. 2.2.5 for more detail).
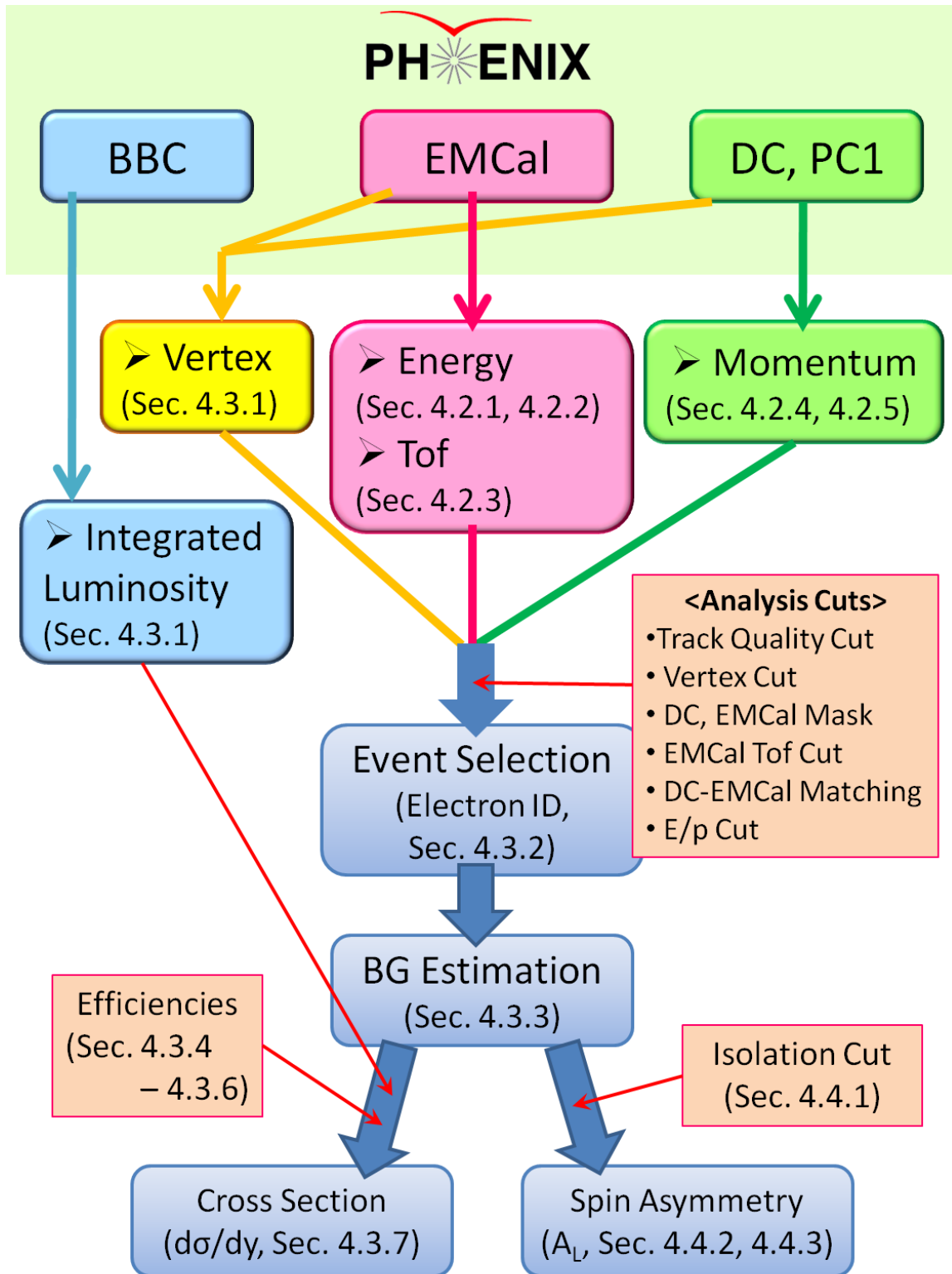
Figure 4.1: The flow chart of analysis procedure in this thesis.

The EMCal and DC/PC1 are key detectors for this analysis. With a summary of energy reconstruction by the EMCal and momentum reconstruction by the DC, the calibration for these detectors are described in Sec. 4.2. In order to obtain the inclusive spectrum of high p_T electrons, various analysis cuts are applied and estimation of background is essential to extract $d\sigma/dy$. They are explained in Sec. 4.3 with the integrated luminosity used in the calculation of $d\sigma/dy$. The trigger efficiency and the efficiencies of geometry/analysis cut are also described in this section. In addition to the cuts for the $d\sigma/dy$ calculation, an isolation cut is also applied to evaluate A_L in order to reduce hadronic background. To fully utilize the available statistics of high p_T $e^\pm$ sample, a maximum likelihood technique is used in "spin fit" procedure by which A_L is calculated. The detail of A_L extraction is represented in Sec. 4.4.

4.2 Calibration

4.2.1 Energy Reconstruction by EMCal

The detail of the energy reconstruction in PHENIX can be found in [107]. From EMCal, the following information about an incident particle is extracted for the analysis;

- Total energy,

- Hit position,

- Time of flight (Tof) information.

The energy deposit of a particle hit at EMCal spreads among several towers. To extract the information of the incident particle, it is necessary to find a group of towers which have energy deposit of the particle. At first, a certain threshold is applied to select a hit tower. The threshold was 10 MeV for PbSc and 14 MeV for PbGl. The higher threshold for PbGl is due to the larger noise in PbGl. The neighboring hit towers around the selected hit tower were grouped into a cluster. If there were more than one maxima of energy deposit in a cluster, they were split into clusters so that a cluster had only one maximum.

In PbGl, all energies in the cluster towers are summed and total energy is corrected for the incident angle dependence which was parameterized from the test beam results [100]. In PbSc, so-called "core" tower technique is utilized to obtain the total energy deposit of a cluster. The sum is performed only for core towers, instead of summing all tower energy in a cluster. Core towers are defined as those in which the incident particle is estimated to deposit the energy more than 2 % of the total energy. The estimation is based on the electromagnetic shower profile which was also parameterized from the test beam experiments. The energy sum of core towers is about 90 % of the total. The total energy is then extracted with the impact angle dependence correction as in the case of PbGl. The impact angle dependence is less than 4 %. At the same time, the energy losses caused by the attenuation in the fibers and shower leakage, are also corrected. The "core" tower technique was introduced to cope with the high occupancy environment in heavy ion collision experiment. This degrades the energy resolution slightly

(the constant term of the energy resolution in Eq. 2.6 is increased by 2 % to 3 %) but the achieved resolution is good enough for the analysis.

The hit position of the incident particle is obtained by the center of gravity method. The positions of towers in a cluster are weight-averaged by tower energies, and the dependence of the impact angle of the particle is also corrected.

The Tof of a cluster is defined by the Tof of the hit tower with maximum energy deposit. As the start time of Tof varies in each tower, offsets need to be adjusted among different towers in offline analysis.

4.2.2   EMCal Energy Calibration

The EMCal is a crucial detector for high p_T electron measurement. The value of p_T is calculated by $E \times \sin \theta$ (E: energy of EMCal cluster, i.e. p_T in this thesis represents E_T) as the energy resolution is better than the momentum resolution in high p_T region ($p_T > \sim 10$ GeV/c). Therefore, energy calibration of EMCal to assure reliable energy measurement in high energy region is very important for this analysis. The energy calibration of EMCal is described in this subsection.

The time dependence of the energy gain is corrected tower by tower using the laser calibration system for both PbSc and PbGl. This semi-online calibration corrects only relative time-drift of each tower separately. Therefore, the gain non-uniformity between towers remains. See Sec. 2.2.4 about the laser calibration system. In the offline analysis, additional energy calibration is carried out utilizing the measured π^0 and η peak, which is the physics signal and therefore most reliable. The offline calibration is divided into 3 steps: tower-by-tower gain correction, run-by-run global gain correction (time dependence) and calibration for the absolute energy scale.

Tower-by-tower Gain Correction

The tower-by-tower energy calibration utilizes the peak position of π^0 in the invariant mass spectrum of the cluster pairs. The deviation of the π^0 peak in the tower-by-tower spectrum from the nominal position is assumed to reflect the gain shift. The mass spectrum for a certain tower (the target tower) consists of the cluster pairs which include the cluster located at the target tower. Figure 4.2 displays the concept schematically. In this step, it is assumed that the shift of the π^0 peak for the target tower is caused by the gain shift of the target tower and the effects from other towers are averaged and negligible. However, to achieve better calibration, this step is iterated several times [3]. The calibration is tried for all towers in EMCal, including even towers with problem in the electrical circuit. Then, towers which cannot be calibrated are included in the masked towers (see Sec. 4.3.2). The reason of the failure in the calibration is mainly due to the malfunctional electrical circuit.

Run-by-run Global Gain Correction

The time dependence of the EMCal energy gain is initially corrected using the laser system for both PbSc and PbGl. This correction is executed semi-online. The residual time dependence is calibrated using the

---

[3]Five times of the iteration processes have been carried out for Run 9 data.
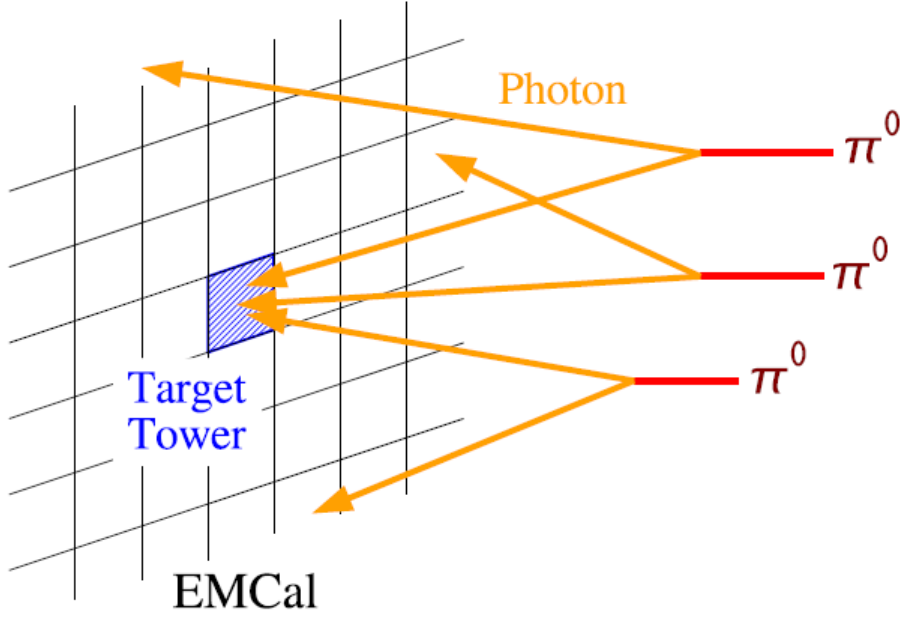
Figure 4.2: The concept of the tower by tower gain correction. π^0s whose decay photon hit the target tower are collected to make the tower-by-tower mass spectrum.

measured π^0 peak. π^0s are reconstructed sector-by-sector in every run [4] and the spectra are fitted to the combination of Gaussian and polynomial. The shift of the π^0 peak from the normal position is assumed to be the shift of the energy gain and additional factor is applied to the gain in the analysis. In this step, the observed π^0 peak is set to a certain value near 0.135 GeV/c^2. Figure 4.3 shows the comparison of the π^0 peak position and the width before (black points) and after (red points) the run-by-run gain correction as a function of the run number.

Calibration of Absolute Energy Scale

Since the run-by-run global gain correction is performed at the π^0 p_T range of 4 to 10 GeV/c, the energy (p_T) dependence of energy scale (non-linearity) still remains [5]. The energy dependence of lower p_T region is caused by the energy threshold for the EMCal tower, $\sim$10 MeV, and it causes that the energy of the reconstructed clusters is lower than the incident energy. The energy dependence of higher p_T region is caused by the depth of Electro-Magnetic (EM) shower. The shower depth originated by a high p_T photon/electron reaches closer to the EMCal photo-tube and larger amount of light is measured than the shower originated by a lower p_T (i.e. $p_T \sim 4$ GeV/c) photon/electron. This effect causes that the energy of the reconstructed clusters is higher than the incident energy. There is also a shower leakage effect for events of high p_T photon/electron due to the limited length of a EMCal tower. This effect causes that reconstructed energy is lower than the incident energy. Therefore, the energy dependence in higher p_T

---

[4] The π^0 p_T range of 4 to 10 GeV/c is selected to earn enough statistics.

[5] When selecting π^0s with $4 \leq p_T < 10$ GeV/c, the mass spectrum is dominated by π^0s with $p_T \sim 4$ GeV/c, and the energy of lower/higher than 4 GeV/c region is not completely corrected yet.
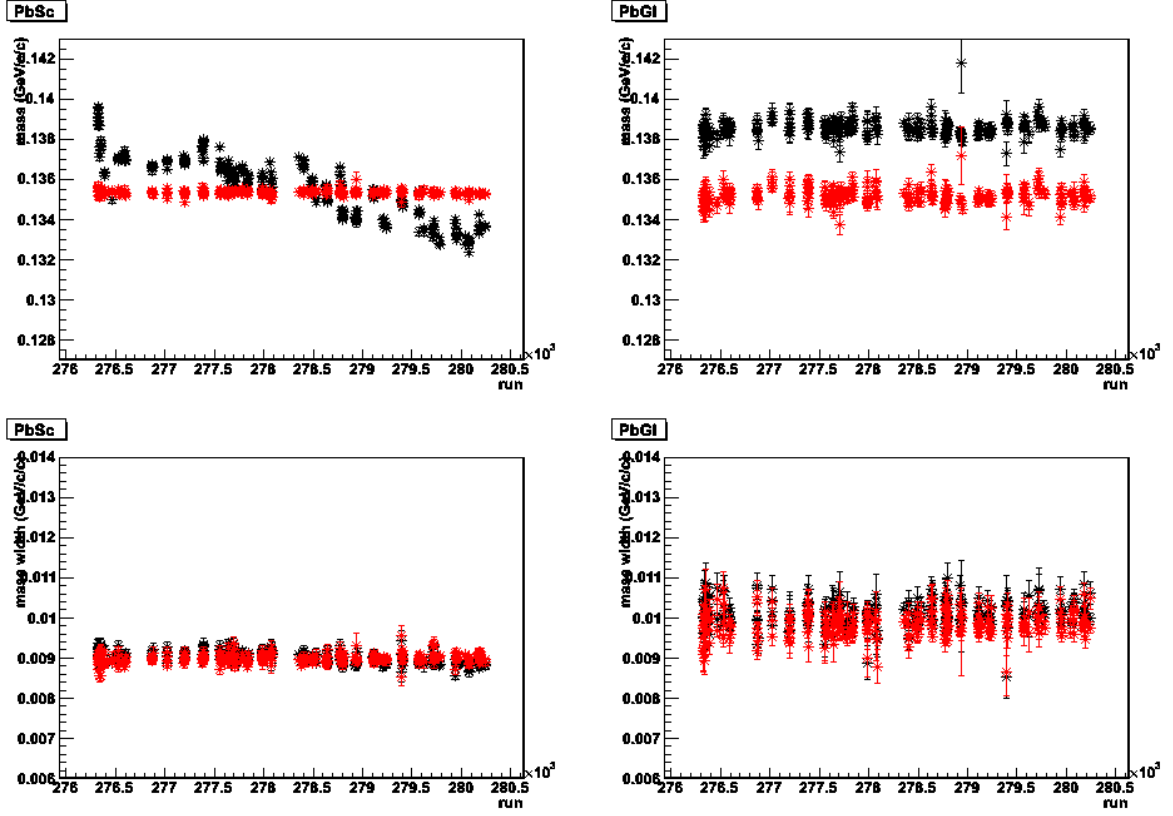
Figure 4.3: π^0 peak position (top) and the width (bottom) before (black points) and after (red points) the run-by-run gain correction. (Left side: PbSc, Right side: PbGl)

region includes these two effects.

The absolute energy scale is calibrated by comparing the p_T dependence of π^0 peak to the fast Monte Carlo simulation (FastMC: more detail is given in Appendix B). The depth of EM shower is taken into account in the FastMC, therefore the behavior of energy scale in higher p_T region can be evaluated in this manner. The energy scale is tuned in the FastMC in term of an additional attenuation length (λ_{add}) [6]. In the tuning of FastMC, $\lambda_{add} = 350$ cm (150 cm) for the additional attenuation length of PbSc (PbGl) were used.

The energy resolution also affects to the p_T dependence of the width of π^0, which is extracted from the data. Accordingly, the energy resolution in the simulation must be also tuned to fit the real data. By the tuning of FastMC, 8.1 % for the energy dependent term and 5.0 % for the constant term of the energy resolution in Eq. 2.6 were used.

Figure 4.4 (4.5) shows the comparison between before and after the the absolute energy scale correction in the position and the width of the π^0 (η) peak. The shift of π^0 mass peak position in PbSc around $p_T \sim 12$ GeV/c (Fig. 4.4) is due to unfolding of overlapped photon showers in the EMCal (merging effect).

---

[6] λ represents the attenuation length in the fibers. The energy is corrected by multiplying $E^{-X_0/\lambda}$ (E: energy without correction, X_0: radiation length). Additional attenuation length is also included by multiplying $E^{-X_0/\lambda_{add}}$, and it mean the effective attenuation length become smaller ($\lambda_{eff} = \lambda\lambda_{add}/(\lambda + \lambda_{add})$).

This effect is not included in MC and is not corrected. On the other hand, the effect is not observed in η mass peak position which is flat well even in high p_T region (Fig. 4.5) because the η mass is heavier than π^0 and the merging effect would be seen in much higher p_T region [7]. The contribution to make the width wider at low p_T is dominated by the energy resolution of EMCal, while that at high p_T is by the position resolution. The difference between PbSc and PbGl is from the method of the clustering. Because only the core towers are used to extract the cluster energy in PbSc, the energy loss due to the tower-by-tower threshold, which is usually caused by the non-core towers, is automatically corrected.

In the real data, π^0 peak position becomes additionally lower compared to FastMC due to the unusual π^0s. The invariant mass of these unusual π^0s has lower peak position than usual π^0s reconstructed by the pure photons (see Appendix B). The size of the shift due to this effect is -1 ± 1 MeV/c^2 [108]. Because FastMC cannot simulate this effect, the peak position of π^0 is simply lowered by 1 MeV/c^2. The error of this effect, 1 MeV/c^2, is included in the uncertainty of the energy scale calibration, and is only 0.7 %. In addition, the slight difference of the π^0 peak position between sectors of EMCal is observed and is expected to be from the mis-alignment of EMCal. The error from the mis-alignment is conservatively evaluated to be 2 % in the energy scale. The systematic uncertainty of the energy scale is calculated by the quadratic sum to be 2.1 %. Note that these uncertainties of the energy scale is for π^0s with p_T range of 4 to 10 GeV/c.

In this analysis, an additional uncertainty due to the extrapolation to high energy around 40 GeV needs to be considered. From the test beam results [100], the linearity was confirmed to 2 %. By adding them in quadrature, the uncertainty of absolute energy scale is 2.9 %.

The extracted energy resolution (8.1 % for the energy dependent term and 5.0 % for the constant term) from the FastMC is used when including energy smearing effect in the theory calculation (e.g. Sec. 4.3.6)

---

[7]The inner angle between 2 photons (θ), the mass of decay particle (m) and the p_T of decay particle have a relation of: $\theta \propto m/p_T$ at lab. frame, when $|\theta| \ll 1$.

Figure 4.4: π^0 peak position (top) and width (bottom) as a function of π^0 p_T. Black (Red) points represents before (after) the absolute energy correction. (Left side: PbSc, Right side: PbGl) The dashed blue lines in top figures indicates the mass value of π^0 (135 MeV/c^2). The sift in high p_T region of π^0 peak position is caused by the merging effect (2 photons from high p_T π^0 are measured as 1 photons because of finite position resolution of EMCal).
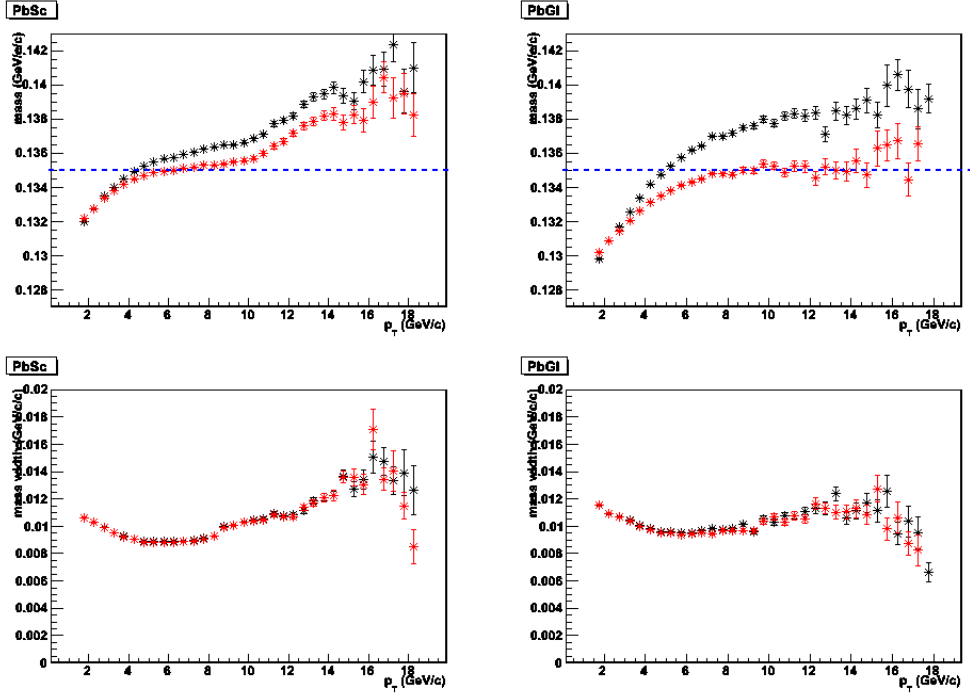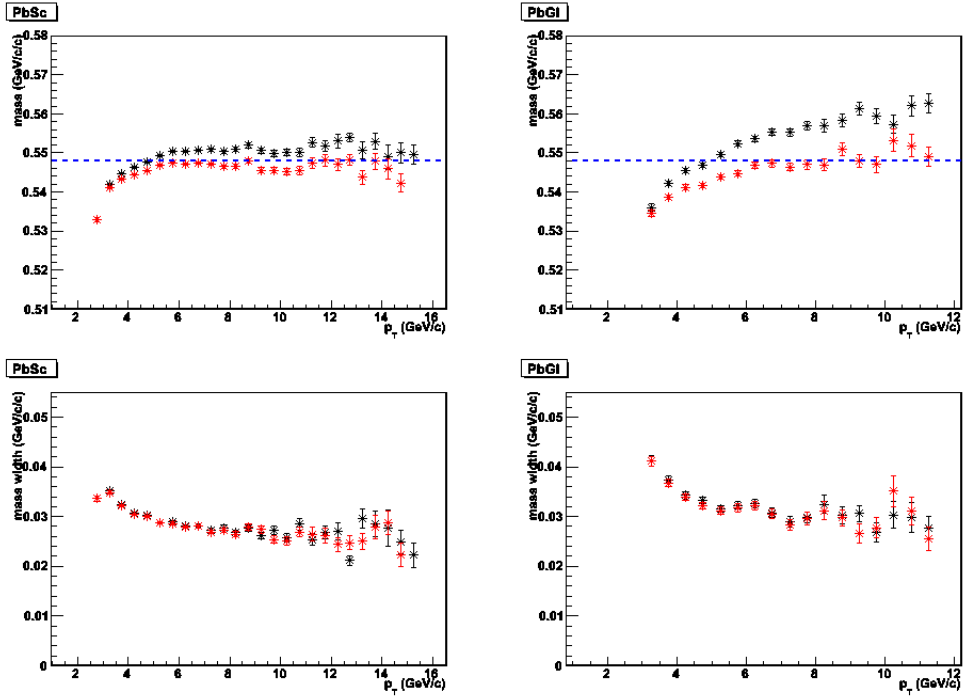

Figure 4.5: η peak position (top) and width (bottom) as a function of η p_T. Black (Red) points represents before (after) the absolute energy correction. (Left side: PbSc, Right side: PbGl) The dashed blue lines in top figures indicates the mass value of η (548 MeV/c^2).

Dynamic Range Check

The dynamic range of the ADC is also important for this analysis since the decay electron from W has quite high p_T (~ 40 GeV/c), and the ADC must cover that energy range. Figure 4.6 shows the central tower energy of clusters (denoted as "E_{cent}") as a function of ADC (left: without applying Tof cut, right: with applying Tof cut). See Sec. 4.2.3 for the Tof cut. Although some events around 60 GeV of E_{cent} seem to be saturated events in the left figure, those events are rejected with Tof cut (right figure) since such a high energy events are mainly caused by cosmic backgrounds. The E_{cent} value bears about 80 % of the whole cluster energy. Since the target energy range for this analysis is $30 <$ (cluster energy) < 50 GeV which corresponding to the E_{cent} range of around 20 to 40 GeV, the right figure shows that energy dynamic range is large enough to cover the target energy region.
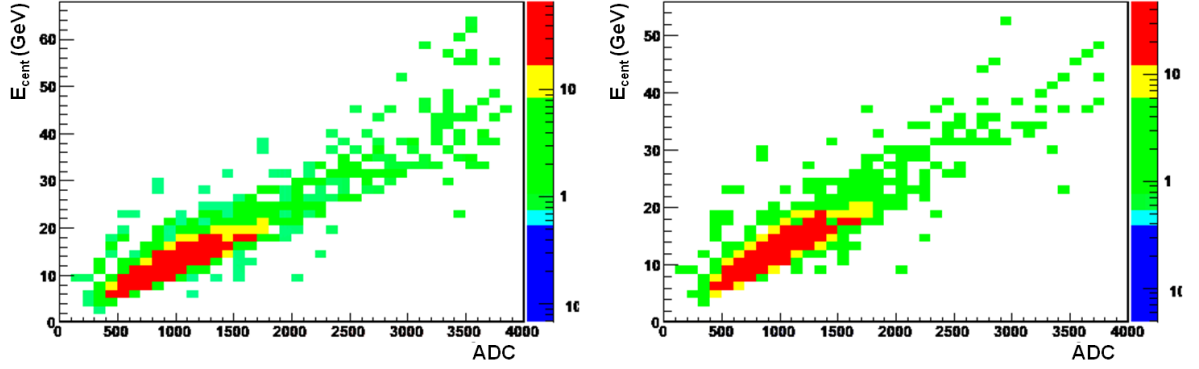
Figure 4.6: Left: ADC vs E_{cent}, Right: ADC vs E_{cent} with Tof cut ($-10 <$ Tof < 20 ns).

4.2.3   EMCal Tof Calibration

Tof (Time of Flight) of EMCal is a used to remove cosmic ray backgrounds in this analysis. The Tof calibration is done by adjusting the offset for each tower. The offset value for each tower is measured in $1 \leq E_{cent} \leq 2$ GeV region and subtracted from Tof value.

Figure 4.7 shows the Tof distribution after subtracting offset values. Although event-by-event origin of the time measured by BBC (t_0) are subtracted in the offset calculation, they are not subtracted in Fig. 4.7 because they can be mis-reconstructed in the multi-collision event and not reliable when calculating event-by-event Tof value [8]. That results in the non-zero mean values and quite broad distribution (~ 2 nsec). This broad distribution is used in this analysis since ~ 2 nsec resolution is enough to reject cosmic ray background, and required Tof cut is $-10 < $ Tof < 20 nsec. Note that any slewing correction is not applied to the Tof value either, since such a good timing resolution is not necessary to reject only cosmic backgrounds.
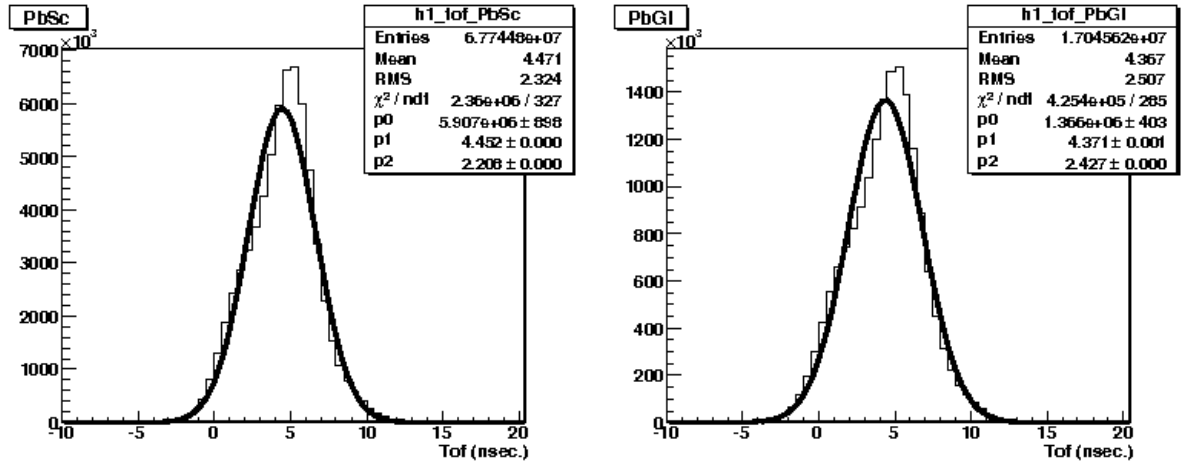
Figure 4.7: ToF distribution without subtraction of the t_0 values fitted with Gaussian distribution (Left: PbSc, Right: PbGl). The non-zero mean value is the result of not subtracting t_0 values, and asymmetric shape is due to without applying slewing correction.

---

[8] See Sec. 4.3.1 about multi-collision effect.

4.2.4 Momentum Reconstruction by DC and PC

The detailed explanation about the track reconstruction technique in PHENIX can be found in [109, 110]. The essential parts are briefly summarized in this subsection.
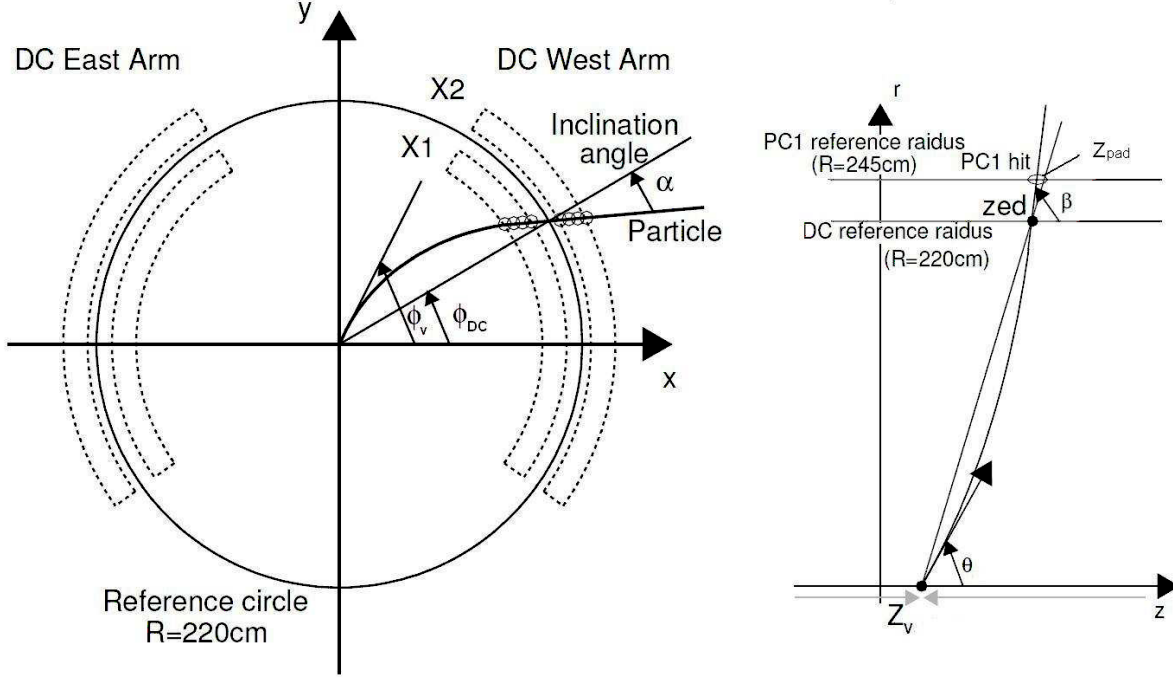
Figure 4.8: A particle trajectory and the parameters used in the track reconstruction. Left: beam view of PHENIX central arm, Right: side view of PHENIX central arm.

Figure 4.8 shows the definition of track parameters in order to describe a charged particle trajectory traveling through the axial magnetic field in PHENIX up to PC1. The track parameters are categorized as follows:

- Measured variables
  - α: The angle between the projection of trajectory in the (x, y) plane and the radial direction, at the intersection point of the trajectory with the circle of reference radius $R_{DC} = 2.2$ m.
  - z_{pad}: The intersection point of the trajectory with PC1 surface radius $R_{PC1} = 2.45$ m.
  - β: Considering the plane which includes the z-axis and z_{pad}, β is defined as the angle between the projection of trajectory onto that plane and the z-axis.
  - ϕ_{DC}: The ϕ-angle of intersection point of particle trajectory with the circle of radius with R_{DC}.

- Variables to be reconstructed
  - θ_v: The angle between the initial direction of the particle trajectory and z-axis.
  - ϕ_v: The initial azimuthal angle of the particle trajectory.
  - p_T: The transverse momentum.

74

The intersection of particle trajectory with various detector planes is uniquely determined by three variables: θ_v, ϕ_v and p_T. They are reconstructed from the measured variables: α, β, z_{pad}, ϕ_{DC} and vertex information. The collision vertex is assumed to be $(0,0)$ in (x, y) plane in PHENIX. The z position of the vertex is determined by the timing information of BBC as described in Sec. 2.2.1. The Hough Transform technique is used for the track reconstruction [111]. In case of PHENIX, track reconstruction started from finding the hits in X1 and X2 wires.

1. Project the DC hits onto (x, y) plane at $z = 0$.

2. Perform the Hough Transform using all possible X1−X2 hit combinations taking α and ϕ_{DC} as the parameters in Hough Space. For example if there are 6 hits in X1-wires and 6 hits in X2-wires, total 36 combination are taken.

3. Associate X-wire hits with the reconstructed track.

4. Perform a Hough Transform of the UV-wires and associate the resulting UV hits with the reconstructed track in order to obtain the z information.

5. Associate PC1 hit.

The α measured in the DC is closely related to the field integral along the track trajectory. The transverse momentum, p_T (GeV/c) and the α-angle (mrad) have the following approximate relation:

$$p_T \sim \frac{K}{\alpha}, \tag{4.1}$$

where $K \sim 0.10$ (rad GeV/c) is the effective field integral, expressed as:

$$K = \frac{e}{R} \int lBdl. \tag{4.2}$$

Here, e is the elementary charge in the hybrid unit ($e = 0.2998$ GeV/c T^{-1} m^{-1}) and R is the DC reference radius.

However, due to the small non-uniformity of the focusing magnetic field along the flight path of charged particles, an accurate analytical expression for the momentum of the particles is not possible. Therefore, the non-linear grid interpolation technique is used [112]. A four-dimensional field integral grid is constructed within the entire radial extent of the central arm for momentum determination based on the DC hits. The parameters of the field integral are momentum p, polar angle at the vertex, θ_v, z_{veretx}, and radial distance r at which the field integral $f(p, r, \theta_v, z_{vertex})$ is calculated.

The field integral grid is generated explicitly by swimming particles through the magnetic field map [9] and numerically integrating to obtain $f(p, r, \theta_v, z_{vertex})$ for each grid point. An iterative procedure is used to determine the momentum for reconstructed tracks, using Eq. 4.1 as an initial value. The initial estimate of θ_v is given by the z_{vertex} and DC hit position.

---

[9]The magnetic field map is from a survey measurement.

The momentum resolution depends on the intrinsic angular resolution of the DC and the multiple scattering of a charged particle as it travels up to DC due to the intervening material. As a result, the momentum resolution is about $\Delta p/p \sim p(\text{GeV}/c) \times 1$ % and the reconstruction efficiency is above 99 % for a single track.

4.2.5 DC/PC Calibration for Charge Sign Determination

The typical bending angles of high p_T electrons ($30 < p_T < 50$ GeV/c), which are the target of this analysis, are quite small (~ 2.5 mrad from Eq. 4.1) and the observed charge signs are occasionally mis-identified due to the angle resolution of the DC (~ 1.1 mrad). Other sources of the charge sign mis-identification in such a high p_T region are the beam position, and tracks incident to the anode wire region of the DC.

The beam offset correction, the treatment of the anode wire region and the charge contamination due to the DC resolution are discussed in this subsection.

Beam Offset

The actual beam position may be slightly different than exactly at the center of PHENIX central arms. Since the carriage of PHENIX central arms were moved occasionally for a maintenance, an additional offset effect was observed. Because tracking algorithm of PHENIX assumes the beam position as $(x, y) = (0, 0)$, the beam position correction is important for the charge sign determination as well as momentum measurement. For a single track, the angle resolution of the DC is about 1.1 mrad, which corresponds to 2.4 mm (= 220 cm × 1.1 mrad) at the beam position.

The DC measures the momentum of a track by measuring α, which is the angle the track projection makes with respect to a perfectly straight track projection at a reference radius of 220 cm (see Sec. 4.2.4). So if there is no magnetic field, the tracks do not bend and α should be equal to zero. Any deviation from $\alpha = 0$ in zero field run data indicates that the beam position is off from $(x, y) = (0, 0)$, and this can be corrected by the apparent α.

Doing some trigonometry (see Fig. 4.9), it can be shown that the beam offset in the x and y direction (dx and dy respectively) are related to α and ϕ_{DC}. Thus, the plot of α vs. ϕ_{DC} gives us a way to extract dx and dy. The relation between α, ϕ_{DC}, dx, and dy is:

$$\alpha = \frac{dx}{R_{DC}} \sin \phi_{DC} - \frac{dy}{R_{DC}} \cos \phi_{DC}. \tag{4.3}$$

Here, R_{DC} denotes the reference radius at the DC (220 cm). This function is fit to the plot of α vs. ϕ_{DC}, and the beam position (dx, dy) are extracted. Two figures in the left side of Fig. 4.10 display an example of the fit. The fit was carried out in west and east arm separately because the location of arms are not exactly symmetric relative to the beam position. Two figures in the right side of Fig. 4.10 show the α distribution after the beam position correction. These figures represents that the deviation from $\alpha = 0$ is very small and the resolution is less than 1.1 mrad after the correction.

Several zero field runs are available through Run 9 to follow the beam position shift. Figure 4.11 shows the beam position (dx, dy) for each run. Although there is a jump around run 278000, which is caused by the carriage movement, they are within a range of ± 300 μm. Compared with other resolution (DC, PC1, EMCal), those shift is small enough.

In this analysis, a correction of α is applied by $\alpha_{recal} = \alpha - \alpha_{offset}(\mathrm{run}, \phi)$ in which α_{offset} is calculated following Eq. 4.3. The correction is also checked using mass peak position of J/ψ.
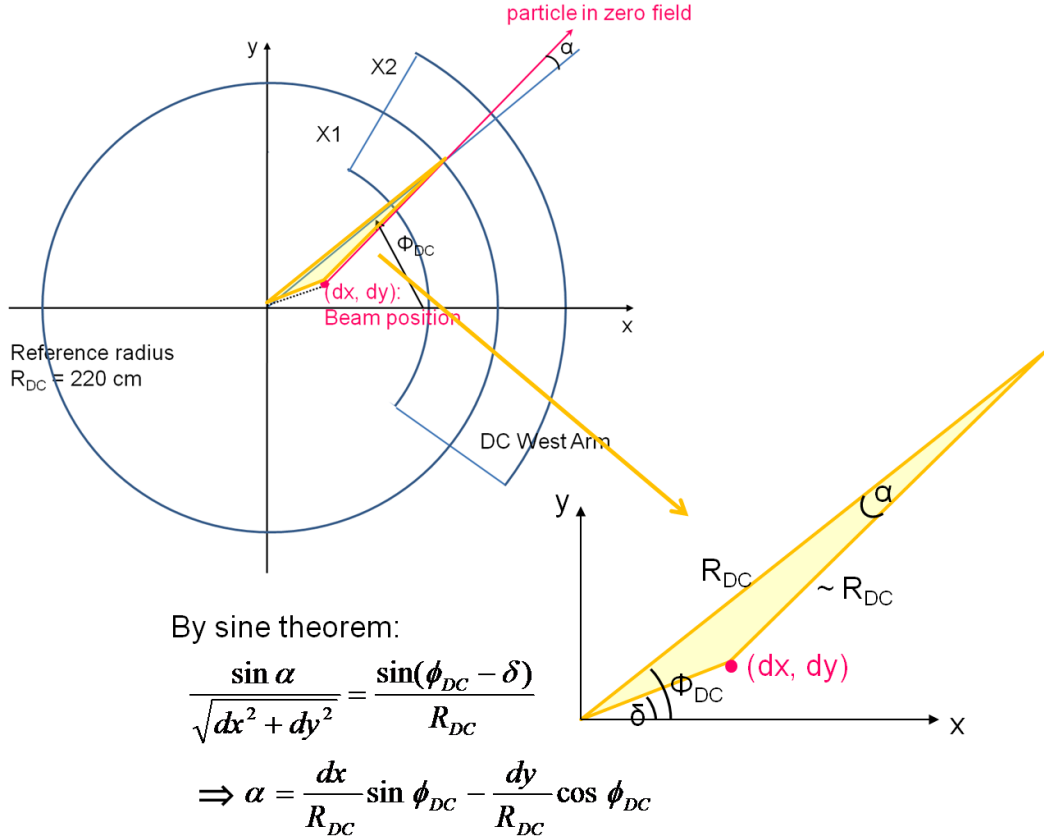
Figure 4.9: Schematic drawing of trigonometry to extract beam position.
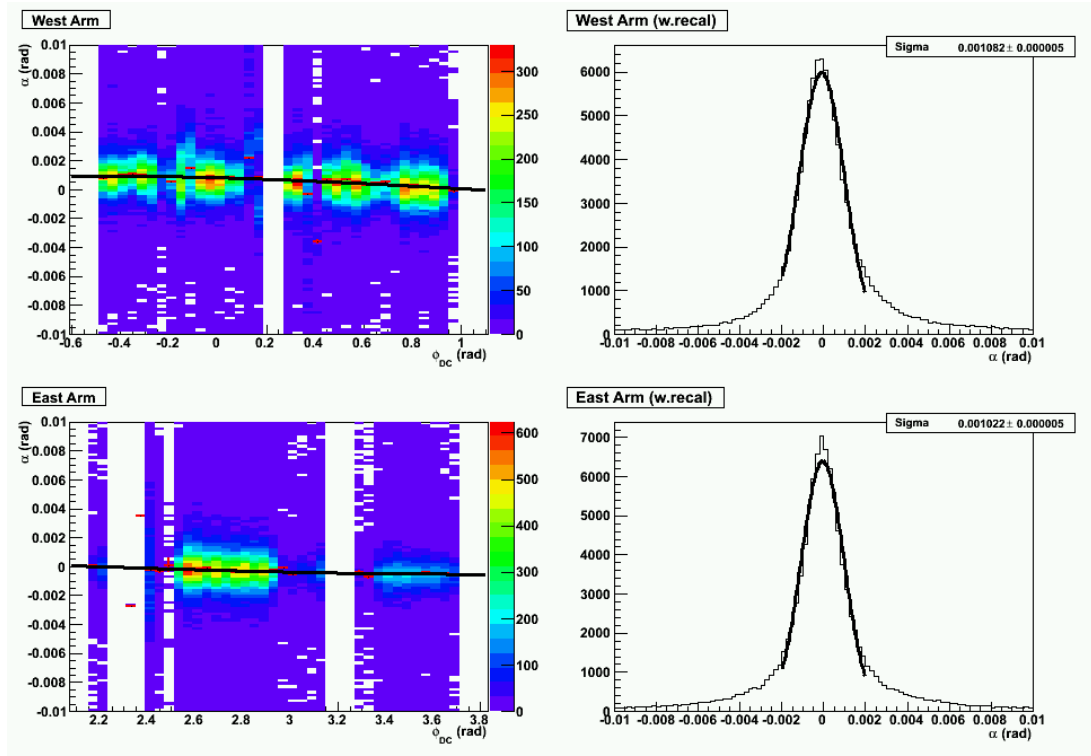
Figure 4.10: An example of the fit to extract the beam position from a zero field run. Left two figures show the fit example and Right two figures show α distribution after the beam position correction. (Top: West arm, Bottom: East arm)
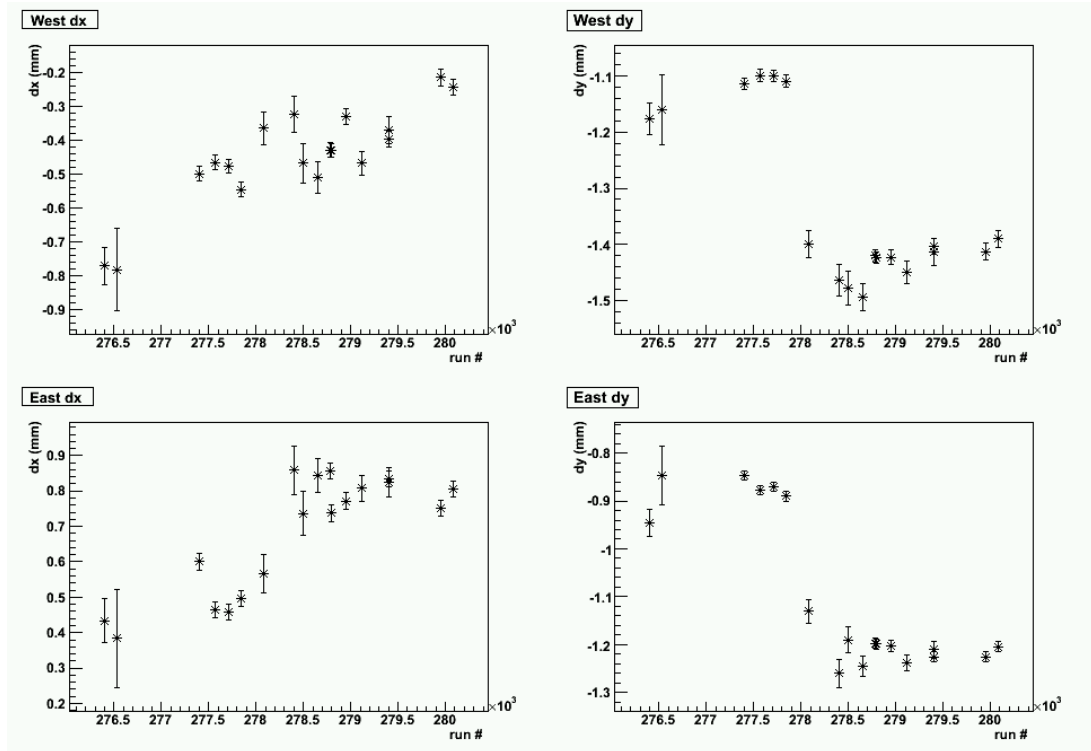
Figure 4.11: Obtained fit parameters from zero field runs. A jump around run 278000 is caused by the carriage movement.

Anode Wire Region

As p_T goes up, the particle go through the DC plane perpendicularly. The left right ambiguity cannot be solved when high p_T track is close to the anode wire due to its small bending angle and the DC design (Fig. 4.12). As a result, more than one track are reconstructed even if only one particle goes through that region (ghost track).
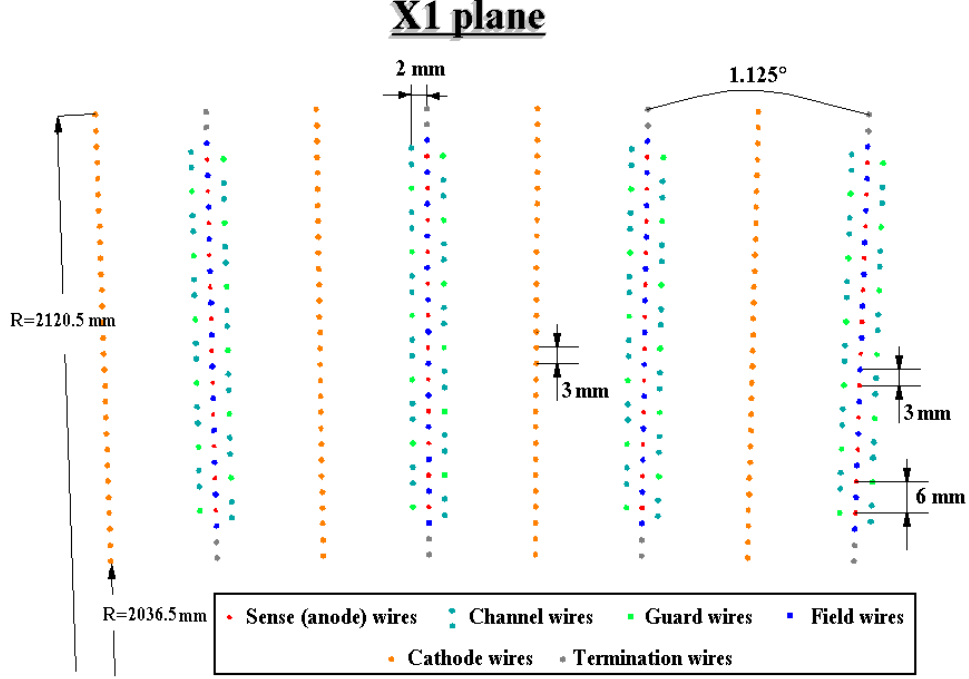
Figure 4.12: DC wire design

The effect is checked using zero field runs. Figure 4.13 displays the number of tracks as a function of ϕ_{DC}. When requiring a pair of tracks with the opening angle less than 2 mrad [10], periodical peaks appear (Red distribution). The interval of the peaks corresponds to that of the anode wires ($\sim$ 0.02 rad from Fig. 4.12). These peaks are produced by the ghost tracks.

Since ghost tracks cause the charge mis-identification and they are not the real tracks, the anode wire regions are removed with ϕ_{DC} mask. In total, 15 % of the DC acceptance is masked to avoid the anode wire region.

---

[10]This can be calculated from the anode wire region. The region is 4 mm from Fig. 4.12 and that corresponds to $\sim$2 mrad by the DC radius of 220 cm.
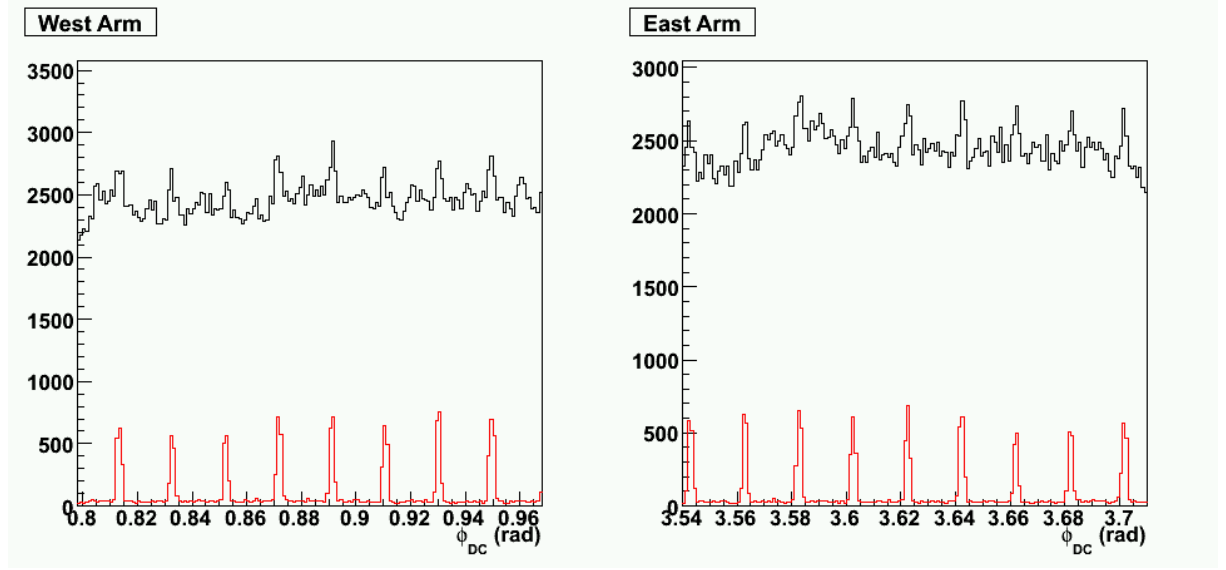
Figure 4.13: Black line shows the number of tracks without any cut as a function of ϕ_{DC}. When requiring pair track, periodical peaks appear. (Red line) These peaks are corresponding to the anode wire region. (Left: West arm, Right: East arm, zoomed in to clearly display intervals of pair track peaks)

Charge Contamination

In the high p_T region, charge mis-identification is unavoidable due to the limited DC resolution in this measurement. Taking the ratio of the bending angle at 40 GeV/c (2.5 mrad) to the resolution of the DC (1.1 mrad), the probability of a positron to be mis-identified as a negative charge (i.e. as electron) is 1.1 % (= 2.3 σ). The charge contamination of electrons to positrons is also the same fraction. Note that this number for the 40 GeV/c track should be taken as the maximum charge contamination because the $e^{\pm}$s from W decays mainly have p_T of 30 to 40 GeV/c.

4.3 Cross Section

The relationship of $d\sigma/dy$ to the experimental observables is the following:

$$\frac{d\sigma}{dy} = \int dp_T \frac{d^2\sigma}{dp_T dy} = \frac{1}{\mathcal{L}} \cdot \frac{1}{\varepsilon_{trig} \cdot \varepsilon_{reco} \cdot \varepsilon_{smear}} \cdot \frac{1}{\Delta y} \cdot \sum_{30 < p_T < 50} \frac{(N^{meas} - N^{bg})}{\Delta p_T}, \qquad (4.4)$$

where:

- $\mathcal{L}$ denotes the integrated luminosity.

- N^{meas} means the number of inclusive electron-candidate in each p_T bin, and $\sum N^{meas}/\Delta p_T$ is the number of counts measured in signal region of $30 < p_T < 50$ GeV/c.

- N^{bg} represents the number of background in each p_T bin, and $\sum N^{bg}/\Delta p_T$ stands for the total number of background in $30 < p_T < 50$ GeV/c region.

- ε_{trig} is the ERT4x4b trigger efficiency.

- ε_{reco} denotes the efficiency of geometry and analysis cuts.

- ε_{smear} means the effect of energy smearing.

- Δy is the rapidity bin width and is set to $\Delta y = 1$ here (PHENIX acceptance is included in ε_{reco}).

The details of the evaluation of every factors are described in this section. First of all, the integrated luminosity used in this analysis ($\mathcal{L}$) is represented in Sec. 4.3.1. Then the p_T spectrum of inclusive electron-candidate (N^{meas}) is measured, and the total number of counts in $30 < p_T < 50$ GeV/c region is extracted in Sec. 4.3.2. Here, several geometry and electron ID cuts are utilized to measure N^{meas}. They are also explained in this subsection. The most essential part of this analysis is the estimation of background (N^{bg}). It is estimated using the real data and MC simulation and the detail is described in Sec 4.3.3. After that, efficiency of trigger (ε_{trig}), geometry and analysis cuts (ε_{reco}) and the effect of energy smearing (ε_{smear}) is evaluated in Sec. 4.3.4, Sec. 4.3.5, and Sec. 4.3.6, respectively. Finally, The calculation of $d\sigma/dy$ at $30 < p_T < 50$ GeV/c region is described in Sec. 4.3.7

4.3.1 Integrated Luminosity at PHENIX

The integrated luminosity is calculated from number of Minimum Bias (MB) trigger (N^{MB}) of the PHENIX. The MB trigger of the PHENIX is BBCLL1 as described in Sec. 2.2.5, and BBCLL1(noVtx) trigger is used as MB trigger in this analysis.

In RHIC Run 9 at $\sqrt{s} = 500$ GeV energy, there is non-negligible probability of multiple collision (multi-collision) event. The expected event rate at $\sqrt{s} = 500$ GeV is ~ 3.3 MHz ($= \sigma_{pp}(500 \text{ GeV}) \times L$) [11], and this event rate means there is a collision almost in every beam crossing (beam crossing rate at RHIC is 9.4 MHz (106 nsec), but this includes empty bunches). Therefore, that results in non-negligible multi-collision event probability (~ 10 %). Because the BBC is not capable to detect multi-collision event, the N^{MB} measured by the BBC underestimates the real rate. The correction to get "true" rate was not only determined by Poisson probability, but also depends on the efficiency of the BBC (the detail how to correct multi-collision effect is described in Appendix C).

N^{MB} is calculated as 5.58×10^{11} after the correction of multi-collision effect. The uncertainty of the correction of multi-collision effect is 2.1 % which comes from single side efficiency of the BBC (denoted as "k_N, k_S" in Appendix C). To get the integrated luminosity, this N^{MB} is multiplied by the BBC cross section (σ_{BBC}) measured by the vernier scan (Sec. 3.3).

An additional factor which should be taken into account is the reduction of the total integrated luminosity caused by the event vertex cut. It depends on the vertex width. Figure 4.14 shows the fraction of the events with 30 cm vertex cut ($f^{vtx}(\pm 30 \text{cm})$) from the BBC trigger sample. It shows a slight run by run variation which is caused by the trigger rate dependence. Figure 4.15 shows the $f^{vtx}(\pm 30 \text{cm})$ as a function of the trigger rate defined as $N^{MB}/(\# \text{ of Beam Crossings})$. Here, the (# of Beam Crossings) is calculated from the run time duration multiplied by the time of 1 beam crossing (106 nsec) with not counting empty bunches. The trigger rate dependence is caused by the multi-collision. Experimentally, the BBC is not capable of handling the multi-collision event, and that leads to the mis-reconstructed vertex position. The $f^{vtx}(\pm 30 \text{cm})$ obtained from luminosity weighted mean of Fig. 4.14 is 0.499, and f^{vtx} with other vertex cuts are also listed in Table 4.1. The uncertainty of the fraction is evaluated from its trigger rate dependence. It is estimated by the inclination of the fit function in Fig. 4.15. As the trigger rate spread over the range of 0.05 to 0.25, the corresponding width of f^{vtx} is $p_1 \times (0.25 - 0.05) = 0.040$. Thus, we assigned the uncertainty of $f^{vtx}(\pm 30 \text{cm})$ as 4.0 % ($= (0.040/2)/0.499$).

vertex cut (cm)	fraction
40	0.620
30	0.499
20	0.352

Table 4.1: Fraction of events with vertex cut (f^{vtx}).

---

[11] $\sigma_{pp}(500 \text{ GeV})$ is the total collision cross section at $\sqrt{s} = 500$ GeV and its value is ~ 61 mb [113]. L is the luminosity of RHIC in Run 9, and it is 5.5×10^{31} cm^{-2}sec^{-1} in average.
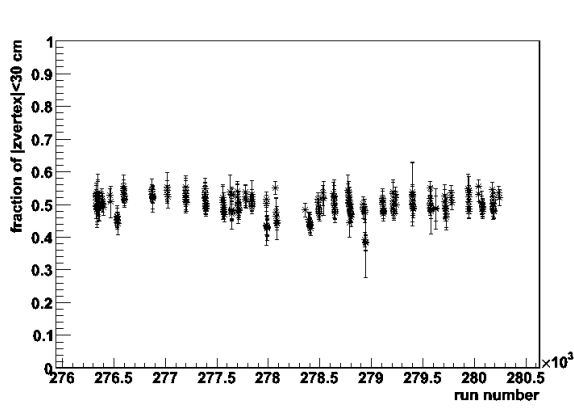
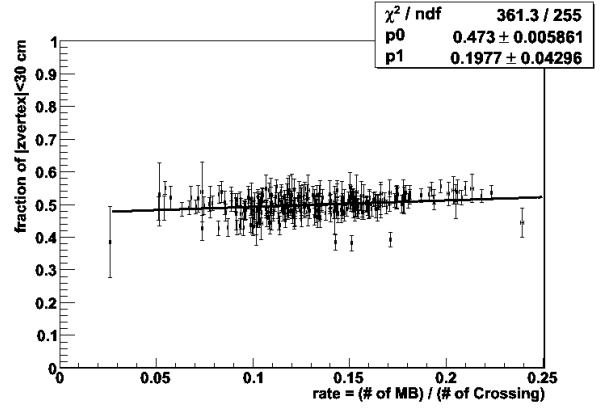Figure 4.14: The fraction of events with a vertex cut to ones with no vertex cut ($f^{vtx}(\pm 30\text{cm})$).

Figure 4.15: The $f^{vtx}(\pm 30\text{cm})$ as a function of the trigger rate, fitted with a polynomial function ($n = 1$). The extrapolated point of (trigger rate) = 0 is used to evaluate the uncertainty of the fraction.

Vertex Reconstruction from EMCal and PC1 Hit Position

Since the multi-collision event causes the BBC to mis-reconstruct the z-vertex position (z_{vertex}), the z_{vertex} reconstructed from EMCal cluster and PC1 hit position was used in this analysis for the vertex cut. Figure 4.16 shows the difference between the EMCal$-$PC1 based z_{vertex} and the BBC based z_{vertex}. The distribution is fit with "Gaussian + constant" and the width is 2.23 ± 0.03 cm (p_2 parameter). This width can be explained by the position resolution of EMCal ($1 \sim 2$ cm), PC1 (~ 1.7 mm) and BBC (~ 2 cm). The tail part contains both mis-reconstructed BBC vertex and mis-association of EMCal and track (DC/PC1 information) [12].

Figure 4.17 shows the distribution of EMCal-PC1 based z_{vertex}. The cut at around 40 cm is due to the nose cone of PHENIX central magnet (Sec. 2.2.3). In the analysis, the EMCal-PC1 based z_{vertex} is used in the vertex cut and the requirement is $|z_{vertex}| < 30$ cm.

The difference between the BBC based z_{vertex} and the EMCal-PC1 based z_{vertex} causes the change in the $f^{vtx}(\pm 30\text{cm})$. Since the width of the difference is 2.2 cm, the fraction of events with 32.2 cm and 27.8 cm vertex cut is calculated. These fractions are different from the $f^{vtx}(\pm 30\text{cm})$ only by 6.0 %. Including this difference, the uncertainty of the fraction becomes 7.2 %.

Summary of Integrated Luminosity

The total integrated luminosity that were analyzed for this analysis is calculated via:

$$\mathcal{L} = \sum_{i=run} f^{vtx}(\pm 30\text{cm}) N_i^{MB} C_i(R_i^{BBC})/\sigma_{BBC}. \tag{4.5}$$

The values with the i subindex are calculated run by run. The factors in this calculation are described in Table 4.2. The calculated total integrated luminosity with 30 cm vertex cut is 8.56 pb^{-1}.

---

[12]The mis-association is caused by the fact that only ϕ matching is required when associating a EMCal cluster to a DC/PC1 position. This loose association is used in this analysis because the BBC based z_{vertex} is mis-reconstructed in multi-collision event and the association of z-direction is not reliable. The detail of the association is described in Sec. 4.3.2.
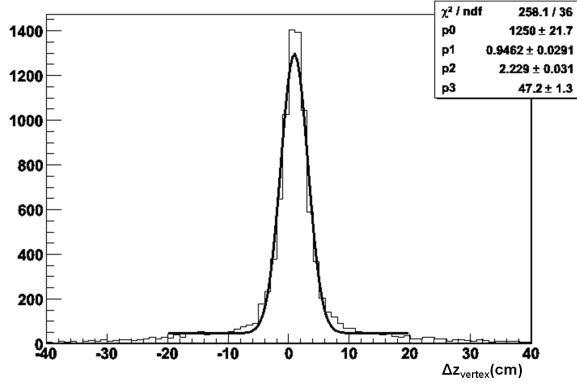
Figure 4.16: Δz cm distribution between the BBC vertex and the reconstructed vertex. The distribution is fit with Gaussian + constant and the width is 2.2 cm (p_2 parameter). This width can be explained by the position resolution of EMCal, PC1 and BBC.
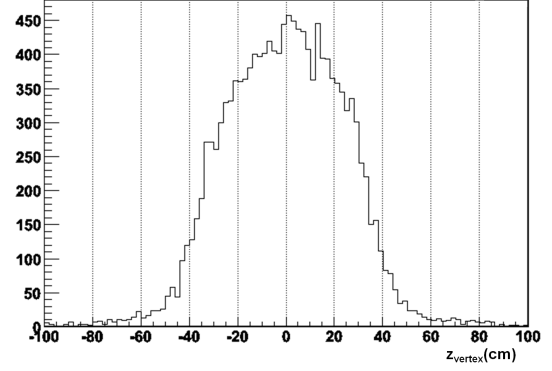
Figure 4.17: z_{vertex} distribution reconstructed from EMCal and PC1 hit position. The cut at around 40 cm is due to the natural cut of the nose cone of PHENIX central arms.

The uncertainty is from correction of multi-collision (2.1 %), f^{vtx} (7.2 %) and σ_{BBC} (10 %). Adding them in quadratic, the uncertainty of integrated luminosity is 13 % in total.

notation	value	uncertainty	explanation
$f^{vtx}(\pm 30\text{cm})$	0.499	7.2 %	The fraction of events which are within the vertex cut.
N_i^{MB}			The number of MB (BBCLL1(noVtx)) trigger.
$C_i(R_i^{BBC})$		2.1 %	The correction factor for multi-collisions. C_i is a function of the trigger rate (R_i^{BBC}). More detailed explanation is given in Appendix C.
σ_{BBC}	32.51 mb	10 %	The cross section seen by BBCLL1(Vtxcut) as determined by vernier scans (Sec. 3.3).

Table 4.2: explanations of factors in Eq. 4.5

4.3.2 Event Selection

In order to evaluate N^{meas} in Eq. 4.4, several cuts are applied in this analysis. They are:

- **Track Quality Cut**: require hits on X1 and X2 plane of the DC and hit on the PC1.

- **DC Mask**: Mask anode wire neighbors [13].

- **Vertex Cut**: $|z_{vertex}| < 30$ cm [14].

- **EMCal Tof Cut**: $-10 < \mathrm{Tof} < 20$ nsec.

- **EMCal Mask**: Mask problematic FEMs of ERT4x4b trigger and EMCal towers.

- **DC-EMCal Matching**: $|\Delta\phi| < 0.01$ rad.

- **E/p Cut**: Reject low momentum accidental match with the cut of $E/p < 2$.

The detail of EMCal mask, DC-EMCal matching and E/p cut is described in this subsection. Note that the performance of the DC/PC1 is not so stable during Run 9 (see Appendix D for tracking performance) while the EMCal performance throughout Run 9 period was quite stable (e.g. see Fig. 4.3). Because a technique to handle the run-by-run acceptance change of the DC/PC1 is employed when calculating the efficiency of geometry and analysis cuts (ε_{reco}) in Sec. 4.3.5, no run is rejected in this analysis to earn as many of $e^{\pm}$s from W decays as possible.

The value of p_T is calculated by $E \times \sin\theta$ (E: energy of EMCal cluster, i.e. p_T in this thesis represents E_T) as the energy resolution is better than the momentum resolution in high p_T region ($p_T > \sim 10$ GeV/c). Figure 4.18 is the raw p_T spectrum of inclusive $e^{\pm}$ candidates with applying all cuts listed above, and Table 4.3 shows the total counts in the figure at $30 < p_T < 50$ GeV/c region. These numbers are used in the calculation of $d\sigma/dy$.

charge	total counts
$+$	62
$-$	17
$\pm$	79

Table 4.3: Total counts in a p_T range of 30 to 50 GeV/c.

EMCal Hot/Dead Tower Mask

A hot tower is defined as a tower sending signals at significantly higher frequency than other towers, which is known to be electronics noise. Distributions of the number of hits of each tower is created for each EMCal sector [15] and towers which have multiplicity greater by 15 σ from the average are identified

---

[13] The junction of North and South side of the DC/PC1 is also masked due to its inefficiency. ± 3 cm from the junction is rejected in this analysis.

[14] EMCal$-$PC1 based z_{vertex} is used for vertex cut (Sec. 4.3.1).

[15] The cut of cluster energy is more than 10 GeV is applied to make this distribution.
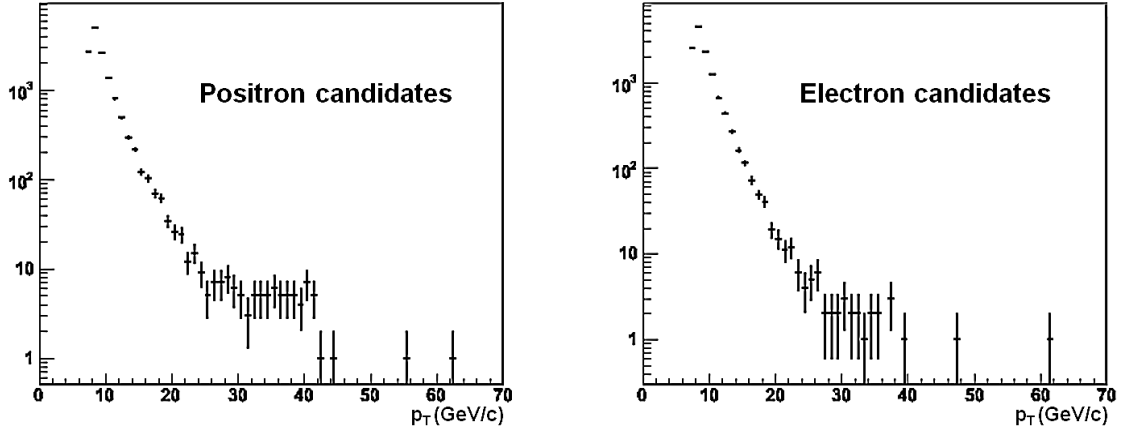
Figure 4.18: p_T spectrum of inclusive electron-candidate with applying all cuts. Left: positive charge, Right: negative charge

as hot tower. This threshold is quite large, but it can reject extremely noisy towers, and can keep the EMCal acceptance as large as possible in order to observe rare W events. When there is a hot tower, towers around that particular tower are also masked to avoid mis-reconstructed energy caused by the hot tower. Towers for which the calibration constants cannot be determined are also masked. These towers remain uncalibrated since most of them are dead towers. The edge towers are also masked to avoid the shower leakage effects. Two towers from each edge are assigned as the edge towers. In total, 4145 towers are masked in this analysis. (PbSc: 2820 (18 %), PbGl: 1325 (14 %), most of them are edge towers)

In addition to hot/dead towers, noisy FEMs of ERT4x4b trigger are also masked (see Sec. 2.2.5 for FEM). Three FEMs in PbSc (2.8%) and one SM (1.6 %) in PbGl are masked because their trigger rate is rather higher than other FEMs.

Removing hot/dead towers and bad FEMs, roughly 79 % of PbSc and 84 % of PbGl are used in this analysis. By weighting on the number of towers of PbSc and PbGl, averaged active area of EMCal is about 81 %. The hot/dead towers and bad FEMs are taken into account when calculating ε_{reco} (detection efficiency and geometrical acceptance) in Sec. 4.3.5.

DC-EMCal Matching

Due to non-negligible fraction of multi-collision events, the z_{vertex} measured by the BBC is not reliable for the track association. Therefore, only ϕ value is used for the association in this analysis. If the internal ϕ angle ($|\Delta\phi|$) between a particular track and a EMCal cluster is less than 0.01 rad, these hits are tagged as originated from the same particle.

Figure 4.19 shows the $\Delta\phi$ distribution for clusters with energy more than 10 GeV. The distribution is fitted with the combination of Gaussian and constant. The width of the peak is ~ 3 mrad (p_2 parameter) and this value can be explained by the ϕ resolution of the EMCal (~ 3 mrad [16]) and the DC (1.1 mrad).

---

[16]This value is calculated from the position resolution of ~ 1.5 cm at 500 cm away from collision point

The tail part of the distribution is corresponding to the random track association and these events are used in the estimation of accidental track match (Sec. 4.3.3). The red histogram in the figure shows the $\Delta\phi$ distribution with E/p cut and it can be noticed the tail part (accidental match) is well reduced by the cut.

This association technique allows one track to match multiple EMCal clusters. If there multiple candidates in $|\Delta\phi| < 0.01$ rad, the one with the highest momentum was selected.

χ^2 / ndf	317.7 / 82
p0	678 ± 9.8
p1	-4.199e-05 ± 3.422e-05
p2	0.002851 ± 0.000036
p3	74.27 ± 1.21

χ^2 / ndf	253.3 / 82
p0	643.9 ± 9.1
p1	-6.556e-05 ± 3.058e-05
p2	0.002727 ± 0.000029
p3	20.29 ± 0.63
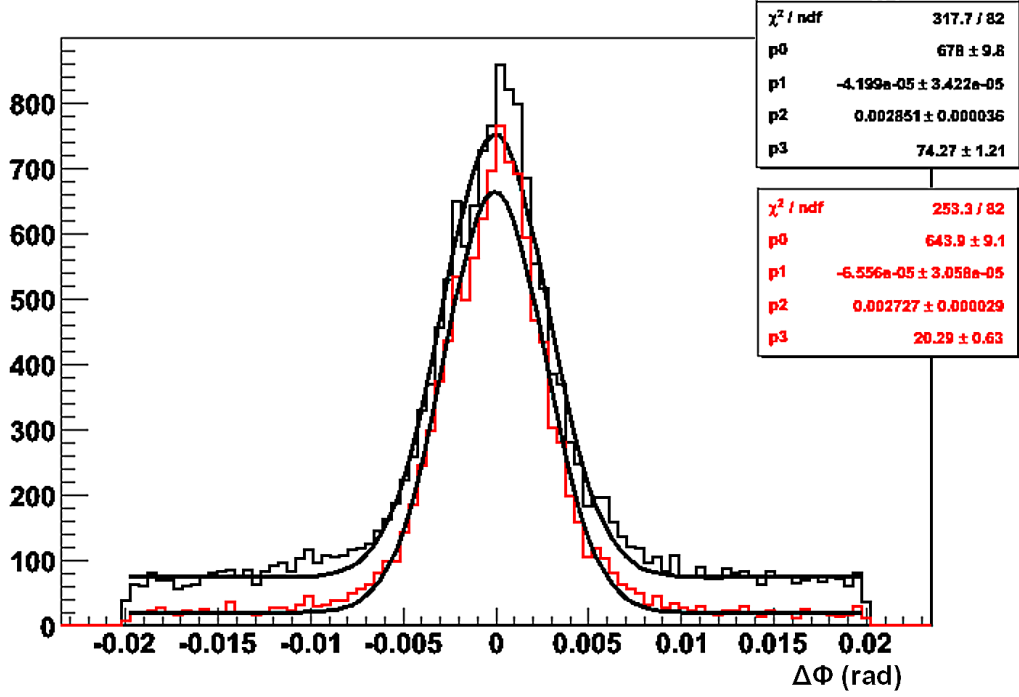
Figure 4.19: $\Delta\phi$ distribution of track matching for the cluster more than 10 GeV. Black: without an E/p cut. Red: with $E/p < 2$ cut.

E/p **Cut**

Since the electron deposits all of its energy in EMCal and the mass is small compared to its momentum, the ratio of the momentum to the energy detected at EMCal (E/p) is around one in case of the electron track. On the other hand, the E/p values for charged hadrons become small because the energy deposit by hadrons at EMCal is smaller than they actually carry. Therefore, the E/p cut can reject the charged hadron track. The cut also rejects the accidental matching in this analysis as the effect is shown in Fig. 4.19. Because the momentum resolution becomes worse in high p_T region, the width of E/p distribution gets wider. In order not to drop W candidate events at high p_T region, very loose cut of $E/p < 2$ is adopted [17].

---

[17]This cut does not reject events with small E/p values and it means the cut does not work for rejecting charged hadron events. However, ERT4x4b trigger has a energy threshold of ~ 8 GeV (Sec. 4.3.4) and it works like a cut for small E/p events.

4.3.3 Background Estimation

Because the PHENIX is not hermetic, missing-momentum technique cannot be used to detect Ws. Therefore the observed process is only the single-inclusive reaction $pp \to lX$, and there are several backgrounds for the measurement:

- **Accidental track match**: γs observed at EMCal accidentally match to charged tracks from jet fragments.

- π^0 **conversion**: A fake high p_T track would be observed when one of γs from π^0 decay is converted to electrons before the DC and another γ is detected at the EMCal.

- **Charged hadron**: There is a possibility that high p_T charged hadron deposit all energy in EMCal, and observed like high p_T electron.

- **Heavy flavor decays**: $e^\pm$s from D/B meson decays contribute to background.

- Z/γ **decays**: Because mass of Z boson is quite close to it of W boson, $e^\pm$s from Z boson decays have similar momentum to $e^\pm$s from W boson decays. However, it is hard to reject $e^\pm$s from Z decays by tagging both electron and positron with the limited PHENIX acceptance. Therefore, they are treated as a part of W signal in the signal extraction. The fraction of Z decay contribution is estimated using NLO calculation, and subtracted in calculation of the $W \to e$ cross section which is described in Sec. 5.1.

- $W \to \tau \to e$ **decays**: The branching ratio of τ to e is about 20%. The contribution of this decay mode was evaluated in event generator (PYTHIA) and found to be negligible in the range of $30 < p_T < 50$ GeV/c with current statistics.

The main components of background are from accidental track match, π^0 conversion and charged hadron. These components are estimated using the real data and MC simulation.

The background estimation is based on the p_T distribution of all EMCal clusters (N^{EMCal}) in which the dominant component is γs from π^0 decays. The EMCal cluster distribution is produced without any vertex cut though the vertex cut of the PHENIX nose cone (40 cm) is applied naturally. The procedure of the background estimation is following:

1. The probabilities of accidental track match (P_{acc}) and π^0 conversion (P_{π^0}) are evaluated by real data and MC simulation.
   Then, the p_T distributions of accidental track match and π^0 conversion are obtained by multiplying those probabilities to N^{EMCal} (($P_{acc} + P_{\pi^0}) \times N^{EMCal}$). Note that N^{EMCal} is made with the 40 cm vertex cut, therefore the probabilities derived here need to be multiplied by the additional factor of vertex cut ($0.80 = f^{vtx}(\pm30\text{cm})/f^{vtx}(\pm40\text{cm})$, see Sec. 4.3.1) in order to compare them with Fig. 4.18.

2. The shape (p_T dependence) of charged hadron background (N^{hadron}) is evaluated using MC simulation. The obtained shape is then scaled so that the low p_T region ($12 < p_T < 20$ GeV/c) of Fig. 4.18 can be explained by the charged hadron (($scale$) $\times N^{hadron}$).

3. The combination of these components are used for the background evaluation:

$$
\begin{aligned}
N^{bg} &= f^{vtx}(\pm 30\text{cm})/f^{vtx}(\pm 40\text{cm}) \times (P_{acc} + P_{\pi^0}) \times N^{EMCal} + (scale) \times N^{hadron} \\
&= 0.80 \times (P_{acc} + P_{\pi^0}) \times N^{EMCal} + (scale) \times N^{hadron}.
\end{aligned}
\tag{4.6}
$$

The detail of each part is described below.

All EMCal Clusters: N^{EMCal}

N^{EMCal} is the p_T distribution of EMCal clusters with subtracting cosmic components. The cosmic components is estimated using the EMCal Tof value (Sec. 4.2.3), with requiring "out" of timing ($-20 <$ Tof < -10 nsec or $20 <$ Tof < 40 nsec) for the EMCal clusters. Here, the Tof window is selected so that the window size matches to the size of Tof window which is used in this analysis ($-10 <$ Tof < 20 nsec). Then the distribution of N^{EMCal} is obtained by statistically subtracting "out" of timing from "in" of timing distribution. The main component of N^{EMCal} is γs from π^0 decays.

In the background estimation, N^{EMCal} extracted here is fitted with a power law function to get smooth spectrum. In the following discussion, the obtained fit function is used as N^{EMCal}.

Accidental Track Match: P_{acc}

The probability of accidental track match is extracted from the tail of $\Delta\phi$ distribution which is used in DC-EMCal matching (Fig. 4.19). The p_T distribution of EMCal clusters with track association in $0.01 < |\Delta\phi| < 0.02$ window is produced and compared to the N^{EMCal} distribution. The obtained ratio is 0.68 ± 0.02 % without any p_T dependence, and this is used as P_{acc}. Note that this number naturally includes the overall efficiency of geometry and analysis cuts (Sec. 4.3.5) since the p_T distribution with track association in $0.01 < |\Delta\phi| < 0.02$ is made with all cuts, which is described in Sec. 4.3.2, except for the 30 cm vertex cut and DC-EMCal matching cut [18].

π^0 Conversion: P_{π^0}

Events which have their origin in π^0 conversion contribute to the background. Because the opening angle of two γs from high p_T π^0 decay can be quite small, a fake high p_T track would be observed when one of γs is converted to electrons before the DC and another γ is detected at the EMCal.

The probability of such events is evaluated using single particle MC simulation. Single π^0 events are thrown to PISA with flat p_T distribution ($20 < p_T < 70$ GeV/c). The output distribution is weighted by the cross section from theory of the NLO perturbative QCD (pQCD) calculation [114] according to

---

[18]P_{acc} is not affected by the change of DC-EMCal matching cut because the width of $\Delta\phi$ window does not change between $|\Delta\phi| < 0.01$ and $0.01 < |\Delta\phi| < 0.02$.

the input p_T of π^0. Then the fraction of EMCal clusters which is associated with the DC/PC1 tracks are studied. As a result, obtained P_{π^0} is 1.07 ± 0.06 % without any p_T dependence. In addition to all cuts described in Sec. 4.3.2, ϕ-dependent efficiency (see Sec. 4.3.5) is included in this study to include the acceptance change of the DC/PC1 during Run 9 period.

The obtained P_{π^0} can be checked with a simple calculation. The conversion probability of γ calculated from the materials before the DC is 2.6 %, and the number which corresponds to P_{π^0} is 0.96 % = $2.6 \times 0.152/0.35 \times 0.85$ (0.152/0.35: the efficiency of geometry and analysis cuts from Sec. 4.3.5, 0.85: DC wire region cut from Sec. 4.2.5). This number is consistent with the value from MC simulation within uncertainty [19].

Uncertainty of Accidental Track Match and π^0 Conversion

It needs careful treatment when adding P_{acc} and P_{π^0}, because these probabilities might have an overlap. As discussed in above, P_{π^0} is 1.07 % from single π^0 MC, and it is 0.68 % for P_{acc}. If all the accidental track match is caused by the π^0 conversion, the added probability would be 1.07 %, and the value would be 1.75 % if two values are fully uncorrelated. Therefore, the factor multiplied to N^{EMCal} (i.e. $0.80 \times (P_{acc} + P_{\pi^0})$) is: 0.86 % as the minimum, 1.40 % as the maximum value. In this analysis, 1.00 % is set as a default value for simplicity.

The uncertainties of P_{acc}, P_{π^0} and the vertex cut factor ($0.80 = f^{vtx}(\pm30\text{cm})/f^{vtx}(\pm40\text{cm})$) are 2.9 %, 5.6 % and 2.0 % of each value [20]. They are ignored here because it is small enough comparing to the uncertainty of $P_{acc} + P_{\pi^0}$ assigned above.

Charged Hadron: N^{hadron}

It is difficult to evaluate the absolute value of N^{hadron} from simulation, so the MC simulation is only used for extracting the relative shape (i.e. p_T dependence) of N^{hadron}. Single $\pi^\pm$ are generated with flat p_T distribution ($0 < p_T < 100$ GeV/c) and thrown to PISA. The output distribution is weighted by the cross section from theory of the NLO pQCD calculation according to the input p_T of $\pi^\pm$.

In the background estimation, only the shape of the obtained distributions is used. After subtracting components of accidental track match and π^0 conversion ($0.80 \times (P_{acc} + P_{\pi^0}) \times N^{EMCal}$) from Fig. 4.18, the shape of charged hadron is scaled so that the low p_T region ($12 < p_T < 20$ GeV/c) of the figure can be explained by the charged hadron.

Uncertainty of Charged Hadron

The uncertainty of charged hadron background is estimated by changing the normalized range. The default normalized range is set as $12 < p_T < 20$ GeV/c, and it was changed to $16 < p_T < 20$ GeV/c. The difference of the scale factor is 17 % and it is included as the systematic uncertainty.

---

[19] The uncertainty of efficiency of geometry and analysis cuts: 9.8 % (Sec. 4.3.5).
[20] The uncertainty of the vertex cut factor is calculated from $f^{vtx}(\pm30\text{cm}) = 0.499$, $f^{vtx}(\pm40\text{cm}) = 0.620$ and the uncertainty of 7.2 % for f^{vtx} (see Sec. 4.3.1).

Note that the theoretical uncertainties from NLO pQCD calculations are ignored here. It might affect to the p_T dependence of N^{hadron}, but is small compared to to other sources of systematic uncertainty (e.g. uncertainty of $P_{acc} + P_{\pi^0}$).

Estimated Background

The background is estimated following Eq. 4.6. Figure 4.20 displays the result of background estimation (Left: positive charge, Righ: negative charge). As the figure shows, the dominant background around 30 to 40 GeV/c is from components of accidental track match plus π^0 conversion $(0.8 \times (P_{acc} + P_{\pi^0}) \times N^{EMCal}$: Red distribution in the figure).
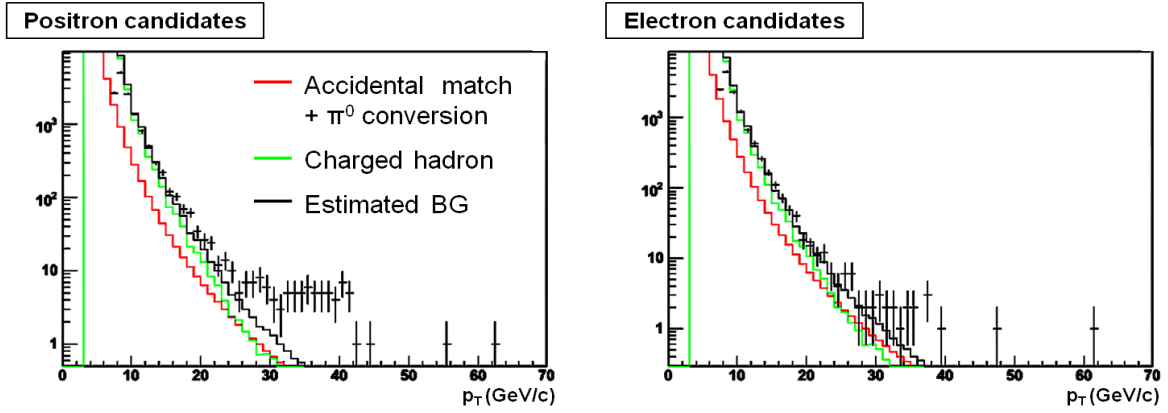

Figure 4.20: Background estimation. (Left: positive charge, Right: negative charge) The Red distribution is components of accidental track match plus π^0 conversion $(0.8 \times (P_{acc} + P_{\pi^0}) \times N^{EMCal})$ and the Green is charged hadron $((scale) \times N^{hadron})$.

Contribution from Heavy Flavor Decays

The contribution of $e^{\pm}$s from heavy flavor decays is ignored in the above discussion. Since the $\pi^{\pm}$ spectra folded by the EMCal response (N^{hadron}) is used to normalize the low p_T region, only the difference in the shape between heavy flavor contribution and $\pi^{\pm}$ contribution is the source of systematics. The FONLL (Fixed-Order plus Next-to-Leading-Log) calculation [21] is used to evaluate the difference as PHENIX single electron measurement at $\sqrt{s} = 200$ GeV agrees with the calculation within uncertainty [119].

Figure 4.21 shows the background estimation including heavy flavor contribution (thick Black distribution). The Red distribution is the components of accidental track match plus π^0 conversion ($0.80 \times (P_{acc} + P_{\pi^0}) \times N^{EMCal}$), the Black shows charged hadron ($(scale) \times N^{hadron}$), and the Blue displays heavy flavor contribution in the figure. It can be noticed that the FONLL spectra shape is similar to the shape of $\pi^{\pm}$ and the contribution of heavy flavor is about 10 % of the whole EMCal clusters with track (Black points with error bar). The difference between two procedures of with/without heavy flavor component is very small, as the process of normalization of the low p_T region with charged hadron shape compensates the difference.

Figure 4.22 shows the difference of two total background spectra (with/without heavy flavor) divided by the one without heavy flavor. The difference is less than 1 % at $p_T > 10$ GeV/c, and it can be safely stated that the background estimation described above covers heavy flavor contribution naturally.
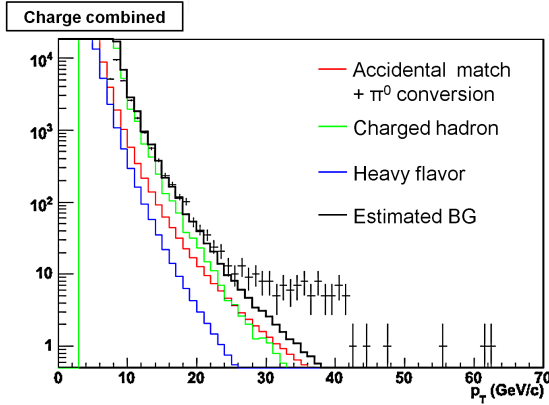
Figure 4.21: Background estimation with heavy flavor component (thick Black distribution). The Red distribution is components of accidental track match + π^0 conversion, the Black shows charged hadron, and the Blue displays heavy flavor contribution (FONLL calculation).
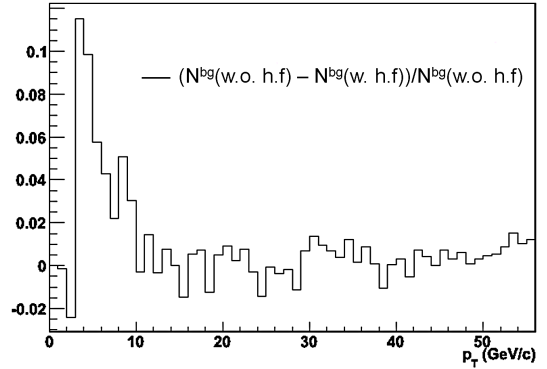
Figure 4.22: The fractional difference of background estimation between with and without heavy flavor contribution. ("N^{bg}(w.o. h.f.)" denotes the estimated background without heavy flavor, and "N^{bg}(w. h.f.)" denotes it with heavy flavor component) The difference is very small.

---

[21] The theory based on pQCD calculation about heavy flavor production [115, 116, 117, 118].

Uncertainty of Background Spectrum (Shape Uncertainty)

It is better to confirm the background spectrum using a different approach. The problem is that it is hard to get a pure background sample at PHENIX. The best spectrum representing the QCD background is obtained by requiring anti-isolation cut in negative particle samples. The isolation cut is explained in Sec. 4.4.1, and anti-isolation cut selects events which is rejected by the isolation cut.

The data points with statistical error bars in Fig. 4.23 show the sample of the QCD background obtained by anti-isolation cut in negative charge events. The Red (Blue) histogram in the figure is the estimated background for positive (negative) charge particles.

The spectrum of the obtained QCD background (distribution of negative charge with anti-isolation cut) is compared with the distribution of estimated background. Figure 4.24 displays the ratio of the QCD background over the estimated background for positive charge. The shape uncertainty is determined by the figure as an angle range which is extracted by fitting with linear function with setting the average value at $12-20$ GeV/c (or $16-20$ GeV/c) as an anchor point. The extracted range (it is 0.0054 ± 0.0078 in the figure) is consistent to 0, and ± 1 σ range is used in the background band calculation.

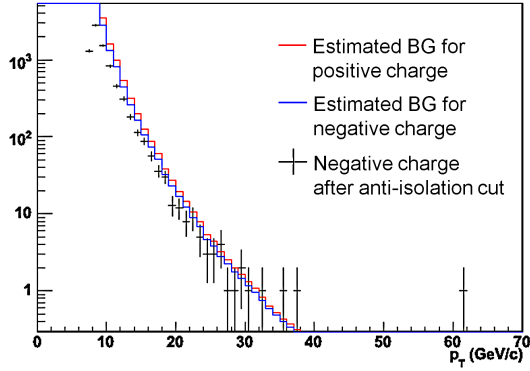Figure 4.23: The p_T distribution of negative particle with applying ant-isolation cut (points with error bar) which represents QCD background spectrum. he Red (Blue) histogram is the estimated background for positive (negative) charge particles.
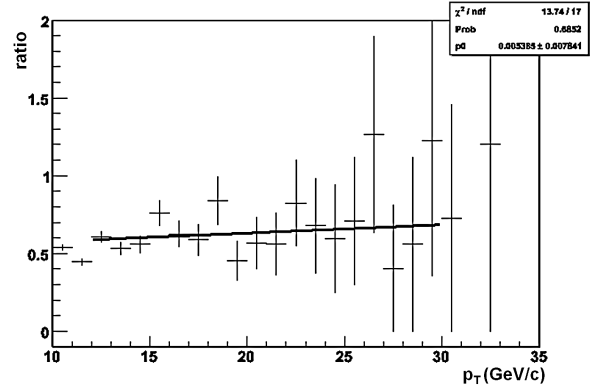
Figure 4.24: the ratio of the QCD background over the estimated background for positive charge. The shape uncertainty is determined by this figure.

Summary of Background Estimation

Considering the uncertainty of $P_{acc} + P_{\pi^0}$ (default, min, max), the normalization range of charged hadron ($12 < p_T < 20$, $16 < p_T < 20$ GeV/c) and the shape uncertainty (default, ± 1 σ), 18 ($= 3 \times 2 \times 3$) background distributions are made in total, and the background band is evaluated by taking the maximum and minimum value at each p_T bin among 18 distributions.

Figure 4.25 displays the evaluated background band (Magenta band) with the whole EMCal clusters with track (Black distribution) (Left: positive, Right: negative charge). The background band at the region of $p_T > 30$ GeV/c is dominated by the shape uncertainty.

The number of background in the range of $30 < p_T < 50$ GeV/c is summarized in Table 4.4, and this number is used in $d\sigma/dy$ calculation.
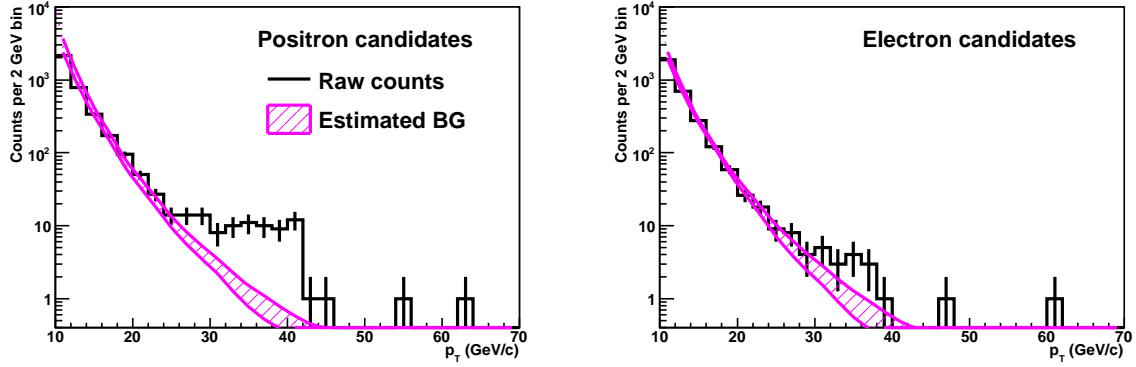
Figure 4.25: The evaluated background band (Magenta) with the whole EMCal clusters with track (Black distribution) (Left: positive, Right: negative charge).

charge	total number	background (min, max)
$+$	62	7.0 (5.7, 11.0)
$-$	17	6.4 (4.1, 9.1)
$\pm$	79	13.3 (9.9, 19.9)

Table 4.4: The number of events and background in the range of $30 < p_T < 50$ GeV/c.

4.3.4 Trigger Efficiency

The threshold and efficiency of ERT4x4b trigger is checked using number of π^0 from MB (BBCLL1) triggered events. Red points in Fig. 4.26 show the turn-on curves of ERT4x4b as a function of π^0 p_T for both PbSc and PbGl. Since statistics is not enough to cover high p_T region in MB triggered sample, the trigger threshold is also checked using ERT2x2 triggered events in the following manner:

$$\begin{cases} \varepsilon^{\mathrm{ERT4x4b}} = N_{\pi^0}^{\mathrm{ERT4x4b}}/N_{\pi^0}^{\mathrm{ERT2x2}} \times \varepsilon^{\mathrm{ERT2x2}}|_{plateau}, \\ \varepsilon^{\mathrm{ERT2x2}} = N_{\pi^0}^{\mathrm{ERT2x2}}/N_{\pi^0}^{MB}, \end{cases} \tag{4.7}$$

where $\varepsilon^{\mathrm{ERT4x4b}}$ ($\varepsilon^{\mathrm{ERT2x2}}$) represents the efficiency of ERT4x4b (ERT2x2) trigger. The plateau of $\varepsilon^{\mathrm{ERT2x2}}$ ($\varepsilon^{\mathrm{ERT2x2}}|_{plateau}$) can be evaluated in MB triggered sample because the threshold of ERT2x2 is lower than ERT4x4b (see Sec. 2.2.5), and statistics of ERT2x2 triggered data is larger than ERT4x4b triggered data. Blue points in Fig. 4.26 displays the turn-on curves of ERT4x4b calculated in this manner. Note that the efficiency value at plateau may exceed 1.0 because of the indirect efficiency calculation. The turn-on curves reach plateau level at 12 GeV and the plateau values are 0.98 ± 0.03 for PbSc and 1.02 ± 0.04 for PbGl. These values are consistent with the expected values with taking masked FEMs into account (see Sec. 4.3.2) and it means the trigger efficiency of each FEMs is 100 % at $p_T > 12$ GeV/c region.
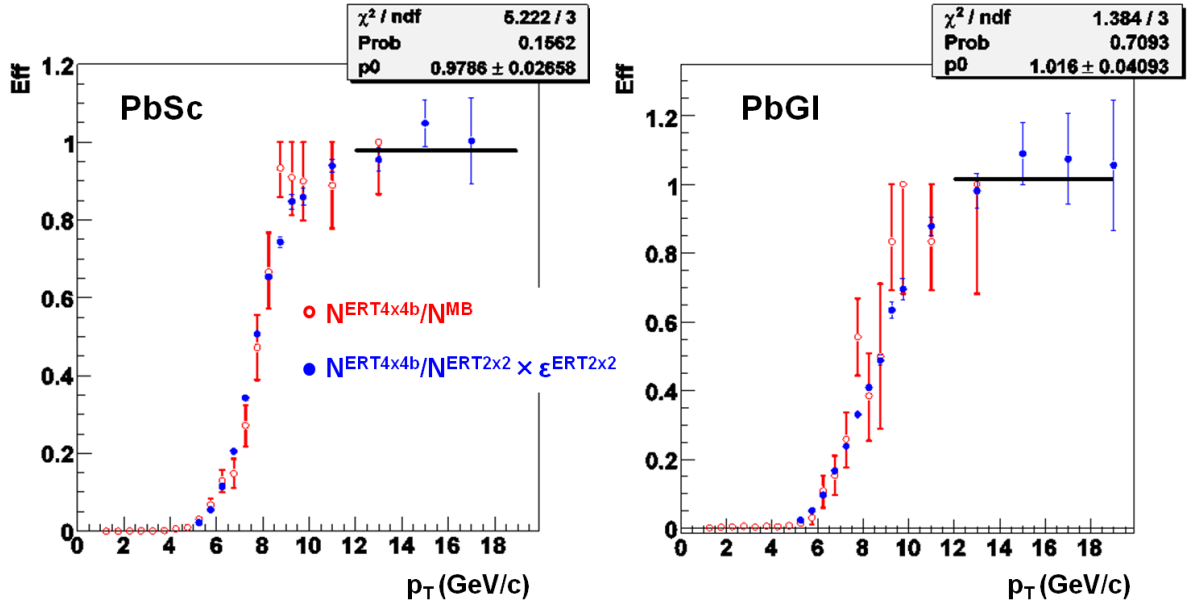

Figure 4.26: ERT4x4b turn on curve (Left: PbSc, Right: PbGl). The red data points are from MB. The blue one is based on clusters fired ERT2x2 multiplied by ERT2x2 efficiency.

4.3.5 Efficiency of Geometry and Analysis Cuts

The efficiency of geometry and the analysis cuts (ε_{reco}) is evaluated using single particle MC simulation. During Run 9 period, run-by-run fluctuation caused by the pile up and the acceptance change of the DC/PC1 is quite large (see Appendix D for tracking performance during Run 9). In order to include this fluctuation in the simulation, the ϕ-dependent efficiency of DC/PC1 is derived.

DC/PC1 Efficiency

The DC/PC1 efficiency including run dependence is extracted comparing the real data with single particle MC. Since the DC and PC dead map input into the simulation is from run 276870, this run is taken as the fiducial run. The procedure is:

Step 1 Compare ϕ distribution of the fiducial run with the simulation to determine the scale factor. (Fig. 4.27)

Step 2 Make ϕ distribution accumulating whole available runs from Run 9 (276 runs). In this procedure, run-by-run rate correction was applied and the ϕ distributions of each run are averaged with a weight of luminosity.

Step 3 Using the scale factor obtained at Step 1, the accumulated ϕ distribution obtained in Step 2 is normalized and compared with the simulation. (Fig. 4.28) Take a ratio for each bin and assigned as an efficiency of that particular ϕ range.

The detail of each steps are described below.

Step 1: The ϕ distributions are generated from MB triggered sample to compare them with the simulation. Applied cut to make histograms are:

- Vertex cut: $|z_{vertex}| < 30$ cm [22]

- Require hits on X1 and X2 plane of the DC, and hit on the PC1

- $p_T > 2.0$ GeV/c cut for real data ($p_T = 10, 20, 30, 40, 50$ GeV/c for simulation)

- Dead map of DC/PC1 in the simulation is taken from run 276870 (fiducial run [23])

- Normalization of hists: by number of MB (for real data) or number of input (for simulation)

Because of a few statistics in real data, it is impossible to set exactly the same p_T cut between the real and the simulation data. Actually, there is a p_T dependence in acceptance value for $p_T < 2$ GeV/c. However, it is constant above $p_T > 2.0$ GeV/c region [119] and the difference of the p_T cut applied here does not affect to the acceptance calculation. The cuts are kept as simple as possible to be independent

---

[22] z_{vertex} used here is reconstructed by the BBC. As described in Sec. 4.3.1, it may be mis-reconstructed, but it does not affect to the evaluated value of ε_{reco} here.

[23] The fiducial run is randomly chosen from runs in which rather larger area of DC/PC1 were active.

from the EMCal effect, and any electron cut that might be strongly coupled to EMCal information is not applied. Overall ε_{reco} value including EMCal acceptance is evaluated after extracting DC/PC1 efficiency and that is described later.

The scale factor to match the scale of the data and the simulation is calculated using the top histogram in Fig. 4.27 (North + South side of the DC/PC1). The same scale factor is used in the middle (North side of the DC/PC1) and bottom (South side of the DC/PC1) histograms of Fig. 4.27 and agreement between real data and simulation looks good. The systematic uncertainty of the scale factor is estimated from the ratio of the real data and simulation in the middle and bottom hists of the figure.
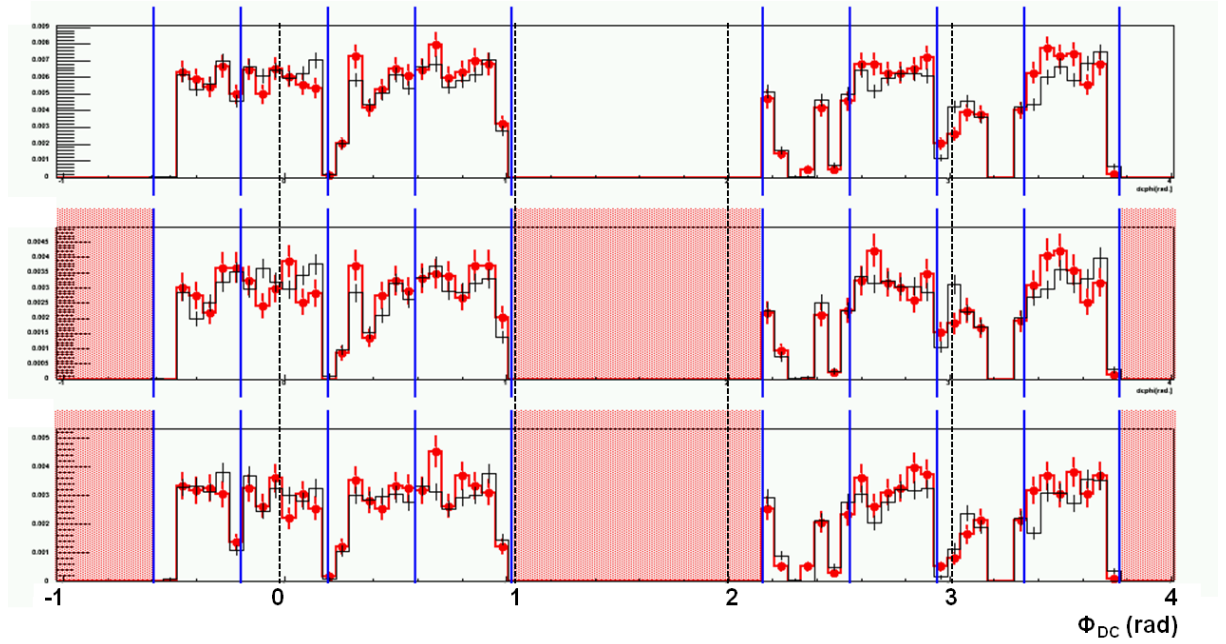
Figure 4.27: Comparison of the ϕ distribution of the fiducial run (Red hist) to the simulation (Black hist). The red shaded areas indicate the out of acceptance of PHENIX. Top: North+South side of the DC/PC1 (the scale factor to match the scale of the data and the simulation is calculated from this figure), Middle: North side, Bottom: South side, Blue lines indicate the rough boarder of EMCal Sectors.

Step 2: In order to accumulate ϕ histograms of whole runs in Run 9, the rate correction and luminosity weighting is necessary.

The run-by-run rate dependence should be corrected when averaging ϕ histograms from different runs. The rate dependence can be explained by the pile up effect of the DC which is studied in Appendix D. The correction factor is calculated based on that study [24].

After correcting the run-by-run rate dependence, ϕ histograms of whole runs are summed up with luminosity weighting.

---

[24]The gate width of the DC (denoted as "NCLK" in the Appendix D) which causes the pile up is fixed at the value of 3.1.

Step 3: Using the scale factor obtained at Step 1, the accumulated histogram is normalized to compare to the simulation. Figure 4.28 shows the comparison of accumulated histogram to the simulation. The ratio of the accumulated histogram and the simulation is assigned as the efficiency of that particular ϕ range. The obtained ϕ-dependent efficiency is included when calculating the efficiency of the geometry and analysis cuts (ε_{reco}) using single particle MC simulation. Note that the efficiency value may exceed 1.0, however the value is included in the MC simulation without modification because the purpose of this ϕ depending efficiency is to reproduce the ϕ distribution of the real data in the MC simulation.
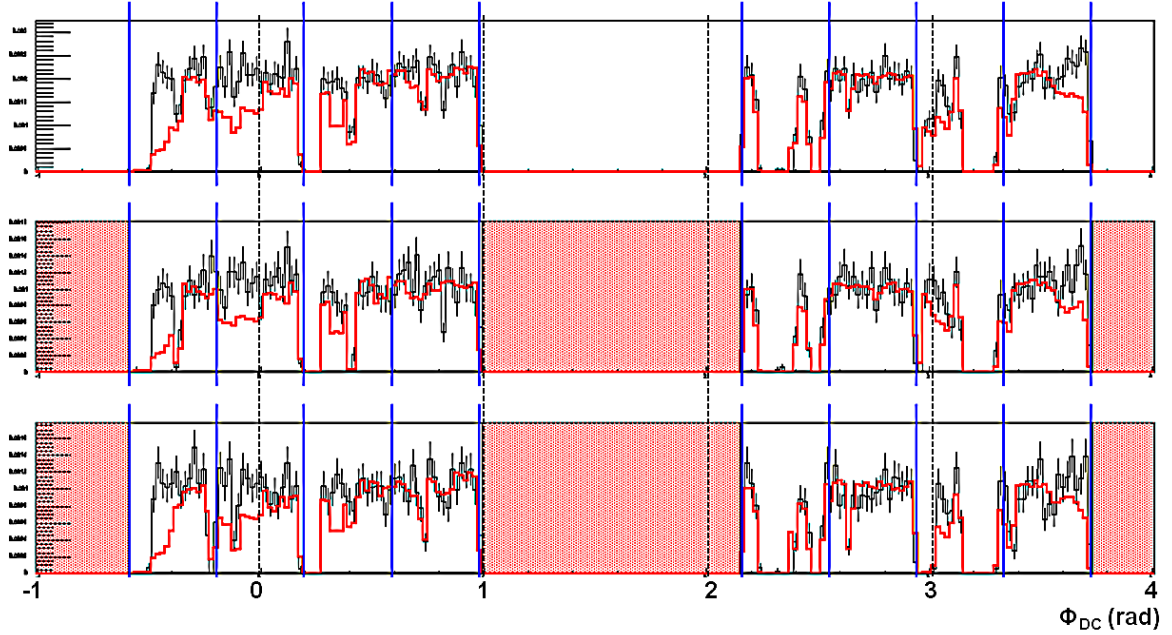
Figure 4.28: Comparison of the accumulated ϕ distribution (Red hist) to the simulation (Black hist). The Black histogram is exactly same as it in Fig. 4.27 except for the number of bins. The accumulated hist is scaled with the factor obtained in Step 1. The red shaded areas indicate the out of acceptance of PHENIX. Top: North+South side of the DC/PC1, Middle: North side, Bottom: South sied, Blue lines indicate the rough boarder of EMCal Sectors.

Efficiency Calculation

The efficiency of geometry and the analysis cuts (ε_{reco}) has been calculated using single electron/positron MC. 50K events ($p_T = 10,\ 20,\ 30,\ 40,\ 50$ GeV/c, 10K events for each p_T, $|z_{vertex}| < 45$ cm) for each particle were generated and thrown to PISA, which is the GEANT based MC simulation including the response of whole PHENIX detector. Number of events in output of PISA was counted to calculate the efficiency. In this process, all cuts, which are described in Sec. 4.3.2, except for the anode wire region cut are applied and ϕ-dependent DC/PC1 efficiency evaluated above was also taken into account.

The bias from the chosen fiducial run at Step 1 of ϕ-dependent efficiency evaluation is estimated by several MC simulation studies including different fiducial runs. The efficiency of geometry and the analysis cuts (ε_{reco}) are calculated for each simulation.

There are three types of systematic uncertainty in this calculation. First one is the uncertainty of the scale factor to match the simulation and the real data [25]. Second one is the uncertainty of the rate correction [26]. This uncertainty is evalated by comparing the efficiency value of "with" and "without" the rate correction The difference can be taken as the maximum uncertainty since the gate width of the DC is certainly more than 1 beam clock and the rate dependence should be corrected. The last one is the variation of ε_{reco} among different MC data set [27].

Combining all data, $\varepsilon_{reco} = 0.152$, and the uncertainty from the scale factor is 7.0 %. The difference of "with" and "without" rate correction is evaluated as 6.6 %. The standard deviation of the efficiency values in different MC data set is only 1.7 %, and therefore it can be stated that there is no charge or p_T dependence in ε_{reco}. As a result, 9.8 % systematic uncertainty is assigned for the efficiency value by adding them in quadratic.

Since the active EMCal fraction is ~ 81 % (see Sec. 4.3.2) and the maximum acceptance value is 0.35 in PHENIX, it means the efficiency of tracking part is ~ 54 % ($= 0.152/0.35/0.81$) at Run 9. Considering the anode wire region cut, this number should be multiplied by a factor of 0.85 since the cut masks 15 % of the acceptance.

4.3.6 Energy Smearing

The energy smearing effect (ε_{smear}) should be taken into account due to the limited energy resolution of EMCal. It is evaluated with NLO based event generator (CHE: see Sec. 1.3) including the energy resolution of EMCal, which is extracted from the FastMC [28].

The obtained cross section values ($d\sigma/dy$) in $30 < p_T < 50$ GeV/c range for with/without smearing effect are compared to evaluate the energy smearing effect ($1/\varepsilon_{smear}$), and the obtained value is 1.01.

---

[25] Introduced at Step 1 of the evaluation of ϕ-dependent DC/PC1 efficiency.
[26] Applied at Step 2 of the evaluation of ϕ-dependent DC/PC1 efficiency.
[27] 2(positron/electron) $\times$ 5(different p_T) $\times$ 5(different fiducial runs) MC simulation are executed in total
[28] used EMCal resolution is: $\Delta E/E = 0.081/\sqrt{E} \oplus 0.05$, see Sec 4.2.2

4.3.7 Cross Section Calculation

The calculation of $d\sigma/dy$ at $30 < p_T < 50$ GeV/c region is represented in this subsection. The relationship of $d\sigma/dy$ to the experimental observables is:

$$\frac{d\sigma}{dy} = \int dp_T \frac{d^2\sigma}{dp_T dy} = \frac{1}{\mathcal{L}} \cdot \frac{1}{\varepsilon_{trig} \cdot \cdot \varepsilon_{reco} \cdot \varepsilon_{smear}} \cdot \frac{1}{\Delta y} \cdot \sum_{30 < p_T < 50} \frac{(N^{meas} - N^{bg})}{\Delta p_T}. \tag{4.8}$$

Each factor is evaluated in previous subsections, and summarized in Table 4.5 with its uncertainty.

factor	value	uncertainty	comment and Section
$\mathcal{L}$	8.56 pb^{-1}	13 %	Sec. 4.3.1
N^{meas}			Summarized in Table 4.6, Sec. 4.3.2
N^{bg}			Summarized in Table 4.6, Sec. 4.3.3
ε_{trig}	100 %		Sec. 4.3.4
ε_{reco}	0.152×0.85	9.8 %	Ideal value is 0.35, Sec. 4.3.5
$1/\varepsilon_{smear}$	1.01		Sec. 4.3.6
Δy	1.00		PHENIX acceptance is included in ε_{reco}

Table 4.5: The summary of each factor in Eq. 4.8.

The uncertainty of energy smearing ($1/\varepsilon_{smear}$) is ignored here, because it is estimated based on the NLO calculation and the theoretical uncertainty is small compared to other sources of systematic uncertainty (e.g. N^{bg}). The uncertainty of $\mathcal{L}$ and ε_{reco} is the scale uncertainties, and its value is 16 % in total by quadratic sum. The uncertainty of N^{bg} affects to the absolute value of the cross section.

Other uncertainties which might affect to the absolute value of the cross section are the uncertainty of absolute energy scale and the charge contamination caused by the DC resolution. The uncertainty of absolute energy scale is 2.9 % (see Sec. 4.2.2), and this is ignored in this analysis as it is small compared to the uncertainty of background estimation. The probability of charge mis-identification is 1.1 % (see Sec. 4.2.5). In term of count, this probability is corresponding to 0.19 ($= 17 \times 0.011$) for positive and 0.68 ($= 62 \times 0.018$) for negative charged particle. As the contamination from charge mis-identification is small compared to the uncertainty of background estimation, it is also ignored in this analysis.

Background counts are subtracted from number of measured events. Figure 4.29 shows dN/dp_T after subtracting the background (Left: positive, Right: negative charge). In this figure, the NLO calculation (CHE) with energy smearing is overdrawn (Red distribution). The yellow bands in the figures show the range of the different background assumptions and the horizontal bars indicate the default data points. The larger bands close to the edge of normalization ($p_T \sim 20$ GeV/c) is mainly caused by the difference of the normalization range of charged hadron ($12 < p_T < 20$ or $16 < p_T < 20$ GeV/c). The statistical uncertainties on each point show 68 %CL calculated with TRolke function in ROOT [29]. When the value

---
[29]This function computes confidence intervals for the rate of a Poisson process in the presence of uncertain background and efficiency [120].

is small, a difference from the simple estimation with Poisson statistics ($= \sqrt{S+N}$) can be noticed.

The number of counts in the signal region are summarized in Table 4.6. The systematic uncertainties from different background estimation are also listed in the table. Note that these numbers are not only including W signal but also including Z/γ signal.

The cross section ($d\sigma/dy$) at $30 < p_T < 50$ GeV/c is then calculated. The numbers in Table 4.6 are multiplied/divided by the factor listed in Table 4.5. The result is shown in Table 4.7 which also includes the systematic uncertainty from the scale factor (16 %). For example, the cross section of positive charge is $50.2 = (62 - 7.0)/8.56/0.152/0.85 \times 1.01)$. These values are compared to theory calculation in Sec. 5.1.
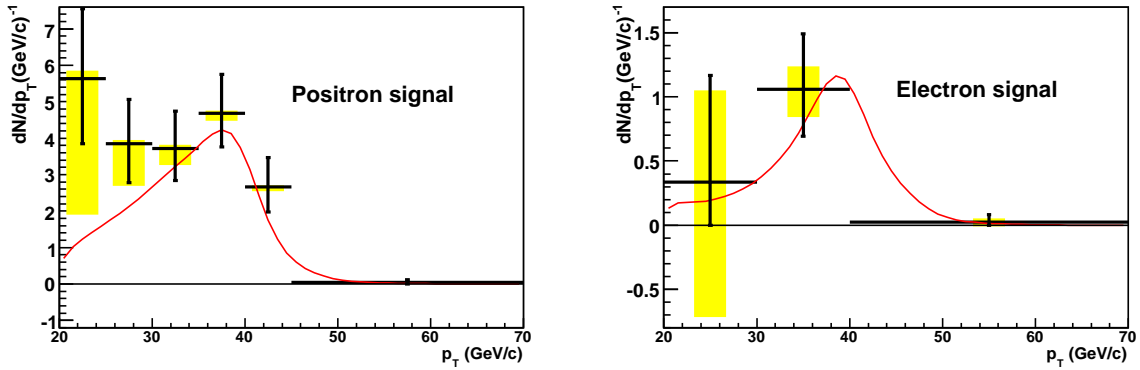
Figure 4.29: dN/dp_T of W/Z decay electrons after background subtraction (Left: positive, Right: negative). The red distribution represents the NLO calculation (CHE) of $W + Z$ with energy smearing.

charge	total number	background (min, max)	signal counts (W and Z)
$+$	62	7.0 (5.7, 11.0)	55.0 ± 7.9(stat.) $^{+1.3}_{-4.0}$(sys.)
$-$	17	6.4 (4.1, 9.1)	10.6 ± 4.1(stat.) $^{+2.3}_{-2.7}$(sys.)
$\pm$	79	13.3 (9.9, 19.9)	65.7 ± 8.9(stat.) $^{+3.4}_{-6.6}$(sys.)

Table 4.6: The number of events in the range of $30 < p_T < 50$ GeV/c.

charge	$d\sigma/dy$ (pb) at $30 < p_T < 50$ GeV/c
$+$	50.2 ± 7.2(stat.) $^{+1.2}_{-3.6}$(sys.) ± 8.0 (normalization)
$-$	9.7 ± 3.7(stat.) $^{+2.1}_{-2.5}$(sys.) ± 1.6 (normalization)
$\pm$	60.0 ± 8.1(stat.) $^{+3.1}_{-6.0}$(sys.) ± 9.6 (normalization)

Table 4.7: $d\sigma/dy$ of electrons form W and Z decay at $30 < p_T^e < 50$ GeV/c.

4.4 Spin Asymmetry

The single spin asymmetry (A_L) is calculated by following formula:

$$\varepsilon_L = \frac{N_+ - N_- \cdot R}{N_+ + N_- \cdot R}, \tag{4.9}$$

$$A_L = \frac{1}{P} \cdot \varepsilon_L, \tag{4.10}$$

where ε_L is called single "raw" asymmetry, N is the electron yield from W and Z decay, R is the relative luminosity and P is the beam polarization. R is defined using luminosity (L) as $R = L_+/L_-$. The sign of $+ (-)$ put on N or L represents the helicity states of proton beam. As RHIC provides 4 helicity states of proton beams ((P_B P_Y) = (++), (+−), (−+), (−−): B (Y) denotes Blue (Yellow) beam), one beam polarization is summed up relative to another beam polarization when calculating N_+, N_-, L_+ and L_- [30]. Since two (Blue and Yellow) polarized beams are available at RHIC, A_L can be measured for both beam polarizations, and a particular observed event can be used in both A_L measurements. However, A_L is not calculated with this manner in this analysis. The uncertainty should be assigned with Poisson statistics due to its small statistics and it is difficult when using Eq. 4.9 and 4.10.

In order to compensate the small statistics, a technique called "spin fit" is engaged in this analysis. This technique is based on the following equations:

$$\begin{cases} \sigma_{++} = N_{++}/L_{++} = (1 + A_L P_B + A_L P_Y + A_{LL} P_B P_Y) \cdot \sigma, \\ \sigma_{+-} = N_{+-}/L_{+-} = (1 + A_L P_B - A_L P_Y - A_{LL} P_B P_Y) \cdot \sigma, \\ \sigma_{-+} = N_{-+}/L_{-+} = (1 - A_L P_B + A_L P_Y - A_{LL} P_B P_Y) \cdot \sigma, \\ \sigma_{--} = N_{--}/L_{--} = (1 - A_L P_B - A_L P_Y + A_{LL} P_B P_Y) \cdot \sigma, \end{cases} \tag{4.11}$$

where σ represents the cross section of electron from W and Z decay without efficiency correction and A_{LL} is the double spin asymmetry. The values of σ, A_L and A_{LL} is obtained by fitting measured N and L with Eq. 4.11. Substituting A_L to ε_L with the relation of $A_L P = \varepsilon_L$ (P: averaged polarization, $P = (P_B + P_Y)/2$), Eq. 4.11 can be written as:

$$\begin{cases} \sigma_{++} = N_{++}/L_{++} = (1 + 2\varepsilon_L + \varepsilon_{LL}) \cdot \sigma, \\ \sigma_{+-} = N_{+-}/L_{+-} = (1 + (P_B - P_Y)/P \cdot \varepsilon_L - \varepsilon_{LL}) \cdot \sigma, \\ \sigma_{-+} = N_{-+}/L_{-+} = (1 + (-P_B + P_Y)/P \cdot \varepsilon_L - \varepsilon_{LL}) \cdot \sigma, \\ \sigma_{--} = N_{--}/L_{--} = (1 - 2\varepsilon_L + \varepsilon_{LL}) \cdot \sigma. \end{cases} \tag{4.12}$$

Using this formula, values of σ, ε_L and $\varepsilon_{LL} = A_{LL} P_B P_Y$ (double "raw" asymmetry) is obtained. Contrast to the separated measurement of A_L for Blue/Yellow beam polarizations, this technique naturally uses all available statistics. In addition, the maximum likelihood method can be used in the fitting process and the uncertainty of small statistics can be treated properly.

The procedure of A_L calculation is fully described in this section [31]. First of all, a cut called isolation cut is explained in Sec. 4.4.1. Since the contribution of background to the A_L value is a serious problem, the fraction of background should be suppressed as lower as possible. Therefore, the isolation cut is employed to improve the signal purity in the A_L measurement. This cut is not used in the cross section

---

[30] For example, $N_+ = N_{++} + N_{+-}$, $N_- = N_{-+} + N_{-+}$ etc.

[31] The study of contamination from a residual transverse component of the beam polarization is described in Appendix E.

measurement as we can reliably subtract the background component with proper background estimation in the cross section calculation. Secondly, the calculation of single raw asymmetry (ε_L) with spin fit technique is presented in Sec. 4.4.2. Finally, A_L value is evaluated in Sec. 4.4.3. The treatment of systematic uncertainty from the dilution factor of hadron background and beam polarization is also explained in this subsection.

4.4.1 Isolation Cut

As the signature of $e^\pm$s from W or Z decays is that they are observed as isolated events, an electron isolation cut, which requires no jet activity in the vicinity of the electron, is applied to improve the signal purity in the spin asymmetry analysis in addition to various cuts which are applied in the cross section measurement (Sec. 4.3.2).

The reason why the isolation cut is not applied in the cross section measurement is originated in the difficulty of its efficiency estimation. When estimating the efficiency of the isolation cut, a complete run-by-run trace of the EMCal and DC acceptance change must be included in the simulation, but it is difficult for Run 9 analysis due to the frequent acceptance change of the DC (see Appendix D). However, the background contribution to the cross section can be reliably subtracted as long as we properly estimate the background. By these reasons, the isolation cut is not employed in the cross section measurement.

On the other hand, the contribution of background to the A_L value is a serious problem because it is hard to estimate [32] and leaves quite large uncertainty in the A_L measurement. However, there is a feature in the A_L measurement that any cut can be applied as long as the cut is spin independent. This is because the cut efficiency does not affect to the spin asymmetry (A_L or A_{LL}) values in Eq. 4.11 and 4.12 though it does affect to the σ value. Therefore, the isolation cut, which requires the sum of EMCal cluster energy and track momentum in the cone radius of 0.5 rad from the electron candidate to be less than 2 GeV (Fig. 4.30), is applied in the spin asymmetry measurement to suppress the background fraction as low as possible. The detail of the selection of EMCal cluster energy and track momentum which is used in the summation of cone energy is summarized in Table 4.8.

In addition to the isolation cut, the zero degree track cut ($|\alpha| > 1$ mrad) is also applied to reject $e^\pm$ candidates which track angle is parallel to the wires of DC, so that the charge contamination can be negligible. It corresponds to 3.2 σ or 0.07 % of the opposite charge sample [33].

Figure 4.31 displays both spectra with (Red) and without (Black) the isolation cut (Left: positive, Right: negative). The Magenta bands is the QCD background estimated in Sec. 4.3.3 scaled by a constant factor which is evaluated by taking a ratio of the with/without isolation cut spectrum at $12 < p_T < 20$ GeV/c region (0.224 for positive, 0.258 for negative). Numbers of signal and background counts in $30 < p_T < 50$ GeV/c region are summarized in Table 4.9.

---

[32] The expected A_L value of the hadron background is 0, but there may be a contribution from hadronic decays of W and Z bosons and they are difficult to estimate accurately.

[33] As the resolution of the DC is 1.1 mrad and α is about 2.5 mrad for 40 GeV/c track (see Sec. 4.2.5), $|\alpha| > 1$ mrad cut corresponding to $(2.5 + 1.0)/1.1 = 3.2$ σ away from the opposite charge, and this reduces the probability of charge contamination.
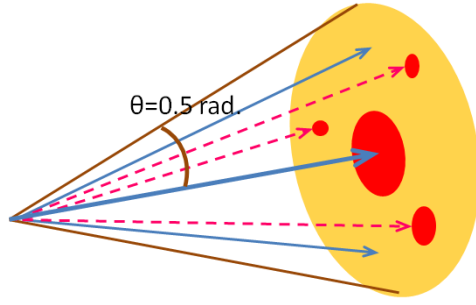
Figure 4.30: Schematical representation of the isolation cut. After calculating a summation of EMCal cluster energy for γs (red circles) and track momentum for charged particles (blue lines) which are observed inside a cone radius of 0.5 rad from a high p_T electron event, require the summation is less than 2 GeV in order to select isolated events.

EMCal cluster	• minimum energy cut: (cluster energy) > 0.15 GeV • charge veto: not requiring track match
DC/PC1 track	• require hits on X1 and X2 plane of the DC and hit on PC1 • minimum momentum cut: (momentum) > 0.2 GeV/c

Table 4.8: The selection of EMCal cluster and DC/PC1 track for the summation of cone energy.
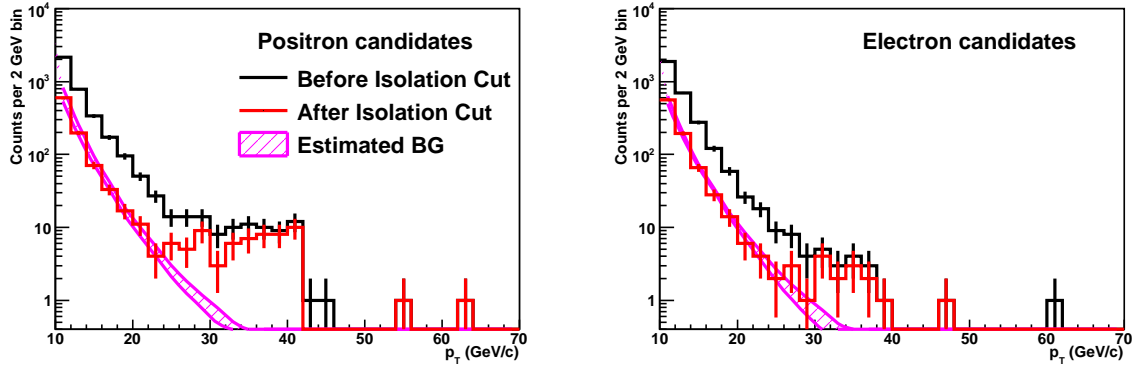
Figure 4.31: The p_T spectra with (Red) and without (Black) the isolation cut (Left: positive, Right: negative). The Magenta band shows the estimated background.

charge	total	estimated background (min, max)	signal (W and Z)
+ (without isolation cut)	62	7.0 (5.7, 11.0)	$55.0 \pm 7.9(\text{stat.})^{+1.3}_{-4.0}(\text{sys.})$
(with isolation cut)	42	1.6 (1.3, 2.5)	$40.4 \pm 6.5(\text{stat.})^{+0.3}_{-0.9}(\text{sys.})$
− (without isolation cut)	17	6.4 (4.1, 9.1)	$10.6 \pm 4.1(\text{stat.})^{+2.3}_{-2.7}(\text{sys.})$
(with isolation cut)	13	1.7 (1.1, 2.4)	$11.4 \pm 3.6(\text{stat.})^{+0.6}_{-0.7}(\text{sys.})$

Table 4.9: Number of events in the signal region ($30 < p_T < 50$ GeV/c)

Check of the Isolation Cut

The signal fraction of with/without the isolation cut is expected to be approximately same for positive and negative. Equation 4.13 shows the definition of the fraction (S denotes the number of signal), where N represents the number of measured count, N^{iso} and x are the number of count which pass the isolation cut, $N^{\overline{iso}}$ and y represent the number of count which is rejected by the isolation cut [34], B and z is the number of estimated background and a is the ratio of with/without isolation cut at $12 < p_T < 20$ GeV/c region (ratio for background: 0.224 for positive, 0.258 for negative). Here, x, y and z are independent values. The uncertainty of this fraction is derived from Eq. 4.14.

$$r = \frac{S^{iso}}{S} = \frac{N^{iso} - B^{iso}}{N - B} = \frac{N^{iso} - aB}{(N^{iso} + N^{\overline{iso}}) - B} = \frac{x - az}{(x + y) - z}, \qquad (4.13)$$

$$\begin{aligned} \Delta r &= \sqrt{(\frac{\partial r}{\partial x}\Delta x)^2 + (\frac{\partial r}{\partial y}\Delta y)^2 + (\frac{\partial r}{\partial z}\Delta z)^2} \\ &= r\sqrt{((\frac{1}{S^{iso}} - \frac{1}{S})\Delta x)^2 + ((-\frac{1}{S})\Delta y)^2 + ((-\frac{a}{S^{iso}} + \frac{1}{S})\Delta z)^2}. \end{aligned} \qquad (4.14)$$

Each term in the equations is shown in Table 4.10 [35], and the fraction is calculated as $r_+ = 0.73 \pm 0.08$, $r_- = 1.08 \pm 0.29$ by substituting these values. They are consistent within uncertainties.

The p_T dependence of the isolation cut is studied based on PYTHIA MC. While there is no p_T dependence for $e^{\pm}$s from W or Z decays, a slight p_T dependence is observed for hadron backgrounds [36]. The study also shows the p_T dependence is absorbed in the estimated background band and does not affect to the result.

charge	S	S^{iso}	a	Δx	Δy	Δz
$+$	55.0	40.4	0.224	$\sqrt{42} = 6.48$	$\sqrt{62 - 42} = 4.47$	4.0
$-$	10.6	11.4	0.258	$\sqrt{13} = 3.61$	$\sqrt{17 - 13} = 2.00$	2.7

Table 4.10: Components to calculate isolation cut ratio.

---

[34] The relation is $N = N^{iso} + N^{\overline{iso}} = x + y$

[35] The uncertainty of the estimated background (Δz) is assigned as 4.0 for positive and 2.7 for negative, so that they can fully cover the background bands.

[36] The rejection for hadron backgrounds becomes larger in higher p_T region ($p_T >\sim 30$ GeV/c) than lower p_T region.

4.4.2 Calculation of Spin Asymmetry with Spin Fit Technique

Luminosity of Four Spin States

Number of BBCLL1 (MB trigger for the PHENIX) counts are sorted into four spin states, and used as luminosity (L_{++}, L_{+-}, L_{-+} and L_{--}). Although these numbers are not converted to the luminosity dimension with some correction factor (e.g. σ_{BBC}, rate correction etc.), it only affects to the scale factor (i.e. σ in Eq. 4.11 and 4.12) and does not matter for spin asymmetry calculation.

Spin Fit with Maximum Likelihood Method

Number of events with applying the isolation cut (Red histograms in Fig 4.31) in the signal region ($30 < p_T < 50$ GeV/c) are sorted into four spin states. As the beam polarization [37] and luminosity of four spin states have been already known, there remains 3 parameters ($\sigma, \varepsilon_L, \varepsilon_{LL}$) in Eq. 4.12. These values can be evaluated by fitting. However, the fit must be carried out with likelihood method in this case due to the small statistics.

The likelihood function can be written as:

$$L = \prod_{\text{4 spin states}} f(N_{data}; \mu_{expected}) = f(N_{++}; \mu_{++}) \cdot f(N_{+-}; \mu_{+-}) \cdot f(N_{-+}; \mu_{-+}) \cdot f(N_{--}; \mu_{--}), \quad (4.15)$$

where $f(N; \mu)$ denotes a Poisson distribution with mean value of μ, and N_i is the number of events in each four spin state (i stands for a spin state). Using luminosity of four spin states (L_i), μ_i is written as:

$$\begin{cases} \mu_{++} = L_{++} \cdot \sigma_{++}, \\ \mu_{+-} = L_{+-} \cdot \sigma_{+-}, \\ \mu_{-+} = L_{-+} \cdot \sigma_{-+}, \\ \mu_{--} = L_{--} \cdot \sigma_{--}. \end{cases} \quad (4.16)$$

The explicit forms of σ_i are represented in Eq. 4.12, and they include 3 parameters of ($\sigma, \varepsilon_L, \varepsilon_{LL}$). In the maximum likelihood method, the most probable values of each parameter are determined so that the value of L become the maximum.

Figure 4.32 displays the result of ($\sigma, \varepsilon_L, \varepsilon_{LL}$) scan for positive particles. The obtained probability distribution is sliced to 3 planes (($\varepsilon_L, \varepsilon_{LL}$), ($\sigma, \varepsilon_L$) and ($\sigma, \varepsilon_{LL}$)) at the point where the likelihood function takes a maximum value (the left row of the figure show the image). The right row of the figure display the probability distribution in each 3 planes (Top: ($\varepsilon_L, \varepsilon_{LL}$), Middle: ($\sigma, \varepsilon_L$), Bottom: ($\sigma, \varepsilon_{LL}$)). The boundaries observed in the probability distributions come from the requirement of $\sigma_i \geq 0$ in Eq. 4.12.

Figure 4.33 shows how the uncertainty is obtained. The uncertainties of ε_L and ε_{LL} are calculated in the following manner:

1. Project the probability distribution to the ε_L or ε_{LL} axis.

2. Normalize the projected distribution.

3. Get the boundary where the integrated probability become 0.68.

---

[37] $P_B = 0.38$, $P_Y = 0.40$ and the averaged value (P) is 0.39 with uncertainty of 9.2 % (see Sec. 3.2).

The shaded red region in Fig. 4.33 displays the assigned uncertainties. Note that the most probable vales is changed between before and after projection because there is a correlation between ε_L and ε_{LL} (see Top Right distribution of Fig. 4.32). We take the most probable value of the before projection as the center value of ε_L (ε_{LL}) and the projected distribution is only used to evaluate uncertainty.

The results of spin fit with maximum likelihood method are summarized in Table 4.11. It includes ε_L and ε_{LL} for signal ($30 < p_T < 50 \, \mathrm{GeV}/c$) and background ($12 < p_T < 20 \, \mathrm{GeV}/c$) region. Table 4.12 shows single raw asymmetries calculated from Eq. 4.9. The assigned uncertainties in this table are calculated in statistical way ($1/\sqrt{2N}$), and displayed here only to give rough idea how large the uncertainties are. They are consistent with the results of the maximum likelihood method within uncertainty, therefore the spin fit seems reliable. The quality check of the spin fit technique is also done with a toy MC which is represented in Appendix F.
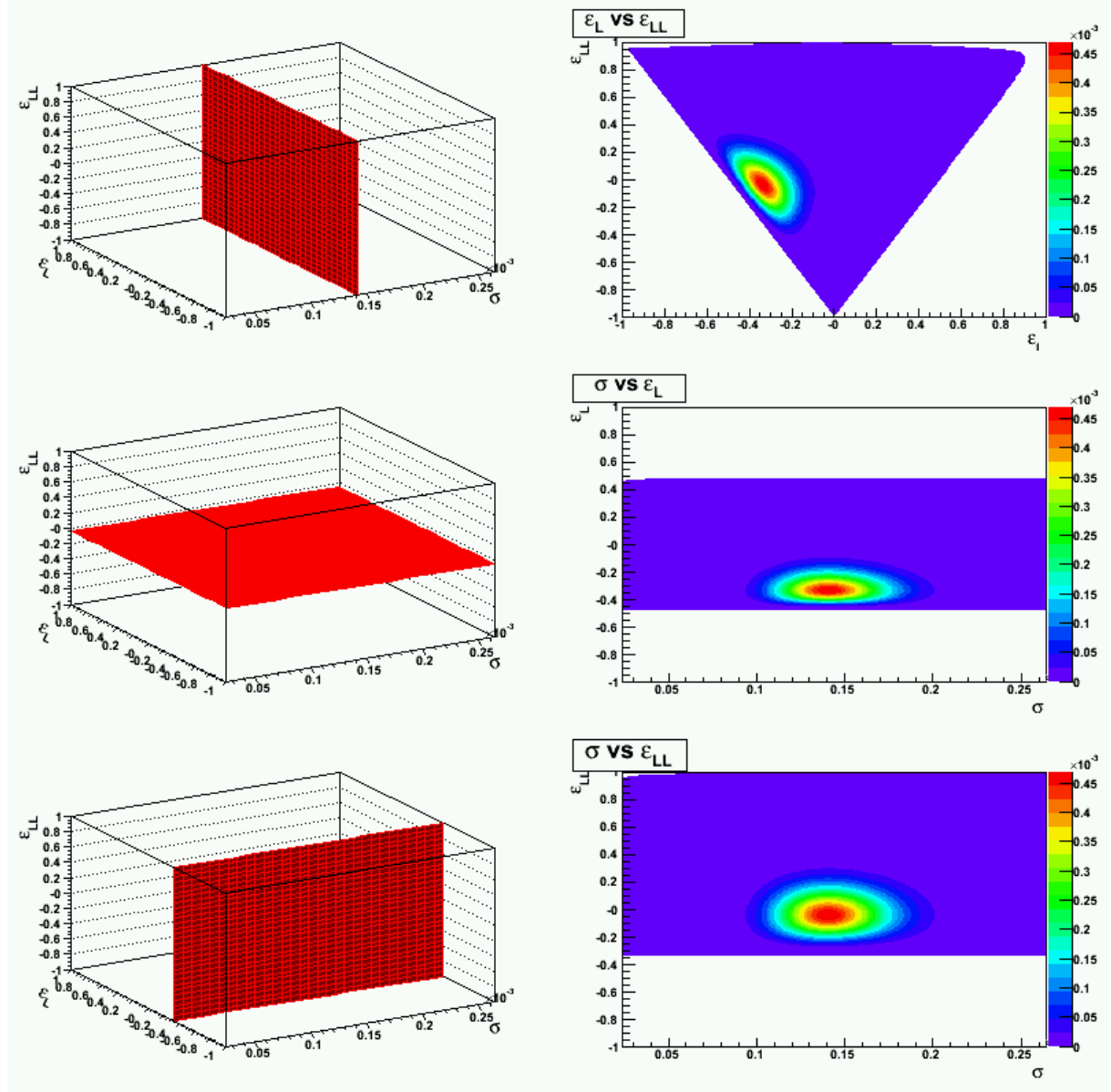
Figure 4.32: The result of $(\sigma, \varepsilon_L, \varepsilon_{LL})$ scan for positive particles ($30 < p_T < 50$ GeV/c). The left row of the figure show the schematical drawing of projection to 3 planes (($\varepsilon_L, \varepsilon_{LL}$), ($\sigma, \varepsilon_L$) and ($\sigma, \varepsilon_{LL}$)). The right row of the figure display the probability distribution in each 3 planes (Top: ($\varepsilon_L, \varepsilon_{LL}$), Middle: ($\sigma, \varepsilon_L$), Bottom: ($\sigma, \varepsilon_{LL}$)).

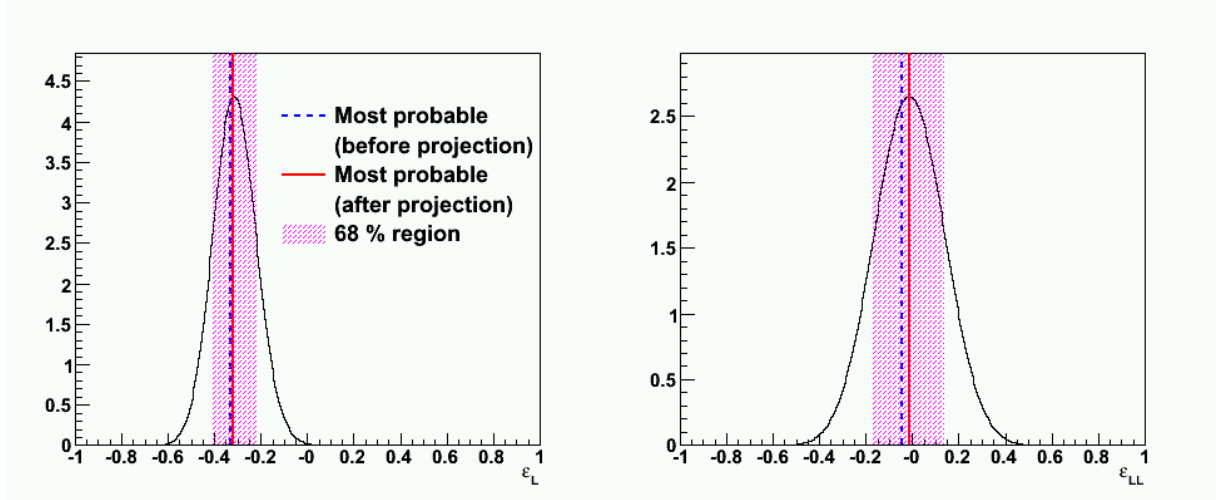Figure 4.33: Left: Projection to the ε_L axis for positive particles ($30 < p_T < 50$ GeV/c). Right: Projection to the ε_{LL} axis for positive particles ($30 < p_T < 50$ GeV/c). Blue (Red) lines display the most probable value before (after) projection, and the Red shaded regions show the 68 % of the total integration.

charge	p_T range (GeV/c)	ε_L	ε_{LL}
$+$	$12-20$: background	-0.02 ± 0.04	0.07 ± 0.06
	$30-50$: signal	$-0.33^{+0.11}_{-0.09}$	$-0.04^{+0.18}_{-0.12}$
		$[-0.42, \ -0.22]$	$[-0.16, \ 0.14]$
$-$	$12-20$: background	-0.03 ± 0.04	0.03 ± 0.06
	$30-50$: signal	$0.31^{+0.18}_{-0.24}$	$0.55^{+0.22}_{-0.21}$
		$[0.07, \ 0.49]$	$[0.34, \ 0.77]$

Table 4.11: Summary of asymmetries calculated from maximum likelihood method. The uncertainties indicate the range in which 68 % of the total integration is included.

charge	p_T range (GeV/c)	counts	Blue Beam (ε_L^B)	Yellow Beam (ε_L^Y)	maximum likelihood
$+$	$12-20$	318	-0.07 ± 0.04	0.03 ± 0.04	-0.02 ± 0.04
	$30-50$	42	-0.19 ± 0.11	-0.47 ± 0.11	$-0.33^{+0.11}_{-0.09}$
$-$	$12-20$	302	-0.06 ± 0.04	0.00 ± 0.04	-0.03 ± 0.04
	$30-50$	13	0.23 ± 0.20	0.39 ± 0.20	$0.31^{+0.18}_{-0.24}$

Table 4.12: Summary of raw asymmetries calculated from Eq. 4.9.

4.4.3 Single Spin Asymmetry

Single spin asymmetry (A_L) is calculated from single raw asymmetry (ε_L). In the calculation, the beam polarization and a dilution factor from background must be taken into account. Their uncertainties are treated in statistical way in this analysis to include them into the probability distribution, which is extracted from likelihood function at the previous section. This treatment enable us to calculate a confidence level of A_L in the range of $-1 \leq A_L \leq 1$ (i.e. in the physics boundary). The procedure to include those factors (polarization and dilution factor) when converting ε_L into A_L is described in this subsection.

Dilution Factor

The background works as a dilution factor to the A_L calculation. Since the background contamination cannot completely removed, measured A_L is written as:

$$
\begin{aligned}
A_L^{meas} &= \frac{\sigma_+^{S+B} - \sigma_-^{S+B}}{\sigma_+^{S+B} + \sigma_-^{S+B}} \\
&= \frac{\sigma_+^S - \sigma_-^S}{\sigma_+^{S+B} + \sigma_-^{S+B}} \\
&= A_L^{W+Z} \cdot \frac{\sigma_+^S + \sigma_-^S}{\sigma_+^{S+B} + \sigma_-^{S+B}},
\end{aligned} \tag{4.17}
$$

where σ_i^{S+B} represents the cross section including both signal and background, and σ_i^S is the cross section of signal ($e^\pm$s from W/Z decay) [38]. Here, we assume that background does not have asymmetry (i.e. $\sigma_+^{BG} = \sigma_-^{BG}$). Using Eq. 4.17, A_L^{W+Z} can be extracted from the measured A_L by:

$$
\begin{aligned}
A_L^{W+Z} &= A_L^{meas} \cdot \frac{\sigma_+^{S+B} + \sigma_-^{S+B}}{\sigma_+^S + \sigma_-^S} \\
&= A_L^{meas} \cdot \frac{N}{S}.
\end{aligned} \tag{4.18}
$$

In the last line, N means the number of observed events and S is the number of signal in observed N. From this relationship, the dilution factor from background contamination is defined as $D = N/S$.

The number of signal and background with the isolation cut is presented in Table. 4.9. It shows the systematic uncertainty of the estimated background is less than 1.0 for positive and negative charge. However, the uncertainty of ± 1.0 is conservatively assigned here. Compared with the statistical uncertainty, this uncertainty is very small and it is not necessary to examine it in detail. The dilution factor and its uncertainty are calculated from:

$$
D = \frac{N^{iso}}{S^{iso}} = \frac{N^{iso}}{N^{iso} - B^{iso}} = \frac{x}{x - az}, \tag{4.19}
$$

$$
\begin{aligned}
\Delta D &= \sqrt{(\frac{\partial D}{\partial x}\Delta x)^2 + (\frac{\partial D}{\partial (az)}\Delta(az))^2} \\
&= D\sqrt{((\frac{1}{N^{iso}} - \frac{1}{S^{iso}})\Delta x)^2 + (\frac{1}{S^{iso}}\Delta(az))^2}.
\end{aligned} \tag{4.20}
$$

---

[38]The index of i denotes the helicity state of proton beam.

Here, the notation of N^{iso}, S^{iso}, B^{iso}, x and az is same with Eq. 4.13 and 4.14. Used numbers for the calculation are also same as listed in Table 4.9 and 4.10, but $\Delta(az) = 1.0$ is assigned here as mentioned above. The results of the calculation is summarized in Table 4.13.

Because of the zero degree track cut (see Sec. 4.4.1), the charge contamination is 0.07 % of the opposite charge and negligible.

charge	total ($N^{iso} = x$)	background ($B^{iso} = az$)	signal of $W + Z$ (S^{iso})	dilution factor (D)
$+$	42	1.6 ± 1.0	$40.4 \pm 6.5\text{(stat.)} \pm 1.0\text{(sys.)}$	1.04 ± 0.03
$-$	13	1.7 ± 1.0	$11.4 \pm 3.6\text{(stat.)} \pm 1.0\text{(sys.)}$	1.14 ± 0.11

Table 4.13: The dilution factors from background.

Treatment of Systematic Uncertainties

The shape of the probability distribution obtained in the spin fit procedure is originated from statistical fluctuation. In order to set a confidence level on the physics asymmetry (A_L^{W+Z}), it needs to consider not only the statistical fluctuation but also uncertainties of dilution (D) and polarization (P). The values of P/D and its uncertainties are listed in Table 4.14. The physics asymmetry (A_L^{W+Z}) is calculated by the formula of:

$$A_L^{W+Z} = \varepsilon_L/(P/D), \tag{4.21}$$

and the uncertainty of P/D is merged into statistical treatments in this analysis.

By smearing the probability distribution with the uncertainty of P/D [39], the effect of the uncertainty of P/D is included. Figure 4.34 shows the distributions with (Red) and without (Black) uncertainty of P/D. The horizontal scale in the figures is converted into the A_L^{W+Z} space, and it can be noticed that the distributions get slightly wider.

charge	P/D	uncertainty
$+$	$0.375 = 0.39/1.04$	9.6 % $(= \sqrt{(\Delta P/P)^2 + (\Delta D/D)^2} = \sqrt{0.092^2 + (0.03/1.04)^2})$
$-$	$0.342 = 0.39/1.14$	13 % $(= \sqrt{(\Delta P/P)^2 + (\Delta D/D)^2} = \sqrt{0.092^2 + (0.11/1.14)^2})$

Table 4.14: The values of P/D and its uncertainties.

The renormalization in the range of $-1 \leq A_L \leq 1$ (indicated as Blue lines in Fig. 4.34) has been done when extracting the confidence level of A_L^{W+Z}. For example, the integration window is extended starting from the most probable value, and the values where the integration become 68 % (95 %) of total integration at $-1 \leq A_L \leq 1$ window are assigned as the range of 68 % (95 %) confidence level. If one side of the integration window reaches 1 or -1, only the other side of the window is extended.

The numbers of 68 % and 95 % confidence levels are shown in Table 4.15. This table also includes ε_L of the background region ($12 < p_T < 20$ GeV/c).

---

[39] For example, the smearing width for the positive charge is: $|A_L \times \Delta(P/D)/(P/D)| = |(-0.33/0.375) \times 0.096| = 0.084$.
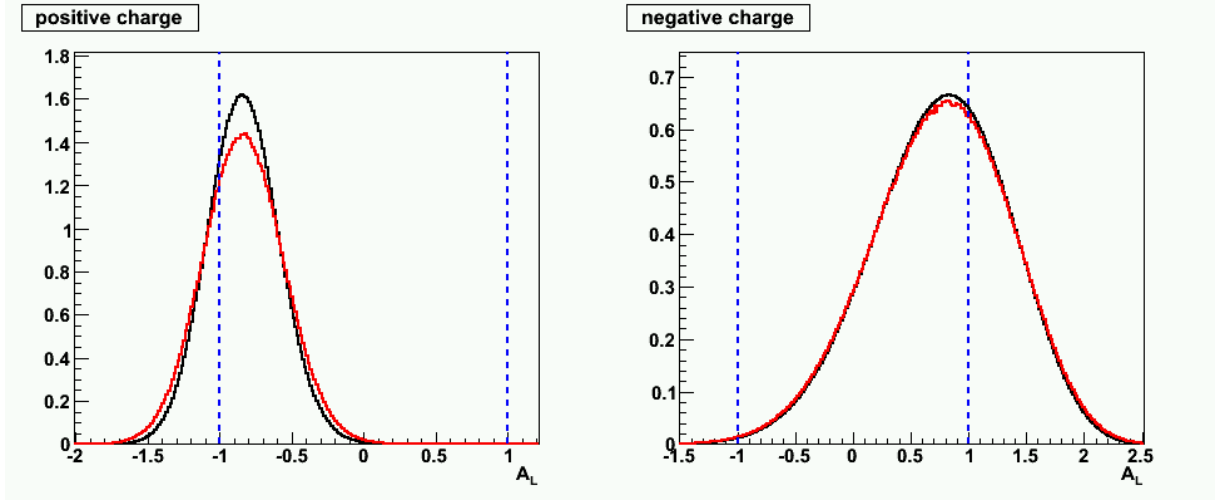
Figure 4.34: The likelihood functions with (Red) and without (Black) P/D uncertainty (Left: positive, Right: negative charge). The horizontal scale is converted in A_L space, and Blue lines indicate the physical boundaries ($-1 \leq A_L \leq 1$)

charge	p_T range (GeV/c)	ε_L	A_L^{W+Z}	A_L 68 % CL	A_L 95 % CL
+	12−20: background	-0.02 ± 0.04	-	-	-
	30−50: signal	$-0.33^{+0.11}_{-0.09}$	-0.88	$[-1, \ -0.61]$	$[-1, \ -0.21]$
−	12−20: background	-0.03 ± 0.04	-	-	-
	30−50: signal	$0.31^{+0.18}_{-0.24}$	0.91	$[0.20, \ 1]$	$[-0.51, \ 1]$

Table 4.15: Longitudinal single spin asymmetries (A_L) with various confidence levels.

Chapter 5

Results and Discussion

The obtained results of $d\sigma/dy$ and A_L are shown again here in Table 5.1 and 5.2. These results are compared to theoretical calculations or the results from previous experiments in this chapter.

As mentioned in Chapter 4, these results include electrons from Z decays as well as W decays because the PHENIX detector cannot distinguish them. Thus, the contamination from Z decays should be taken into account in the calculation of the cross section of $W \rightarrow e\nu$ decay. In addition to the Z contribution, the fraction of W decays that were outside of the detector acceptance also must be corrected. The subtraction of Z contribution and evaluation of the cross section of $W \rightarrow e\nu$ decay is discussed in Sec. 5.1. The charge ratio of W production and its brief future prospects are also described in that section. The measured single spin asymmetry can be directly compared to theoretical calculations because the Z contribution is already taken into account (see Sec. 1.3). The comparison of A_L^{W+Z} to the theoretical calculations is described in Sec. 5.2 followed by the future prospects of spin asymmetry measurement of W production at RHIC in Sec. 5.3.

charge	$d\sigma/dy$ (pb)
$+$	50.2 ± 7.2(stat.) $^{+1.2}_{-3.6}$(sys.) ± 8.0 (normalization)
$-$	9.7 ± 3.7(stat.) $^{+2.1}_{-2.5}$(sys.) ± 1.6 (normalization)
$\pm$	60.0 ± 8.1(stat.) $^{+3.1}_{-6.0}$(sys.) ± 9.6 (normalization)

Table 5.1: $d\sigma/dy$ of electrons from W and Z decay at $30 < p_T^e < 50$ GeV/c.

charge	A_L^{W+Z}	A_L 68 % CL	A_L 95 % CL
$+$	-0.88	$[-1, \ -0.61]$	$[-1, \ -0.21]$
$-$	0.91	$[0.20, \ 1]$	$[-0.51, \ 1]$

Table 5.2: A_L with various confidence level at $30 < p_T^e < 50$ GeV/c.

5.1 Cross Section of $W \to e\nu$ Decay

The cross section of $W \to e\nu$ decay ($\sigma(W) \cdot BR(W \to e\nu)$) is estimated from the differential cross section ($d\sigma/dy$). The relationship of the cross section to the $d\sigma/dy$ is:

$$\frac{d\sigma}{dy}(W) \cdot BR(W \to e\nu) = \frac{d\sigma}{dy} \cdot (1 - f_z), \tag{5.1}$$

$$\sigma(W) \cdot BR(W \to e\nu) = \frac{d\sigma}{dy} \cdot (\Delta y \Delta \phi / 2\pi) \cdot \frac{1 - f_z}{s_W} = \sigma(W + Z)|_{\mathrm{PHENIX}} \cdot \frac{1 - f_z}{s_W}, \tag{5.2}$$

where the term of $\Delta y \Delta \phi$ denotes the PHENIX acceptance ($\Delta y = 0.35 \times 2$, $\Delta \phi = \pi$), f_z represents the Z contribution ($f_z = Z/(W + Z)$) and s_W is the fraction of the cross section within $|y| < 0.35$ in rapidity [1], $30 < p_T < 50$ GeV/c and $|\Delta \phi| < \pi$.

The values of f_z and s_W are estimated from NLO (Next-to-Leading-Order) and NNLO (Next-Next-to-Leading-Order) perturbative-QCD calculations [12, 121], and listed in Table 5.3 with input PDFs [46, 122]. By taking the average among different calculations, f_z is 6.72, 24.4, 10.5 %; s_W is estimated to be 11.2, 7.50, 10.2 % for W^+, W^- and $W^\pm$, respectively. The theoretical uncertainties from NLO and NNLO calculations and varied parton-distribution functions (PDFs) are negligible compared to other sources of systematic uncertainty from the data.

The cross section of $W \to e\nu$ is summarized in Table 5.4, and compared with the S$p\bar{p}$S, Tevatron and LHC data [123, 124, 74, 125, 126] in Fig. 5.1. The statistical and systematic uncertainties are added in quadrature. Our results are the first measurement of the W cross section in pp collisions. The curves in the figure show theoretical calculations [121]. The difference of theoretical calculation between $p\bar{p}$ and pp collisions at lower $\sqrt{s}$ is originated from the difference of involved quarks. In $p\bar{p}$ collisions, quarks which couple to W-boson are mainly valence quarks, while the dominant process of W production in pp collisions is the coupling of the valence and sea quarks. However, in much higher $\sqrt{s}$, the momentum fractions (x) of the involved quarks become smaller and the coupling of sea quarks dominates the process of W production in both pp and $p\bar{p}$ collisions. Therefore, the difference of W cross section between $p\bar{p}$ and pp collisions disappears in higher $\sqrt{s}$ collisions as can be noticed in the figure. In such a high $\sqrt{s}$ collisions, heavy flavors, such as s, c and b quarks, also contribute to the W production, while they are very small and ignored in lower $\sqrt{s}$ collisions. It is noticeable that all of the measured cross sections are consistent with the theoretical calculation. This means that the established NLO and NNLO QCD calculations and our knowledge of unpolarized PDF in wide x range (from ~ 0.16 at RHIC to ~ 0.01 at LHC [2]) are quite reliable.

---

[1] Because the exact PHENIX acceptance is $|\eta| < 0.35$, it corresponding to $|y| < 0.35$ for electrons due to their small mass value.

[2] The Bjorken x is calculated as $\sim M_W/\sqrt{s}$ at central rapidity region.

	PDF	charge	$d\sigma/dy$ (pb) of $W + Z$ $(30 < p_T^e < 50\ \mathrm{GeV}/c)$	f_z	s_W
CHE (NLO)	MRST2002	$+$	43.2	0.0701	-
		$-$	11.3	0.267	-
		$\pm$	54.5	0.111	-
NLO	MSTW2008	$+$	46.5	0.0647	0.113
		$-$	12.8	0.235	0.0744
		$\pm$	59.3	0.101	0.103
NNLO	MSTW2008	$+$	46.9	0.0669	0.111
		$-$	13.5	0.231	0.0755
		$\pm$	60.4	0.104	0.101

Table 5.3: f_z and s_W values estimated from NLO and NNLO calculations.

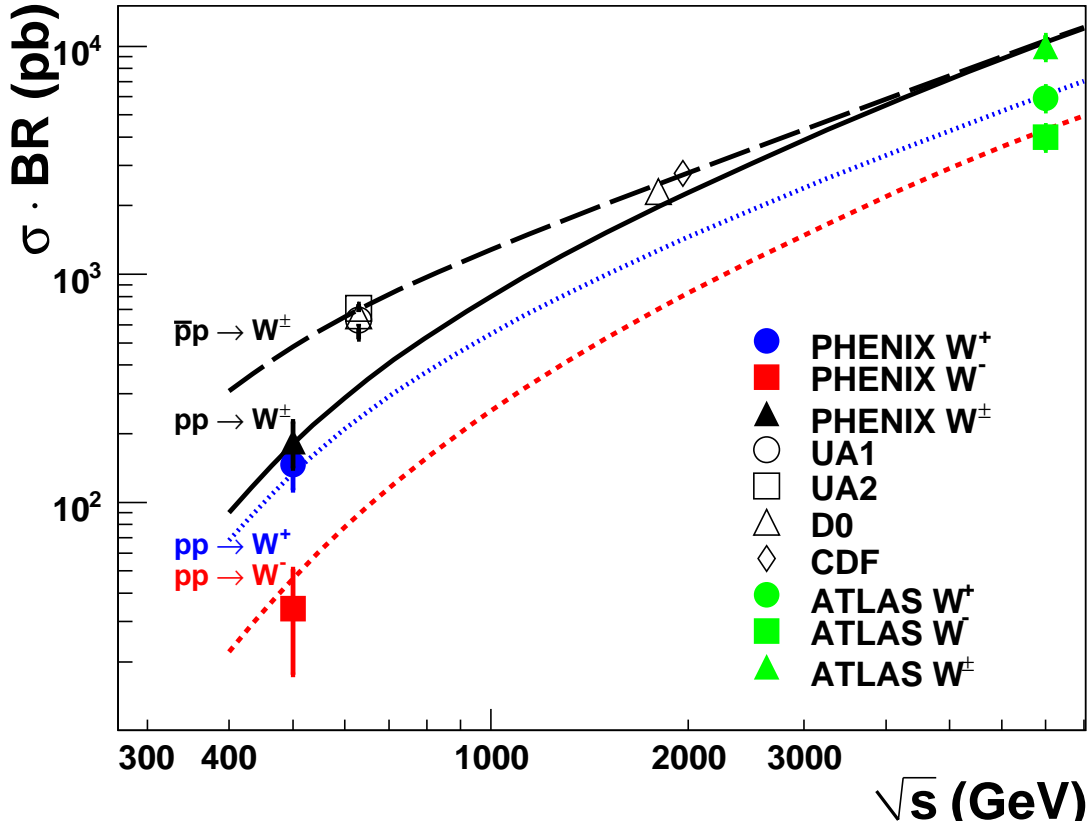| charge	cross section of $W \to e\nu$ (pb)
$+$	$146.3 \pm 21.0(\mathrm{stat.})\ ^{+3.5}_{-10.5}(\mathrm{sys.}) \pm 23.3(\mathrm{norm.})$
$-$	$34.2 \pm 13.1(\mathrm{stat.})\ ^{+7.4}_{-8.8}(\mathrm{sys.}) \pm 5.6(\mathrm{norm.})$
$\pm$	$184.0 \pm 24.9(\mathrm{stat.})\ ^{+9.5}_{-18.4}(\mathrm{sys.}) \pm 29.5(\mathrm{norm.})$

Table 5.4: Cross section of $W \to e\nu$ decay.

Figure 5.1: Inclusive cross sections for W leptonic decay channel of this thesis and other measurements [123, 124, 74, 125, 126]. The curves are theory calculations [121].

5.1.1 Charge Ratio of W production

The W production at RHIC offers the unique opportunity of extracting the $\bar{d}/\bar{u}$ flavor asymmetry at very high Q^2 without the complications associated with the charge symmetry breaking effect and nuclear binding effect. As discussed in Sec. 1.3.3, the charge ratio of W^+ and W^- production in central rapidity region at PHENIX is a good probe for $\bar{d}/\bar{u}$ with distinguishing flavor symmetric and asymmetric sea quark distributions.

Using Eq. 5.1, the evaluated charge ratio with obtained $d\sigma/dy$ at PHENIX central rapidity is:

$$R = 6.4 \pm 2.6(\text{stat.}) \pm 1.7(\text{sys.}). \tag{5.3}$$

Here, the systematic uncertainty is calculated from larger value of the background estimation in Table 5.1 for simplicity, and assumed there is no correlation between positive and negative charge. Due to the large uncertainty from the small statistics of negative charge, the obtained value cannot distinguish flavor symmetric and asymmetric anti-quark sea [3]. However, the result also indicate that we can probe $\bar{d}/\bar{u}$ asymmetry directly with more statistics, and the demonstration is shown below.

Future Prospect

Figure 5.2 displays the predicted charge ratios $R(y_l)$ calculated for various PDFs, with the projected sensitivities [86]. The statistical uncertainties of the projections are estimated for recorded luminosity of 300 pb^{-1} at RHIC [127]. The acceptance is for the PHENIX detector, which is $|\eta| < 0.35$ in central rapidities, $-2.2 < \eta < -1.1$ and $1.1 < \eta < 2.4$ in forward rapidities. The figure has clearly demonstrated that a measurement of $R(y_l)$ at PHENIX with more statistics is able to distinguish SU(2) flavor symmetric (assumed in MRS S0') and asymmetric (assumed in other three PDFs) sea quark distributions.

In the aspect of the $\bar{d}/\bar{u}$ measurement, all of the theoretical models have difficulties to explain $\bar{d}/\bar{u}$ asymmetry at large x ($x > 0.2$), and E906 Drell-Yan experiment at Fermilab [79] plans to extend the measurement in wide x range ($0.1 \sim < x \sim < 0.4$) to resolve the behavior of $\bar{d}/\bar{u}$ at large x region as described in Sec. 1.3.3. The future R measurement at RHIC can also provide complementary measurement of $\bar{d}/\bar{u}$ at x range of ~ 0.05 to 0.16 without the complications which come from the charge symmetry breaking effect and nuclear binding effect.

---

[3]Note that the value of f_z depends on assumed PDF and the central value will vary with different PDF, but it is not taken into account here because of rather large uncertainty.
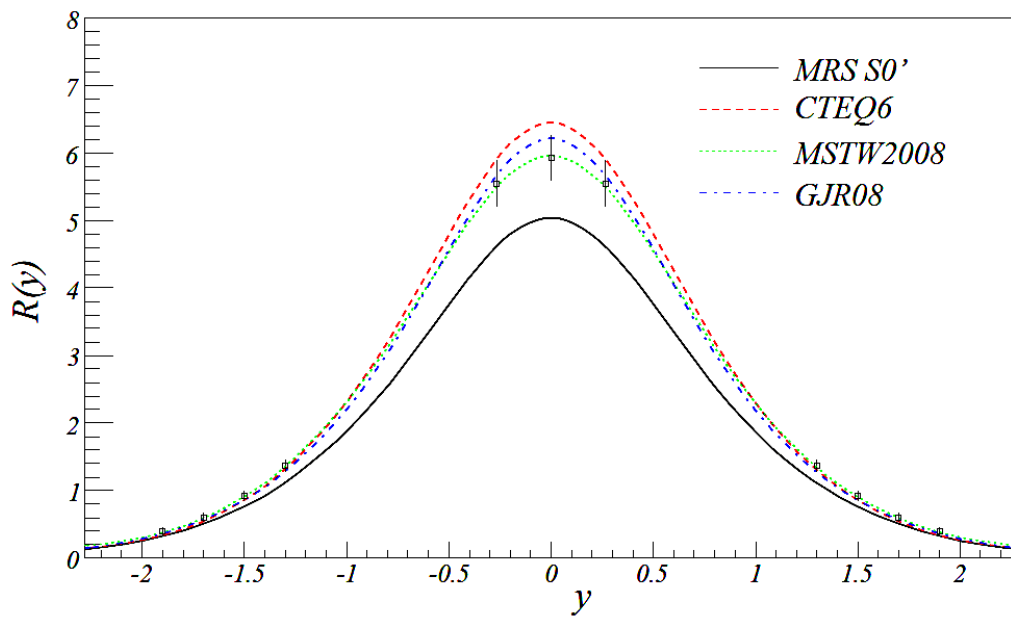
Figure 5.2: Prediction of the charge ratio $R(y_l)$ as a function of lepton rapidity for pp collision at $\sqrt{s} = 500$ GeV using various PDFs. The projected sensitivities for a run with recorded luminosity of 300 pb^{-1} for the PHENIX detector are also shown [86].

5.2 Comparison of A_L to various Polarized PDFs

Measured single spin asymmetry is directly compared to various polarized PDFs. The polarized PDFs are extracted from fits of DIS and Semi-Inclusive DIS data [64, 67, 68, 62], and the theoretical A_L values are calculated using NLO with different polarized PDFs [12]. Table 5.5 shows the range of the theoretical A_Ls of $e^\pm$ from W and Z decay in rapidity of $|y| < 0.35$ with $30 < p_T < 50$ GeV/c range. The measured A_L of 68 % confidence level and the value from DSSV PDF [67, 68] is also listed in the table.

Figure 5.3 displays the comparison of measured A_L to the calculations. The discrimination power to the choice of the underlying PDF is smaller comparing to Fig. 1.13 because of the different electron p_T cut. Nevertheless, there is still a band in A_L of negative charge which comes from the uncertainty of $\Delta \bar{u}$ and Δd. Using the likelihood function obtained in Sec. 4.4.3, the confidence level at the theoretical A_Ls are evaluated. The experimental results are consistent with the theoretical calculations at $5-15$ % confidence level for $A_L^{e^+}$ and at $18-36$ % for $A_L^{e^-}$. An independent measurement of the single spin asymmetries of W boson production at RHIC has been reported by the STAR collaboration [128], and it also shows the consistent results with our measurement as well as theoretical predictions.

The observed asymmetries are sensitive to the polarized quark distributions at $x \sim M_W/\sqrt{s} \simeq 0.16$. Although the uncertainties of the obtained results are quite large due to limited statistics, this is the first measurement of the single spin asymmetry of $W + Z$ production and the results directly demonstrate the parity violating coupling between W bosons and light quarks. That means our analysis has established a new and direct way to probe the spin structure of the proton using the weak interactions. It is expected that our knowledge of flavor-separated polarized PDFs will be improved in near future with the upgrades of RHIC luminosity and PHENIX detector. The future prospects of the A_L measurement is described in the next section.

charge	measured A_L (68 % CL)	A_L from DSSV ($|y| < 0.35$, $30 < p_T^e < 50$)	A_L from various PDFs ($|y| < 0.35$, $30 < p_T^e < 50$)
$+$	$-0.88^{+0.27}_{-0.12}$ $(-1 \leq A_L \leq -0.61)$	-0.35	-0.37 to -0.21
$-$	$0.91^{+0.09}_{-0.71}$ $(0.20 \leq A_L \leq 1)$	0.05	-0.06 to 0.26

Table 5.5: A_L values from theory calculation with various polarized PDFs.
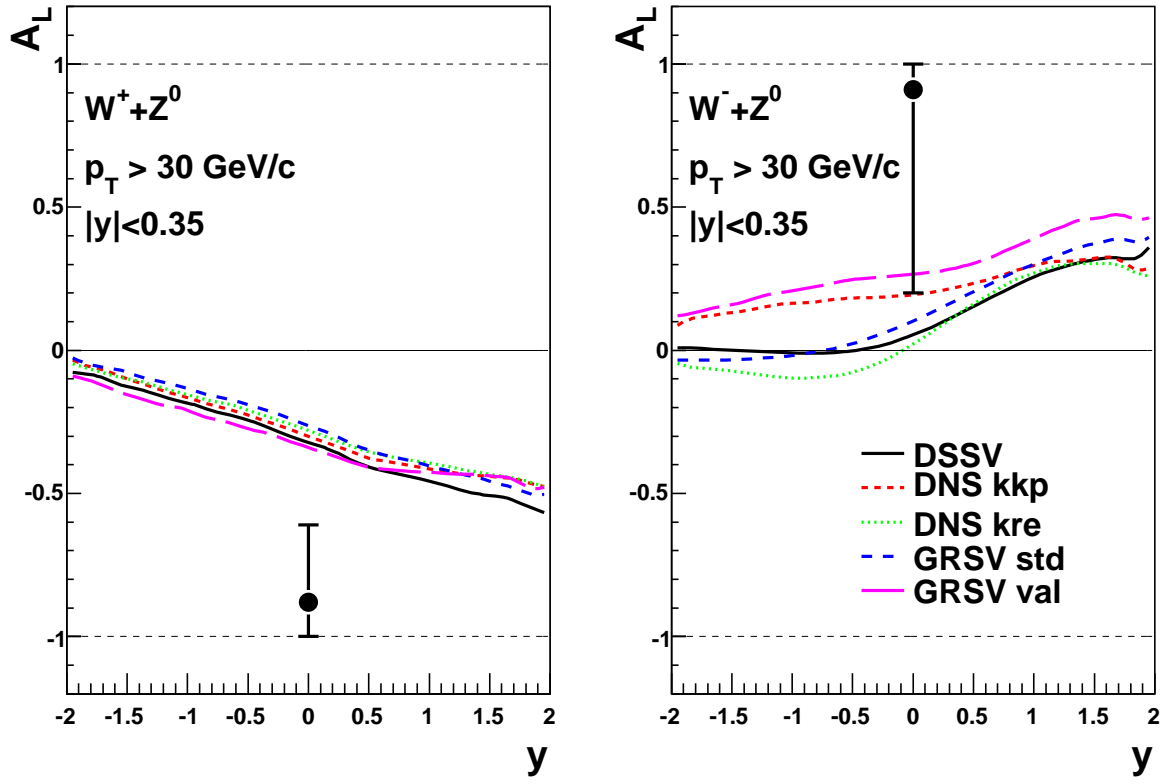
Figure 5.3: A_L for electrons and positrons from W and Z decays. The error bars represent 68 % CL. The theoretical curves are calculated using NLO with different polarized PDFs [12].

5.3 Future Prospects of Single Spin Asymmetry of W Production

RHIC luminosity and PHENIX detector upgrades are ongoing in order to reduce the uncertainties of A_L and extend the A_L measurement to forward/backward rapidity. The upgrades lead to our better understanding of the flavor separated polarized PDFs. Figure 5.4 displays the current constraints on the polarized anti-quark distributions from the DSSV result [67, 68]. The uncertainties of the polarized PDFs are shown with Yellow bands which mainly come from the uncertainty of the fragmentation functions assumed in SIDIS measurements. The impact of the future A_L measurement on anti-quark distribution, which is estimated by one of global analysis groups, is presented in this section [12].
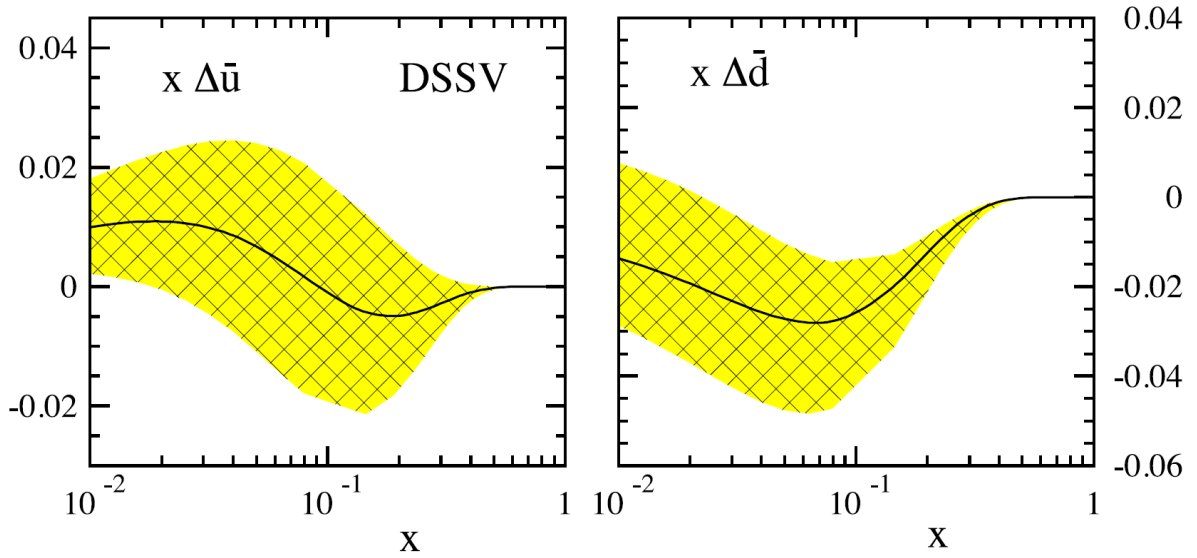

Figure 5.4: $\Delta u(x, Q^2 = 10 \text{ GeV}^2)$ and $\Delta d(x, Q^2 = 10 \text{ GeV}^2)$ as obtained in the DSSV global analysis [67, 68]. The bands correspond to changes of 2 % in the total χ^2 of the fit.

The study is based on NLO calculation with PDFs from the DSSV global analysis. A pseudo-"RHIC data set" was produced from the NLO calculation, using the central value of DSSV PDFs, by computing single spin asymmetries of $A_L^{e^+}$ and $A_L^{e^-}$ [4]. Then the calculated asymmetries are randomly shifted, assuming a Gaussian distribution of their statistical uncertainties. The statistical uncertainties are estimated using the formula of $\Delta A_L = 1/(P\sqrt{\mathcal{L}\sigma})$, where σ is the cross section of W production. The assumed polarization (P) is 60 %, and the integrated luminosity of $\mathcal{L} = 200$ pb^{-1} and 800 pb^{-1} were produced. The rapidity coverage which is exactly same as the PHENIX and STAR detectors is taken into account in this study. A new global fit for the polarized PDFs is then performed, for which the simulated data set is included, and the impact of future W data from RHIC is estimated.

The result of this study is shown in Fig. 5.5, including their $\Delta\chi^2/\chi^2 = 2$ % uncertainties [12]. Note

---

[4]Asymmetries are evaluated including both W and Z/γ boson exchange contributions

that this global fit only include the detector acceptance which is currently used for W measurement [5]. By comparing the figure to Fig. 5.4, we can notice that there is a slight modification of the central distributions due to the statistical fluctuation, however a clear reduction can be observed in their uncertainty bands. This effect is very clear for $x > 0.1$ as expected, considering the rapidity coverage of the pseudo-"RHIC data set" added to the global fit [6]. The decrease in the uncertainty band is more noticeable in $\Delta \bar{u}$ distribution, which confirms the larger sensitivity of the e^- asymmetries. At $x \sim 0.01$ values, there is almost no change in the distributions and uncertainties, because the single-spin asymmetries at RHIC are rather insensitive to such small x values.

The impact of extending rapidity coverage by $|\eta| < 0.35$ and $1 < |\eta| < 2$ for PHENIX and $|\eta| < 2$ for STAR is also studied with psedo-"RHIC data set". The extended rapidity for the PHENIX and STAR is corresponding to the ongoing forward upgrade project of both experiments. Figure 5.6 shows the result of the global fit with the case of larger luminosity and rapidity coverage [12]. The impact of RHIC data can be noticed down to x of ~ 0.05, thanks to the extended coverage in η.

The study described in this section does not include experimental issues (such as efficiencies for lepton detection, correction of background subtraction and other systematic uncertainties, etc.), and that would decrease the impact of the real data in the global fit. Nevertheless, the study shows that future RHIC W measurement can definitely improve our knowledge of flavor separated polarized PDFs, and contribute to our deeper understanding of the proton spin structure.

---

[5] $|\eta| < 0.35$ for the PHENIX and $|\eta| < 1$ for the STAR.
[6] Using the lepton rapidity (y_l), the Bjorken x is: $\langle x_{1,2} \rangle \sim (M_W / \sqrt{s}) e^{\pm y_l / 2}$, and its value at $y_l \sim 0$ is $x \sim 0.16$
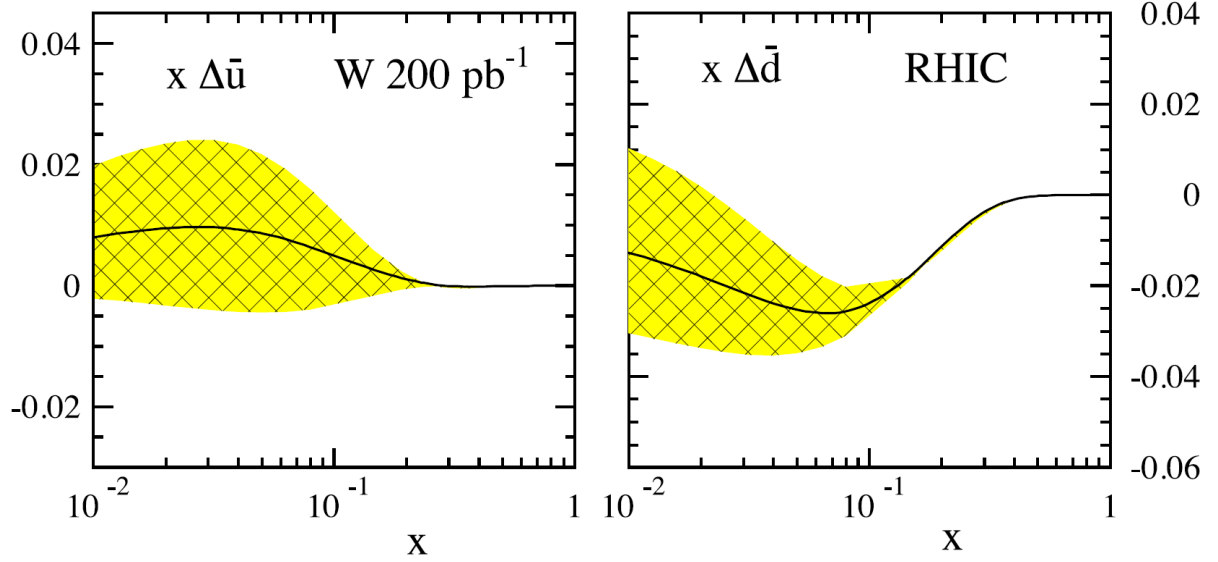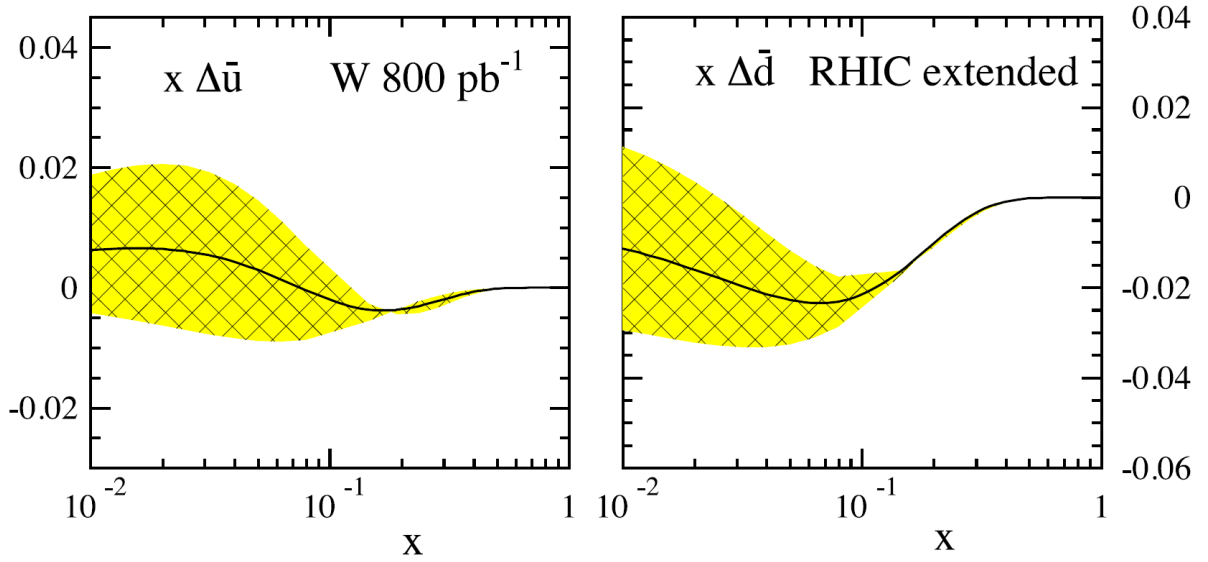
Figure 5.5: $\Delta u(x, Q^2 = 10 \text{ GeV}^2)$ and $\Delta d(x, Q^2 = 10 \text{ GeV}^2)$ as obtained from a global analysis performed by including the simulation data generated with the luminosity of 200 pb^{-1} and the current rapidity coverage of RHIC detectors [12]. The bands correspond to changes of 2 % in the total χ^2 of the fit.

Figure 5.6: $\Delta u(x, Q^2 = 10 \text{ GeV}^2)$ and $\Delta d(x, Q^2 = 10 \text{ GeV}^2)$ as obtained from a global analysis performed by including the simulation data generated with the luminosity of 800 pb^{-1} and extended rapidity coverage of RHIC detectors [12]. The extended rapidity coverage is corresponding to the ongoing forward upgrade project of PHENIX and STAR. The bands correspond to changes of 2 % in the total χ^2 of the fit.

Chapter 6

Conclusion

In summary, the first measurements of cross section and single spin asymmetry (A_L) of W and Z production in polarized pp collisions at $\sqrt{s} = 500$ GeV were reported in this thesis. Contrast to previous (SI)DIS measurements, the W boson production at pp collisions is free from any fragmentation process by measuring its decay lepton, therefore provides us more direct probe for both polarized and unpolarized anti-quark (sea quark) distributions, and it leads to our deeper understanding of the proton structure. W bosons couple only the left-handed quarks and right-handed anti-quarks ($u_L \bar{d}_R \rightarrow W^+$ and $d_L \bar{u}_R \rightarrow W^-$), so the single spin asymmetry of the W yield is sensitive to the flavor separated Δq and, especially, $\Delta \bar{q}$. In addition, the measurement of cross section and charge ratio of W production in spin-averaged collisions also provides a sensitive test of the current unpolarized PDFs by probing $\bar{d}/\bar{u}$ asymmetry, as well as it is an important confirmation of the theoretical understanding of the W production.

The experiment was performed with the PHENIX detector with the polarized proton beams provided by RHIC at BNL. The data used in this thesis were taken during Year-2009 run. The analyzed data sample has the integrated luminosity of 8.57 pb^{-1}, with average polarization of 39 %. W and Z production was measured through inclusive $pp \rightarrow e^{\pm} + X$ production over a pseudo-rapidity range of $|\eta| < 0.35$, where the $e^{\pm}$ with transverse momentum of $p_T > 30$ GeV/c mainly come from W and Z decays. The electrons were detected by the PHENIX DC, PC1 and EMCal. The high p_T photon/electron trigger which is constructed by the signals from EMCal was used to collect the data sample.

The obtained $W^{\pm}$ boson production cross sections for the $e^{\pm}$ channels are $\sigma(pp \rightarrow W^+ X) \times BR(W^+ \rightarrow e^+ \nu_e) = 146.3 \pm 21.0(\text{stat.})^{+3.5}_{-10.5}(\text{sys.}) \pm 23.3(\text{norm.})$ pb, and $\sigma(pp \rightarrow W^- X) \times BR(W^- \rightarrow e^+ \nu_e) = 34.2 \pm 13.1(\text{stat.})^{+7.4}_{-8.8}(\text{sys.}) \pm 5.6(\text{norm.})$ pb. This is the first measurement of W cross section in pp collisions. The results are consistent with NLO and NNLO perturbative QCD (pQCD) calculations, and validity of the theoretical understanding of the W production is confirmed.

The single spin asymmetries of $A_L^{e^+} = -0.88^{+0.27}_{-0.12}$ and $A_L^{e^-} = 0.91^{+0.09}_{-0.71}$ are also measured for inclusive high transverse momentum $e^{\pm}$s ($30 < p_T < 50$ GeV/c) for the first time. The non-zero A_Ls show the direct demonstration of the parity-violating coupling of W to light quarks, and the results are consistent with NLO pQCD based predictions from polarized PDFs which are extracted from previous polarized (SI)DIS results.

Acknowledgment

First of all, I would like to acknowledge Prof. T. Nagae, who is the leader of the experimental Nuclear and Hadronic physics (NH) group, for his essential advice and comments about the experiment and physics. He has read my thesis carefully and given me useful suggestions. I am deeply grateful to Prof. N. Saito, who has been my supervisor. His abundant knowledge and precise suggestion always guided me. He has helped me not only with his advice but also with support to concentrate on the research. Without his help, I could not finish this work. I would like to express my sincere thanks to Dr. T. Murakami for his kind supports for a great deal of encouragements. I could learn many techniques of the experiments and analysis from him and could enjoy the research with his support. I also wish to thank Dr. T. Mibe and Dr. M. Niiyama, who have also read my thesis thoroughly and given me useful comments, for their encouragement for the completion of this work.

I would like to express my deep thanks to Dr. K. Okada for his many thoughtful comments and suggestions. This work is benefited especially from his idea and suggestions. I am grateful to the members of W working group: Dr. M. Chiu, Dr. A. Bazilevsky, Dr. J. Haggerty, Dr. D. Kawall and Dr. E. Kistenev. Discussion with them was beneficial and I was able to polish the analysis working with them. I also would like to thank the members of the internal review committee (IRC120): Dr. M GrossePerdekamp, Dr. A. Deshpande and Dr. B Sahlmueller.

I would like to acknowledge the Radiation Laboratory (Rad. Lab.) at RIKEN and RIKEN BNL Research Center (RBRC) for the research activity as well as financial supports. Especially, Dr. H. En'yo, who is the chief scientist of the Rad. Lab., often advised me about the research plan. I also would like to express my gratitude to the members of RBRC: Dr. Y. Akiba, Dr. Y. Goto and Dr. I. Nakagawa. I would like to thank the administrators of the PHENIX Computing Center in Japan (CCJ): Dr. T. Ichihara, Dr. Y. Watanabe, Dr. S. Yokkaichi, Dr. T. Nakamura and Dr. Y. Ikeda. The analysis was done on CCJ and it was very effective with their supports. I am deeply grateful to all the collaborators of the PHENIX experiment, and the staff of Collider Accelerator Department at BNL. Without them the experiment would not be possible.

I would like to express my thanks to the past and present staff of the NH group: Prof. K. Imai, Dr. T. Kawabata, Dr. Kiyoshi Tanida, and Dr. H. Fujioka. Especially, to Prof. K. Imai who is the former leader of the NH group. His deep understanding of nature and passion for physics always stimulated my work. I am also grateful to the past and present member of our group: Dr. Y. Fukao, Dr. M. Togawa,

Appendix A

Fragmentation Function

In DIS or hard pp collision, a single parton with large momentum is knocked out from the proton. Since the quark or the gluon cannot exist by itself, such a parton is hadronized and generates a "jet", which consists of many hadrons with momentum almost parallel to that of the initial parton.
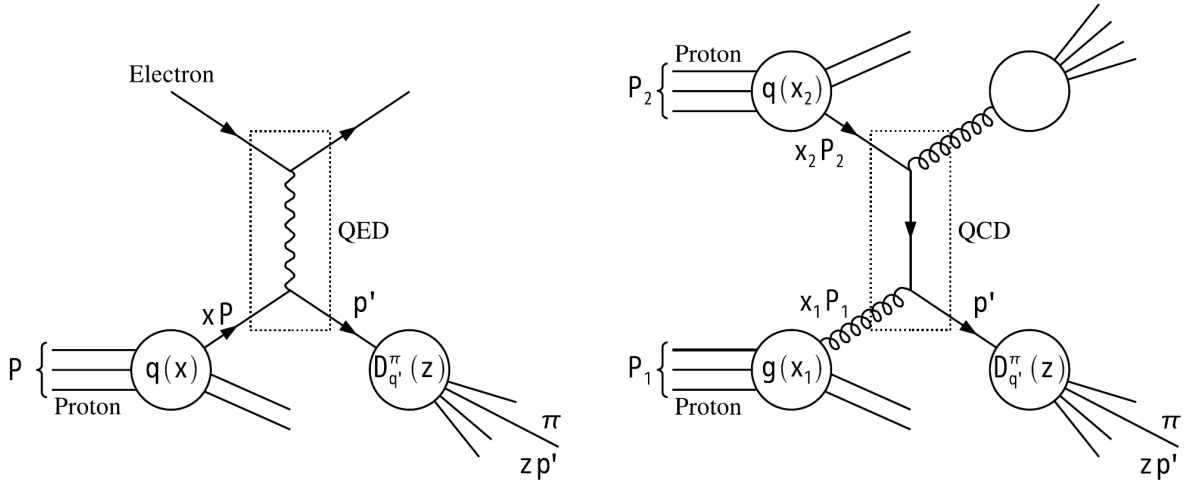

Figure A.1: Left: Diagram of SIDIS. In SIDIS experiment, one or more hadrons at the final state are detected. Right: Diagram of hard pp collision. Inclusive measurement of hadrons is often performed. In both SIDIS and pp collision, the reaction is divided into parts of PDF, FF and partonic cross section (factorization theorem).

In ep scattering, the reaction is divided into two parts; PDF and partonic cross section (factorization theorem). While the cross section between the parton and the electron (partonic cross section) can be calculated precisely using perturbative QED, it is difficult to theoretically calculate PDF. When hadron at the final state is measured in DIS, so-called Semi-Inclusive DIS (SIDIS) measurement, it is necessary to formalize the hadronization process. The hadronization from the scattered parton is "soft" QCD process, where pQCD does not work due to low energy scale, and the process is described by "fragmentation function" (FF). FF is represented as $D_h^f(z)$, where f and h indicate the parent parton and the hadron after the fragmentation, respectively, and z is energy fraction of the hadron to the parton. $D_h^f(z)dz$ is

defined as the probability density that the hadron h with momentum of zp to $(z + dz)p$ is generated in the jet originating in the parton f with momentum of p. For example, the differential cross section of SIDIS with pion (π) measured in the final state (Left of Fig. A.1) is written as:

$$d\sigma^{ep \to \pi X} = \sum_{q,\bar{q}} \int_0^1 dx \int_0^1 dz q(x) d\hat{\sigma}^{ep \to q'X} D_{q'}^{\pi}(z), \tag{A.1}$$

where $d\hat{\sigma}$ indicates the partonic cross section. The summation is performed for possible combinations of the initial and the final parton (and anti-parton). When the hadron at the final state has spin, polarized FF is defined in analogy with polarized PDF.

In the same way, reaction of pp collision can also be factorized as displayed in the right side of Fig. A.1. Inclusive measurement of pion in pp collisions is divided into three parts; PDF, FF and partonic cross section. Corresponding to the initial two protons, two PDFs appear. Unlike ep scattering, gluons in the proton directly participate in the reaction in pp collisions. The cross section between partons is calculated by pQCD instead of QED [1]. Then, the scattered parton is hadronized following FF. The process is written as:

$$d\sigma^{pp \to \pi X} = \sum_{f_1, f_2, f'} \int dx_1 dx_2 dz f_1(x_1) f_2(x_2) d\hat{\sigma}^{f_1 f_2 \to f'X} D_{f'}^{\pi}(z), \tag{A.2}$$

where f indicates type of the parton and includes both the quark and the gluon.

It is important to note that, in ep scattering, this picture is valid at large Q^2 where the virtual photon interacts with a single parton in the proton. Similarly, large Q^2 is required in pp scattering and it is confirmed by the hadron production with high transverse momentum (p_T) [2]. Here, p_T is defined as the momentum component perpendicular to momentum of the initial protons in center-of-mass system. The large Q^2 results in small α_s, which assures validity of pQCD.

One of the remarkable features of the factorization theorem is the universality of PDF and FF. Thanks to this feature, PDF or FF obtained by a certain experiment is available for other experiments and it results in versatility and predictability of the theory. Based on the feature, FF is generally measured by e^+e^- collision because the reaction of $e^+e^- \to q\bar{q}$ is precisely calculable by QED and there is no other theoretical uncertainty except for FF. In e^+e^- collision with center-of-mass system of the incident electrons, FF is related to cross section in the leading order as follows:

$$\frac{1}{\sigma_{tot}^{e^+e^- \to Z}} \frac{d\sigma^{e^+e^- \to hX'}}{dz} = \frac{\sum_{q,\bar{q}} e_q^2 D_q^h(z)}{\sum_{q,\bar{q}} e_q^2}, \qquad z = \frac{2E_h}{\sqrt{s}} = \frac{E_h}{E_q}. \tag{A.3}$$

Here, σ_{tot} is the total cross section of e^+e^- collision. The summation is executed over possible quark flavors, while contribution from gluon does not appear in the leading order. $\sqrt{s}$, E_h and E_q are center-of-mass energy, energy of the hadron and energy of the parton, respectively. Although only FFs of quarks appear and the cross section has scaling on z in this equation, FF actually depends on Q^2 with higher order QCD, like PDF, and evolves following DGLAP equation for FF [129, 130, 131].

---

[1] QED also contributes the process, but it is small due to smaller coupling constant of the electromagnetic interaction than the strong interaction.

[2] Empirically, boundary for the validity of the factorization theorem is around 1 GeV/c in p_T.

To determine FF, several experiments of e^+e^- collision and analyses to unify the experimental data are performed (see [69, 70, 132, 133, 134] and references in them). However, from Eq. A.3, it can be noticed that it is difficult to distinguish FFs of each quark flavor because the right-hand side of the equation is always sum of FFs. For this reason, symmetric properties and phenomenological assumptions are often adopted to extract FF from measured data. For instance, charge conjugation results in:

$$D_f^h = D_{\bar{f}}^{\bar{h}}, \tag{A.4}$$

and additional isospin symmetry derives for positive pion:

$$D_u^{\pi^+} = D_{\bar{d}}^{\pi^+}, \qquad D_d^{\pi^+} = D_{\bar{u}}^{\pi^+}. \tag{A.5}$$

In addition to these "reliable" conditions, some constraints are imposed, such as $D_d^{\pi^+} = D_s^{\pi^+} = D_{\bar{s}}^{\pi^+}$ based on symmetry for non-valence quarks [69, 134]. Flavor-separated FFs are often obtained utilizing experimental data where two hadrons are tagged at the final state [133]. For example, pion measured with D meson tagged lead to pion FF from c quark, D_c^π. It is also hard to extract gluon FF in simple measurement with one hadron tagged. To determine gluon FF, method with three jets tagged is applied. One of the three jets originates in the gluon radiated by the quark which is the source of other jets.

After the determination of FFs, PDFs of quarks are extracted by SIDIS measurements in which obtained FFs are used. To measure gluon PDF, pp collision is effective because gluon appears in the reaction at the leading order, and PDFs/FFs obtained above are valid in analyzing pp collisions.

In the same way as the unpolarized case, cross section of polarized DIS and pp collision can be also factorized, and the universality of polarized PDF and FF is also available. Polarized FFs and PDF are obtained by polarized e^+e^- collision and (SI)DIS, respectively. However, compared with unpolarized experiments, precision of the polarized experimental data is limited and rather larger uncertainties of polarized FFs and PDFs still remain as described in Sec. 1.2.2.

Appendix B

Fast Monte Carlo (FastMC) Simulation

FastMC is a simple numerical simulation unlike GEANT and utilizes the measured cross section of π^0 or η as the particle generator. The produced π^0s decay into two photons isotropically in the rest frame of π^0. In the generation of π^0, the spread of the event vertex is simulated based on Gaussian with a width of 30 cm, which is a little narrower than the measured width but the difference does not change the results. FastMC simulates the photons from π^0 with the following setup:

- Energy and position resolution

  The initial energy and position is fluctuated following Gaussian distribution. The resolutions are evaluated by the test beam. In this simulation, the additional factor is applied to fit the real data.

- Electromagnetic shower profile

  The profile of the electromagnetic shower is simulated and tower-by-tower energy threshold ($\sim$10 MeV) is applied based on the profile. Selection of the core towers in the PbSc clustering is also simulated. See Sec. 4.2.1 about the clustering.

- Warn and edge towers

  Masked region of EMCal due to the warn or edge towers is simulated. See Sec. 4.3.2 about the warn and edge towers.

- Trigger efficiency of ERT

  The trigger efficiency of ERT is applied for the single photon. See Sec. 2.2.5 about the ERT.

Because the Tof cut is difficult to simulate, they are not applied in the comparison between the data and FastMC.

The absolute energy scale is calibrated by comparing the p_T dependence of π^0/η peak to the FastMC simulation. The energy scale is tuned in the FastMC with additional attenuation length (λ_{add}).

As well as the energy scale, the resolutions of the energy and position are also reflected in the p_T dependence of the measured width of π^0/η. Therefore, the energy and position resolution in the FastMC must be also tuned to fit the real data.

In the real data, the π^0 peak position becomes lower due to the unusual π^0s. One of the sources of such π^0 is the case that photons from the decay of π^0 convert into the electron positron pairs. π^0 is well reconstructed using such e^+e^- pairs, when they do not separate each other to form the single clusters.

π^0 from the decay of other hadrons, such as K_s^0 and η, is another source. One other is π^0 generated in the secondary interaction with the beam pipe or detectors. The invariant mass of two photon pair, $M_{\gamma\gamma}$ are calculated as:

$$
\begin{aligned}
M_{\gamma\gamma}^2 &= 2E_1E_2(1-\cos\theta) \\
&= 4E_1E_2\sin^2\frac{\theta}{2},
\end{aligned}
\tag{B.1}
$$

where E_1 and E_2 represent energy of two photon clusters and θ is the opening angle between the clusters. Because we assume photons detected in the EMCal are originated from the collision vertex when reconstructing $M_{\gamma\gamma}$, the reconstructed mass of the unusual π^0s have lower peak position than the usual π^0s (see Fig. B.1).

The size of the shift due to these effect is evaluated by means of the GEANT simulation, and is -1 ± 1 MeV/c^2 [108]. Because the FastMC cannot simulate this effect, the peak position of π^0s is simply lowered by 1 MeV/c^2 in the FastMC.
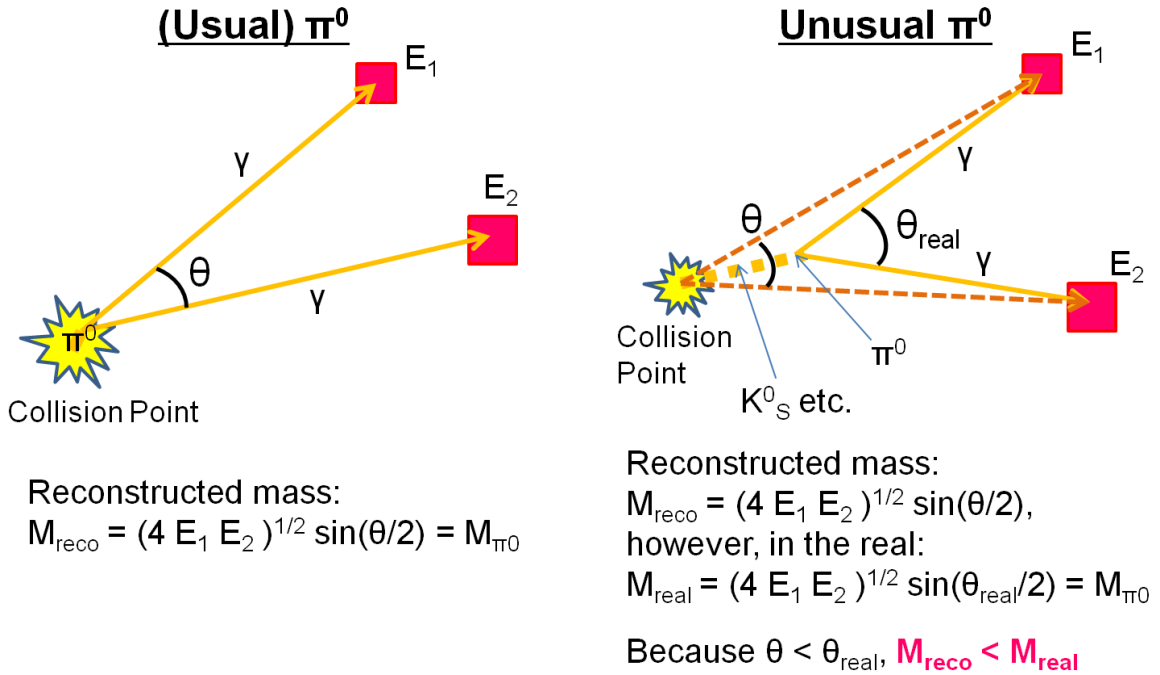

Figure B.1: Left: A schematic drawing of (usual) π^0 mass reconstruction. Right: A schematic drawing of unusual π^0 mass reconstruction.

Appendix C

Luminosity Corrections for Pile-up and Accidentals

The formulae of the rate corrections for the multi-collision effect is derived in this appendix.

The distribution for the number of collisions in a crossing follows a Poisson distribution:

$$P(n; \mu) = \sum_{n=0}^{\infty} \frac{e^{-\mu} \mu^n}{n!}, \tag{C.1}$$

where μ is the true rate of collisions per crossing which produce hits in the luminosity detectors. Once one knows μ, the luminosity can be easily obtained as:

$$L = R_{BBC}^{true}/\sigma_{BBC} = \mu \epsilon_{BBC}/\sigma_{BBC} = \mu/\sigma_{pp,total}, \tag{C.2}$$

where the BBC is used as the example luminosity detector. ϵ_{BBC} is the BBC efficiency and σ_{BBC} is the cross section seen by the BBC. The total collision cross section $\sigma_{pp,total}$ can be taken from the PDG parameterization [113]. $\sigma(s) = 35.45 + 0.308 \log^2(s/28.94) + 42.53(1/s)^{0.458} - 33.34(1/s)^{0.545}$ which gives 60.859 mb for $\sqrt{s} = 500$ GeV.

A collision can produce one of only four outcomes: only the North BBC is hit, only the South BBC is hit, both are hit, or neither detector is hit. The luminosity correction must be applied for the mis-measurement of luminosity when using the BBC trigger rate as a luminosity monitor. For example, the mis-measurements occur when more than one collision in the crossing produces events where both BBCs are hit. The BBC only counts once and it undercounts in this case. There is also the possibility that one can have a crossing where one collision produces a hit in the North BBC, and another produces a hit in the South BBC. In this case, the BBC coincidence counts up when it should not, producing an over counting of the coincidence rate.

For the following discussion, we define the following notation:

- μ = true rate of all collisions which produce hits in the BBC per crossing. Note that $\mu \in [0, 1]$.

- $\epsilon_{B,N}(z)$ = Probability given that there is a collision for having a hit only in the North BBC.

- $\epsilon_{B,S}(z)$ = Probability given that there is a collision for having a hit only in the South BBC.

- $\epsilon_0(z)$ = Probability given that there is a collision for having no hits in either BBC.

- $\epsilon_{BB}(z)$ = Probability given that there is a collision for having hits in both BBCs, i.e. there is a trigger.

- R_{BBN} is the rate of BBC North triggers, including both singles and doubles.

- R_{BBS} is the rate of BBC South triggers, including both singles and doubles.

- R_{BBC} is the rate of BBC coincidence triggers.

- R_{BN} is the rate of BBC north triggers, "excluding" the contribution from ϵ_{BB} events.

- R_{BS} is the rate of BBC south triggers, "excluding" the contribution from ϵ_{BB} events.

Note that for a two arm detector, there are only the above four possibilities $\epsilon_{B,N}$, $\epsilon_{B,S}$, ϵ_0, ϵ_{BB}, and thus there is the condition of:

$$1 = \epsilon_{BB}(z) + \epsilon_{B,N}(z) + \epsilon_{B,S}(z) + \epsilon_0(z). \tag{C.3}$$

The true rates are given by $R_{BBC}^{true} = \mu\epsilon_{BB}$, $R_{BN}^{true} = \mu\epsilon_{B,N}$, and so on. For completeness, there is a relation of $R_{BN}^{true} = R_{BBN}^{true} - R_{BBC}^{true}$, i.e., a single sided detector counts both singles and coincidence events.

To calculate the distortion to the rates from pileup events and accidental coincidences from single hits, we need to work out all the combinatoric probabilities of the four event types for crossings with n collisions. Then, we need to select out the combinations of collisions which would count as a BBC coincidence, and sum them over the distribution of collisions per crossing given by Eq. C.1. Alternatively, we can calculate the probability $P(0)$ for the various combinations of collisions which do not trigger the BBC, and get the probability of the BBC firing directly from $1 - P(0)$. In practice, this way is much easier. The probability of no coincidence in the BBC consists of collisions in which any combination of events produces hits only in one arm. Summing up all these probabilities, one gets:

$$R_{BBC} = 1 - P(0) = 1 - \sum_{n=0}^{\infty} \frac{e^{-\mu}\mu^n}{n!} \left(\sum_{m=0}^{n} (_nC_m\epsilon_{B,N}^m\epsilon_0^{n-m} +_n C_m\epsilon_{B,S}^m\epsilon_0^{n-m}) - \epsilon_0^n \right)$$
$$= 1 - e^{-\mu(\epsilon_{BB}+\epsilon_{B,N})} - e^{-\mu(\epsilon_{BB}+\epsilon_{B,S})} + e^{-\mu(\epsilon_{BB}+\epsilon_{B,N}+\epsilon_{B,S})}. \tag{C.4}$$

The second line of Eq. C.4 follows from the binomial theorem and the Taylor series expansion for e. The ϵ values can be extracted from beam clock triggered events and the vernier scan. Note that effects from non-collisions, such as beam gas or beam scrape is ignored here. At low rates μ, the measured coincidence rate reduces to:

$$R_{BBC} = 1 - e^{-\mu\epsilon_{BB}} + \mu^2\epsilon_{B,N}\epsilon_{B,S}. \tag{C.5}$$

The $1 - e^{-\mu\epsilon_{BB}}$ term corrects for the under counting due to multiple BBC coincidence events occurring in the same crossing, while the $\mu^2\epsilon_{B,N}\epsilon_{B,S}$ term accounts for the single hits accidentally forming a coincidence, which is exactly consistent with the prior expectations.

Although Eq. C.4 expresses the measured BBC coincidence rate (R_{BBC}) as a function of the true singles and coincidence rates ($\mu\epsilon_{B,N}, \mu\epsilon_{B,S}$ and $\mu\epsilon_{BB}$), it is possible to reformulate the equation in terms of only the measured singles rates (R_{BBN}, R_{BBS}), coincidence rates (R_{BBC}), and the true BBC coincidence rate ($\mu\epsilon_{BB}$). Therefore, one can solve for the true BBC coincidence rate in terms of only measured quantities. For instance, the inclusive rate in the North BBC (R_{BBN}) is calculated in the following manner: Firstly the probabilities of "no" having any hit in the north BBCs ($P_N(0)$) is calculated, and then take $1 - P_N(0)$ as discussed above. $P_N(0)$ consists of all the combinations of collisions which produce either no hit in either BBC or hits in only the south BBC, properly summed over the distribution of the number of collisions, and R_{BBN} is written as:

$$R_{BBN} = 1 - P_N(0) = 1 - \sum_{n=0}^{\infty} \frac{e^{-\mu}\mu^n}{n!} \sum_{m=0}^{n} ({}_nC_m \epsilon_{B,S}^m \epsilon_0^{n-m})$$

$$= 1 - e^{-\mu(1-\epsilon_0-\epsilon_{,S})} \tag{C.6}$$

$$= 1 - e^{-\mu(\epsilon_{B,N}+\epsilon_{BB})}. \tag{C.7}$$

A similar equation exists for R_{BBS}. Substituting into Eq. C.4:

$$R_{BBC} = 1 - (1 - R_{BBN}) - (1 - R_{BBS}) + e^{\mu\epsilon_{BB}}(1 - R_{BBN})(1 - R_{BBS}), \tag{C.8}$$

which becomes:

$$R_{BBC}^{true} = \ln\left(\frac{(1 - R_{BBN}) + (1 - R_{BBS}) - (1 - R_{BBC})}{(1 - R_{BBN})(1 - R_{BBS})}\right), \tag{C.9}$$

when solved for the true BBC coincidence rate ($R_{BBC}^{true} = \mu\epsilon_{BB}$). For the exclusive singles rate, the equation is:

$$R_{BN}^{true} = -\ln(1 - R_{BBN}) - R_{BBC}^{true}. \tag{C.10}$$

Therefore, we can get the true rates directly using Eq. C.9 and C.10 when measuring the singles and coincidence rates of a detector.

Equation C.4 can be expressed in terms of R_{BBC}^{true} ($= \mu\epsilon_{BB}$) only by substituting in $k_N = \epsilon_{B,N}/\epsilon_{BB}$ and $k_S = \epsilon_{B,S}/\epsilon_{BB}$ as:

$$R_{BBC} = 1 - e^{-\mu\epsilon_{BB}(1+k_N)} - e^{-\mu\epsilon_{BB}(1+k_S)} + e^{-\mu\epsilon_{BB}(1+k_N+k_S)}. \tag{C.11}$$

k_N and k_S can be determined when the cross sections seen by a single BBC versus the coincidence is evaluated, or one can empirically determine the ratios from data, such as beam clock triggered data or from scalers. For the 500 GeV pp case, we have determined that $k_N = k_S = 0.282 \pm 0.006$. Then, the rate correction factor ($C(R_{BBC})$: see Table 4.2) is calculated using Eq. C.11.

Appendix D

Tracking Performance

As a quality assurance of the DC and PC1 data set, number of tracks per MB (Minimum Bias: BBCLL1) event (N_{trk}/N^{MB}) was checked. Tracks with hits on X1 and X2 plane of the DC and on the PC1 with $p_T > 2.0$ GeV/c are selected.

Figure D.1 shows N_{trk}/N^{MB} in each ϕ_{DC} bin as a function of run number (run number of the horizontal axis is in arbitrary unit. Top panel: East arm, Bottom panel: West arm, Left side: South side, Right side: North side). It can be noticed that some part of the DC/PC1 is unstable (e.g. $3.6 < \phi_{DC} < 3.7$) and some part of the DC/PC1 become dead (e.g. $-0.2 < \phi_{DC} < 0$) during Run 9 period.
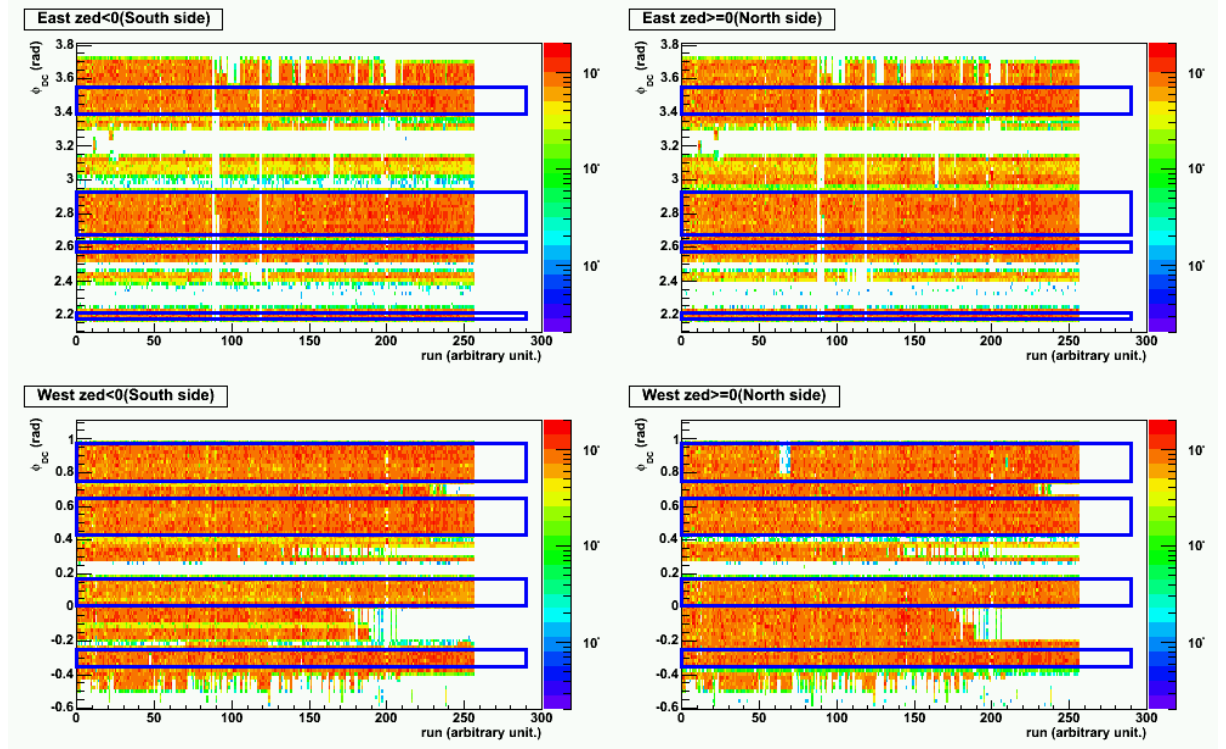

Figure D.1: N_{trk}/N^{MB} in each ϕ_{DC} bin as a function of run number. (positive charge, Top panel: East arm, Bottom panel: West arm, Left side: South side, Right side: North side). Blue boxes indicate the stable parts during Run 9 where is picked up to make Fig. D.2 and D.3.

Figure D.2 displays the N_{trk}/N^{MB} as a function of run number when choosing stable parts which are indicated with blue boxes in Fig. D.1 [1] (Top panel: East arm, Bottom panel: West arm, Left side: South side, Right side: North side). The N_{trk}/N^{MB} in this figure is slightly increased with time throughout the Run 9 period. It turned out to be explained by multiple events in data holding period of the DC (pile up effect). Since the data holding time of DC is not one beam crossing clock, it results in counting track events which occurred in the previous crossing at the recorded crossing in high trigger rate runs.

Figure D.3 shows the rate $(= N^{MB}/(\# \text{ of Beam Crossings}))$ dependence of N_{trk}/N^{MB} and clear correlation is observed. Expected rate dependence caused by the pile up effect are also drawn in the figure. The function form of the expected rate dependence is:

$$y = y_0 \times \frac{x_0}{\ln(1 - \text{NCLK} \times x_0)} \times \frac{\ln(1 - \text{NCLK} \times x)}{x}, \tag{D.1}$$

where x represents the rate $(N^{MB}/(\# \text{ of Beam Crossings}))$, y is the N_{trk}/N^{MB}, (x_0, y_0) stands for an arbitrary point (in Fig. D.3, x_0 is fixed at 0.1214 and y_0 is a free parameter for fitting), and "NCLK" represents the data holding period of the DC (i.e. gate width, unit: beam crossing clock, this is also a free parameter for fitting). This function form is extracted by the following manner:

1. Take two points in N_{trk}/N^{MB} vs rate plane, for example, (x_0, y_0) and (x, y).

2. Assuming N_{trk}/N^{MB} does not depend on the collision rate when N^{MB} is calculated properly, the following expression should have equality:

$$\frac{N_{trk}}{N^{MB} \times (-\ln(1 - \text{NCLK} \times x)/(\text{NCLK} \times x))} = (const.), \tag{D.2}$$

where the term of $(-\ln(1 - \text{NCLK} \times x)/(\text{NCLK} \times x))$ is the correction factor of the multiple collision effect [2].

3. Applying the relationship of Eq. D.2 to (x_0, y_0) and (x, y), the function form of Eq. D.1 can be obtained.

The obtained NCLK from fitting is about 3.1 clocks that is consistent with the DC design (3 clocks). This number is used in the acceptance calculation for rate correction (Sec. 4.3.5)

Figure D.4 shows the N_{trk}/N^{MB} as a function of run number (including unstable parts) and run-by-run fluctuation become larger than Fig. D.2. The larger fluctuation are considered to come from the run-by-run acceptance change of the DC/PC1. Since a technique to handle this fluctuation is employed in acceptance calculation (see Sec. 4.3.5), no run is rejected and no ϕ_{DC} region is masked in this thesis.

---

[1] N_{trk}/N^{MB} in this figure is calculated by integral over ϕ_{DC} bin of each part (i.e. East arm South side, East arm North side, West arm South side and West arm North side).
[2] This correction is the first order approximation of the correction described in the Appendix C.
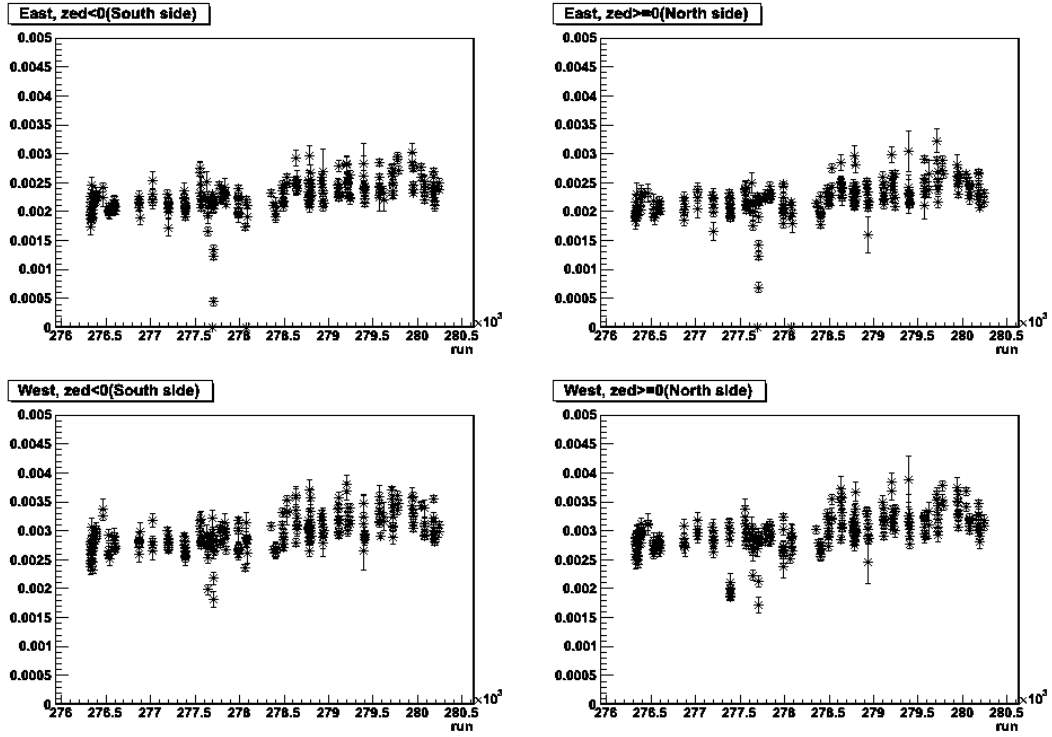
Figure D.2: Number of tracks per MB event (N_{trk}/N^{MB}) at stable parts of the DC/PC1 as a function of run number (positive combined, Left:South side, Right:North side, Top: East arm, Bottom: West arm). The N_{trk}/N^{MB} is slightly increased with time throughout the Run 9 period due to the pile up effect. The fluctuation observed in short time period is originated from the rate degeneration during a beam fill.
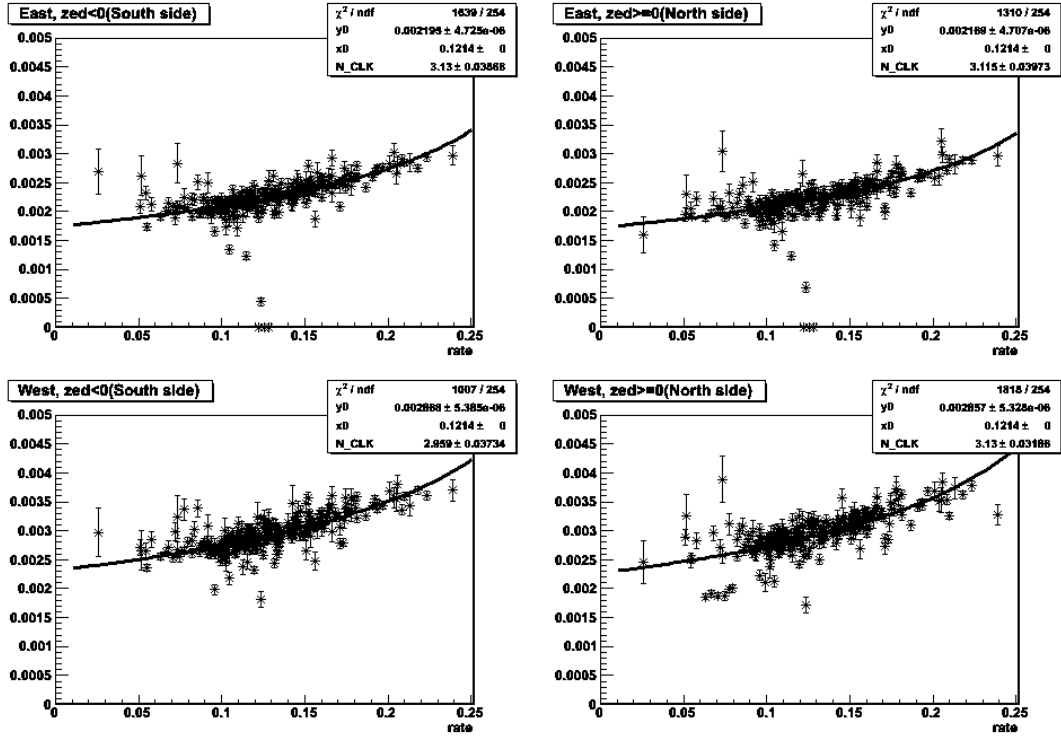

Figure D.3: Number of tracks per MB event at stable parts of DC/PC1 as a function of beam rate. (positive charge, Left:South Side, Right:North Side)

136
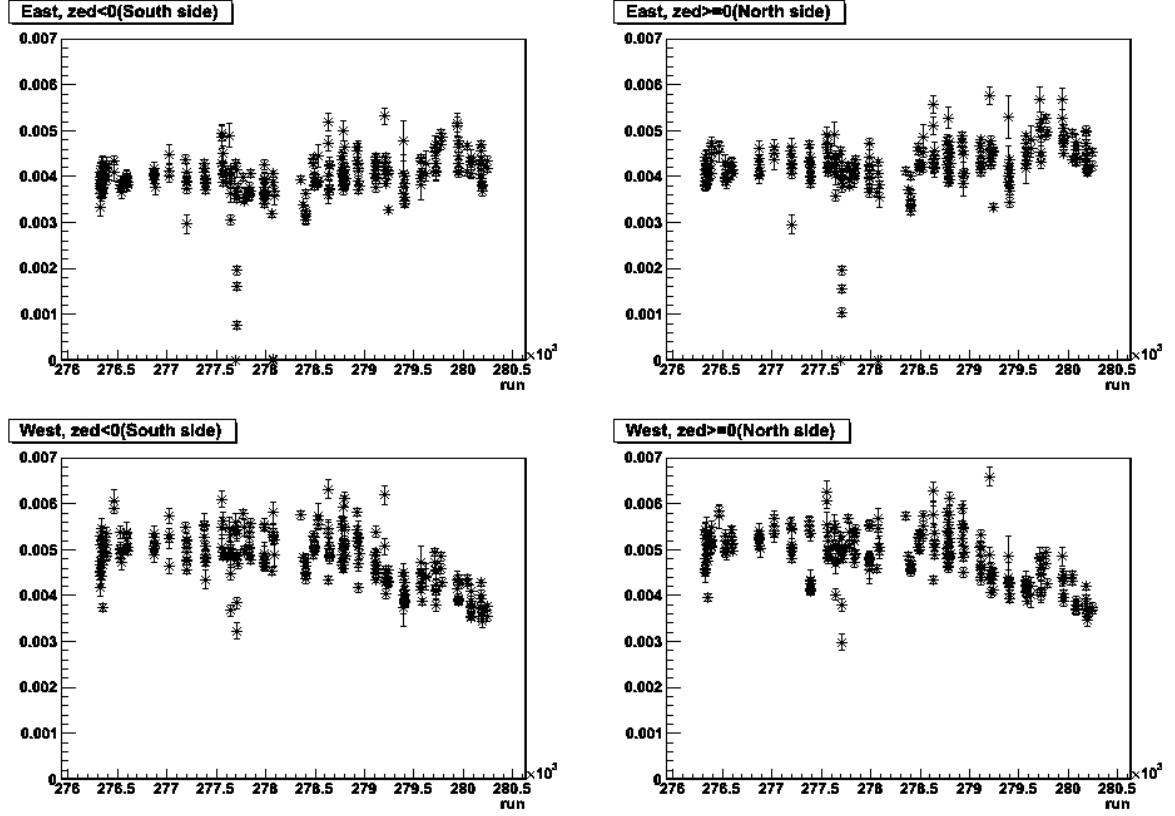
Figure D.4: number of tracks per MB event as a function of run number. (positive charge, Left:South Side, Right:North Side) A large run dependence comes from the acceptance change is observed. For example, large drop around run 277700 and run 278000 in East arm are corresponding to the acceptance lost and the decrease in West arm after run 279100 is mainly due to the dead area of $-0.2 < \phi_{DC} < 0$ (you can also notice these acceptance lost in Fig. D.1. The fluctuation observed in short time period is originated from the rate degeneration during a beam fill.

Appendix E

Contamination from Residual Transverse Polarization

E.1   Residual Transverse Polarization

As described in Sec. 2.1.3, the polarization direction is rotated from transverse to longitudinal just before the interaction point (IP) and the presence of any residual transverse polarization should be monitored at the PHENIX IP. The single transverse spin asymmetry (A_N: Eq. 2.1 in Sec. 2.1.3) of forward neutron production measured with ZDCs and SMDs is utilized for this purpose. The spin direction at the PHENIX IP is evaluated by the comparison of the measured A_N amplitude at longitudinal run period, $A_N^{Longitudinal}$, and that at transverse run period, $A_N^{Transverse}$. The longitudinal and transverse components of the polarization direction at longitudinal period is extracted by:

$$\frac{P_L}{P} = \sqrt{1 - \left(\frac{P_T}{P}\right)^2}, \qquad \frac{P_T}{P} = \frac{A_N^{Longitudinal}}{A_N^{Transverse}}. \tag{E.1}$$

Since it is possible that the transverse component is diagonal after the spin rotation, comparison should be performed by not only the amplitude but also the phase of azimuthal dependence. However, it is difficult to obtain correct values from the fit results of sine modulation [1] in case of nearly zero asymmetry as fit result is labile. For the stable operation, the comparison has been performed with the LR (Left-Right) asymmetry, $A_{LR}^{Longitudinal}$, and UD (Up-Down) asymmetry, $A_{UD}^{Longitudinal}$. P_T/P can be represented as:

$$\frac{P_T}{P} = \sqrt{\kappa_{LR}^2 + \kappa_{UD}^2}, \quad \text{where } \kappa_{LR} \equiv \left(\frac{A_{LR}^{Longitudinal}}{A_N^{Transverse}}\right), \kappa_{UD} \equiv \left(\frac{A_{UD}^{Longitudinal}}{A_N^{Transverse}}\right). \tag{E.2}$$

The phase information is included in the relation of them (e.g. κ_{LR}/κ_{UD}).

During the Run 9 period, the LocalPol team at PHENIX has measured fill by fill residual transverse polarization (P_T/P) with newly implemented local polarimeter scaler. The measured P_T/P are $7-12$ % in the blue beams and $3-5$ % in the yellow beam [95]. These values are corresponding to more than 99 % of the relative longitudinal polarization (P_L/P). The uncertainty of the blue beam is larger due to a sign error in some of the RHIC beam position monitors, which caused errors in the orbit of the blue beam.

---

[1] A_N is governed with the sine modulation to the transverse spin component.

E.2 Contamination to Measured A_L

The residual transverse polarization, along with a nonzero A_N for the electron/positron candidates in our sample, would create a left-right asymmetry, and that causes a contamination to the measured A_L. Considering the transverse polarization, the yield of electrons/positrons detected by PHENIX at the angle of (θ, ϕ) in polarized pp collisions is written as:

$$
\begin{aligned}
N(\theta, \phi) = \sigma(\theta)\, \varepsilon(\theta, \phi)\, \mathcal{L}\, [\, 1 \quad &+ \quad A_L^B(\theta)P_L^B + A_N^B(\theta)P_T^B \cos(\phi - \phi_B) \\
&+ \quad A_L^Y(\theta)P_L^Y + A_N^Y(\theta)P_T^Y \cos(\phi - \phi_Y) \\
&+ \quad A_{LL}(\theta)P_L^B P_L^Y + \mathrm{O}(\vec{P}_T^B \cdot \vec{P}_T^Y) + ... \,].
\end{aligned}
\tag{E.3}
$$

Here, θ and ϕ represent the polar angle relative to z-axis and the azimuthal angle relative to the positive x direction, respectively (see Fig. 2.9 in Sec. 2.2). The variables in this equation are described in Table E.1. $\mathrm{O}(\vec{P}_T^B \cdot \vec{P}_T^Y)$ in the equation shows higher order terms involving squared P_T, and are ignored in the following discussion because the magnitudes are $10^{-2} \sim 10^{-3}$ lower than the longitudinal polarization.

notation	explanation
$\sigma(\theta)$	Unpolarized cross section at a scattering angle θ. (there is no ϕ dependence)
$\mathcal{L}$	Integrated luminosity.
$\varepsilon(\theta, \phi)$	Electron/positron reconstruction efficiency
$A_L^j(\theta)$	Longitudinal single spin asymmetry for the j (Blue or Yellow) beam and the electron/positron measured at a scattering angle θ.
$A_N^j(\theta)$	Transverse single spin asymmetry for the j beam. The azimuthal angle dependence in the equation is taken from [135].
$A_{LL}(\theta)$	Longitudinal double spin asymmetry.
P_L^j	Longitudinal polarization of the j beam.
P_T^j	Transverse polarization of the j beam.
ϕ_j	Azimuthal angle of the P_T^j relative to the vertical direction (i.e. positive y direction).

Table E.1: explanations of variables in Eq. E.3.

The number of recorded electrons/positrons is given by the integral of Eq. E.3:

$$
\begin{aligned}
N_e &= \int_{\mathrm{PHENIX}} d\theta d\phi\, N(\theta, \phi) \\
&= \sigma\, \mathcal{L}\, (\, 1 + \widetilde{A_L^B}P_L^B + \widetilde{A_N^B}\delta_B P_T^B + \widetilde{A_L^Y}P_L^Y + \widetilde{A_N^Y}\delta_Y P_T^Y + \widetilde{A_{LL}}P_L^B P_L^Y\,),
\end{aligned}
\tag{E.4}
$$

where:

$$
\sigma = \int d\theta d\phi\, \sigma(\theta)\varepsilon(\theta, \phi),
$$

$$
\widetilde{A_L^j} = \frac{1}{\sigma} \int d\theta d\phi\, A_L^j(\theta)\sigma(\theta)\varepsilon(\theta, \phi),
$$

$$
\widetilde{A_N^j}\delta_j = \frac{1}{\sigma} \int d\theta d\phi\, A_N^j(\theta)\sigma(\theta)\varepsilon(\theta, \phi) \cos(\phi - \phi_j) \quad \left(\delta_j \sim \int d\phi\, \varepsilon(\phi) \cos(\phi - \phi_j)\, /\, \int d\phi\, \varepsilon(\phi) \right),
$$

$$
\widetilde{A_{LL}} = \frac{1}{\sigma} \int d\theta d\phi\, A_{LL}(\theta)\sigma(\theta)\varepsilon(\theta, \phi).
$$

Here, j denotes the beam (Blue or Yellow) and all integrals should be performed in the PHENIX acceptance ($|\eta| < 0.35$, $\Delta\phi = \pi$). Since Blue and Yellow beams are identical except for left-right reversal, the following relation holds:

$$\widetilde{A_L^B} = \widetilde{A_L^Y} \equiv A_L, \qquad \widetilde{A_N^B} = -\widetilde{A_N^Y} \equiv A_N, \tag{E.5}$$

so that Eq. E.4 can be written as:

$$N_e = \sigma\, \mathcal{L}\, (\, 1 + A_L P_L^B + A_L P_L^Y + A_N \delta_B P_T^B - A_N \delta_Y P_T^Y + A_{LL} P_L^B P_L^Y\,), \tag{E.6}$$

with one more substitution of $A_{LL} \equiv \widetilde{A_{LL}}$. Using this relation, Eq. 4.11 in Sec. 4.4 is modified as:

$$
\begin{cases}
\sigma_{++} = (1 + A_L P_L^B + A_L P_L^Y + A_N \delta_B P_T^B - A_N \delta_Y P_T^Y + A_{LL} P_L^B P_L^Y) \cdot \sigma, \\
\sigma_{+-} = (1 + A_L P_L^B - A_L P_L^Y + A_N \delta_B P_T^B + A_N \delta_Y P_T^Y - A_{LL} P_L^B P_L^Y) \cdot \sigma, \\
\sigma_{-+} = (1 - A_L P_L^B + A_L P_L^Y - A_N \delta_B P_T^B - A_N \delta_Y P_T^Y - A_{LL} P_L^B P_L^Y) \cdot \sigma, \\
\sigma_{--} = (1 - A_L P_L^B - A_L P_L^Y - A_N \delta_B P_T^B + A_N \delta_Y P_T^Y + A_{LL} P_L^B P_L^Y) \cdot \sigma.
\end{cases}
\tag{E.7}
$$

One can see from the above equations that for a perfect PHENIX detector with the perfectly vertical transverse polarization (i.e. $\phi_j = 0$), the residual A_N contributions are naturally suppressed by δ_j factors as PHENIX covers symmetric regions around y-axis [2].

However, in the real world, the effect on A_L from a residual transverse polarization might not exactly cancel because of (θ, ϕ) dependence of the acceptance from dead areas or other cuts, and also because it is possible that there is a non-vertical transverse polarization (i.e. finite ϕ_j). Using a toy MC where particles were distributed with $\cos(\phi - \phi_j)$, we evaluated the effect which a non-zero vertical polarization would have on the A_L. At a phase of $\phi_j = 15°$, the residual effect on A_L is 5 % of A_N ($\delta_j \sim 0.05$). Putting realistic dead areas in the MC, the 5 % of the residual effect on A_L is changed by only O(10 %). Taking into account all effects, the A_L could be modified by:

$$A_N \delta_j P_T^j \sim 5\ \% \times (12\ \% P_L) \times A_N = 0.006 \times P_L \times A_N. \tag{E.8}$$

With a 12 % of relative transverse component (P_T/P), the A_N is still suppressed by over a factor of 100. Even assuming that A_N were 10 %, any contribution to A_L from a nonzero A_N and realistic residual transverse polarization would be at $\sim 10^{-3}$ level, and could be ignored. Note that it is likely that the A_N is negligibly small since the A_N at mid-rapidity has been measured to be zero up to p_T of ~ 10 GeV/c at 200 GeV [136, 137], therefore the assumption of 10 % A_N is a very conservative estimation.

---

[2]In this case, $\delta_j \sim \int d\phi\ \cos\phi\ /\ \int d\phi = 0$.

Appendix F

Spin Fit Quality Check

Spin asymmetries in Sec. 4.4.2 are calculated from the maximum likelihood method. Although the results are compared to the calculation from Eq. 4.9 and they are consistent with each other, it is better to confirm the reliability of fitting process in different way.

As the likelihood function (Eq. 4.15) has three parameters $(\sigma, \varepsilon_L, \varepsilon_{LL})$, and only four spin states $(++, +-, -+, --)$ is available in the fitting process, only one degree of freedom (DOF) remains. When there are plenty of statistics, it can be checked whether the fit is reasonable or not by calculating chi-square value and comparing it to the chi-square distribution with one DOF. However, it is difficult for this analysis to be checked in that manner because the uncertainty does not follow the Gaussian distribution due to the small statistics.

The easiest way to check the validity of the spin fit is to produce a probability distribution of Eq. 4.15. Once three parameters are determined, $L = \prod f_i$ (i denotes four spin states) can be calculated. In order to make a probability distribution of $L = \prod f_i$, a toy MC is demonstrated in the following procedures:

1. Using σ^{data}, ε_L^{data}, ε_{LL}^{data} (evaluated values from the data) and L_i (relative luminosity), generate a set of pseudo four spin states (N_i^{MC}) with TRandom3::Poisson() [1].

2. Fit N_i^{MC} with the maximum likelihood method to get σ^{MC}, ε_L^{MC} and ε_{LL}^{MC}. Note that these values are not exactly same as σ^{data}, ε_L^{data} and ε_{LL}^{data}, respectively.

3. Using σ^{MC}, ε_L^{MC}, ε_{LL}^{MC}, L_i and N_i^{MC}, calculate $L = \prod f_i$.

These procedures are repeated 500 times and a probability distribution of $L = \prod f_i$ is generated.

Figure F.1 shows the probability distribution of $L = \prod f_i$ made by this toy MC (Left: positive, Right: negative charge). In order to compare the probability distribution to chi-square distribution with one DOF, L is converted in the following variable [2]:

$$var. = -2 \cdot (\ln(L) - \ln(A)),$$

$$A = \prod_{4 \text{ spin states}} 1/\sqrt{2\pi}\sigma_i, \ \sigma_i = \sqrt{\mu_i^{MC}} \tag{F.1}$$

---

[1] TRandom3 is a random number generator implemented in ROOT.

[2] The probability distribution is not expected to match to the chi-square distribution because of our small statistics. This variable transformation is just to check how the probability distribution differs from the chi-square distribution.

(μ_i is calculated from Eq. 4.16). This formula is extracted by comparing chi-square to $L = \prod f_i$ in the large statistical limit where f_i (Poisson distribution) can be approximated to Gaussian distribution. The Red lines drawn in Fig. F.1 are the probability value of the real data. Since they seem normal value in the probability distribution, it can be concluded that the spin fit with the maximum likelihood method is reasonable.
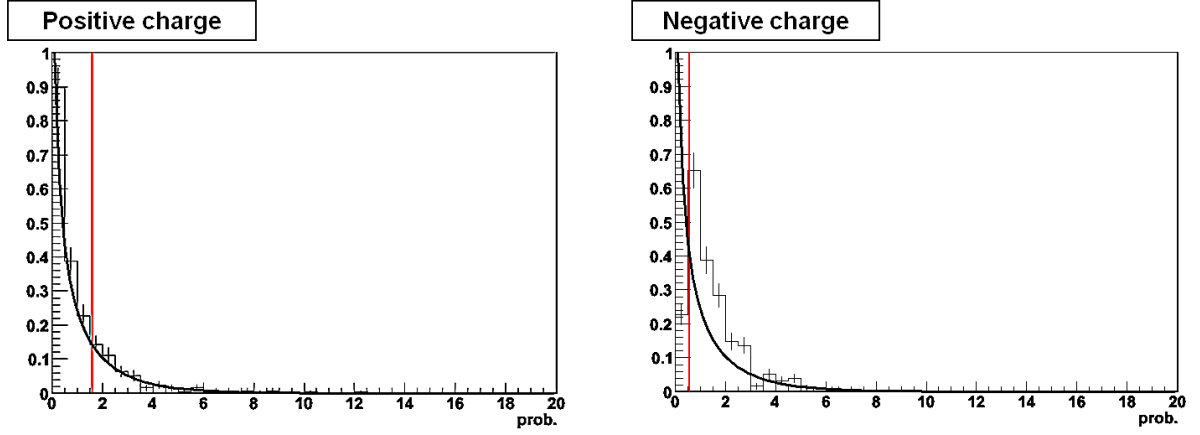

Figure F.1: Probability distribution obtained by repeating process (1-3) 500 times (Left: positive, Right: negative charge). The Red line indicates the probability value of the real data and it looks normal value in the distribution. The Black curve shows the chi-square distribution with one DOF. The probability distribution is not so different from the chi-square distribution for positive charge. On the other hand, it is slightly different for negative charge because of the small statistics.

Reference

[1] M. Gell-Mann, Phys. Lett. **8**, 214 (1964).

[2] J. Ashman et al. (European Muon), Phys. Lett. **B206**, 364 (1988).

[3] J. Ashman et al. (European Muon), Nucl. Phys. **B328**, 1 (1989).

[4] A. Airapetian et al. (HERMES Collaboration), Phys. Rev. D **75**, 012007 (2007).

[5] V. Alexakhin et al., Physics Letters B **647**, 8 (2007).

[6] K. Nakamura et al. (Particle Data Group), J. Phys. **G37**, 075021 (2010).

[7] M. G. Alekseev et al. (COMPASS), Phys. Lett. **B693**, 227 (2010), `1007.4061`.

[8] A. Airapetian et al. (HERMES), Phys. Rev. **D71**, 012003 (2005), `hep-ex/0407032`.

[9] B. Adeva et al., Physics Letters B **420**, 180 (1998).

[10] G. Bunce, N. Saito, J. Soffer, and W. Vogelsang, Ann. Rev. Nucl. Part. Sci. **50**, 525 (2000), `hep-ph/0007218`.

[11] C. Bourrely and J. Soffer, Physics Letters B **314**, 132 (1993).

[12] D. de Florian and W. Vogelsang, Phys. Rev. **D81**, 094020 (2010), `1003.4533`.

[13] P. M. Nadolsky and C. P. Yuan, Nuclear Physics B **666**, 31 (2003).

[14] M. A. Doncheski, F. Halzen, C. S. Kim, and M. L. Stong, Phys. Rev. D **49**, 3261 (1994).

[15] J. C. Peng and D. M. Jansen, Physics Letters B **354**, 460 (1995).

[16] C. Bourrely and J. Soffer, Nuclear Physics B **423**, 329 (1994).

[17] F. Abe et al. (CDF Collaboration), Phys. Rev. Lett. **81**, 5754 (1998).

[18] V. M. Abazov et al. (D0 Collaboration), Phys. Rev. Lett. **101**, 211801 (2008).

[19] T. Aaltonen et al. (CDF Collaboration), Phys. Rev. Lett. **102**, 181801 (2009).

[20] S. D. Ellis and W. J. Stirling, Physics Letters B **256**, 258 (1991).

[21] A. Baldit et al., Physics Letters B **332**, 244 (1994).

[22] E. A. Hawker et al. (Fermilab E866/NuSea Collaboration), Phys. Rev. Lett. **80**, 3715 (1998).

[23] J. C. Peng et al. (FNAL E866/NuSea Collaboration), Phys. Rev. D **58**, 092004 (1998).

[24] R. S. Towell et al. (FNAL E866/NuSea Collaboration), Phys. Rev. D **64**, 052002 (2001).

[25] P. Amaudruz et al., Phys. Rev. Lett. **66**, 2712 (1991).

[26] M. Arneodo et al., Phys. Rev. D **50**, R1 (1994).

[27] K. Ackerstaff et al. (HERMES Collaboration), Phys. Rev. Lett. **81**, 5519 (1998).

[28] R. Devenish and A. C-Sarkar, *Deep Inelastic Scattering* (Oxford University Press, 2005).

[29] J. Callan, Curtis G. and D. J. Gross, Phys.Rev.Lett. **22**, 156 (1969).

[30] A. Pich (1995), `hep-ph/9505231`.

[31] K. Abe et al. (E143 Collaboration), Phys. Rev. **D58**, 112003 (1998), `hep-ph/9802357`.

[32] P. L. Anthony et al. (E155 Collaboration), Physics Letters B **458**, 529 (1999), `hep-ex/9901006`.

[33] G. Altarelli and G. Parisi, Nuclear Physics B **126**, 298 (1977).

[34] Y. L. Dokshitzer, Sov. Phys. JETP **46**, 641 (1977).

[35] V. N. Gribov and L. N. Lipatov, Sov. J. Nucl. Phys. **15**, 438 (1972).

[36] U. K. Yang et al. (CCFR/NuTeV Collaboration), Phys. Rev. Lett. **86**, 2742 (2001).

[37] J. J. Aubert et al., Nuclear Physics B **213**, 1 (1983).

[38] S. Chekanov et al. (ZEUS Collaboration), Phys. Rev. **D69**, 012004 (2004), `hep-ex/0308068`.

[39] C. Adloff et al. (H1 Collaboration), Physics Letters B **528**, 199 (2002).

[40] A. Aktas et al. (H1 Collaboration), Eur. Phys. J. **C40**, 349 (2005), 10.1140/epjc/s2005-02154-8.

[41] A. Aktas et al. (H1 Collaboration), Eur. Phys. J. **C45**, 23 (2006), 10.1140/epjc/s2005-02415-6.

[42] T. Affolder et al. (CDF Collaboration), Phys. Rev. D **64**, 032001 (2001).

[43] A. Abulencia et al. (CDF Collaboration), Phys. Rev. Lett. **96**, 122001 (2006).

[44] A. Abulencia et al. (CDF Collaboration), Phys. Rev. D **74**, 071103 (2006).

[45] B. Abbott et al. (D0 Collaboration), Phys. Rev. D **64**, 032003 (2001).

[46] A. D. Martin, W. J. Stirling, R. S. Thorne, and G. Watt, Eur. Phys. J. **C63**, 189 (2009), `0901.0002`.

[47] C. Adloff et al. (H1 Collaboration), Eur. Phys. J. **C30**, 1 (2003), 10.1140/epjc/s2003-01257-6.

[48] S. Chekanov et al. (ZEUS Collaboration), Eur. Phys. J. **C42**, 1 (2005), 10.1140/epjc/s2005-02293-x.

[49] J. Pumplin et al. (CTEQ Collaboration), JHEP **07**, 012 (2002), `hep-ph/0201195`.

[50] M. Gluck, P. Jimenez-Delgado, and E. Reya, Eur. Phys. J. **C53**, 355 (2008), 10.1140/epjc/s10052-007-0462-9.

[51] S. Alekhin, K. Melnikov, and F. Petriello, Phys. Rev. D **74**, 054033 (2006).

[52] J. D. Bjorken, Phys. Rev. **148**, 1467 (1966).

[53] J. D. Bjorken, Phys. Rev. D **1**, 1376 (1970).

[54] P. Anthony et al., Physics Letters B **493**, 19 (2000).

[55] F. E. Close and R. G. Roberts, Phys. Rev. Lett. **60**, 1471 (1988).

[56] F. E. Close and R. G. Roberts, Physics Letters B **316**, 165 (1993).

[57] M. J. Alguard et al., Phys. Rev. Lett. **37**, 1261 (1976).

[58] M. J. Alguard et al., Phys. Rev. Lett. **41**, 70 (1978).

[59] G. Baum et al., Phys. Rev. Lett. **45**, 2000 (1980).

[60] G. Baum et al., Phys. Rev. Lett. **51**, 1135 (1983).

[61] T. Gehrmann and W. J. Stirling, Phys. Rev. D **53**, 6100 (1996).

[62] M. Glück, E. Reya, M. Stratmann, and W. Vogelsang, Phys. Rev. D **63**, 094005 (2001).

[63] J. Blümlein and H. Böttcher, Nuclear Physics B **636**, 225 (2002).

[64] D. de Florian, G. A. Navarro, and R. Sassot, Phys. Rev. D **71**, 094018 (2005).

[65] M. Hirai, S. Kumano, and N. Saito (Asymmetry Analysis Collaboration), Phys. Rev. D **74**, 014015 (2006).

[66] E. Leader, A. V. Sidorov, and D. B. Stamenov, Phys. Rev. D **73**, 034023 (2006).

[67] D. de Florian, R. Sassot, M. Stratmann, and W. Vogelsang, Phys. Rev. Lett. **101**, 072001 (2008).

[68] D. de Florian, R. Sassot, M. Stratmann, and W. Vogelsang, Phys. Rev. D **80**, 034030 (2009).

[69] S. Kretzer, Phys. Rev. D **62**, 054001 (2000).

[70] B. A. Kniehl, G. Kramer, and B. Potter, Nuclear Physics B **582**, 514 (2000).

[71] A. Adare et al. (PHENIX Collaboration), Phys. Rev. Lett. **103**, 012003 (2009).

[72] B. I. Abelev et al. (STAR Collaboration), Phys. Rev. Lett. **100**, 232003 (2008).

[73] J. C. Collins et al., *Factorization of Hard Process in QCD in Perturbative Quantum Chromodynamics* (World Scientific, 1989).

[74] J. Alitti et al. (UA2 Collaboration), Z. Phys. **C47**, 11 (1990).

[75] J. M. Conrad, M. H. Shaevitz, and T. Bolton, Rev. Mod. Phys. **70**, 1341 (1998).

[76] K. Gottfried, Phys. Rev. Lett. **18**, 1174 (1967).

[77] S. Kumano, Physics Reports **303**, 183 (1998).

[78] G. T. Garvey and J. C. Peng, Prog. Part. Nucl. Phys. **47**, 203 (2001).

[79] D. Geesaman et al., Fermilab Proposal P906 (1999).

[80] B.-Q. Ma, Physics Letters B **274**, 111 (1992).

[81] B.-Q. Ma, A. Schäfer, and W. Greiner, Phys. Rev. D **47**, 51 (1993).

[82] W. Melnitchouk and A. W. Thomas, Phys. Rev. D **47**, 3783 (1993).

[83] M. A. Braun and M. V. Tokarev, Physics Letters B **320**, 381 (1994).

[84] M. Sawicki and J. P. Vary, Phys. Rev. Lett. **71**, 1320 (1993).

[85] I. Schmidt and J.-J. Yang, Eur. Phys. J. C **20**, 63 (2001).

[86] R. Yang, J.-C. Peng, and M. Grosse-Perdekamp, Phys. Lett. **B680**, 231 (2009), 0905.3783.

[87] A. D. Martin, W. J. Stirling, and R. G. Roberts, Physics Letters B **306**, 145 (1993).

[88] Z.-B. Kang, J.-W. Qiu, and W. Vogelsang, Phys. Rev. D **79**, 054007 (2009).

[89] A. Zelenski et al., Hyperfine Interactions **127**, 475 (2000), 10.1023/A:1012682104479.

[90] P. Sona, Energia Nucleare **14**, 295 (1967).

[91] Y. S. Derbenev et al., Part. Accel. **8**, 115 (1978).

[92] O. Jinnouchi et al., RHIC/CAD Accelerator Physics Note **171** (2004).

[93] H. Okada et al., Phys. Lett. **B638**, 450 (2006), nucl-ex/0502022.

[94] A. Bazilevsky et al., Phys. Lett. **B650**, 325 (2007), hep-ex/0610030.

[95] M. Togawa and the LocalPol Team, Run9pp 500GeV Local Polarimeter Result (2009), https://www.phenix.bnl.gov/WWW/p/draft/togawa/run9/LP/PHENIX_LP_PolWorkshop.pdf.

[96] K. Adcox et al. (PHENIX Collaboration), Nucl. Instrum. Meth. **A499**, 469 (2003).

[97] K. Ikematsu et al., Nucl. Instrum. Meth. pp. 238–248 (1998), `arXiv:physics/9802024`.

[98] C. Adler et al., Nucl. Instrum. Meth. **A470**, 488 (2001), `nucl-ex/0008005`.

[99] G. David et al., IEEE Trans. Nucl. Sci. **45**, 705 (1998).

[100] T. C. Awes et al., ArXiv Nuclear Experiment e-prints (2002), `arXiv:nucl-ex/0202009`.

[101] M. M. Aggarwal et al. (WA98 Collaboration), Phys. Rev. Lett. **81**, 4087 (1998), `nucl-ex/9806004`.

[102] W. Fischer et al., RHIC Collider Projections (FY 2011 − FY 2015) (2010).

[103] RHIC Polarimeter Group (2010), http://www4.rcf.bnl.gov/∼cnipol/pubdocs/Run09Offline/.

[104] A. Adare et al. (PHENIX Collaboration), Phys. Rev. D **79**, 012003 (2009).

[105] S. Belikov et al., PHENIX Internal Analysis Note **184** (2003).

[106] A. Datta et al., PHENIX Internal Analysis Note **888** (2010).

[107] H. Torii, Ph. D. thesis, Department of Physics, Kyoto University (2004).

[108] A. Bazilevsky et al., PHENIX Internal Analysis Note **176** (2003).

[109] J. T. Mitchell et al., Nucl. Instrum. Meth. **A482**, 491 (2002).

[110] A. Chikanian et al., Nucl. Instrum. Meth. **A371**, 480 (1996).

[111] K. Adcox et al. (PHENIX Collaboration), Nucl. Instrum. Meth. **A499**, 489 (2003).

[112] J. Myrheim and L. Bugge, Nucl. Instrum. Meth. **160**, 43 (1979).

[113] Particle Data Group (2009), http://pdg.lbl.gov/2009/hadronic-xsections/.

[114] W. Vogelsang, Private communication (2010).

[115] M. Cacciari, P. Nason, and R. Vogt, Phys. Rev. Lett. **95**, 122001 (2005).

[116] M. Cacciari and P. Nason, JHEP **09**, 006 (2003), `hep-ph/0306212`.

[117] M. Cacciari et al., JHEP **07**, 033 (2004), `hep-ph/0312132`.

[118] M. Cacciari et al., JHEP **05**, 007 (1998).

[119] A. Adare et al., Phys. Rev. Lett. **97**, 252002 (2006).

[120] W. A. Rolke, A. M. Lopez, and J. Conrad, Nucl. Instrum. Meth. **A551**, 493 (2005), `physics/0403059`.

[121] K. Melnikov and F. Petriello, Phys. Rev. **D74**, 114017 (2006), `hep-ph/0609070`.

[122] A. Martin, R. Roberts, W. Stirling, and R. Thorne, Eur. Phys. J. **C28**, 455 (2003), 10.1140/epjc/s2003-01196-2.

[123] D. Acosta et al. (CDF Collaboration), Phys. Rev. Lett. **94**, 091803 (2005).

[124] B. Abbott et al. (D0 Collaboration), Phys. Rev. D **61**, 072001 (2000).

[125] C. Albajar et al. (UA1 Collaboration), Z. Phys. **C44**, 15 (1989).

[126] G. Aad et al. (ATLAS Collaboration), JHEP **12**, 060 (2010), `1010.2130`.

[127] G. Bunce et al., Plans for the RHIC Spin Physics Program (2008), http://spin.riken.bnl.gov/rsc/.

[128] M. M. Aggarwal et al. (STAR Collaboration), Phys. Rev. Lett. **106**, 062002 (2011).

[129] P. J. Rijken and W. L. van Neerven, Phys. Lett. **B386**, 422 (1996), `hep-ph/9604436`.

[130] P. J. Rijken and W. L. van Neerven, Nucl. Phys. **B487**, 233 (1997), `hep-ph/9609377`.

[131] P. J. Rijken and W. L. van Neerven, Phys. Lett. **B392**, 207 (1997), `hep-ph/9609379`.

[132] L. Bourhis et al., Eur.Phys.J. **C19**, 89 (2001), `hep-ph/0009101`.

[133] S. Albino, B. Kniehl, and G. Kramer, Nucl.Phys. **B725**, 181 (2005), `hep-ph/0502188`.

[134] M. Hirai et al., Phys.Rev. **D75**, 094009 (2007), `hep-ph/0702250`.

[135] J. P. Ralston and D. E. Soper, Nuclear Physics B **152**, 109 (1979).

[136] S. Dairaku, PHENIX Internal Analysis Note **848** (2009).

[137] J. Koster, Ph. D. thesis, University of Illinois at Urbana-Champaign (2010).